frontiers | Research Topics

Ano-rectal and gastro-esophageal cancer: Diving into diagnostic and therapeutic imaging modalities for radiotherapy

Edited by
Berardino De Bari, Pierfrancesco Franco
and Letizia Deantonio

Published in
Frontiers in Oncology

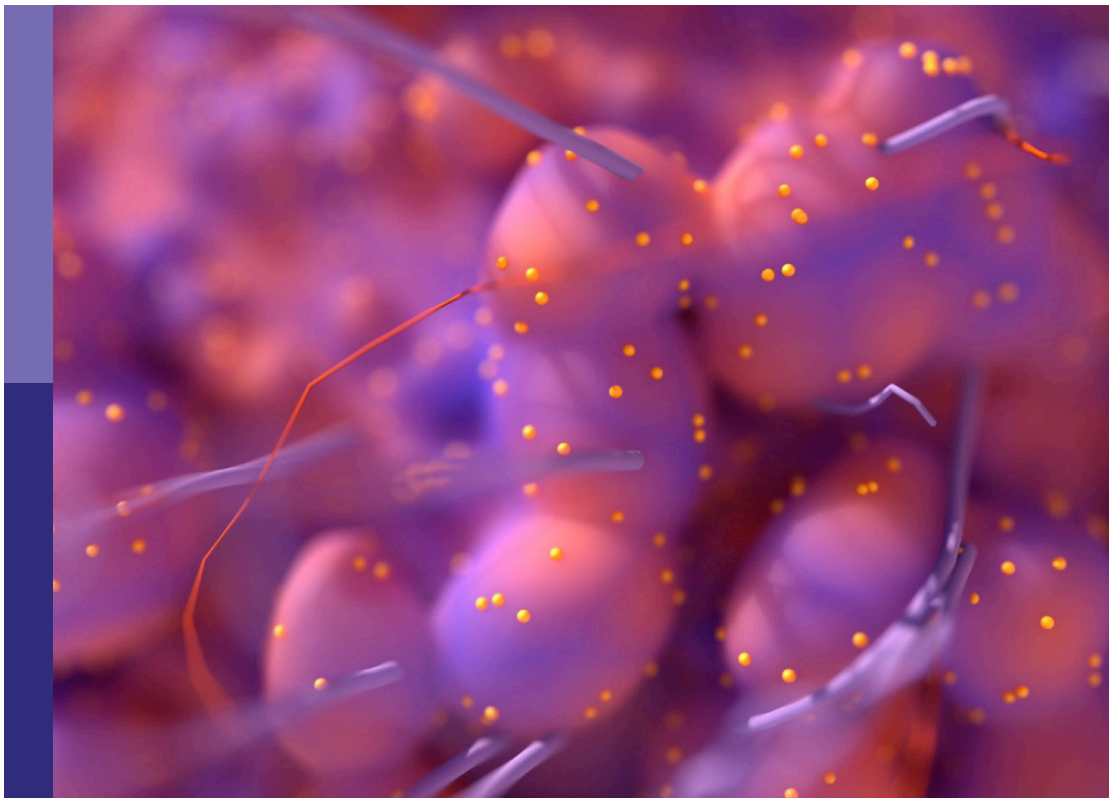

ISSN 1664-8714
ISBN 978-2-8325-3483-0
DOI 10.3389/978-2-8325-3483-0

About Frontiers

Frontiers is more than just an open access publisher of scholarly articles: it is a pioneering approach to the world of academia, radically improving the way scholarly research is managed. The grand vision of Frontiers is a world where all people have an equal opportunity to seek, share and generate knowledge. Frontiers provides immediate and permanent online open access to all its publications, but this alone is not enough to realize our grand goals.

Frontiers journal series

The Frontiers journal series is a multi-tier and interdisciplinary set of open-access, online journals, promising a paradigm shift from the current review, selection and dissemination processes in academic publishing. All Frontiers journals are driven by researchers for researchers; therefore, they constitute a service to the scholarly community. At the same time, the *Frontiers journal series* operates on a revolutionary invention, the tiered publishing system, initially addressing specific communities of scholars, and gradually climbing up to broader public understanding, thus serving the interests of the lay society, too.

Dedication to quality

Each Frontiers article is a landmark of the highest quality, thanks to genuinely collaborative interactions between authors and review editors, who include some of the world's best academicians. Research must be certified by peers before entering a stream of knowledge that may eventually reach the public - and shape society; therefore, Frontiers only applies the most rigorous and unbiased reviews. Frontiers revolutionizes research publishing by freely delivering the most outstanding research, evaluated with no bias from both the academic and social point of view. By applying the most advanced information technologies, Frontiers is catapulting scholarly publishing into a new generation.

What are Frontiers Research Topics?

Frontiers Research Topics are very popular trademarks of the *Frontiers journals series*: they are collections of at least ten articles, all centered on a particular subject. With their unique mix of varied contributions from Original Research to Review Articles, Frontiers Research Topics unify the most influential researchers, the latest key findings and historical advances in a hot research area.

Find out more on how to host your own Frontiers Research Topic or contribute to one as an author by contacting the Frontiers editorial office: frontiersin.org/about/contact

Ano-rectal and gastro-esophageal cancer: Diving into diagnostic and therapeutic imaging modalities for radiotherapy

Topic editors

Berardino De Bari — Department of Oncology, Hospital Neuchâtelois, Switzerland
Pierfrancesco Franco — University of Eastern Piedmont, Italy
Letizia Deantonio — Oncology Institute of Southern Switzerland (IOSI), Switzerland

Citation

De Bari, B., Franco, P., Deantonio, L., eds. (2023). *Ano-rectal and gastro-esophageal cancer: Diving into diagnostic and therapeutic imaging modalities for radiotherapy*. Lausanne: Frontiers Media SA. doi: 10.3389/978-2-8325-3483-0

Table of contents

05 Editorial: Ano-rectal and gastro-esophageal cancer: diving into diagnostic and therapeutic imaging modalities for radiotherapy
Letizia Deantonio, Berardino De Bari and Pierfrancesco Franco

07 Predicting Treatment Response of Neoadjuvant Chemoradiotherapy in Locally Advanced Rectal Cancer Using Amide Proton Transfer MRI Combined With Diffusion-Weighted Imaging
Weicui Chen, Liting Mao, Ling Li, Qiurong Wei, Shaowei Hu, Yongsong Ye, Jieping Feng, Bo Liu and Xian Liu

19 Rectal Tumor Stiffness Quantified by *In Vivo* Tomoelastography and Collagen Content Estimated by Histopathology Predict Tumor Aggressiveness
Jiaxi Hu, Jing Guo, Yigang Pei, Ping Hu, Mengsi Li, Ingolf Sack and Wenzheng Li

30 Fractal-Based Radiomic Approach to Tailor the Chemotherapy Treatment in Rectal Cancer: A Generating Hypothesis Study
Carmela Di Dio, Giuditta Chiloiro, Davide Cusumano, Francesco Catucci, Luca Boldrini, Angela Romano, Elisa Meldolesi, Fabio Marazzi, Barbara Corvari, Brunella Barbaro, Riccardo Manfredi, Vincenzo Valentini and Maria Antonietta Gambacorta

38 Amide Proton Transfer Weighted and Intravoxel Incoherent Motion Imaging in Evaluation of Prognostic Factors for Rectal Adenocarcinoma
Juan Li, Liangjie Lin, Xuemei Gao, Shenglei Li and Jingliang Cheng

49 Multi-Institutional Validation of Two-Streamed Deep Learning Method for Automated Delineation of Esophageal Gross Tumor Volume Using Planning CT and FDG-PET/CT
Xianghua Ye, Dazhou Guo, Chen-Kan Tseng, Jia Ge, Tsung-Min Hung, Ping-Ching Pai, Yanping Ren, Lu Zheng, Xinli Zhu, Ling Peng, Ying Chen, Xiaohua Chen, Chen-Yu Chou, Danni Chen, Jiaze Yu, Yuzhen Chen, Feiran Jiao, Yi Xin, Lingyun Huang, Guotong Xie, Jing Xiao, Le Lu, Senxiang Yan, Dakai Jin and Tsung-Ying Ho

61 Updated Evaluation of the Diagnostic Performance of Double Contrast-Enhanced Ultrasonography in the Preoperative T Staging of Gastric Cancer: A Meta-Analysis and Systematic Review
Xin Zhang, Jun Yao, Yu Zhang, Xin Huang, Weijun Wang and Hejing Huang

72 18F-FDG PET Radiomics as Predictor of Treatment Response in Oesophageal Cancer: A Systematic Review and Meta-Analysis
Letizia Deantonio, Maria Luisa Garo, Gaetano Paone, Maria Carla Valli, Stefano Cappio, Davide La Regina, Marco Cefali, Maria Celeste Palmarocchi, Alberto Vannelli and Sara De Dosso

80 Quantitative Dynamic-Enhanced MRI and Intravoxel Incoherent Motion Diffusion–Weighted Imaging for Prediction of the Pathological Response to Neoadjuvant Chemotherapy and the Prognosis in Locally Advanced Gastric Cancer
Yongjian Zhu, Zhichao Jiang, Bingzhi Wang, Ying Li, Jun Jiang, Yuxin Zhong, Sicong Wang and Liming Jiang

98 A Dual-Energy CT Radiomics of the Regional Largest Short-Axis Lymph Node Can Improve the Prediction of Lymph Node Metastasis in Patients With Rectal Cancer
Dongqing Wang, Zijian Zhuang, Shuting Wu, Jixiang Chen, Xin Fan, Mengsi Liu, Haitao Zhu, Ming Wang, Jinmei Zou, Qun Zhou, Peng Zhou, Jing Xue, Xiangpan Meng, Shenghong Ju and Lirong Zhang

frontiers | Frontiers in Oncology

TYPE Editorial
PUBLISHED 31 August 2023
DOI 10.3389/fonc.2023.1276334

OPEN ACCESS

EDITED AND REVIEWED BY
Zaver Bhujwalla,
Johns Hopkins University, United States

*CORRESPONDENCE
Letizia Deantonio
letizia.deantonio@eoc.ch

RECEIVED 11 August 2023
ACCEPTED 23 August 2023
PUBLISHED 31 August 2023

CITATION
Deantonio L, De Bari B and Franco P (2023) Editorial: Ano-rectal and gastro-esophageal cancer: diving into diagnostic and therapeutic imaging modalities for radiotherapy. *Front. Oncol.* 13:1276334. doi: 10.3389/fonc.2023.1276334

Editorial: Ano-rectal and gastro-esophageal cancer: diving into diagnostic and therapeutic imaging modalities for radiotherapy

Letizia Deantonio[1,2]*, Berardino De Bari[3] and Pierfrancesco Franco[4,5]

[1]Radiotherapy Clinic, Oncology Institute of Southern Switzerland, Ente Ospedaliero Cantonale, Bellinzona, Switzerland, [2]Faculty of Biomedical Sciences, University of Southern Switzerland, Lugano, Switzerland, [3]Department of Radiation Oncology, Réseal Hospitalier Neuchâtelois, La-Chaux-de Fonds, Switzerland, [4]Radiation Oncology Department, Azienda Ospedaliera Universitaria (AOU)'Maggiore della Carità', Novara, Italy, [5]Department of Translational Medicine, University of Eastern Piedmont, Novara, Italy

KEYWORDS

magnetic resonance imaging, PET/CT, cancer treatment, radiation therapy, radiomics

Editorial on the Research Topic
Ano-rectal and gastro-esophageal cancer: diving into diagnostic and therapeutic imaging modalities for radiotherapy

Morphologic and functional imaging applied to radiation therapy (RT) has a valuable role in both diagnostic and therapeutic setting. In recent years, there has been an increasing interest focused on imaging application as biomarker of tumor aggressiveness, treatment response, patients' survival, and radiation-induced normal tissue toxicity aimed at better personalizing treatment approaches and potentially reducing acute and late effects, together with treatment burden.

This more extensive application of imaging in upper and lower gastro-intestinal tumor is intriguing considering the new treatment approaches evaluated in several clinical trials in this clinical setting. In rectal cancer, the new evidence in favor of total neoadjuvant therapy (TNT) and organ preservation strategies may replace the standard multimodality approach according to refined risk stratification. Moreover, the concept of wait and see in squamous cell esophageal cancer after neoadjuvant concurrent chemo-radiation achieving complete clinical response is under investigation.

In this Research Topic, nine articles were published, addressing recent advances in the use of imaging as potential marker of tumor aggressiveness and predictor of treatment response in patients with upper and lower gastro-intestinal cancer.

Few studies so far have explored novel diagnostic sequences for tumor staging and treatment response.

In gastric cancer, a study by Zhu et al. showed pretreatment dynamic contrast-enhanced magnetic resonance imaging (DCE-MRI) quantitative parameters and intravoxel incoherent motion diffusion-weighted images (IVIM-DWI) to predict for

response to neoadjuvant treatment and help in recurrence free survival patients' stratification.

In the era of TNT and organ preservation strategy for rectal cancer, MR imaging has a crucial role in the therapeutic assessment both staging and treatment response in order to optimize treatment strategy. In this Research Topic, Chen et al. evaluated a particular MR sequence, amide proton transfer weighted (APTw) MRI, combined with diffusion-weighted imaging (DWI) in predicting pathological complete response (pCR) in a series of 53 locally advanced rectal cancer (LARC). Pre-APT combined with pre-DWI achieved a good diagnostic performance in predicting good response to neoadjuvant treatment (AUC 0.89). APTw MRI was also analyzed by Li et al. showed that APT helped to assess rectal cancer prognostic factors, including tumor grade, histopathological type, and extramural vascular invasion (EMVI) status, but not primary tumor (T) and lymph nodes (N) status. Similarly, to predict tumor aggressiveness Hu et al. explored the significance of collagen examined *in vivo* based on rectal tomoelastography quantified stiffness and by histologically measured collagen volume fraction (CVF). Tomoelastography is a technique based on multifrequency MR elastography with diagnostic power as shown in other tumors. The overexpression of collagen was correlated with increased tumor stiffness and high risk of tumor aggressiveness. MR elastography seemed to add diagnostic value to MRI.

Another diagnostic technique was explored for primary tumor staging of gastric cancer. In several situation, tumor identification and staging is challenging and standard imaging techniques may not be able to detect the tumor, while others may mislead accurate staging. A meta-analysis by Zhang et al. evaluated the diagnostic performance of an innovative modality, a double-enhanced ultrasonography (DCEUS), for clinical T staging in gastric cancer. The findings by the 8 studies included were promising, however, still requiring confirmation before considering DCEUS in routine clinical practice.

There has been increasing interest in radiomics as new image-based markers that can predict survival outcome to personalize treatment strategy.

One meta-analysis (Deantonio et al.) showed the promising performance of 18F-flourodeoxyglucose positron emission tomography/computed tomography (18F-FDG PET/CT)-based radiomics models in predicting pCR following neoadjuvant chemoradiation in esophageal cancer (AUC 0.81, 95% CI: 0.74-0.9). Because the evidence is based on few retrospective and monocentric studies often using in-house software, the Authors highlighted the importance of planning clinical trials with a well-designed radiomics analysis.

Of a potential great interest and worthy of further studies is the Italian hypothesis-generating study by Di Dio et al. that explored the potential of radiomics elaborating a predictive model to support oncologists in deciding which drug to prescribe between oxaliplatin-based regimen and 5-fluorouracil or capecitabine regimen for neoadjuvant treatment of LARC. The radiomics analysis of T2-weighted (T2-w) MRI seems able to predict the probability of disease-free survival (DFS) discriminating those patients who can benefit from oxaliplatin-based regimen.

A study by Wang et al. focused on the value of dual-energy CT radiomics and showed that a radiomics model combined with longest short-axis parameter may become an effective biomarker for assessing lymph node metastasis in rectal cancer.

Furthermore, Ye et al. conducted an interesting study investigating deep learning-based tumor volume delineation in esophageal cancer. Gross tumor volume (GTV) delineation is an essential task in RT planning and require efforts, expertise, and time because it is in many cases a manual process. For esophageal cancer, GTV delineation is often highly variable and radiation oncologists need contrast-enhanced CT, FDG-PET/CT and esophago-gastric endoscopy information for an accurate identification. The authors developed and validated a two- streamed three-dimensional deep learning GTV segmentation model using the planning CT or planning CT and FDG-PET/CT. The performance of the two-streamed models was better for cT3 and cT4 primary tumor improving contouring accuracy with a reduction of inter-observer variation by 37% and contouring time with an average of 48%. The deep learning methods for delineation of target volumes are interestingly studying and may be potentially clinically relevant in this crucial and time-consuming medical task also in the era of adaptive RT.

In summary, the studies published in this Research Topic explored the capability of peculiar MR sequences and radiomics features derived from MRI, CT, and 18F-FDG PET in detecting tumor aggressiveness and assessing treatment response. The primary aim was to provide new knowledge and possibilities for a tailored treatment approach in this clinical setting.

Functional imaging analysis along with radiomics need to be upfront integrated in prospective multicentric study design to achieve robust clinical results and support further evidence to enrich clinical practice.

Author contributions

LD: Conceptualization, Writing – original draft. BB: Conceptualization, Writing – review & editing. PF: Conceptualization, Writing – review & editing.

Conflict of interest

The authors declare that the research was conducted in the absence of any commercial or financial relationships that could be construed as a potential conflict of interest.

Publisher's note

frontiers in Oncology

ORIGINAL RESEARCH
published: 01 July 2021
doi: 10.3389/fonc.2021.698427

Predicting Treatment Response of Neoadjuvant Chemoradiotherapy in Locally Advanced Rectal Cancer Using Amide Proton Transfer MRI Combined With Diffusion-Weighted Imaging

*Weicui Chen[1], Liting Mao[1], Ling Li[1], Qiurong Wei[1], Shaowei Hu[2], Yongsong Ye[1], Jieping Feng[1], Bo Liu[1] and Xian Liu[1]**

[1] Department of Radiology, The Second Affiliated Hospital, Guangzhou University of Chinese Medicine, Guangzhou, China, [2] Department of Pathology, The Second Affiliated Hospital, Guangzhou University of Chinese Medicine, Guangzhou, China

OPEN ACCESS

Edited by:
Pierfrancesco Franco, University of Eastern Piedmont, Italy

Reviewed by:
Luca Boldrini, Dipartimento di Radioterapia Oncologica, Fondazione Policlinico A. Gemelli IRCCS, Italy
Luciana Caravatta, SS Annunziata Polyclinic Hospital, Chieti, Italy

***Correspondence:**
Xian Liu
liuxian74@hotmail.com

Specialty section:
This article was submitted to Cancer Imaging and Image-directed Interventions, a section of the journal Frontiers in Oncology

Received: *21 April 2021*
Accepted: *03 June 2021*
Published: *01 July 2021*

Citation:
Chen W, Mao L, Li L, Wei Q, Hu S, Ye Y, Feng J, Liu B and Liu X (2021) Predicting Treatment Response of Neoadjuvant Chemoradiotherapy in Locally Advanced Rectal Cancer Using Amide Proton Transfer MRI Combined With Diffusion-Weighted Imaging. Front. Oncol. 11:698427. doi: 10.3389/fonc.2021.698427

Objective: To evaluate amide proton weighted (APTw) MRI combined with diffusion-weighted imaging (DWI) in predicting neoadjuvant chemoradiotherapy (NCRT) response in patients with locally advanced rectal cancer (LARC).

Methods: 53 patients with LARC were enrolled in this retrospective study. MR examination including APTw MRI and DWI was performed before and after NCRT. APTw SI, ADC value, tumor size, CEA level before and after NCRT were assessed. The difference of the above parameters between before and after NCRT was calculated. The tumor regression grading (TRG) was assessed by American Joint Committee on Cancer's Cancer Staging Manual AJCC 8th score. The Shapiro-Wilk test, paired t-test and Wilcoxon Signed Ranks test, two-sample t-test, Mann-Whitney U test and multivariate analysis were used for statistical analysis.

Results: Of the 53 patients, 19 had good responses (TRG 0-1), 34 had poor responses (TRG 2-3). After NCRT, all the rectal tumors demonstrated decreased APT values, increased ADC values, reduced tumor volumes and CEA levels (all $p < 0.001$). Good responders demonstrated higher pre-APT values, higher Δ APT values, lower pre- ADC values and higher Δ tumor volumes than poor responders. Pre-APT combined with pre-ADC achieved the best diagnostic performance, with AUC of 0.895 (sensitivity of 85.29%, specificity of 89.47%, $p < 0.001$) in predicting good response to NCRT.

Conclusion: The combination of APTw and DWI may serve as a noninvasive biomarker for evaluating and identifying response to NCRT in LARC patients.

Keywords: Amide proton transfer, diffusion-weighted imaging, neoadjuvant chemoradiotherapy, locally advanced rectal cancer (LARC), treatment response

HIGHLIGHTS

- After NCRT, All the rectal tumors demonstrated decrease APT values, increased ADC values, reduced tumor volumes and CEA levels.
- Good responders to NCRT demonstrated higher pre-APT values, higher Δ APT values, lower pre-ADC values and higher Δ tumor volumes than poor responders.
- A combination of APT and ADC values before NCRT exhibited a good diagnostic performance in predicting a good response to NCRT (with AUC of 0.895, sensitivity of 85.29% and specificity of 89.47%).

INTRODUCTION

Currently, preoperative neoadjuvant chemoradiotherapy (NCRT) followed by total mesorectal excision surgery is the standard treatment protocol for locally advanced rectal cancer (LARC) (1). NCRT aims to downstage the tumor, enable complete surgical resection, and reduce the risk of recurrence and metastases (2). Some strictly selected patients can even achieve complete clinical response with a "wait and see" policy after NCRT, avoiding surgical treatment (3). However, significant unexplained variation remains in the responses to NCRT. A series of clinical trials demonstrated that 8% to 27.5% of patients who achieved pathologic complete response (pCR) after NCRT have a better long-term outcome, lower recurrence risk, and improved overall survival (4). Approximately 54–75% of patients had tumor downstaging, and the remainder had no treatment response. Therefore, predicting the response to NCRT is important for patients with potentially curable LARC who wish to explore personalized treatment to improve their therapeutic outcomes.

MRI plays an important role in the therapeutic assessment of rectal carcinoma, particularly beneficial to surgical planning and optimize treatment strategies for patients with different responses (5). MR-based tumor regression grade (mrTRG) was validated to be associated with disease-free and survival outcomes by The MRI and Rectal Cancer European Equivalence (MERCURY) trial (6). However, conventional T2WI MRI is limited by its inability to differentiate post-therapeutic edema and fibrosis from residual tumor tissue. Morphological parameters were also proved to be helpful in assessing pCR. Some studies demonstrated a significant correlation between tumor volume reduction and pCR (7–9). Furthermore, Fiorino C et al. introduced an early regression index based on a logarithmic transformation of change in tumor volume (10). This new predictive index showed great discriminative power in evaluating tumor response to NCRT and long-term disease-free survival (10, 11). Functional MRI, such as diffusion-weighted imaging (DWI) and dynamic-contrast-enhanced MRI (DCE-MRI) can provide additional physiological information about a tumor's cellular environment and perfusion characteristics, offering great potential to assess the therapeutic response of rectal cancer (12–15). DWI has been widely used in the evaluation of tumor response to NCRT in rectal cancer, as its capability of providing information on tumor cellular architecture. However, results regarding the use of ADC in predicting the NCRT response have been inconsistent. This variation may be due to a lack of standardized imaging, acquisition techniques, and analysis methods (5, 12).

Lately, considerable progress has been made in devising radiomics or deep learning techniques to assess the treatment response of NCRT in LARC (13, 16, 17). Horvat et al. found that radiomics provided a significantly greater diagnostic capability than T2WI or DWI alone when using a random forest classifier to investigate T2WI-based radiomics while evaluating complete clinical response in rectal cancer patients after NCRT (17). Zhang et al. used a deep learning model based on diffusion kurtosis MRI to predict pCR in assessing the response of LARC after NCRT. The deep learning model showed good diagnostic performance and aided radiologists in assessing pCR (18). However, these extracted radiomics features depend on image acquisition, reconstruction, and processing methods, which naturally vary among different institutes and operators (19). Their clinical application is restricted by reproducibility and reliability. Besides, the deep learning model is typically too complex to interpret the relationship between extracted properties and tumor biology (20). To our knowledge, a reliable classification system has yet to be developed.

Amide proton transfer-weighted (APTw) MRI is a molecular MRI technique based on chemical exchange saturation transfer (CEST), which is achieved through qualifying the exchange between amide proton (-NH) groups of endogenous mobile proteins/peptides and bulk water (21). The APTw signal is related mainly to the concentration of mobile proteins, making it beneficial for assessing tumor grade and differentiation (22–24). Clinical APTw imaging has also shown promise in tumor monitoring in gliomas. Several studies have reported that APTw imaging helps differentiate between pseudo-progression, radiation necrosis, and tumor recurrence in gliomas (25)—it is superior to conventional MRI contrasts as well as to advanced functional imaging methods such as perfusion (dynamic susceptibility contrast and dynamic-contrast-enhanced) and spectroscopy (24, 26–28). However, only one study assessed APTw MRI in evaluating the effect of chemoradiotherapy in LARC (29).

Therefore, considering the characteristics of APTw imaging and DWI, we aimed to investigate the value of APTw imaging combined with DWI for predicting the treatment response of NCRT in patients with LARC.

Abbreviations: ADC, apparent diffusion coefficient; APT, amide proton transfer; AUC, area under the curve; CEST, chemical exchange saturation transfer; DCE, dynamic contrast enhanced; DWI, diffusion weighted; LARC, locally advanced rectal cancer; NCRT, neoadjuvant chemoradiotherapy; ROC, receiver operating characteristic; ROI, region of interest; SD, standard deviation; pCR, pathologic complete response; TRG, tumor regression grade.

MATERIALS AND METHODS

Participants

The current study was approved by the Medical Ethics Committee of our hospital (Ref. No. YE2019-274-01) and written informed consent was obtained from each patient before the MR examination. Between February 2019 to May 2021, 88 consecutive patients diagnosed with LARC were included. All the patients received preoperative NCRT followed by TME surgery.

The inclusion criteria were as follows: 1) biopsy-proven rectal non-mucinous adenocarcinoma histologically, 2) LARC (category cT3 or cT4, node-positive status) defined on primary MR staging, 3) treatment consisting of NCRT followed by surgical resection. The exclusion criteria were as follows: 1) recurrent rectal cancer, (b) additional treatment (targeted therapy or immunotherapy), 3) interval between restaging rectal MRI and surgery of more than three months, 4) NCRT was incomplete, 5) poor image quality (included motion artifacts and image distortion from susceptibility effect due to bowel gas). **Figure 1** displays the patient selection flowchart.

NCRT Treatment

NCRT consisted of 45–50 Gy of radiation delivered in daily doses of 1.5 or2 Gy, five fractions per week, and concomitant chemotherapy. Neoadjuvant chemotherapy regimens were as follows: (1) oxaliplatin 130 mg/m^2 (iv gtt, d1) and capecitabine 1000 mg/m^2 (per os, bid, d1-14) every three weeks for 6–8 courses (XELOX) in eighteen patients; (2) folinic acid 200 mg/m^2 (d1), fluorouracil 400 mg/m^2 (d1), fluorouracil 2400 mg/m^2 (d1-d2), and oxaliplatin 85mg/m^2 (d1) for 3–7 courses (mFOLFOX6) in ten patients; (3) capecitabine 1250 mg/m^2 (per os, bid, d1-d14) for 3–6 courses in 25 patients. Surgery with total mesorectal excision was performed within 6–8 weeks after the completion of NCRT.

MRI Protocol

All participants received two MRI examinations: the first within one week before NCRT (pre-NCRT MRI) and the second within one week before surgery (post-NCRT MRI).

All MRI examinations were performed on a 3.0T MRI scanner (Ingenia, Philips Healthcare, Best, the Netherlands) using a 32-channel phased-array coil. A glycerin enema was performed before the examination to reduce distortion due to gas in the rectum. At 30 min before the MR examination, 5 mg of raceanisodamine hydrochloride was injected intramuscularly to reduce peristaltic movement.

The initial sagittal and axial T2-weighted turbo spin echo (TSE) sequences were performed to determine the location of the rectal tumor. For APTw imaging, we used the Philips product implementation. More specifically, axial APTw images were acquired using a 3D TSE mDIXON sequence. The B1 field strength was 2 μT; continuous RF saturation pulse train had a duration of 2 s. The entire z-spectrum contains nine images acquired at various saturation frequency offsets, including ±3.5, ± 3.42, ± 3.58, and −1560 ppm. To enhance the signal-to-noise ratio in the APTw images, three of the Z-spectral images are acquired at +3.5 ppm using different echo shifts on the order of 0.5 ms. This allows us to calculate a B0 field map directly from APTw image acquisition *via* the mDIXON algorithm. Correction of B0 field homogeneity was achieved by a Lagrange interpolation among the different saturation frequency offsets on a voxel-by-voxel basis. mDIXON was applied to suppress lipid artifacts in APTw images. Other imaging parameters were as follows:

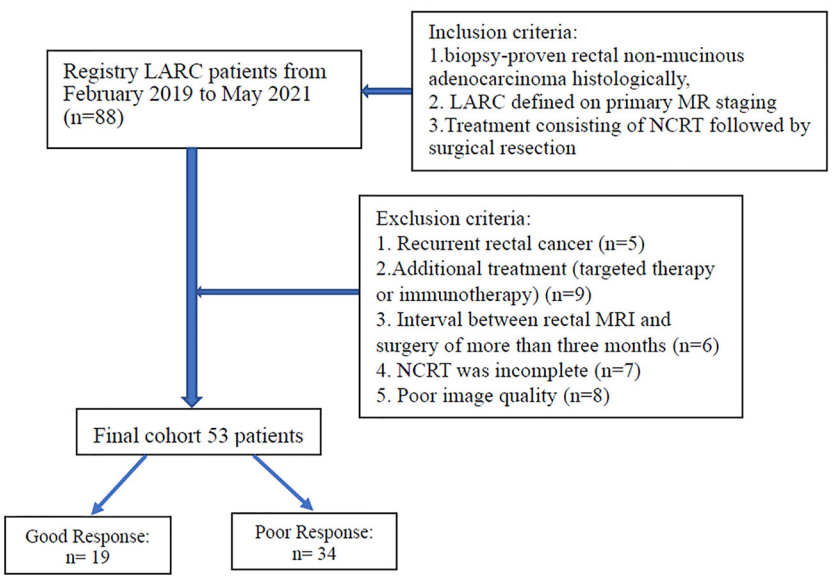

FIGURE 1 | Flowchart of patient selection.

repetition time (TR)/echo time (TE): 5864 ms/10 ms; field of view (FOV) 250 × 346; section thickness 5 mm; voxel size 1.8 × 1.8 × 5 mm; TSE factor 35.

Other MR sequences included high-resolution T2-weighted imaging (Turbo SE, TR/TE: 3900/100 ms, flip angle 90°, FOV 200 × 200 mm, section thickness 3 mm, matrix 288 × 228, TSE factor 17) in the axial, coronal, and sagittal planes; conventional axial DWI (echo planar SE, TR/TE 3000/72 ms, flip angle 90°, b = 0, 1000 s/mm^2, section thickness 3 mm, matrix 82 × 82); plain and gadolinium-enhanced T1-weighted (turbo spin echo, TR/TE 578/10 ms, FOV 240 × 240 mm, section thickness 3 mm, matrix 300 × 230) in the axial, coronal, and sagittal planes.

Image Analysis

All raw data were transferred to an Intellispace Portal workstation (Philips Healthcare, Best, the Netherlands). According to the principle of the APT algorithm, APTw signal was defined as the asymmetric magnetization transfer ratio (MTR_{asym}) at 3.5ppm from the corrected Z spectrum and displayed as amide proton transfer weighted percentage.

$$MTR_{asym}(3.5ppm) = \frac{S_{sat}(-3.5ppm) - S_{sat}(+3.5ppm)}{S_0},$$

where MTR_{asym} [+3.5 ppm] is magnetization transfer ratio (MTR) asymmetry at +3.5 ppm offset frequency, and S_{sat} and S_0 are the signal intensity acquired with and without selective saturation, respectively.

$$\text{APTw SI} = \text{MTRasym}\,[\Delta\omega = +3.5\ \text{ppm}](\%).$$

The apparent diffusion coefficient (ADC) was calculated from two DWI image sets of different b values (b = 0, 1000 s/mm^2).

Image analysis was performed in consensus by two radiologists (YY and LM, with 20 and 10 years of experience in rectal cancer MRI, respectively) identified rectal lesions from T2WI together with DWI images. For quantitative analysis of APT SI, MRIcro software was used for manual segmentation of the rectal tumor. The outline of the rectal tumor was drawn manually with a freehand tool on high-resolution T2WI images and defined as the region of interest, avoiding the intestinal cavity. The region of interest was then copied to the corresponding APT image to obtain the average APT SI. The mean APT SI values of all slices were recorded for further analysis.

The changes in APT (ΔAPT) and ADC (ΔADC) values were defined as the difference between the corresponding post and pre-values.

Tumor Volume Evaluation

Tumor volume was measured before and after NCRT by manually drawing the tumor margin with a PACS system (YLZ Ruitu Information Technology, Guangzhou, China) on T2-weighted images comprising the continuous tumor-containing image. The whole-tumor volume was then calculated by adding up each cross-sectional volume. Two radiologists (YY and LM) assessed the images in consensus. Tumor volume reduction (Δ tumor volume) was calculated as follows:

$$\Delta\ \text{tumor volume} = \text{pre-tumor volume} - \text{post-tumor volume}$$

Carcinoembryonic Antigen (CEA) Level Evaluation

Serum CEA levels were measured by the chemiluminescent method. The normal range of CEA is < 5ng/ml. Serum CEA levels before (pre-CEA) and after NCRT (post-CEA) were assessed approximately one week before CRT and within one week before surgery, respectively. The reduction of CEA was calculated as follows: ΔCEA = post-CEA – pre-CEA.

Histological Analysis

All resected specimens were fixed in buffered formalin, embedded in paraffin and then made into 4-μm tissue sections for pathologic diagnosis. A pathological evaluation was performed by one pathologist (HS, with 21 years of experience). The pathologic tumor staging and tumor response to CRT were assessed according to the criteria described in the American Joint Committee on Cancer's Cancer Staging Manual (AJCC 8th edition) (30). The grade of tumor response to CRT was classified into four categories: TRG 0 (complete regression): no residual cancer cells; TRG 1 (near-complete regression): single or small groups of cancer cells; TRG 2 (moderate regression): residual cancer with desmoplastic response; TRG 3 (minimal regression): minimal evidence of tumor response. Patients with TRG 0–1 were considered to have a good response, whereas those with TRG 2–3 were considered to show a poor response to CRT (30).

Statistical Analysis

Statistical analysis was performed using SPSS 20.0 (IBM, Armonk, New York) and MedCalc Statistical Software version 19.1.2 (MedCalc Software bv, Ostend, Belgium; https://www.medcalc.org; 2019).

The inter-class correlation coefficient was used to assess inter-observer agreement for the measurement of APT values, ADC values, and tumor volume values before and after NCRT. Inter-class correlation coefficient estimates above 0.75 were considered to have good reliability.

The Shapiro-Wilk test was used to determine the normality of data distribution. The paired t-test (normal distribution) and Wilcoxon signed-rank test (normality test failed) were used to assess the changes in APT, ADC, tumor volume, and CEA level between pre-NCRT and post-NCRT. A two-sample t-test and Mann-Whitney U test were used to assess the difference in the variances between good responders and poor responders. Logistic regression analysis was used to combine pre-APT and pre-ADC values to build a multi-parametric model. The Hosmer- Lemeshow test was used to measure the goodness- of- fit of the multivariate logistic model, and odds ratio (OR) and 95% CI was calculated.

Receiver operating characteristic (ROC) curve analysis was performed to evaluate the ability of six MR parameters (pre-APT& pre-ADC, pre-APT, pre-ADC, ΔAPT, ΔADC and

Δ tumor volume) in discriminating good responders from poor responders. The sensitivity, specificity, positive predictive value (PPV), and negative predictive value (NPV) were calculated. A pairwise comparison of receiver-operating-characteristic curves was applied to test for significant differences between the areas under six receiver-operating-characteristic curves. A statistically significant difference was defined to be $p < 0.05$.

RESULTS

Patient Characteristics

Eventually, 53 patients (average age, 60.2 years; range, 31–85 years) met the inclusion criteria and were enrolled in this study, consisting of 15 females and 38 males. The distribution of patients' characteristics, including age, sex, histologic grade, TNM stage, and TRG status, is shown in **Table 1**. Of the 53 patients, 19 patients were defined as good responders (TRG 0–1) and 34 patients as poor responders (TRG 2-3).

TABLE 1 | Clinic pathologic characteristics of enrolled patients.

Characteristic	Number of Patients
Age (y)	31-85y (60.2±12.6y)*
Gender	
Male	38
Female	15
Clinical Stage before NCRT	
cT3N+	26
cT4N0	16
cT4N+	11
Histological grade	
G1 (Well differentiated)	
G2 (Moderately differentiated)	45
G3 (Poorly differentiated)	8
ypT Stage	
T2	10
T3	36
T4	7
ypN Stage	
N0	16
N1a	20
N1b	11
N1c	N/A
N2a	6
N2b	N/A
Tumor regression grade (TRG)	
TRG 0	6
TRG 1	13
TRG 2	27
TRG 3	7
Good Responders	19
Bad Responders	34

*Unless otherwise indicated, data are numbers of patients. *Data are mean ± standard deviation (range). Staging of tumors and TRG were in accordance with American Joint Committee on Cancer TNM classification. Grading of tumors was based on the WHO grading criteria.*

Inter-Observer Agreement

The interclass correlation coefficient of the two observers' measurements were 0.934 (95% CI: 0.876–0.966) for pre-APT, 0.856 (95% CI: 0.739–0.923) for post-APT, 0.840 (95% CI:0.711–0.915) for pre-ADC, 0.862 (95% CI: 0.748–0.926) for post-ADC, 0.990 (95% CI: 0.981–0.995) for pre-volume, and 0.973 (95% CI 0.946–0.986) for post-volume. The two observers' measurements of APT values, ADC values and tumor volumes showed strong agreement (**Table 2**).

Comparison of APT, ADC, Tumor Volume, and CEA Level Between Pre- and Post-NCRT

After NCRT, all the rectal tumors had lower APT values (2.794 ± 0.575 vs 1.687 ± 0.527, t = 12. 315, p < 0.001) and higher ADC values (1.020 ± 0.105 $10^{-3}mm^2/s$ vs 1.120 ± 0.111 10^{-3} mm^2/s, t = -10.475, p < 0.001). The tumor volume decreased significantly from a median of 31.95 cm^3 (range 7.68–115.60 cm^3) before NCRT to a median of 11.73 cm^3 (range 1.25–42.50 cm^3) after NCRT (z = -6.334, p < 0.001). A median volume reduction rate of 63.3% was found. The CEA level decreased significantly from a median of 21.87ng/ml (range of 3.26–169.70 ng/ml) before NCRT to a median of 5.30 ng/ml (range 0.81–63.04 ng/ml) after NCRT (z = -6.335, p < 0.001) (**Figure 2**).

Parameter Comparison Between Good and Poor Responders to NCRT

Significant differences were found between good and poor responders for pre-APT values, Δ APT, pre-ADC, and Δ tumor volume. The good responder group demonstrated higher pre-APT values, higher ΔAPT values, lower pre-ADC values and higher Δ tumor volumes than the poor responder group (**Figures 3**–**6**). However, no difference was found in post-APT values, post-ADC values, ΔADC values, pre-volumes, post-volumes, pre-CEA levels, post-CEA levels and ΔCEA levels between the good and poor responder groups (all p > 0.05) (**Table 3**).

Diagnostic Capacity of APT and ADC in Predicting NCRT Treatment Response

The significant level of the Hosmer-Lemeshow test was 0.245, ORs of pre-APT and pre-ADC were 0.044 (p<0.001), 0.001 (p=0.006), respectively, suggesting the fit of the model had good goodness.

The sensitivity, specificity, PPV, and NPV of pre-APT combined with pre-ADC, pre-APT, ΔAPT, pre-ADC value, ΔADC and Δ tumor volume for predicting the response to

TABLE 2 | ICC for APT, ADC and volume values before and after NCRT measured by two radiologists.

	Pre-APT	Post-APT	Pre-ADC	Post-ADC	Pre-Volume	Post-Volume
ICC (95% CI)	0.934 (0.876-0.966)	0.856 (0.739–0.923)	0.840 (0.711-0.915)	0.862 (0.748-0.926)	0.990 (0.981-0.995)	0.973 (0.946-0.986)

ICC, interclass correlation coefficient; 95% CI, 95% confidence interval.

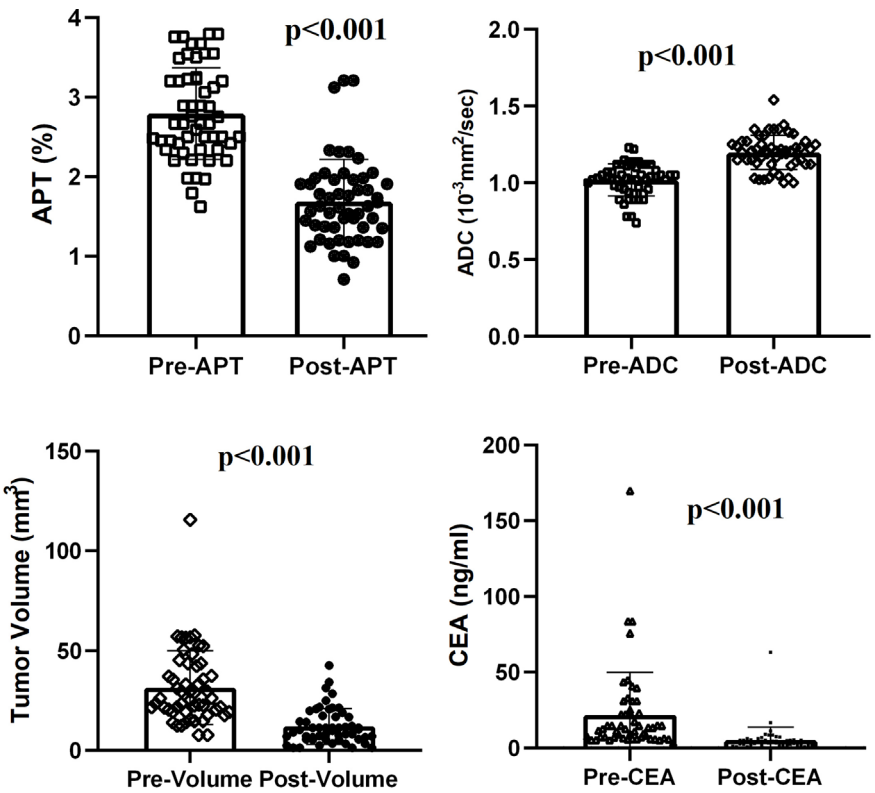

FIGURE 2 | Comparison of APT, ADC, tumor volume, and CEA level between pre- and post-NCRT.

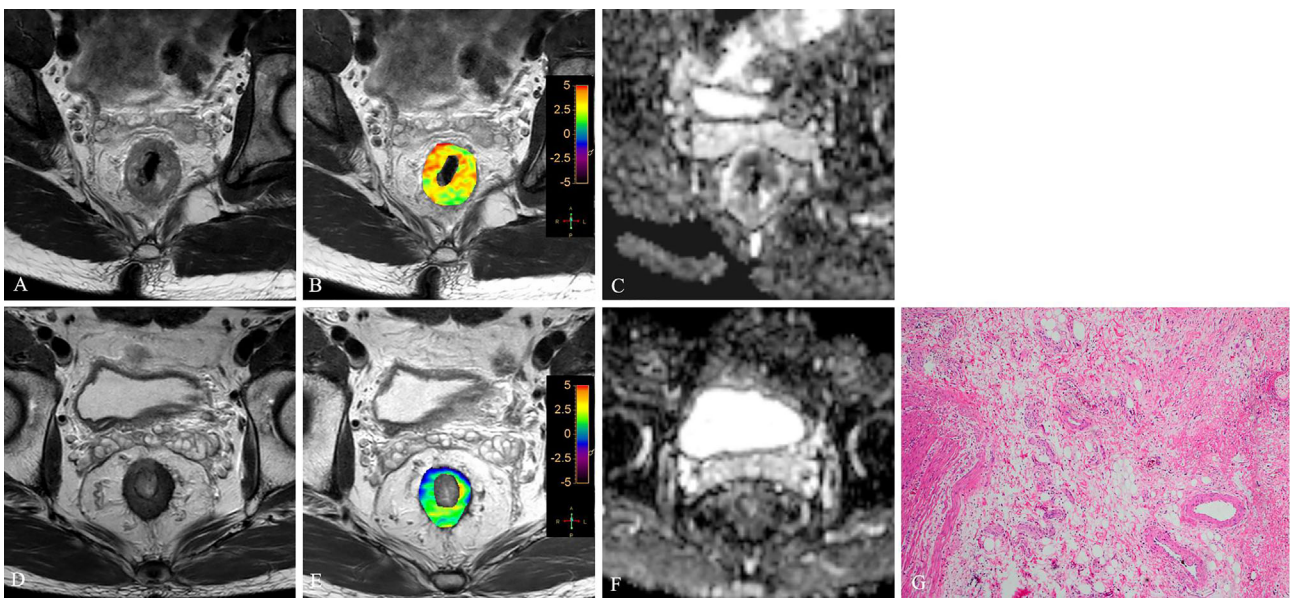

FIGURE 3 | T2WI **(A, D)**, APTw **(B, E)** and ADC map **(C, F)** of a 63-year-old male with LARC before and after NCRT. At 8 weeks after NCRT, compared to the MR performed at baseline **(A–C)**, the mean APTw SI decreased from 3.23% **(B)** to 1.54%, the mean ADC value increased from $1.042\times10^{-3}mm^2/s$ **(C)** to 1.112×10^{-3} mm^2/s **(F)**. Histopathological examination after surgery shows the degree of tumor regression is TRG 0 (H. E staining, ×40, **G**).

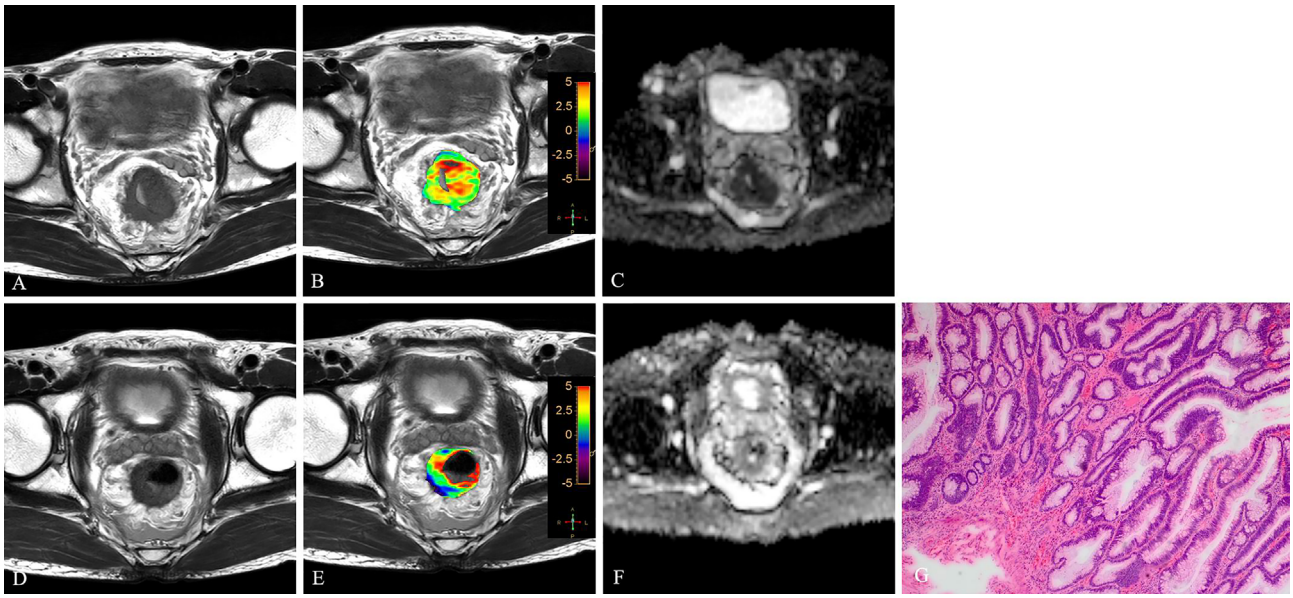

FIGURE 4 | T2WI **(A, D)**, APTw **(B, E)** and ADC map **(C, F)** of a 56-year-old male with LARC before and after NCRT. At 8 weeks after NCRT, compared to the MR performed at baseline **(A–C)**, the mean APTw SI decreased from 3.20% **(B)** to 1.614%, the mean ADC value increased from $0.89\times10^{-3}mm^2/s$ **(C)** to 1.234×10^{-3} mm^2/s **(F)**. Histopathological examination after surgery shows the degree of tumor regression is TRG 1 (H. E staining, ×40, **G**).

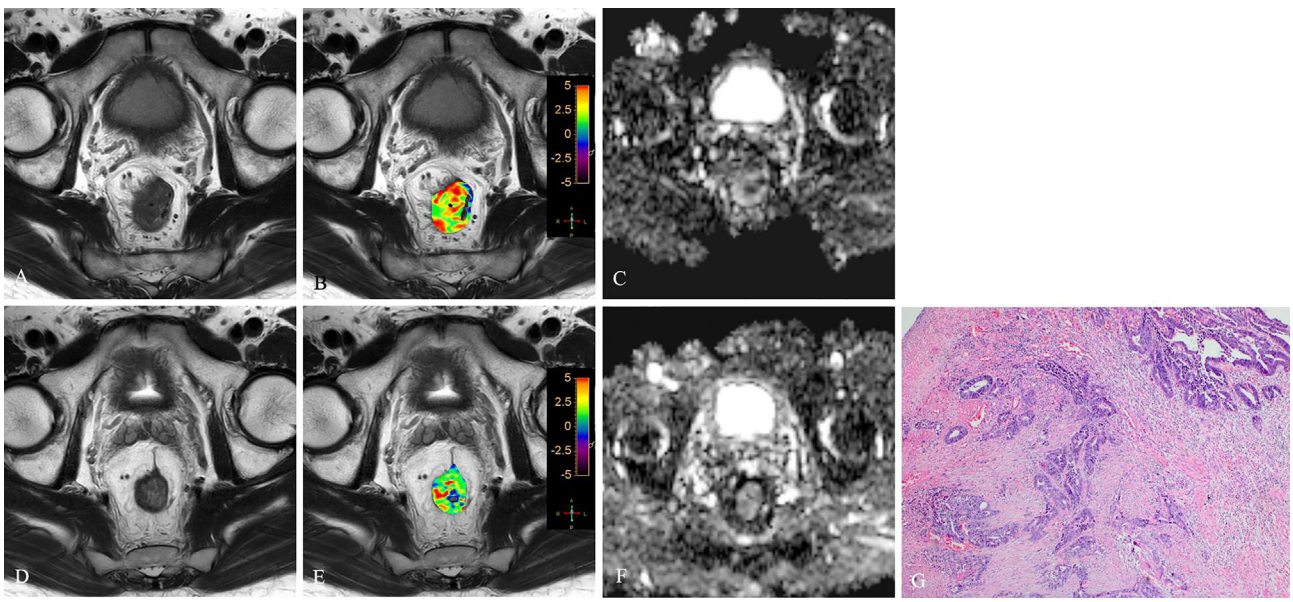

FIGURE 5 | T2WI **(A, D)**, APTw **(B, E)** and ADC map **(C, F)** of a 51-year-old female with LARC before and after NCRT. At 6 weeks after NCRT, compared to the MR performed at baseline **(A–C)**, the mean APTw SI decreased from 2.20% **(B)** to 1.783%, the mean ADC value increased from $1.120\times10^{-3}mm^2/s$ **(C)** to 1.205×10^{-3} mm^2/s **(F)**. Histopathological examination after surgery shows the degree of tumor regression is TRG 3 (H. E staining, ×40, **G**).

NCRT are summarized in **Table 4**. The AUCs were 0.895, 0.800, 0.778, 0.691, 0.543 and 0.680 for pre-APT& pre-ADC, pre-APT, pre-ADC, ΔAPT, ΔADC and Δ tumor volume, respectively. A combination of APT and ADC values before NCRT achieved a sensitivity of 85.29% and specificity of 89.47% for predicting a good response to NCRT, whereas PPV and NPV were 93.50% and 77.30%, respectively (**Table 4**). Compare to pre-ADC, ΔADC and Δ tumor volume, pre-APT combined with pre-

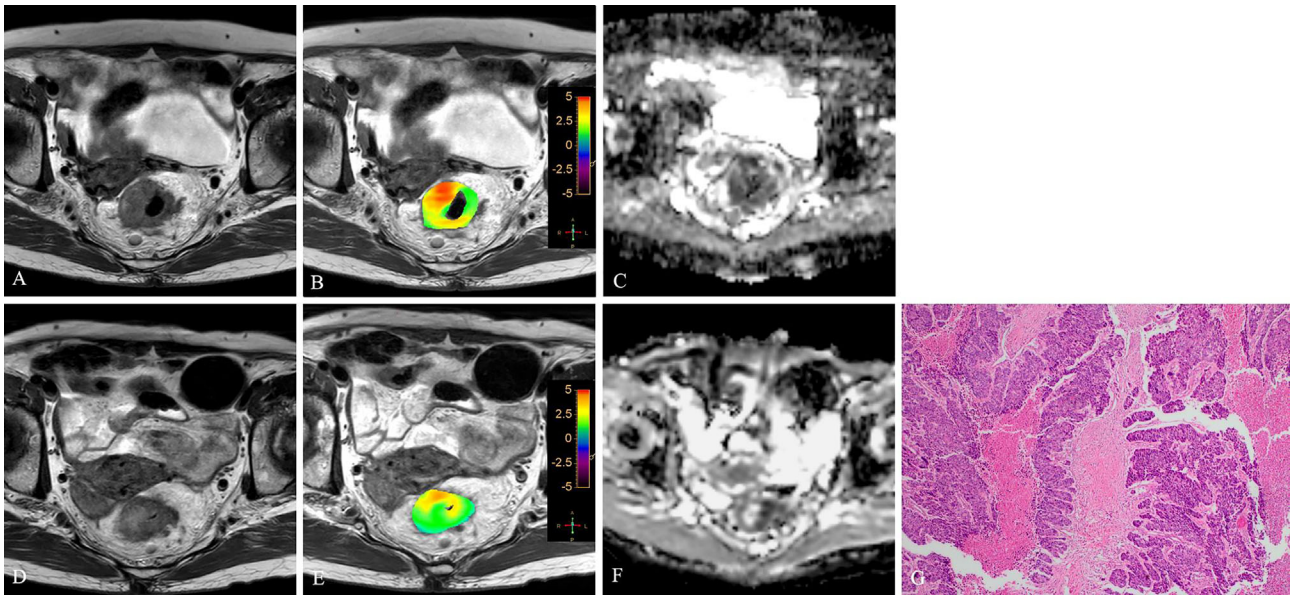

FIGURE 6 | T2WI **(A, D)**, APTw **(B, E)** and ADC map **(C, F)** of a 47-year-old male with LARC before and after NCRT. At 6 weeks after NCRT, compared to the MR performed at baseline **(A–C)**, the mean APTw SI decreased from 2.50% **(B)** to 1.83%, the mean ADC value increased from $1.040\times10^{-3}mm^2/s$ **(C)** to 1.245×10^{-3} mm^2/s **(F)**. Histopathological examination after surgery shows the degree of tumor regression is TRG 3 (H. E staining, ×40, **G**).

TABLE 3 | Comparison of variables between good and poor responders.

	Responders	Two-sample T test (Mean± SD)	Mann-Whitney U Test (Mean Rank)	Z	*P value*
Pre-APT (%)	Good (n=19)	3.222 ± 0.516			<0.001
	Poor (n=34)	2.554 ± 0.459			
Post-APT (%)	Good (n=19)		28.26	-0.045	0.656
	Poor (n=34)		32.00		
Δ APT (%)	Good (n=19)		18.05	-3.154	0.002
	Poor (n=34)		32.00		
Pre-ADC	Good (n=19)	0.970 ± 0.107			0.009
($10^{-3}mm^2/s$)	Poor (n=34)	1.047 ± 0.095			
Post-ADC	Good (n=19)	1.162 ± 0.118			0.09
($10^{-3}mm^2/s$)	Poor (n=34)	1.216 ± 0.103			
Δ ADC	Good (n=19)		28.71	-0.604	0.546
($10^{-3}mm^2/s$)	Poor (n=34)		26.04		
Pre-Volume (mm^3)	Good (n=19)		30.63	-1.286	0.202
	Poor (n=34)		24.97		
Post-Volume (mm^3)	Good (n=19)		25.97	-0.362	0.718
	Poor (n=34)		27.57		
Δ Volume (mm^3)	Good (n=19)		33.11	-2.152	0.031
	Poor (n=34)		23.59		
Pre-CEA (ng/ml)	Good (n=19)		24.74	-0.795	0.425
	Poor (n=34)		28.26		
Post-CEA (ng/ml)	Good (n=19)		28.53	-0.538	0.591
	Poor (n=34)		26.15		
Δ CEA (ng/ml)	Good (n=19)		23.37	-1.280	0.201
	Poor (n=34)		29.03		

Data are means ± standard deviations (normal distribution), mean rank (normal distribution failed). ADC values are given in $10^{-3}mm^2/sec$, volume is given in mm^3, CEA level is given in ng/ml.

ADC showed greater diagnostic performance (p=0.019, p<0.001and p= 0.013, respectively). However, there was no statistical difference among pre-APT & ADC, pre-APT, and Δ APT (all p>0.05) (**Figure 7**).

DISCUSSION

In this study, we investigated the ability of APTw MRI combined with DWI to evaluate pathologic tumor down-staging and predict

TABLE 4 | Performance of different MR parameters in predicting NCRT response in the patients with LARC.

Parameter	AUC	*P* value	Youden Index	Sensitivity (%)	Specificity (%)	PPV (%)	NPV (%)
Pre-APT & Pre-ADC	0.895 (0.780-0.962)	<0.001	0.748	85.29	89.47	93.5	77.3
Pre-APT (%)	0.824 (0.694-0.915)	<0.001	0.517	88.24	68.42	88.3	76.5
Δ APT (%)	0.763 (0.626-0.869)	<0.001	0.543	91.18	63.16	81.6	80.0
Pre-ADC ($10^{-3}mm^2/s$)	0.707 (0.566-0.824)	0.007	0.333	91.18	42.11	73.8	72.7
Δ ADC ($10^{-3}mm^2/s$)	0.550 (0.408-0.687)	0.558	0.156	73.52	42.11	69.4	47.1
Δ tumor volume (mm^3)	0.680 (0.537-0.801)	0.030	0.495	70.59	78.95	68.6	44.4

Data in parentheses are numerators and denominators and data in brackets are 95% confidence intervals. APT, amide proton transfer; ADC, apparent diffusion coefficient; AUC, area under curve; NPV, negative predictive value; PPV, positive predictive value.

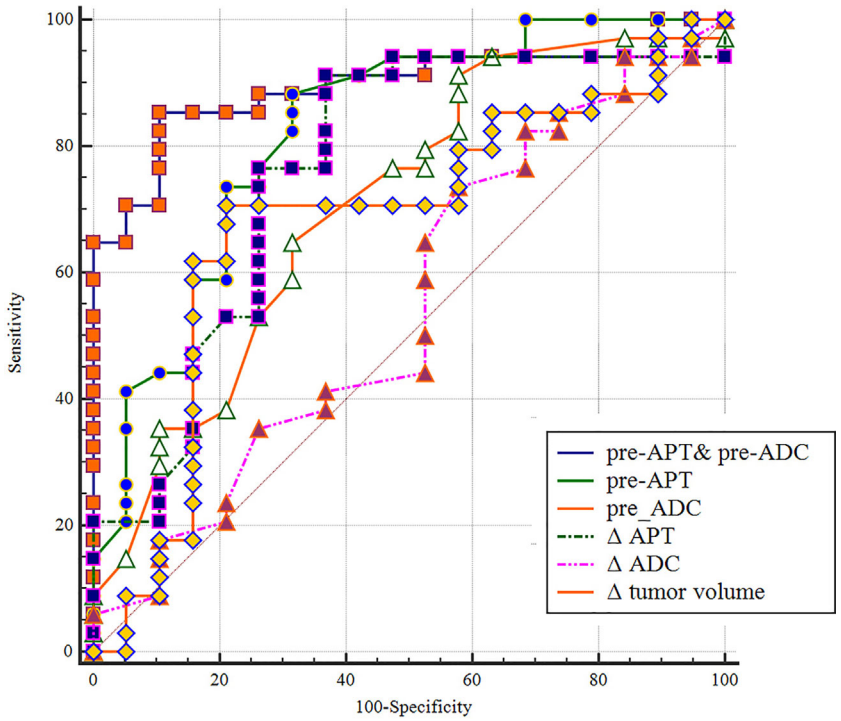

FIGURE 7 | A comparison of the diagnostic capability in predicting in discriminating good responders from poor responders between pre-APT & pre-ADC, pre-APT, pre-ADC, ΔAPT, ΔADC and Δ tumor volume. ROC analysis shows pre-APT combine with pre-ADC has a higher AUC (0.895) than the other parameters.

treatment responses after NCRT in rectal adenocarcinoma. After NCRT, all rectal tumors demonstrated significantly lower APT values and higher ADC values, as well as significantly smaller tumor volumes and lower CEA levels. APTw imaging is a new MRI contrast method based on CEST, using the signal of amide protons (NH groups) contained in proteins and peptides. It has been suggested that endogenous mobile cytoplasmic proteins are the major source of APT signals (31). NCRT causes a series of pathological changes in rectal cancer, including cellular damage, tumor necrosis, local inflammatory reaction, and fibrosis replacing tumor glands (32), which leads to a lower content of proteins and peptides than in viable tumors and thus is expected to demonstrate a lower APTw signal. However, the increase in ADC after NCRT is due to increased diffusion of water molecules caused by cell damage, tumor necrosis, and extracellular edema.

When we compared these parameters between different therapeutic effect groups, we noted that the good responders demonstrated significantly higher APT values and lower ADC values before NCRT than the poor responders. Significantly higher ΔAPT values were also observed in patients with good responses. We suggest that the following factors might have contributed to this phenomenon. First, a high APT value for the tumor was associated with cellular proliferation and proved to be positively correlated with Ki67 expression level (33, 34), which is a cellular marker for cell proliferation and growth. Cellular proliferation is relevant to radiation response. Rapidly proliferating cells are more susceptible to NCRT-induced damage than quiescent cells because they have less time to repair the damage. Studies found that patients with higher Ki67 expression are associated with better response and downstaging

in highly proliferative tumors, exhibiting a greater tumor regression grade response and pCR rate (35, 36). Second, tumor proliferation also depends on angiogenesis. Better-perfused tumors demonstrated higher proliferation capability, and blood could also generate sufficient CEST contrast. Studies have found high blood flow and permeability in good responders. Increased blood flow and enhanced microvascular permeability in the tumor bed provide not only better access for chemotherapy, but also less hypoxia-mediated radio-resistance, which contribute to good responses to NCRT (37). DCE-MRI of rectal cancer demonstrated that tumors with better perfusion showed greater nodal and tumor downstaging after radiotherapy than poorly perfused tumors (38). However, our result on APT changes after NCRT contrasted with that of Nishie et al., who found that pretherapeutic mean APTw SI of low-response group was significantly higher than that of the high-response group (29). This difference may be explained by the fact that Nieshi et al. used a different TRG grading criteria, which is according to necrosis or cytological changes of the tumor. In contrast, the TRG system in our study is based on the evaluation of residual tumor cells. Additionally, single-slice APT MR sequence in Nieshi et al.'s study may not reflect complete characteristics of the tumor.

DWI has been extensively used for prediction of response to neoadjuvant treatment in rectal cancer, and has been recommended in international clinical guidelines as a valuable adjunct to a restaging MRI protocol. All studies reported that tumor ADC values increased after NCRT, which is due to radiation-induced cellular damage and necrosis (39). However, results regarding the use of ADC in predicting the NCRT response have been inconsistent. Some studies demonstrated significantly lower pre-NCRT ADC values in the good responders (40–42), whereas Monguzzi L et al. found no benefit of pre- treatment ADC in assessing NCRT response (13). These conflicting results may be attributed to variations in DWI protocol, end-points, and variabilities in the patient selection criteria. Besides, it has been difficult to identify treatment response accurately based on DWI alone (39).

Additionally, tumor size and CEA level have proven to be independent predictors of pCR to NCRT in rectal cancer. Based on the results of systemic review and meta-analysis, small tumor size and low levels of pre-treatment CEA are associated with pCR or good response (43, 44). We found a significant reduction of tumor volume in good responders, which is in agreement with previous studies (7, 8). Although in the present study the good responders have lower CEA levels before NCRT, the difference is not significant.

Accurate early prediction of the response to NCRT would aid in the stratification of patients into optimal therapy managements and improve therapeutic outcomes in rectal cancer. Concerning discriminating tumor response to NCRT, we demonstrated that pre-APT combined with pre-ADC had the highest AUC (0.895) among all parameters. This combined parameter, with 85.29% sensitivity and 89.47% specificity, achieved greater efficacy than pre-ADC ($p=0.029$), ΔADC ($p<0.001$), pre-APT and ΔAPT, although differences of AUCs between pre-APT& pre-ADC, pre-APT, and ΔAPT were not statistically significant.

Our study has several limitations. The primary limitations were small sample size and lack of external validation steps. Second, we used the American Joint Committee on Cancer system for evaluating tumor regression. However, several grading systems are proposed for tumor regression, which may yield variable results owing to their different TRG components and grading criteria. Third, our study did not include evaluation of lymph node involvement, and it is known that presence of lymph node metastasis can be found in patients with pCR. Fourth, different chemotherapy regimens in our study may have an impact on the therapy efficacy. Lastly, our interpretation of APTw signal changes and tumor regression was based on the quantity of residual tumor cells and cytoplasmic protein. However, pathologic changes after NCRT are diverse and complex. Besides reduced tumor cellularity, variable histology changes after NCRT—including submucosal fibrosis, mucin pool formation, and calcification—could affect APT signal changes. Therefore, further research should be conducted to explain the biophysical sources of altered APT changes in rectal cancer after NCRT.

In conclusion, the combination of APTw MRI and DWI before NCRT holds potential in evaluating NCRT response of LARC, as is the capability to detect changes in cellular protein and cellularity density noninvasively, might provide additional information for clinical decision making in the management after NCRT.

DATA AVAILABILITY STATEMENT

The original contributions presented in the study are included in the article/**Supplementary Material**. Further inquiries can be directed to the corresponding author.

ETHICS STATEMENT

The studies involving human participants were reviewed and approved by The Second Affiliated Hospital, Guangzhou University of Chinese Medicine. The patients/participants provided their written informed consent to participate in this study.

AUTHOR CONTRIBUTIONS

The authors confirm contribution to the paper as follows: study conception and design: XL, WC, and LL. Data collection: QW, JP, and SH. Analysis and interpretation of results: WC, LM, and YY. Draft manuscript preparation: WC, BL, and XL. All authors contributed to the article and approved the submitted version.

SUPPLEMENTARY MATERIAL

The Supplementary Material for this article can be found online at: https://www.frontiersin.org/articles/10.3389/fonc.2021.698427/full#supplementary-material

REFERENCES

1. Oronsky B, Reid T, Larson C, Knox SJ. Locally Advanced Rectal Cancer: The Past, Present, and Future. *Semin Oncol* (2020) 47(1):85–92. doi: 10.1053/j.seminoncol.2020.02.001
2. Petrelli F, Trevisan F, Cabiddu M, Sgroi G, Bruschieri L, Rausa E, et al. Total Neoadjuvant Therapy in Rectal Cancer: A Systematic Review and Meta-Analysis of Treatment Outcomes. *Ann Surg* (2020) 271(3):440–8. doi: 10.1097/SLA.0000000000003471
3. Dossa F, Chesney TR, Acuna SA, Baxter NN. A Watch-and-Wait Approach for Locally Advanced Rectal Cancer After a Clinical Complete Response Following Neoadjuvant Chemoradiation: A Systematic Review and Meta-Analysis. *Lancet Gastroenterol Hepatol* (2017) 2(7):501–13. doi: 10.1016/S2468-1253(17)30074-2
4. Riesco-Martinez MC, Fernandez-Martos C, Gravalos-Castro C, Espinosa-Olarte P, La Salvia A, Robles-Diaz L, et al. Impact of Total Neoadjuvant Therapy vs. Standard Chemoradiotherapy in Locally Advanced Rectal Cancer: A Systematic Review and Meta-Analysis of Randomized Trials. *Cancers* (2020) 12(12):3655. doi: 10.3390/cancers12123655
5. Kalisz KR, Enzerra MD, Paspulati RM. MRI Evaluation of the Response of Rectal Cancer to Neoadjuvant Chemoradiation Therapy. *Radiographics: Rev Publ Radiol Soc North Am Inc* (2019) 39(2):538–56. doi: 10.1148/rg.2019180075
6. Patel UB, Taylor F, Blomqvist L, George C, Evans H, Tekkis P, et al. Magnetic Resonance Imaging-Detected Tumor Response for Locally Advanced Rectal Cancer Predicts Survival Outcomes: MERCURY Experience. *J Clin Oncol: Off J Am Soc Clin Oncol* (2011) 29(28):3753–60. doi: 10.1200/JCO.2011.34.9068
7. Curvo-Semedo L, Lambregts DM, Maas M, Thywissen T, Mehsen RT, Lammering G, et al. Rectal Cancer: Assessment of Complete Response to Preoperative Combined Radiation Therapy With Chemotherapy–Conventional MR Volumetry Versus Diffusion-Weighted MR Imaging. *Radiology* (2011) 260(3):734–43. doi: 10.1148/radiol.11102467
8. Kang JH, Kim YC, Kim H, Kim YW, Hur H, Kim JS, et al. Tumor Volume Changes Assessed by Three-Dimensional Magnetic Resonance Volumetry in Rectal Cancer Patients After Preoperative Chemoradiation: The Impact of the Volume Reduction Ratio on the Prediction of Pathologic Complete Response. *Int J Radiat Oncol Biol Phys* (2010) 76(4):1018–25. doi: 10.1016/j.ijrobp.2009.03.066
9. Neri E, Guidi E, Pancrazi F, Castagna M, Castelluccio E, Balestri R, et al. MRI Tumor Volume Reduction Rate vs Tumor Regression Grade in the Pre-Operative Re-Staging of Locally Advanced Rectal Cancer After Chemo-Radiotherapy. *Eur J Radiol* (2015) 84(12):2438–43. doi: 10.1016/j.ejrad.2015.08.008
10. Fiorino C, Gumina C, Passoni P, Palmisano A, Broggi S, Cattaneo GM, et al. A TCP-Based Early Regression Index Predicts the Pathological Response in Neo-Adjuvant Radio-Chemotherapy of Rectal Cancer. *Radiother Oncol: J Eur Soc Ther Radiol Oncol* (2018) 128(3):564–8. doi: 10.1016/j.radonc.2018.06.019
11. Fiorino C, Passoni P, Palmisano A, Gumina C, Cattaneo GM, Broggi S, et al. Accurate Outcome Prediction After Neo-Adjuvant Radio-Chemotherapy for Rectal Cancer Based on a TCP-Based Early Regression Index. *Clin Trans Radiat Oncol* (2019) 19:12–6. doi: 10.1016/j.ctro.2019.07.001
12. Lambregts DMJ, van Heeswijk MM, Delli Pizzi A, van Elderen SGC, Andrade L, Peters N, et al. Diffusion-Weighted MRI to Assess Response to Chemoradiotherapy in Rectal Cancer: Main Interpretation Pitfalls and Their Use for Teaching. *Eur Radiol* (2017) 27(10):4445–54. doi: 10.1007/s00330-017-4830-z
13. Nie K, Shi L, Chen Q, Hu X, Jabbour SK, Yue N, et al. Rectal Cancer: Assessment of Neoadjuvant Chemoradiation Outcome Based on Radiomics of Multiparametric MRI. *Clin Cancer Res: an Off J Am Assoc Cancer Res* (2016) 22(21):5256–64. doi: 10.1158/1078-0432.CCR-15-2997
14. Dijkhoff RAP, Beets-Tan RGH, Lambregts DMJ, Beets GL, Maas M. Value of DCE-MRI for Staging and Response Evaluation in Rectal Cancer: A Systematic Review. *Eur J Radiol* (2017) 95:155–68. doi: 10.1016/j.ejrad.2017.08.009
15. Intven M, Reerink O, Philippens ME. Dynamic Contrast Enhanced MR Imaging for Rectal Cancer Response Assessment After Neo-Adjuvant Chemoradiation. *J Magn Reson Imaging: JMRI* (2015) 41(6):1646–53. doi: 10.1002/jmri.24718
16. Shaish H, Aukerman A, Vanguri R, Spinelli A, Armenta P, Jambawalikar S, et al. Radiomics of MRI for Pretreatment Prediction of Pathologic Complete Response, Tumor Regression Grade, and Neoadjuvant Rectal Score in Patients With Locally Advanced Rectal Cancer Undergoing Neoadjuvant Chemoradiation: An International Multicenter Study. *Eur Radiol* (2020) 30(11):6263–73. doi: 10.1007/s00330-020-06968-6
17. Horvat N, Veeraraghavan H, Khan M, Blazic I, Zheng J, Capanu M, et al. MR Imaging of Rectal Cancer: Radiomics Analysis to Assess Treatment Response After Neoadjuvant Therapy. *Radiology* (2018) 287(3):833–43. doi: 10.1148/radiol.2018172300
18. Zhang XY, Wang L, Zhu HT, Li ZW, Ye M. Predicting Rectal Cancer Response to Neoadjuvant Chemoradiotherapy Using Deep Learning of Diffusion Kurtosis MRI. *Radiology* (2020) 296(1):56–64. doi: 10.1148/radiol.2020190936
19. Peeken JC, Bernhofer M, Wiestler B, Goldberg T, Cremers D, Rost B, et al. Radiomics in Radiooncology - Challenging the Medical Physicist. *Physica Med: PM: an Int J Devoted to Appl Phys to Med Biol: Off J Ital Assoc Biomed Phys (AIFB)* (2018) 48:27–36. doi: 10.1016/j.ejmp.2018.03.012
20. Ching T, Himmelstein DS, Beaulieu-Jones BK. Opportunities and Obstacles for Deep Learning in Biology and Medicine. *J R Soc Interface* (2018) 15(141):20170387. doi: 10.1098/rsif.2017.0387
21. Zhou J, Heo HY, Knutsson L, van Zijl PCM, Jiang S. APT-Weighted MRI: Techniques, Current Neuro Applications, and Challenging Issues. *J Magn Reson Imaging: JMRI* (2019) 50(2):347–64. doi: 10.1002/jmri.26645
22. Togao O, Yoshiura T, Keupp J, Hiwatashi A, Yamashita K, Kikuchi K, et al. Amide Proton Transfer Imaging of Adult Diffuse Gliomas: Correlation With Histopathological Grades. *Neuro-Oncology* (2013) 16(3):441–8. doi: 10.1093/neuonc/not158
23. Chen W, Li L, Yan Z, Hu S, Feng J, Liu G, et al. Three-Dimension Amide Proton Transfer MRI of Rectal Adenocarcinoma: Correlation With Pathologic Prognostic Factors and Comparison With Diffusion Kurtosis Imaging. *Eur Radiol* (2021) 31(5):3286–96. doi: 10.1007/s00330-020-07397-1
24. Suh CH, Park JE, Jung SC, Choi CG, Kim SJ, Kim HS. Amide Proton Transfer-Weighted MRI in Distinguishing High- and Low-Grade Gliomas: A Systematic Review and Meta-Analysis. *Neuroradiology* (2019) 61(5):525–34. doi: 10.1007/s00234-018-02152-2
25. Mehrabian H, Desmond KL, Soliman H, Sahgal A, Stanisz GJ. Differentiation Between Radiation Necrosis and Tumor Progression Using Chemical Exchange Saturation Transfer. *Clin Cancer Res: an Off J Am Assoc Cancer Res* (2017) 23(14):3667–75. doi: 10.1158/1078-0432.CCR-16-2265
26. Park JE, Kim HS, Park KJ, Kim SJ, Kim JH, Smith SA. Pre- and Posttreatment Glioma: Comparison of Amide Proton Transfer Imaging With MR Spectroscopy for Biomarkers of Tumor Proliferation. *Radiology* (2016) 278(2):514–23. doi: 10.1148/radiol.2015142979
27. Park KJ, Kim HS, Park JE, Shim WH, Kim SJ, Smith SA. Added Value of Amide Proton Transfer Imaging to Conventional and Perfusion MR Imaging for Evaluating the Treatment Response of Newly Diagnosed Glioblastoma. *Eur Radiol* (2016) 26(12):4390–403. doi: 10.1007/s00330-016-4261-2
28. Zhou J, Tryggestad E, Wen Z, Lal B, Zhou T, Grossman R, et al. Differentiation Between Glioma and Radiation Necrosis Using Molecular Magnetic Resonance Imaging of Endogenous Proteins and Peptides. *Nat Med* (2011) 17(1):130–4. doi: 10.1038/nm.2268
29. Nishie A, Asayama Y, Ishigami K, Ushijima Y, Takayama Y, Okamoto D, et al. Amide Proton Transfer Imaging to Predict Tumor Response to Neoadjuvant Chemotherapy in Locally Advanced Rectal Cancer. *J Gastroenterol Hepatol* (2019) 34(1):140–6. doi: 10.1111/jgh.14315
30. Amin MB ES, Greene F, Byrd DR, Brookland RK, Washington MK. *Ajcc Cancer Staging Manual. 8th ed*. New York (NY): Springer (2016).
31. Zhou J, Lal B, Wilson DA, Laterra J, van Zijl PC. Amide Proton Transfer (APT) Contrast for Imaging of Brain Tumors. *Magn Reson Med* (2003) 50(6):1120–6. doi: 10.1002/mrm.10651
32. Hav M, Libbrecht L, Ferdinande L, Geboes K, Pattyn P, Cuvelier CA. Pathologic Assessment of Rectal Carcinoma After Neoadjuvant Radio(Chemo)Therapy: Prognostic Implications. *BioMed Res Int* (2015) 2015:574540. doi: 10.1155/2015/574540
33. Yu H, Wen X, Wu P, Chen Y, Zou T, Wang X, et al. Can Amide Proton Transfer-Weighted Imaging Differentiate Tumor Grade and Predict Ki-67

Proliferation Status of Meningioma? *Eur Radiol* (2019) 29(10):5298–306. doi: 10.1007/s00330-019-06115-w
34. Chen Y, Li X, Song Y, Zhu X, Zhao J, Yan X, et al. The Diagnostic Efficacy of Amide Proton Transfer Imaging in Grading Gliomas and Predicting Tumor Proliferation. *Neuroreport* (2019) 30(2):139–44. doi: 10.1097/WNR.0000000000001174
35. Kim NK, Park JK, Lee KY, Yang WI, Yun SH, Sung J, et al. P53, BCL-2, and Ki-67 Expression According to Tumor Response After Concurrent Chemoradiotherapy for Advanced Rectal Cancer. *Ann Surg Oncol* (2001) 8 (5):418–24. doi: 10.1007/s10434-001-0418-5
36. Melling N, Kowitz CM, Simon R, Bokemeyer C, Terracciano L, Sauter G, et al. High Ki67 Expression Is an Independent Good Prognostic Marker in Colorectal Cancer. *J Clin Pathol* (2016) 69(3):209–14. doi: 10.1136/jclinpath-2015-202985
37. Höckel M, Vaupel P. Biological Consequences of Tumor Hypoxia. *Semin Oncol* (2001) 28(2 Suppl 8):36–41. doi: 10.1053/sonc.2001.25392
38. Zahra MA, Hollingsworth KG, Sala E, Lomas DJ, Tan LT. Dynamic Contrast-Enhanced MRI as a Predictor of Tumour Response to Radiotherapy. *Lancet Oncol* (2007) 8(1):63–74. doi: 10.1016/S1470-2045(06)71012-9
39. Kim SH, Lee JM, Hong SH, Kim GH, Lee JY, Han JK, et al. Locally Advanced Rectal Cancer: Added Value of Diffusion-Weighted MR Imaging in the Evaluation of Tumor Response to Neoadjuvant Chemo- and Radiation Therapy. *Radiology* (2009) 253(1):116–25. doi: 10.1148/radiol.2532090027
40. Jung SH, Heo SH, Kim JW, Jeong YY, Shin SS, Soung MG, et al. Predicting Response to Neoadjuvant Chemoradiation Therapy in Locally Advanced Rectal Cancer: Diffusion-Weighted 3 Tesla MR Imaging. *J Magn Reson Imaging: JMRI* (2012) 35(1):110–6. doi: 10.1002/jmri.22749
41. Chen YG, Chen MQ, Guo YY, Li SC, Wu JX, Xu BH. Apparent Diffusion Coefficient Predicts Pathology Complete Response of Rectal Cancer Treated With Neoadjuvant Chemoradiotherapy. *PloS One* (2016) 11(4):e0153944. doi: 10.1371/journal.pone.0153944
42. Jacobs L, Intven M, van Lelyveld N, Philippens M, Burbach M, Seldenrijk K, et al. Diffusion-Weighted MRI for Early Prediction of Treatment Response on Preoperative Chemoradiotherapy for Patients With Locally Advanced Rectal Cancer: A Feasibility Study. *Ann Surg* (2016) 263(3):522–8. doi: 10.1097/SLA.0000000000001311
43. Lee YC, Hsieh CC, Chuang JP. Prognostic Significance of Partial Tumor Regression After Preoperative Chemoradiotherapy for Rectal Cancer: A Meta-Analysis. *Dis Colon Rectum* (2013) 56(9):1093–101. doi: 10.1097/DCR.0b013e318298e36b
44. Colloca G, Venturino A, Vitucci P. Pre-Treatment Carcinoembryonic Antigen and Outcome of Patients With Rectal Cancer Receiving Neo-Adjuvant Chemo-Radiation and Surgical Resection: A Systematic Review and Meta-Analysis. *Med Oncol (Northwood London England)* (2017) 34(10):177. doi: 10.1007/s12032-017-1037-8

Conflict of Interest: The authors declare that the research was conducted in the absence of any commercial or financial relationships that could be construed as a potential conflict of interest.

frontiers in Oncology

ORIGINAL RESEARCH
published: 13 August 2021
doi: 10.3389/fonc.2021.701336

Rectal Tumor Stiffness Quantified by *In Vivo* Tomoelastography and Collagen Content Estimated by Histopathology Predict Tumor Aggressiveness

Jiaxi Hu[1†], *Jing Guo*[2†], *Yigang Pei*[1], *Ping Hu*[1], *Mengsi Li*[1], *Ingolf Sack*[2] *and Wenzheng Li*[1*]

[1] Department of Radiology, Xiangya Hospital, Central South University, Changsha, China, [2] Department of Radiology, Charité – Universitätsmedizin Berlin, Berlin, Germany

OPEN ACCESS

Edited by:
Letizia Deantonio, Oncology Institute of Southern Switzerland (IOSI), Switzerland

Reviewed by:
Carla Pisani, Azienda Ospedaliero Universitaria Maggiore della Carità, Italy
Jean-Jacques Stelmes, Ente Ospedaliero Cantonale (EOC), Switzerland

***Correspondence:**
Wenzheng Li
wenzheng727@163.com

[†]These authors have contributed equally to this work and share first authorship

Specialty section:
This article was submitted to Cancer Imaging and Image-directed Interventions, a section of the journal Frontiers in Oncology

Received: 27 April 2021
Accepted: 29 July 2021
Published: 13 August 2021

Citation:
Hu J, Guo J, Pei Y, Hu P, Li M, Sack I and Li W (2021) Rectal Tumor Stiffness Quantified by In Vivo Tomoelastography and Collagen Content Estimated by Histopathology Predict Tumor Aggressiveness. Front. Oncol. 11:701336. doi: 10.3389/fonc.2021.701336

Purpose: To investigate the significance of collagen in predicting the aggressiveness of rectal tumors in patients, examined *in vivo* based on tomoelastography quantified stiffness and *ex vivo* by histologically measured collagen volume fraction (CVF).

Experimental Design: 170 patients with suspected rectal cancer were prospectively enrolled and underwent preoperative magnetic resonance imaging (MRI) and rectal tomoelastography, a technique based on multifrequency magnetic resonance elastography. Histopathologic analysis identified eighty patients with rectal cancer who were divided into subgroups by tumor-node (TN) stage, prognostic stage, and risk level. Rectal tumor stiffness was correlated with histopathologic CVF. Area-under-the-curve (AUC) and contingency analysis were used to evaluate the performance of rectal stiffness in distinguishing tumor stages which was compared to standard clinical MRI

Results: *In vivo* tomoelastography revealed that rectal tumor stiffened significantly with increased TN stage ($p<0.05$). Tumors with poorly differentiated status, perineural and lymphovascular invasion also displayed higher stiffness than well-to-moderately differentiated, noninvasive tumors (all $p<0.05$). Similar to *in vivo* stiffness, CVF indicated an abnormally high collagen content in tumors with perineural invasion and poor differentiation status. CVF was also positively correlated with stiffness ($p<0.05$). Most importantly, both stiffness (AUROC: 0.82) and CVF (AUROC: 0.89) demonstrated very good diagnostic accuracy in detecting rectal tumors that have high risk for progressing to an aggressive state with poorer prognosis.

Conclusion: In human rectal carcinomas, overexpression of collagen is correlated with increased tissue stiffness and high risk for tumor advancing more aggressively. *In vivo* tomoelastography quantifies rectal tumor stiffness which improves the diagnostic

performance of standard MRI in the assessment of lymph nodes metastasis. Therefore, *in vivo* stiffness mapping by tomoelastography can predict rectal tumor aggressiveness and add diagnostic value to MRI.

Keywords: tomoelastography, rectal cancer, collagen content, tumor aggressiveness, multifrequency magnetic resonance elastography, stiffness, risk factors

INTRODUCTION

Colorectal cancer (CRC) is the third most common cancer in men and the second most common cancer in women (1). The Union for International Cancer Control and American Joint Committee on Cancer (AJCC) tumor-node-metastasis (TNM) staging system is widely used for the clinical assessment of patients with colorectal cancer (2). The TNM system has been updated and refined over the years by incorporating new risk factors and introducing finer subcategories to improve its accuracy and robustness (3). As recommended by the National Comprehensive Cancer Network (NCCN), histopathologic features such as number of positive nodes, lymphovascular invasion (LVI), perineural invasion (PNI), and poor differentiation have been recognized as high-risk factors for local recurrence and distant metastasis (4). Moreover, observations of increased collagen crosslinking and linearization in human CRC samples (5, 6) contributed to the recognition that the amount, composition and structure of extracellular matrix (ECM) in the tumor microenvironment promotes CRC progression (7–11).

Altered collagen content and alignment translates to macroscopic changes in biomechanical tissue properties that can be non-invasively quantified *in vivo* by magnetic resonance elastography (MRE) (12). As demonstrated by extensive literature data, MRE uniquely provides parameters of viscoelasticity that are sensitive to the amount and structure of collagen networks (13–15). The diagnostic power of MRE has been demonstrated in patients with tumors in the liver (16, 17), breast (18, 19), kidney (20), brain (21–23), prostate (15, 24) and pancreas (25–27). To date, MRE has never been applied to patients with CRC and hence stiffness has not yet been used as a diagnostic parameter for assessing CRC. Magnetic resonance imaging (MRI) based on the enhancement of contrast agents and magnetic relaxation times depicts tumor morphology and is recommended as key modality for the noninvasive staging of rectal tumors by international guidelines (28–30). However, morphological features provided by routine MRI are limited in assessing lymph nodes status (31–33), histopathologic risk factors such as PNI, LVI, as well as the degree of tumor differentiation. MRE could be of complementary value to current MRI by providing stiffness as a quantitative imaging marker for ECM remodeling during tumor progression for improved preoperative staging, risk stratification, and prediction of therapeutic efficiency in rectal cancer.

The general feasibility of MRE in colorectal cancer has been demonstrated in a mouse model (34); however, clinical rectal MRE has been compromised by introducing shear waves into the gastrointestinal tract and generating consistent stiffness maps of this body region. We here overcome these challenges by employing a novel tomoelastography technique that includes multiple actuators operated by compressed air, multifrequency MRE, and noise-robust data processing (35, 36).

We hypothesize that tomoelastography-measured rectal stiffness may discriminate patients with different prognostic stages of rectal cancer. Our study has four objectives: 1) to demonstrate the feasibility and reproducibility of rectal MRE based on tomoelastography in healthy volunteers and patients; 2) to quantify for the first time values of rectal tumor stiffness for clinical diagnosis; 3) to investigate the correlation between histopathologically measured collagen content with tumor stiffness; and 4) to analyze if tomoelastography adds diagnostic value to standard clinical MRI using histopathology as reference standard.

MATERIAL AND METHODS

Study Design and Participants

The institutional review board approved our prospective study (No.201903078), and all participants gave written informed consent.

Twelve healthy volunteers (median age, 25 years; range, 23-54 years; 4 females; BMI, 20.8 ± 2.6), and 170 patients (median age, 56 years; range, 22-82 years; 65 females; BMI, 22.6 ± 4.4) with suspected rectal cancer were recruited from Nov. 2018 to Dec. 2019.

To test the feasibility and reproducibility of colorectal tomoelastography, all volunteers were investigated twice, separated by 35 ± 5 days.

All 170 patients underwent routine clinical rectal MRI and tomoelastography. Exclusion criteria were: 1) adjuvant treatment between MRI and surgery (n=53); 2) time between MRI and surgery ≥2weeks (n=12); 3) transfer to other hospitals for further treatment (n=10); 4) endoscopic submucosal dissection instead of radical surgery (n=6); 5) histopathologically proven nonrectal adenocarcinoma (n=7); and 6) poor image quality due to severe peristaltic artifacts (n=2). We finally included 80 patients with histopathologically proven rectal adenocarcinoma in surgical specimens. **Supplementary Figure 1** provides a flowchart of patient recruitment and selection criteria for MRI and tomoelastography.

Image Acquisition

All patients started a fluid diet one day before MRI and followed a strict 4-hour fasting regimen prior to imaging. MRI was performed at 3T (Magnetom Prisma, Siemens Healthcare, Germany) with an 18-channel phased-array body coil. Routine rectal T2-weighted (T2w) images with 3×3 mm^2 in-plane

resolution were acquired with a 2D fast-spin-echo (FSE) sequence in oblique axial, sagittal, and coronal planes. Additionally, 3D FSE (SPACE) T2w images with 0.8×0.8mm^2 in-plane resolution were obtained. Total acquisition time for the anatomical images was 12 min.

Rectal tomoelastography was performed using a similar sequence and setup as described in (35). Briefly, mechanical waves of vibration frequencies of 40, 50, 60, and 70 Hz were transferred to the pelvic region by three surface-based, pressurized-air-driven actuators – two placed posterior (0.8 bar static pressure) and one anterior to the pelvis, i.e., on top of the pubic symphysis (0.7 bar static pressure). The complete 3D wave field was acquired using a single-shot, spin-echo echo-planar-imaging (SE-EPI) sequence with flow-compensated motion-encoding gradient (MEG). The full vibration period was sampled at eight phase offsets. Fifteen consecutive 5-mm-thick sagittal slices with 3×3 mm^2 resolution were acquired during free breathing. MRE frequencies were set to 47.89, 47.89, 47.89 and 52.41 Hz which were optimized for the vibration frequencies of 40, 50, 60 Hz and 70 Hz, correspondingly. Further imaging parameters were: echo time=56ms; repetition time=1670ms; parallel imaging with GRAPPA factor 2; and MEG amplitude of 50mT/m. Total acquisition time was 3.5 min.

Image Analysis

A radiologist with 5 years of experience in gastrointestinal imaging assessed tumor location, TNM stage, circumferential resection margin (CRM) involvement, and extramural vascular invasion (EMVI) on T2w images using the DISTANCE method (37). DISTANCE is a systematic approach for an adequate assessment of all clinically relevant features based on MR images. It is essential for treatment decision making. In DISTANCE, DIS stands for the distance from the inferior part of the tumor to the transitional skin; T is for T staging, A is for Anal complex, N is for Nodal staging, C refers to Circumferential resection margin, and E stands for Extramural vascular invasion. Using DISTNACE approach, MRI based T and N staging were assigned to each patient.

MRE datasets were processed using wave-number multifrequency-inversion (k-MDEV) (36) to generate parameter maps of shear wave speed *c* (in m/s). Being recovered from the real part of complex wave numbers, *c* is considered a surrogate parameter of stiffness. We use *c* when providing quantitative information and the term "stiffness" when discussing qualitative changes in *c*. Data processing was performed using the *k*-MDEV pipeline available at www.bioqic-apps.com. For tumor characterization, 9 to 18 circular regions of interest (ROIs) measuring 0.3 ± 0.02 cm^2 were placed in the anterior and/or posterior rectal wall in 3 consecutive slices of covering the largest solid tumor cross-section with reference to anatomical T2w images, avoiding necrosis, cyanosis, and blood vessels. Stiffness values were averaged within these manually defined ROIs. Distal tumor-adjacent tissue (DTT) 2 cm away from the tumor was analyzed in 6 circular ROIs measuring 0.1 ± 0.02 cm^2 as reference. For healthy rectal wall assessment in volunteers, ROIs identical to those used for DTT in patients were placed in both the anterior and posterior wall in 3 consecutive slices. A radiologist blinded to clinical outcome placed all ROIs using both MRE magnitude images and the corresponding elastograms.

Histopathologic Analysis

Tumor tissue samples from 80 patients were firstly stained with hematoxylin and eosin (H&E). Based on H&E staining, routine histopathologic reports of resected specimens provided TN stages, tumor differentiation, PNI, and LVI. Overall tumor differentiation was categorized as well to moderate *vs*. poor (≥50 *vs*. <50% glandular area) using the WHO classification system (38). Staging was done by two pathologists specializing in digestive tract tumors using the TNM classification system (8th edition) recommended by the American Joint Committee on Cancer (AJCC).

To visualize and quantify collagen content, Masson's trichrome staining was additionally performed in tissue sections from 69 patients (11 cases were not stained due to insufficient tissue after H&E) according to protocol described in (39). The sections were scanned using KFBIO KF-PRO-005 EX Digital Imaging System (Ningbo Konfoong Bioinformation Tech Co., Ltd. China) and imaged using a Zeiss microscope. The quantification of histologic fibrosis was performed in three representative fields at 200x magnification with ImageJ software (NIH, USA, http://rsb.info.nih.gov/ij) and expressed as collagen volume fraction (CVF). Color deconvolution was applied to the images using Masson Trichrome vector derived from a color-based calculation algorithm within ImageJ software (40). After deconvolution, the area with green pixels which represent collagen fibers was analyzed and recorded for each image. Finally, CVF was calculated as the ratio between the area with green pixels and the total area of the original, non-deconvoluted image. Analysis of the Masson's trichrome stained images was performed with the examiner blinded to the clinical histopathologic findings.

Statistical Analysis

Group means and standard deviations were calculated for different patient groups. Normal distribution was tested with the Shapiro-Wilk test. Significant differences between groups were identified using the unpaired t-test (groups with normal distribution) or Mann-Whitney test (nonnormal distribution). Kruskal-Wallis test was used for 3-group comparison. Categorical variables were analyzed using a chi-square test.

For reproducibility analysis in healthy volunteers, coefficient of repeatability (CR), intraclass correlation coefficient (ICC), and relative absolute difference (RADi) were calculated. Interobserver agreement was evaluated using the ICC along with its 95% confidence interval (CI).

Area-under-the-curve (AUC) and contingency analysis were used to assess diagnostic accuracy in distinguishing tumor stages. The diagnostic performance of combined biomarkers was established using logistic regression analysis. Correlation analysis was performed between *in vivo* rectal tumor stiffness quantified by tomoelastography and the amount of collagen calculated as CVF based on histopathologic staining. Correlation was analyzed by Spearman (nonnormal distribution, categorical variables) and Pearson correlation (normal distribution, continuous variables). To assess the predictive accuracy of tomoelastography and routine MRI for tumor staging, contingency analysis was performed using histopathology as reference standard. For the contingency analysis,

as shear wave speed *c* obtained from tomoelastography is a continuous variable, it was dichotomized with the corresponding cutoffs from the AUC analysis for different cancer staging. Statistical analysis was performed using SPSS (version 22.0; IBM, Armonk, NY). P-values <.05 were considered statistically significant.

RESULTS

Clinicopathologic Characteristics

Based on histopathological analysis of surgically resected specimens, 32 patients whose tumors did not extend beyond the rectal muscularis propria were grouped and assigned to pT1–2 stages (16 pT1 cases and 16 pT2 cases), while the remaining 48 patients with confirmed tumor infiltration beyond the muscularis propria were pooled into pT3–4 stages (41 pT3 cases and 7 pT4 cases). In terms of lymph node involvement, 54 patients were free of lymph node metastasis (pN0) whereas 26 patients had different degrees of lymph node metastasis (21 pN1 cases and 5 pN2 cases) were pooled into the pN1–2 group. The prefix p in the stages represents pathology.

Furthermore, according to the 8th version of the TNM classification system recommended by the AJCC (2), patients were assigned to three different pathology-based prognostic stages (progStages): 0-I (n=26), II (n=27), and III-IV (n=27), based on a collective consideration of their individual T, N, and M stages. Additionally, patients were divided into a high-risk and a low-risk group for local tumor recurrence and aggressive progression, according to the management strategies of rectal cancer in Europe (5). The risk of cancer progression and prognosis were assessed in order to make appropriate treatment decisions. Patients with lymph node involvement, positive LVI and PNI status, and poorly differentiated tumors were assigned to the high-risk group (n=36), and the remaining patients (n=44) were classified as low-risk. The clinicopathologic features, routine MRI findings, and tomoelastography parameters of the total population and subgroups are presented in **Table 1**.

In Vivo Rectal Tomoelastography in Healthy Controls and Patients

Rectal tomoelastography procedure including the placement of surface-based drivers and 3.5 mins of continuous vibration were well tolerated by all volunteers and patients. All tomoelastography examinations were run to completion. For illustration, **Figure 1A** presents a 3D-SPACE T2w image, an MRE magnitude image, and the corresponding elastogram (*c*-map) of a healthy control (HC) in grayscale and as a color map. In HC, the rectal wall shown by the row of circular ROIs appears thin and smooth. Mean *c* in the healthy rectum was 1.4 ± 0.1 m/s. All 80 patients (mean age, 58 years± 11; 36 females) were analyzed. **Figure 1B, C** show examples of SPACE T2w images, MRE magnitude images, and the corresponding *c*-maps of one patient from the low-risk group (Pat. #1) and one patient from the high-risk group (Pat. #2). It is apparent in the *c*-maps that rectal cancer parenchyma is stiffer than the DTT and normal rectal wall in HC. As shown in **Figure 2A**, *c* in rectal adenocarcinoma was significantly higher than in DTT ($p<0.0001$) and healthy rectum ($p<0.0001$). *c* did not differ significantly between DTT and the healthy rectum.

Reproducibility was tested in HC. In all 12 volunteers (mean age, 28 years ± 10; 4 females), rectal tomoelastography was well reproducible with CR, ICC, and RADi of 0.87, 0.77 and 0.02, respectively. In a group of 15 randomly selected patients (mean

TABLE 1 | Clinical and pathologic characteristics of the patient population and subgroups.

	All patients (n=80)	High-risk group (n=36)	Low-risk group (n=44)	*P* value (low- *vs* high-risk)
Patient characteristics				
Age (year)	57.8 ± 11.2	57.3 ± 13.6	58.2 ± 9.2	0.73
Sex (M/F)	44/36	19/17	25/19	0.72
BMI (kg/m^2)	21.9 ± 4.1	21.1 ± 4.6	22.5 ± 3.5	0.14
CEA (ug/L)	4.6 ± 1.2	6.0 ± 15.1	3.5 ± 5.1	0.32
MRI features				
mT (T1/T2/T3/T4)	13/18/38/11	1/5/26/4	12/13/17/2	<0.001
mN (N0/N1/N2)	37/31/12	9/17/10	28/14/2	<0.001
mM (M0/M1)	79/1	35/1	44/0	–
CRM (-/+)	74/6	31/5	43/1	<0.05
EMVI (-/+)	67/13	26/10	41/3	0.012
Thickness (mm)	14.7 ± 7.8	13.8 ± 6.3	15.4 ± 8.8	0.377
Length (mm)	41.0 ± 16.8	44.9 ± 16.0	37.8 ± 17.0	0.060
Hyperintensity on T2w images (-/+)	67/13	25/11	42/2	0.002
Histopathologic features				
pT (Tis/T2/T3/T4)	16/16/41/7	1/5/23/7	15/11/18/0	–
pN (N0/N1/N2)	54/21/5	10/21/5	44/0/0	–
LVI (-/+)	68/12	24/12	44/0	–
PNI (-/+)	72/8	28/8	44/0	–
Mucinous differentiation (-/+)	74/6	30/6	44/0	<0.001
Tumor differentiation (well-to-moderate *vs* poor)	71/9	36/9	44/0	–

CEA, carcinoembryonic antigen; T, tumor; N, node; M, metastasis; CRM, circumferential resection margin; EMVI, extramural vascular invasion; LVI, lymphovascular invasion; PNI, perineural invasion. Prefixes m and p in the stages represent MRI and pathology, respectively.

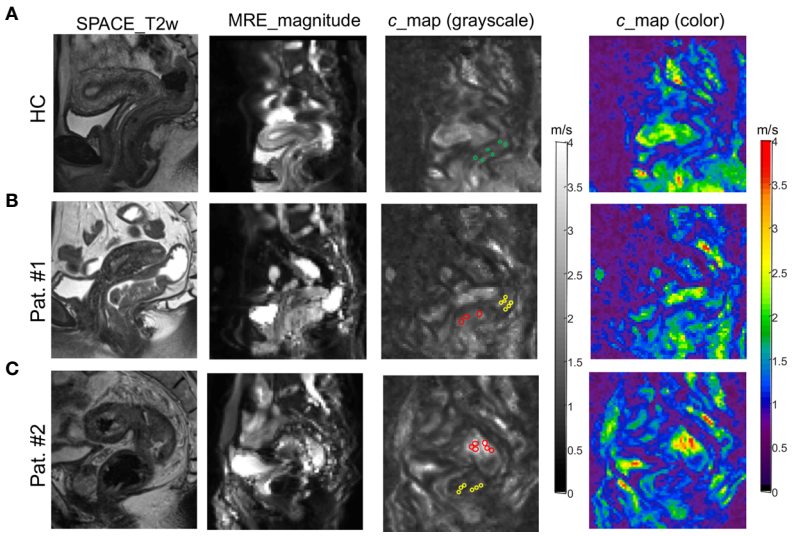

FIGURE 1 | 3D SPACE T2w images, MRE magnitude images, and *c*-maps (in grayscale and color) of a healthy control [**(A)**: HC] and two patients [**(B)**: Pat. #1 and **(C)**: #2] in one selected sagittal slice. The grayscale *c*-maps show the circular ROIs placed on healthy rectal wall in HC (green), distal tumor-adjacent tissue (DTT, yellow), and rectal tumor (red) in patients.

age, 58 years± 10; 4 females), another radiologist independently analyzed the *c*-maps. Excellent interobserver concordance was obtained for *c* with ICC and Cronbach's α of 0.958 and 0.979 for tumor and 0.777 and 0.987 for DTT, respectively.

Correlation analysis in all patients showed that *c* of rectal tumor was significantly associated with pT stage ($p<0.0001$), pN stage ($p<0.05$), degree of tumor differentiation ($p<0.05$) as well as LVI and PNI status ($p<0.05$). There was no significant correlation of *c* with sex, age, or BMI.

Furthermore, as shown in **Figure 2B**, tumors with advance pT stage, metastatic lymph node involvement, LVI, PNI, and poor differentiation status displayed significantly higher *c* values (all $p<0.05$). Additionally, higher *c* was also found in patients with an increased risk ($p<0.001$) and poorer prognosis ($p<0.005$). Group mean values of *c* in the different pathology-based subgroups are collected in **Table 2**.

Ex Vivo Collagen Volume Fraction Quantification in Patients

Figure 3 shows micrographs of rectal tumors stained with Masson trichrome from representative patients in the low-risk and high-risk groups as defined earlier. It was visible that

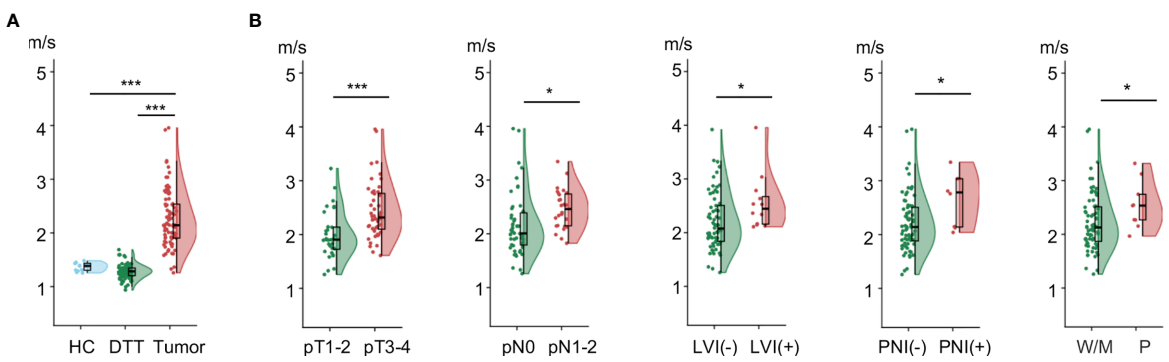

FIGURE 2 | Flat-violin plot combined with boxplot of shear wave speed *c* comparing **(A)** healthy rectum in healthy control (HC), distal tumor-adjacent tissue (DTT), and rectal tumor in patients; **(B)** rectal tumor with different pathology-based pT, pN stages, LVI, PNI status, and degrees of tumor differentiation. ***$p < 0.001$, *$p < 0.05$. LVI, lymphovascular invasion; PNI, perineural invasion; -, negative; +, positive; W/M, well to moderately differentiated; P, poorly diffrentiated. Prefix *p* in the stages represents pathology.

TABLE 2 | Group mean value of shear wave speed *c* in all 80 patients and collagen volume fraction (CVF) in a subgroup of 69 patients by pathology-based TN stage, LVI and PNI status, degree of tumor differentiation, prognostic stage, and risk level of all patients.

Prognostic factor	No. of patients (total n=80)	Shear wave speed *c* (m/s)	p value	No. of patients (total n=69)	CVF	p value
pT stage			<0.0001			0.0086
pT1-2	32	2.0 ± 0.4		27	0.13 ± 0.11	
pT3-4	48	2.4 ± 0.5		42	0.21 ± 0.12	
pN stage			0.013			<0.0001
pN0	54	2.2 ± 0.6		45	0.12 ± 0.091	
pN1-2	26	2.5 ± 0.4		24	0.29 ± 0.097	
LVI			0.017			0.1675
Negative	68	2.2 ± 0.5		57	0.17 ± 0.12	
Positive	12	2.6 ± 0.5		12	0.23 ± 0.12	
PNI			0.018			0.0269
Negative	72	2.2 ± 0.5		61	0.17 ± 0.12	
Positive	8	2.7 ± 0.5		8	0.27 ± 0.11	
Degree of tumor differentiation			0.040			0.0007
Well to moderately differentiated	71	2.2 ± 0.5		62	0.17 ± 0.11	
Poorly differentiated	9	2.6 ± 0.5		7	0.32 ± 0.084	
Prognostic stage			0.0022			<0.0001
Stage 0-I	26	1.9 ± 0.5		22	0.010 ± 0.082	
Stage II-III	27	2.3 ± 0.6		20	0.15 ± 0.085	
Stage III-IV	27	2.5 ± 0.4		27	0.27 ± 0.11	
Risk stratification			<0.001			<0.001
Low-risk	44	2.1 ± 0.5		37	0.11 ± 0.08	
High-risk	36	2.5 ± 0.5		32	0.27 ± 0.10	

CVF, collagen volume fraction; LVI, lymphovascular invasion, PNI, perineural invasion. Prefix p in the stages represents pathology.

compared with the low-risk group, the collagen (blue-green) content was higher and the collagen fibers were compacted to thick bundles in the high-risk group.

In all 69 patients where collagen content was quantified, similar to *c* obtained by tomoelastography, CVF was significantly higher in tumors with advanced pT and pN stages, positive PNI and poor differentiation status (all $p<0.05$). However, unlike *c*, no significant difference of CVF were observed between tumors with different LVI status. Significantly elevated CVF was also found in tumor samples from patients with higher risk ($p<0.001$) and poorer prognosis ($p<0.001$). Group mean values of CVF in the different pathology-based subgroups are compiled in **Table 2** and plotted in **Figure 4A**. Furthermore, correlation analysis in these patients showed that CVF of rectal tumor was positivity correlated with *c* ($r = 0.3$, $p < 0.05$), as shown in **Figure 4B**.

Diagnostic Performance of Shear Wave Speed *c* and Comparison with MRI-Based Staging

AUC for the differentiation between pathology-based pT stages, pN stages, PNI and LVI status, and degree of tumor differentiation was 0.77, 0.66, 0.72, 0.75), and 0.71, respectively. As shown in **Figure 5A**, AUC for the differentiation of pathology-based prognostic stages (progStages) 0-I *vs* II-IV and 0-II *vs* III-IV was 0.79 and 0.72, respectively. In terms of risk levels, AUC for distinguishing high-risk and low-risk patients was 0.78 (**Figure 5B**). All results pertaining to diagnostic accuracy of *c* in 80 patients are summarized in **Table 3**.

In the group of 69 patients where CVF was quantified, *c* showed a very good diagnostic accuracy (AUROC: 0.82) in separating high-risk (n=32) from low-risk (n=37) patients similarly to CVF (AUROC: 0.89, p=0.32), as illustrated in **Figure 5C**.

Additionally, to assess the possible added value of tomoelastography to the standard MRI based clinical diagnostic, we compared the diagnostic performance of MRI and tomoelastography in assigning T and N stages using histopathological results as reference standard. Therefore, *c* was dichotomized using its corresponding threshold values for distinguishing pT1-2 from pT3-4 and for distinguishing pN0 from pN1-2. Based on histopathology, contingency analysis of *c*, MRI, and combined MRI and *c* yielded predictive accuracy as well as positive and negative predictive values for distinguishing pT1-2 (40) *versus* pT3-4(+) and pN0 (40) *versus* pN1-2(+). The results, summarized in **Table 4**, show that MRI was superior to *c* in differentiating pT stages (kappa: 0.92 *vs*. 0.49). Therefore, adding *c* to MRI did not improve pT staging. Since MRI and *c* had similar performance in differentiating pN stages (kappa: 0.49 *vs*. 0.38), the combination of *c* and MRI significantly improved overall pN diagnostic accuracy from 74% to 84% with a higher specificity of 83% (kappa=0.65).

DISCUSSION

There is a need for improved staging of rectal cancer by clinical diagnostic imaging. Our study addresses this need by rectal tomoelastography which, for the first time, allowed us to quantify *in vivo* stiffness in patients with rectal cancer as a new imaging marker for ECM protein deposition. A key finding of our study was that *in vivo* stiffness correlates with the amount of collagen quantified by histopathology. Furthermore, tumor stiffness and collagen content were indicative of higher risk of aggressive rectal tumor progression that leads to a poorer prognosis.

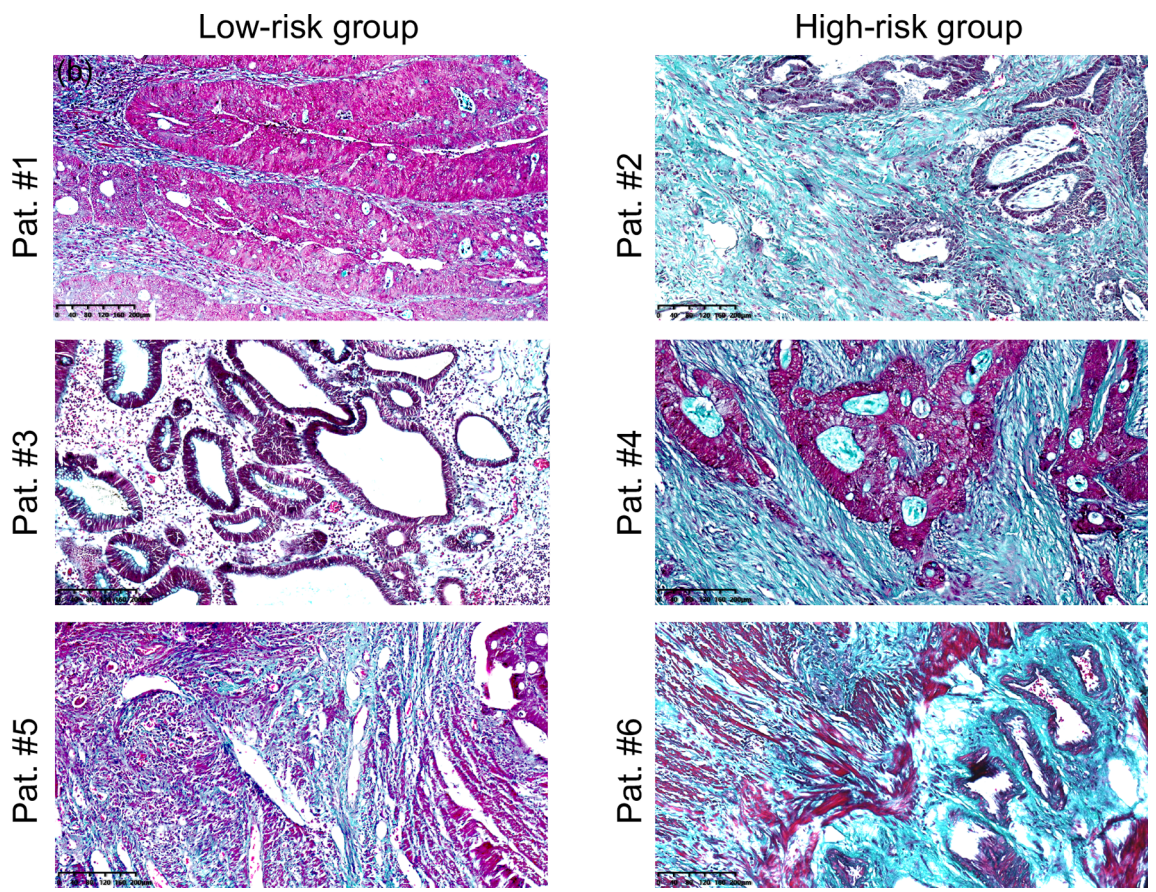

FIGURE 3 | Microscopic images of rectal tumour tissues stained with Masson's trichrome from representative patients in the low-risk (Pat. #1, #3, #5) and high-risk (Pat. #2, #4, #6) groups. Collagen fibbers was stained blue/green. Scale bars equal 40 μm. Pat.1 and Pat.2 are the same patients as shown in **Figure 1**.

Our data show that rectal tumor tissue is on average stiffer than DTT and healthy rectum – consistent with findings obtained *ex vivo* in colorectal cancer specimens (41). The authors of this study performed histopathological analysis and reported that elevated stiffness of rectal tumors is associated with accumulation of collagen fibers and proliferation of fibroblasts in cancer stroma (41). In our study, stiffening of rectal tumor tissue was observed from early to advanced stages, a finding that is consistent with results obtained by ultrasound-based elastography (42, 43). While these studies only examined tumor stiffness in different pT stages, our results show that rectal stiffness varies significantly not only between pT stages but also between pN stages. For this reason, tumor stiffness can be of value for differentiating pathology-based prognostic stages in rectal cancer. Moreover, our study, for the first time, shows that rectal stiffness also differentiates low-risk and high-risk patients with good accuracy. This is an important finding since risk assessment is crucial for making treatment decisions in rectal cancer. Our results show that abnormal tumor stiffness is associated with poor tumor differentiation and LVI and PNI status, suggesting that tomoelastography may be a potential marker of patient prognosis and the risk of local tumor recurrence and aggressive progression.

Histopathologic analysis revealed increasing CVF values in patients with advanced tumor pathologies. Tumor spread and invasive growth involve changes in collagen architecture which contribute largely to substantial ECM remodeling (11). For example, collagen is crosslinked and degraded in the tumor niche by enzymes such as lysyl oxidase and matrix metalloproteinases (44). In our patients, dense and bundled collagen fibers were abundantly visible in poorly differentiated rectal tumors with lymphovascular and perineural invasion. Changes in collagen content and alignment during rectal tumor progression as observed in our study could be due to the alterations of lysyl oxidase level in the neoplastic ECM which regulates collagen crosslinking as observed in CRC tissue samples (5, 6).

Earlier work on cancer biomechanics revealed that variations of biochemical and biophysical features of the tumor-hosting ECM could alter the stiffness of biological tissues across multiple tissue length scales (10, 17, 45, 46). The positive correlation between stiffness and CVF in our data suggests that tomoelastography is

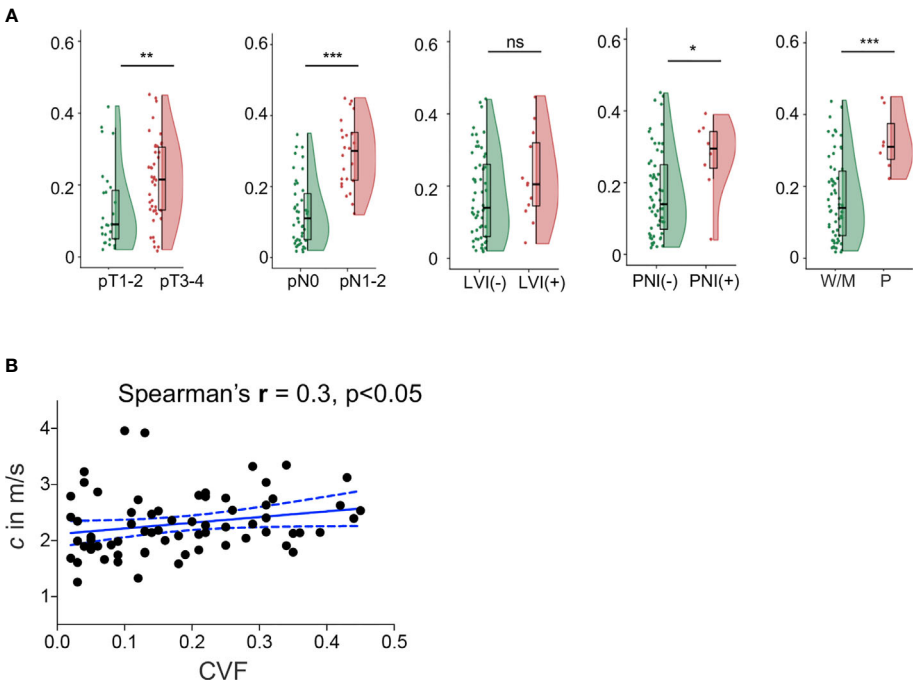

FIGURE 4 | **(A)** Flat-violin plot combined with boxplot of collagen volume fraction (CVF) of rectal tumor with different pathology-based pT, pN stages, LVI, PNI status, and degrees of tumor differentiation, measured in a subgroup of 69 patients. **(B)** Correlation between shear wave speed *c* and CVF in 69 patients. ***p < 0.001, **p < 0.01, *p < 0.05. ns, no significance. LVI, lymphovascular invasion; PNI, perineural invasion; -, negative; +, positive; W/M, well to moderately differentiated; P, poorly diffrentiated. Prefix *p* in the stages represents pathology.

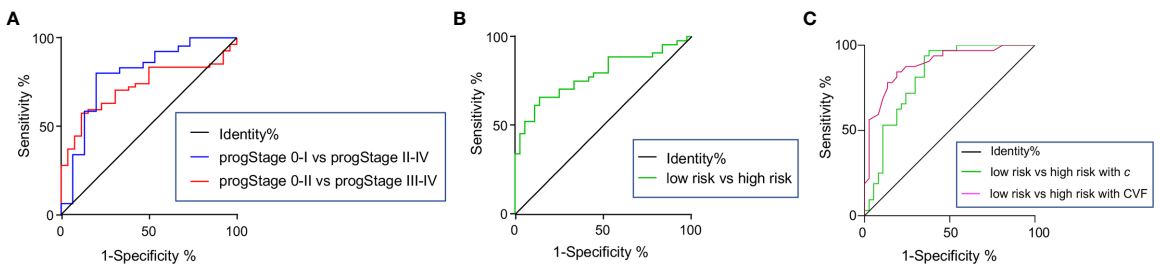

FIGURE 5 | Receiver-operating characteristic curves for assessing the diagnostic accuracy of shear wave speed *c* in differentiating **(A)** pathology-based prognostic stages (progStages) and high- and low-risk levels based on pathology in the total population of 80 patients. receiver-operating characteristic curves of *c* **(B)** and CVF **(C)** in detecting high- and low-risk levels shown for a subgroup of 69 patients.

sensitive to alterations of ECM architecture on the microscopic level. Furthermore, our study indicates that collagen is a hallmark of advanced tumor stages and associated with the risk of aggressive progression in rectal cancer. Interestingly, tomoelastography was sensitive to lymphvascular invasion which was not detectable by CVF. This disparity in sensitivity of stiffness and CVF might be due to 1) the contribution of other ECM components than collagen such as fibronectin, proteoglycans, or glycosaminoglycans to tumor stiffness (47, 48), or 2), *in vivo* factors such as blood perfusion and vascular resistance (49) to which tomoelastography is sensitive (17). Tumor angiogenesis and the migration status of neoplastic cells into the vasculature or the lymphatic system probably better reflects lymphvascular invasion than the amount of collagen in the ECM.

Irrespective the underlying pathophysiology, our data suggested that *in vivo* tomoelastography could have important implications for the clinical diagnostics of rectal cancer. Firstly, adding stiffness as an imaging parameter to clinical MRI improved lymph node staging, which is notoriously challenging in MRI (31, 32). Conventional MRI focuses on the morphologic appearance of lymph nodes such as size

TABLE 3 | Receiver-operating characteristic analysis of all 80 patients' sheer wave speed *c* in distinguishing different pathologic categories.

Category	AUC	Cutoff (m/s)	Sensitivity (%)	Specificity (%)	p value
pT1-2 *vs* pT3-4	0.77 (0.66-0.88)	<1.9	87.23 (74.26-95.17)	60.61 (42.14-77.09)	<0.0001
pN0 *vs* pN1-2	0.66 (0.53-0.78)	<2.1	84.62 (65.13-95.64)	57.41 (43.21-70.77)	0.0232
LVI– *vs* LVI+	0.72 (0.60-0.84)	<2.9	100.00 (73.54-100.00)	51.47 (39.03-63.78)	0.0180
PNI– *vs* PNI+	0.75 (0.59-0.92)	<2.8	62.50 (24.49-91.48)	86.11 (75.94-93.13)	0.0192
W/M vs P differentiated	0.71 (0.57-0.85)	<2.1	88.89 (51.75-99.72)	56.34 (44.05-68.09)	0.0406
progStage 0-I *vs* progStage II-IV	0.79 (0.65-0.94)	<1.9	80.00 (68.23-88.90)	80.00 (51.91-95.67)	0.0004
progStage 0-II *vs* progStage III-IV	0.72 (0.61-0.83)	<2.1	57.41 (43.21-70.77)	88.46 (69.85-97.55)	0.0013
Low-risk *vs* high-risk	0.78 (0.68-0.88)	<2.1	65.91 (50.08-79.51)	86.11 (70.50-95.33)	<0.0001

LVI, lymphovascular invasion; PNI, perineural invasion; -, negative; +, positive; W/M, well to moderately; P, poorly; progStage, pathology-based prognostic stage.

TABLE 4 | Contingency analysis of *c*, MRI, and combined MRI and *c* for predicting pT3-4 and pN1-2 using histopathology as reference standard.

	Overall accuracy (%)	Weighted Kappa (95%CI)	Sensitivity (%)	Specificity (%)	PPV (%)	NPV (%)
Predicting pT1-2 (40) *vs* pT3-4(+)						
MRI	96 (77/80)	0.92 (0.83-1.00)	98 (47/48)	94 (30/32)	96 (47/49)	97 (30/31)
c	76 (61/80)	0.49 (0.29-0.68)	88 (42/48)	59 (19/32)	76 (42/55)	76 (19/25)
MRI + *c*	96 (77/80)	0.92 (0.83-1.00)	98 (47/48)	94 (30/32)	96 (47/49)	97 (30/31)
Predicting pN0 (40) *vs* pN1-2(+)						
MRI	74 (59/80)	0.49 (0.32-0.66)	92 (24/26)	65 (35/54)	56 (24/43)	95 (35/37)
c	68 (54/80)	0.38 (0.21-0.56)	88 (23/26)	57 (31/54)	50 (23/46)	91 (31/34)
MRI + *c*	84 (67/80)	0.65 (0.47-0.82)	85 (22/26)	83 (45/54)	71 (22/31)	92 (45/49)

Prefix p in the stages represents pathology. PPV, positive predictive value; NPV, negative predictive value.

and shape and is thus limited in identifying micrometastasis within the nodes. By contrast, stiffness is a biophysical parameter that scales from micro to macro, and thus allows to infer the metastatic status of a tumor from the macroscopic image contrast (50–52). Taken together, the apparent clinical impact and usefulness of rectal tomoelastography are precisely its added value to MRI for lymph node staging. Secondly, although ultrasound elastography has preliminarily demonstrated the value of stiffness for the diagnosis of rectal cancer (42, 43), unlike ultrasound-based stiffness measurements, which are performed with an endorectal transducer, tomoelastography is entirely noninvasive. Therefore, tomoelastography is better suited for screening examinations. With short acquisition times of 3.5 min, tomoelastography can easily be integrated into clinical MRI protocols. Furthermore, ultrasound elastography can only access lesions which are located within 15 cm from the anal verge while tomoelastography covers the entire colorectal segment by volumetric acquisitions.

Our study is limited by its single-center design and the lack of a large validation patient cohort. However, as this is the first application of rectal tomoelastography in patients our study was designed to demonstrate the feasibility, reproducibility, and clinical potential of this technique. Moreover, our focus at this early stage of rectal tomoelastography was on demonstrating its validity using gold-standard histopathology. Building on our encouraging results, multicenter studies with more patients and serial monitoring after treatment are planned. Tomoelastography for evaluating treatment response in patient who receive chemotherapy and stiffness-based assessment for survival rate and cancer recurrence in a large patient cohort are planned as the next steps.

In summary, *in vivo* rectal tumor stiffness quantified by tomoelastography was positively correlated with collagen content measured by histopathology. Both markers were indicative of tumorigenic stages and the risk of aggressive tumor progression. These results suggest that collagen associated tumor stiffening due to alterations in the tumor ECM is a hallmark of rectal cancer progression and can be exploited for an improved imaging-based diagnosis, and possibly a prediction of therapeutic response.

Tomoelastography was highly reproducible and provided vital information on the tumor's predisposition to proliferate and invade, which helped to differentiate tumors with different prognostic stages and progression risks as needed for therapeutic decision making. In term of clinical impact, rectal tomoelastography adds diagnostic value to standard MRI in the assessment of lymph nodes metastasis which is a big challenge for MRI-based clinical diagnostics in rectal cancer. Moreover, as demonstrated by this prospective pilot study, rectal tomoelastography is reproduceable, noninvasive, user-friendly and easy to incorporate into clinical imaging workflow. These features should facilitate the application of rectal tomoelastography in screening and longitudinal post-treatment monitoring. The relatively easy implementations of the technique might also promote the dissemination of tomoelastography to other clinical sites and allow conduct of larger studies in the future.

DATA AVAILABILITY STATEMENT

The original contributions presented in the study are included in the article/**Supplementary Material**. Further inquiries can be directed to the corresponding author.

ETHICS STATEMENT

The studies involving human participants were reviewed and approved by Medical Ethics Committee of Xiangya Hospital Central South University. The patients/participants provided their written informed consent to participate in this study.

AUTHOR CONTRIBUTIONS

JH: Conceptualization, Methodology, Data curation, Validation, Writing- Original draft preparation, Formal analysis, Investigation. JG: Software, Methodology, Visualization, Writing-Original draft preparation. YP: Methodology, Investigation, Writing- Reviewing and Editing. PH: Software, Investigation. ML: Data curation, Validation. IS: Writing-Reviewing and Editing, WL: Project administration, Writing- Reviewing and Editing, Resources, Supervision, Funding acquisition. All authors contributed to the article and approved the submitted version.

FUNDING

This work was supported by Hunan Science and Technology Department Plan Project (grant number 2018XK2304 to WL), the National Natural Science Foundation of China (grant number 82071895 to WL), and the Deutsche Forschungsgemeinschaft (BIOQIC to IS, SFB1340 Matrix-In-Vision to JG).

SUPPLEMENTARY MATERIAL

The Supplementary Material for this article can be found online at: https://www.frontiersin.org/articles/10.3389/fonc.2021.701336/full#supplementary-material

Supplementary Figure 1 | Flowchart of patient inclusion and exclusion for MRI and tomoelastography. TRA, Transverse; SAG, sagittal; COR, coronal; LVI, lymphovascular invasion; PNI, perineural invasion. Prefix p in the stages represents pathology.

REFERENCES

1. Siegel RL, Miller KD, Fedewa SA, Ahnen DJ, Meester RGS, Barzi A, et al. Colorectal Cancer Statistics, 2017. *CA Cancer J Clin* (2017) 67(3):177–93. doi: 10.3322/caac.21395
2. Amin MB. *AJCC Cancer Staging Manual*. (2017).
3. Nagtegaal ID, Quirke P, Schmoll HJ. Has the New TNM Classification for Colorectal Cancer Improved Care? *Nat Rev Clin Oncol* (2011) 9(2):119–23. doi: 10.1038/nrclinonc.2011.157
4. Benson AB, Venook AP, Al-Hawary MM, Cederquist L, Chen YJ, Ciombor KK, et al. Rectal Cancer, Version 2.2018, NCCN Clinical Practice Guidelines in Oncology. *J Natl Compr Canc Netw* (2018) 16(7):874–901. doi: 10.6004/jnccn.2018.0061
5. Brauchle E, Kasper J, Daum R, Schierbaum N, Falch C, Kirschniak A, et al. Biomechanical and Biomolecular Characterization of Extracellular Matrix Structures in Human Colon Carcinomas. *Matrix Biol* (2018) 68-69:180–93. doi: 10.1016/j.matbio.2018.03.016
6. Nebuloni M, Albarello L, Andolfo A, Magagnotti C, Genovese L, Locatelli I, et al. Insight On Colorectal Carcinoma Infiltration by Studying Perilesional Extracellular Matrix. *Sci Rep* (2016) 6:22522. doi: 10.1038/srep22522
7. Fritsch A, Höckel M, Kiessling T, Nnetu KD, Wetzel F, Zink M, et al. Are Biomechanical Changes Necessary for Tumour Progression? *Nat Phys* (2010) 6(10):730–2. doi: 10.1038/nphys1800
8. Friedl P, Gilmour D. Collective Cell Migration in Morphogenesis, Regeneration and Cancer. *Nat Rev Mol Cell Biol* (2009) 10(7):445–57. doi: 10.1038/nrm2720
9. Levental KR, Yu H, Kass L, Lakins JN, Egeblad M, Erler JT, et al. Matrix Crosslinking Forces Tumor Progression by Enhancing Integrin Signaling. *Cell* (2009) 139(5):891–906. doi: 10.1016/j.cell.2009.10.027
10. Butcher DT, Alliston T, Weaver VM. A Tense Situation: Forcing Tumour Progression. *Nat Rev Cancer* (2009) 9(2):108–22. doi: 10.1038/nrc2544
11. Fang M, Yuan J, Peng C, Li Y. Collagen as a Double-Edged Sword in Tumor Progression. *Tumor Biol* (2014) 35(4):2871–82. doi: 10.1007/s13277-013-1511-7
12. Muthupillai R, Ehman RL. Magnetic Resonance Elastography. *Nat Med* (1996) 2(5):601–3. doi: 10.1038/nm0596-601
13. Li J, Zormpas-Petridis K, Boult J, Reeves KR, Heindl EL, Vinci A, et al. Investigating the Contribution of Collagen to the Tumor Biomechanical Phenotype With Noninvasive Magnetic Resonance Elastography. *Cancer Res* (2019) 79(22):5874–83. doi: 10.1158/0008-5472.CAN-19-1595
14. Pepin KM, Ehman RL, McGee KP. Magnetic Resonance Elastography (MRE) in Cancer: Technique, Analysis, and Applications. *Prog Nucl Magn Reson Spectrosc* (2015) 90-91:32–48. doi: 10.1016/j.pnmrs.2015.06.001
15. Asbach P, Ro SR, Aldoj N, Snellings J, Reiter R, Lenk J, et al. *In Vivo* Quantification of Water Diffusion, Stiffness, and Tissue Fluidity in Benign Prostatic Hyperplasia and Prostate Cancer. *Invest Radiol* (2020) 55(8):5246–30. doi: 10.1097/RLI.0000000000000685
16. Wang J, Shan Q, Liu Y, Yang H, Kuang S, He B, et al. 3d MR Elastography of Hepatocellular Carcinomas as a Potential Biomarker for Predicting Tumor Recurrence. *J Magn Reson Imaging* (2019) 49(3):719–30. doi: 10.1002/jmri.26250
17. Shahryari M, Tzschatzsch H, Guo J, Marticorena Garcia S, Boning R, Fehrenbach G, et al. Tomoelastography Distinguishes Noninvasively Between Benign and Malignant Liver Lesions. *Cancer Res* (2019) 79 (22):5704–10. doi: 10.1158/0008-5472.CAN-19-2150
18. McKnight AL, Kugel JL, Rossman PJ, Manduca A, Hartmann LC, Ehman RL, et al. MR Elastography of Breast Cancer: Preliminary Results. *AJR Am J Roentgenol* (2002) 178(6):1411–7. doi: 10.2214/ajr.178.6.1781411
19. Xydeas T, Siegmann K, Sinkus R, Krainick-Strobel U, Miller S, Claussen CD. Magnetic Resonance Elastography of the Breast: Correlation of Signal Intensity Data With Viscoelastic Properties. *Invest Radiol* (2005) 40(7):412–20. doi: 10.1097/01.rli.0000166940.72971.4a
20. Prezzi D, Neji R, Kelly-Morland C, Verma H, O'Brien T, Challacombe B, et al. Characterization of Small Renal Tumors With Magnetic Resonance Elastography: A Feasibility Study. *Invest Radiol* (2018) 53(6):344–51. doi: 10.1097/RLI.0000000000000449
21. Murphy MC, Huston J, Glaser KJ, Manduca A, Meyer FB, Lanzino G, et al. Preoperative Assessment of Meningioma Stiffness Using Magnetic Resonance Elastography. *J Neurosurg* (2013) 118(3):643–8. doi: 10.3171/2012.9.JNS12519
22. Streitberger KJ, Reiss-Zimmermann M, Freimann FB, Bayerl S, Guo J, Arlt F, et al. High-Resolution Mechanical Imaging of Glioblastoma by Multifrequency Magnetic Resonance Elastography. *PloS One* (2014) 9(10): e110588. doi: 10.1371/journal.pone.0110588
23. Yin Z, Hughes JD, Trzasko JD, Glaser KJ, Manduca A, Van Gompel J, et al. Slip Interface Imaging Based on MR-Elastography Preoperatively Predicts Meningioma-Brain Adhesion. *J Magn Reson Imaging* (2017) 46(4):1007–16. doi: 10.1002/jmri.25623
24. Li M, Guo J, Hu P, Jiang H, Chen J, Hu J, et al. Tomoelastography Based on Multifrequency MR Elastography for Prostate Cancer Detection: Comparison With Multiparametric MRI. *Radiology* (2021) p:201852. doi: 10.1148/radiol.2021201852
25. Shi Y, Gao F, Li Y, Tao S, Yu B, Liu Z, et al. Differentiation of Benign and Malignant Solid Pancreatic Masses Using Magnetic Resonance Elastography With Spin-Echo Echo Planar Imaging and Three-Dimensional Inversion Reconstruction: A Prospective Study. *Eur Radiol* (2018) 28(3):936–45. doi: 10.1007/s00330-017-5062-y

26. Marticorena Garcia SR, Zhu L, Gultekin E, Schmuck R, Burkhardt C, Bahra M, et al. Tomoelastography for Measurement of Tumor Volume Related to Tissue Stiffness in Pancreatic Ductal Adenocarcinomas. *Invest Radiol* (2020) 55(12):769–774. doi: 10.1097/RLI.0000000000000704
27. Zhu L, Guo J, Jin Z, Xue H, Dai M, Zhang W, et al. Distinguishing Pancreatic Cancer and Autoimmune Pancreatitis With *In Vivo* Tomoelastography. *Eur Radiol* (2020) 31(5):3366–3374. doi: 10.1007/s00330-020-07420-5
28. Van Cutsem E, Verheul HMW, Flamen P, Rougier P, Beets-Tan R, Glynne-Jones T, et al. Imaging in Colorectal Cancer: Progress and Challenges for the Clinicians. *Cancers (Basel)* (2016) 8(9):81. doi: 10.3390/cancers8090081
29. Horvat N, Carlos Tavares Rocha C, Clemente Oliveira B, Petkovska I, Gollub MJ, et al. MRI of Rectal Cancer: Tumor Staging, Imaging Techniques, and Management. *Radiographics* (2019) 39(2):367–87. doi: 10.1148/rg.2019180114
30. Norenberg D, Sommer WH, Thasler W, D–Haese J, Rentsch M, Kolben T, et al. Structured Reporting of Rectal Magnetic Resonance Imaging in Suspected Primary Rectal Cancer: Potential Benefits for Surgical Planning and Interdisciplinary Communication. *Invest Radiol* (2017) 52(4):232–9. doi: 10.1097/RLI.0000000000000336
31. Akasu T, Iinuma G, Takawa M, Yamamoto S, Muramatsu Y, Moriyama N. Accuracy of High-Resolution Magnetic Resonance Imaging in Preoperative Staging of Rectal Cancer. *Ann Surg Oncol* (2009) 16(10):2787–94. doi: 10.1245/s10434-009-0613-3
32. Grone J, Loch FN, Taupitz M, Schmidt C, Kreis ME. Accuracy of Various Lymph Node Staging Criteria in Rectal Cancer With Magnetic Resonance Imaging. *J Gastrointestinal Surg* (2018) 22(1):146–53. doi: 10.1007/s11605-017-3568-x
33. Kim SH, Lee JM, Lee MW, Kim GH, Han JK, Choi BI, et al. Diagnostic Accuracy of 3.0-Tesla Rectal Magnetic Resonance Imaging in Preoperative Local Staging of Primary Rectal Cancer. *Invest Radiol* (2008) 43(8):587–93. doi: 10.1097/RLI.0b013e31817e9083
34. Juge L, Doan BT, Seguin J, Albuquerque M, Larrat B, Mignet N, et al. Colon Tumor Growth and Antivascular Treatment in Mice: Complementary Assessment With MR Elastography and Diffusion-Weighted MR Imaging. *Radiology* (2012) 264(2):436–44. doi: 10.1148/radiol.12111548
35. Dittmann F, Tzschatzsch H, Hirsch S, Barnhill E, Braun J, Sack I, et al. Tomoelastography of the Abdomen: Tissue Mechanical Properties of the Liver, Spleen, Kidney, and Pancreas From Single MR Elastography Scans at Different Hydration States. *Magn Reson Med* (2017) 78(3):976–83. doi: 10.1002/mrm.26484
36. Tzschatzsch H, Guo J, Dittmann F, Hirsch S, Barnhill E, Johrens K, et al. Tomoelastography by Multifrequency Wave Number Recovery From Time-Harmonic Propagating Shear Waves. *Med Image Anal* (2016) 30:1–10. doi: 10.1016/j.media.2016.01.001
37. Nougaret S, Reinhold C, Mikhael HW, Rouanet P, Bibeau F, Brown G. The Use of MR Imaging in Treatment Planning for Patients With Rectal Carcinoma: Have You Checked the "DISTANCE"? *Radiology* (2013) 268 (2):329–43. doi: 10.1148/radiol.13121361
38. Bosman FT, World Health O, International Agency for Research on C. *WHO Classification of Tumours of the Digestive System*. Lyon: IARC Press (2010).
39. Schipke J, Brandenberger C, Rajces A, Manninger M, Alogna A, Post H, et al. Assessment of Cardiac Fibrosis: A Morphometric Method Comparison for Collagen Quantification. *J Appl Physiol* (1985) 122(4):1019–30. doi: 10.1152/japplphysiol.00987.2016
40. Nakamori S, Dohi K, Ishida M, Goto Y, Imanaka-Yoshida K, Omori T, et al. Native T1 Mapping and Extracellular Volume Mapping for the Assessment of Diffuse Myocardial Fibrosis in Dilated Cardiomyopathy. *JACC Cardiovasc Imaging* (2018) 11(1):48–59. doi: 10.1016/j.jcmg.2017.04.006
41. Kawano S, Kojima M, Higuchi Y, Sugimoto M, Ikeda K, Sakuyama N, et al. Assessment of Elasticity of Colorectal Cancer Tissue, Clinical Utility, Pathological and Phenotypical Relevance. *Cancer Sci* (2015) 106(9):1232–9. doi: 10.1111/cas.12720
42. Waage JE, Bach SP, Pfeffer F, Leh S, Havre RF, Odegaard S, et al. Combined Endorectal Ultrasonography and Strain Elastography for the Staging of Early Rectal Cancer. *Colorectal Dis* (2015) 17(1):50–6. doi: 10.1111/codi.12764
43. Chen LD, Wang W, Xu JB, Chen JH, Zhang XH, Wu H, et al. Assessment of Rectal Tumors With Shear-Wave Elastography Before Surgery: Comparison With Endorectal US. *Radiology* (2017) 285(1):279–92. doi: 10.1148/radiol.2017162128
44. Xiao Q, Ge G. Lysyl Oxidase, Extracellular Matrix Remodeling and Cancer Metastasis. *Cancer Microenviron* (2012) 5(3):261–73. doi: 10.1007/s12307-012-0105-z
45. Wirtz D, Konstantopoulos K, Searson PC. The Physics of Cancer: The Role of Physical Interactions and Mechanical Forces in Metastasis. *Nat Rev Cancer* (2011) 11(7):512–22. doi: 10.1038/nrc3080
46. Riegler J, Labyed Y, Rosenzweig S, Javinal V, Castiglioni A, Dominguez CX, et al. Tumor Elastography and Its Association With Collagen and the Tumor Microenvironment. *Clin Cancer Res* (2018) 24(18):4455–67. doi: 10.1158/1078-0432.CCR-17-3262
47. Wang K, Andresen Eguiluz RC, Wu F, Seo BR, Fischbach C, Gourdon D. Stiffening and Unfolding of Early Deposited-Fibronectin Increase Proangiogenic Factor Secretion by Breast Cancer-Associated Stromal Cells. *Biomaterials* (2015) 54:63–71. doi: 10.1016/j.biomaterials.2015.03.019
48. Wei H, Cheng Z, Ouyang C, Zhang Y, Hu Y, Chen S, et al. Glycoprotein Screening in Colorectal Cancer Based on Differentially Expressed Tn Antigen. *Oncol Rep* (2016) 36(3):1313–24. doi: 10.3892/or.2016.4937
49. Pries AR, Hopfner M, le Noble F, Dewhirst MW, Secomb TW. The Shunt Problem: Control of Functional Shunting in Normal and Tumour Vasculature. *Nat Rev Cancer* (2010) 10(8):587–93. doi: 10.1038/nrc2895
50. Whatcott CJ, Diep CH, Jiang P, Watanabe A, LoBello J, Sima C, et al. Desmoplasia in Primary Tumors and Metastatic Lesions of Pancreatic Cancer. *Clin Cancer Res* (2015) 21(15):3561–8. doi: 10.1158/1078-0432.CCR-14-1051
51. Yu H, Mouw JK, Weaver VM. Forcing Form and Function: Biomechanical Regulation of Tumor Evolution. *Trends Cell Biol* (2011) 21(1):47–56. doi: 10.1016/j.tcb.2010.08.015
52. Schedin P, Keely PJ. Mammary Gland ECM Remodeling, Stiffness, and Mechanosignaling in Normal Development and Tumor Progression. *Cold Spring Harb Perspect Biol* (2011) 3(1):a003228. doi: 10.1101/cshperspect.a003228

Conflict of Interest: The authors declare that the research was conducted in the absence of any commercial or financial relationships that could be construed as a potential conflict of interest.

frontiers in Oncology

ORIGINAL RESEARCH
published: 09 December 2021
doi: 10.3389/fonc.2021.774413

Fractal-Based Radiomic Approach to Tailor the Chemotherapy Treatment in Rectal Cancer: A Generating Hypothesis Study

Carmela Di Dio[1], Giuditta Chiloiro[2], Davide Cusumano[1,2], Francesco Catucci[1], Luca Boldrini[2], Angela Romano[2], Elisa Meldolesi[2], Fabio Marazzi[2], Barbara Corvari[2], Brunella Barbaro[2], Riccardo Manfredi[2], Vincenzo Valentini[2] and Maria Antonietta Gambacorta[2]*

[1] UOC Radioterapia Oncologica, Mater Olbia Hospital, Olbia, Italy, [2] Dipartimento Diagnostica per Immagini, Radioterapia Oncologica ed Ematologia, Fondazione Policlinico Universitario Agostino Gemelli IRCCS, Rome, Italy

OPEN ACCESS

Edited by:
Berardino De Bari,
Hospital Neuchâtelois, Switzerland

Reviewed by:
Katsuya Yamada,
Hirosaki University, Japan
Sikandar Shaikh,
Shadan Hospital and Institute of Medical Sciences, India

***Correspondence:**
Davide Cusumano
davide.cusumano@policlinicogemelli.it

Specialty section:
This article was submitted to Cancer Imaging and Image-directed Interventions, a section of the journal Frontiers in Oncology

Received: 11 September 2021
Accepted: 18 November 2021
Published: 09 December 2021

Citation:
Di Dio C, Chiloiro G, Cusumano D, Catucci F, Boldrini L, Romano A, Meldolesi E, Marazzi F, Corvari B, Barbaro B, Manfredi R, Valentini V and Gambacorta MA (2021) Fractal-Based Radiomic Approach to Tailor the Chemotherapy Treatment in Rectal Cancer: A Generating Hypothesis Study. Front. Oncol. 11:774413. doi: 10.3389/fonc.2021.774413

Introduction: The aim of this study was to create a radiomic model able to calculate the probability of 5-year disease-free survival (5yDFS) when oxaliplatin (OXA) is or not administered in patients with locally advanced rectal cancer (LARC) and treated with neoadjuvant chemoradiotherapy (nCRT), allowing physicians to choose the best chemotherapy (CT) regimen.

Methods: LARC patients with cT3–4 cN0 or cT1–4 cN1–2 were treated according to an nCRT protocol that included concomitant CT schedules with or without OXA and radiotherapy dose of 55 Gy in 25 fractions. Radiomic analysis was performed on the T2-weighted (T2-w) MR images acquired during the initial tumor staging. Statistical analysis was performed separately for the cohort of patients treated with and without OXA. The ability of every single radiomic feature in predicting 5yDFS as a univariate analysis was assessed using the Wilcoxon–Mann–Whitney (WMW) test or t-test. Two logistic models (one for each cohort) were calculated, and their performance was assessed using the area under the receiver operating characteristic (ROC) curve (AUC).

Results: A total of 176 image features belonging to four families (morphological, statistical, textural, and fractal) were calculated for each patient. At the univariate analysis, the only feature showing significance in predicting 5yDFS was the maximum fractal dimension of the subpopulation identified considering 30% and 50% as threshold levels ($maxFD_{30–50}$). Once the models were developed using this feature, an AUC of 0.67 (0.57–0.77) and 0.75 (0.56–0.95) was obtained for patients treated with and without OXA, respectively. A $maxFD_{30–50}$ >1.6 was correlated to a higher 5yDFS probability in patients treated with OXA.

Conclusion: This study suggests that radiomic analysis of MR T2-w images can be used to define the optimal concomitant CT regimen for stage III LARC cancer patients. In

particular, by providing an indication of the gross tumor volume (GTV) spatial heterogeneity at initial staging, $maxFD_{30–50}$ seems to be able to predict the probability of 5yDFS. New studies including a larger cohort of patients and external validation sets are recommended to verify the results of this hypothesis-generating study.

Keywords: radiomics, MRI, oxaliplatin, rectal cancer, predictive modeling

INTRODUCTION

Colorectal cancer is one of the most widespread cancer diseases in the world, causing the death of thousands of people each year, as recently estimated in the latest epidemiological studies (1, 2).

The standard treatment for locally advanced rectal cancer (LARC) consists of neoadjuvant chemoradiotherapy (nCRT) followed by surgery (1, 3).

Recent experiences demonstrated that local control (LC) can be improved by the combination of nCRT and surgery, but no significant benefit has been observed in terms of disease-free (DFS) and overall survival (OS) (4). Furthermore, it has been observed that the 25% of patients develop metastases within 5 years after the end of the surgery, mainly located in the liver (5).

In this context, the intensification of nCRT could be a valid strategy. In recent years, several studies have been conducted to evaluate the efficacy of adding oxaliplatin to nCRT; however, the benefit of oxaliplatin-based nCRT in stage II or III rectal cancer remains unclear. Several randomized trials investigated the effect of oxaliplatin-based nCRT: efficacy data are controversial, and the addition of oxaliplatin often resulted in increased acute toxicity (6–11). For this reason, the role of oxaliplatin is still a matter of debate, especially in patients with stage III rectal cancer.

Radiomics is playing a primary role in proposing new image-based markers that can predict surrogate endpoints of survival outcomes such as pathological complete response (pCR) or DFS in order to personalize neoadjuvant treatment (12–14). These predictors are generally based on MR image analysis, as it is the gold standard for diagnosis and staging of rectal cancer (12, 15, 16).

First experiences proposing radiomic models able to predict different outcomes, such as OS or metastasis-free survival, have recently been reported in the literature (17, 18).

Although the potential of radiomics in extracting prognostic factors from image analysis is now widely accepted by the scientific community, to the best of our knowledge, there are no predictive models in the literature that support the oncologist in deciding which drug to prescribe for neoadjuvant treatment.

In this experience, we want to explore the potential of radiomics in drug personalization, proposing an MRI-based indicator able to predict the DFS probability at 5 years after the end of treatment (5yDFS) with a high level of accuracy in two cohorts of patients (one in which oxaliplatin was administered and one in which it was not administered).

In particular, the final goal of this hypothesis-generating study is to obtain a model that can calculate the probability of 5yDFS for both oxaliplatin administration and non-administration, allowing clinicians to choose the best chemotherapy (CT) regimen based on the highest probability of 5yDFS.

MATERIALS AND METHODS

Patients' Selection Criteria and Treatment Workflow

Patients enrolled in this retrospective study were affected by locally advanced rectal adenocarcinoma, with cT3–4 cN0 or cT1–4 cN1–2 or with mesorectal fascia involvement (MRF+), according to the American Joint Committee on Cancer (AJCC) TNM (19).

Treatments were delivered from May 2008 to June 2015 at Fondazione Policlinico Universitario Agostino Gemelli IRCCS in Rome. Ethics committee approval was obtained for this study, and all patients gave signed informed consent to be enrolled. At the time of diagnosis, patients had to be older than 18 years with pathologically confirmed rectal adenocarcinoma; cases with mucinous variants were excluded from the study.

All selected LARC patients received nCRT followed by surgery. Patients with missing treatment information, with metastatic disease at diagnosis, and alive patients without evidence of local or distant recurrence with a follow-up time less than 5 years were excluded.

MRI safety screening forms were administered to all patients: those who showed clinical contraindications to MRI or denied specific consent were considered not eligible for the study. Clinical and radiological follow-up was performed for all the patients for a period of at least 5 years after surgery.

For tumor staging, MRI acquisition was performed using a 1.5-T scanner (Signa Excite, GE Medical Systems, Milwaukee, WI, USA) in the supine position. The MRI protocol consisted of four T2-weighted fast spin-echo (FSE) MR sequences (axial, coronal, sagittal, and volumetric) and one diffusion-weighted imaging (DWI) acquisition obtained using b values of 0 and 1,000 s/mm^2. No intravenous contrast agents were administered.

Radiotherapy (RT) treatment was delivered in 25 fractions, following a simultaneous integrated boost (SIB) technique with 55 Gy in fractions of 2.2 Gy/die to gross tumor volume (GTV) and corresponding mesorectum and 45 Gy in fractions of 1.8 Gy/die to selected lymph nodes according to the clinical disease (20). Neoadjuvant CT was administered according to two regimens based on initial clinical stage and patient compliance:

i. *OXA-based regimen:* CapOx (60 mg/m^2 of i.v. oxaliplatin at the first day plus 1,300 mg/die/mq of oral chronomodulated

capecitabine 1,650 mg/mq/die, during RT q7) or Xelox (oxaliplatin 130 mg/mq q 1, 19, and 38 plus oral chronomodulated capecitabine 1,300 mg/mq/die during RT).

ii. *No-OXA-based regimen:* 5-fluorouracil in continuous infusion (225 mg/mq/die during RT) or oral chronomodulated capecitabine (1,650 mg/mq/die during RT).

At 6 to 10 weeks after the end of nCRT, patients underwent clinical restaging, consisting of a restaging MRI and digital rectal examination. Surgery was performed 8 to 12 weeks after the end of nCRT and consisted of abdominal-perineal resection, anterior resection, or transanal endoscopic microsurgery, depending on the residual disease and surgical evaluation.

The postoperative histopathological specimen was classified following the tumor regression grading (TRG) according to the Mandard classification (21).

Adjuvant CT was administered for selected patients in relation to clinical and pathological stages and high-risk factors such as tumor lymph vascular invasion and TRG4.

Radiomic Analysis

Radiomic analysis was performed on the T2-weighted FSE MR images acquired in a transverse plane orthogonal to the tumor longitudinal axis during initial disease staging (22). The MR images subject to radiomic analysis were those acquired during the initial tumor staging.

Such images had a spatial resolution of 0.8×0.8 mm^2 and a slice thickness of 3 mm, with no intersection gap between the slices. Repetition time ranged from 2,500 to 5,000 ms, inversion time from 100 to 110 ms, and echo train length from 16 to 24.

The Dicom files containing the MR images were imported into an RT delineation console (Eclipse, Varian Medical System™, Palo Alto, CA, USA) where a radiologist in cooperation with a radiation oncologist experienced in rectal cancer diagnosis and treatment delineated the GTV, following the ICRU n.83 guidelines (23).

Delineations were blinded between the two experts, and a final consensus was discussed and obtained with a shared delineation in case of disagreement. Dicom files containing MR images and contours were exported and processed using Moddicom, an R package (R Core Team, Vienna, Austria) designed to perform radiomic analysis of biomedical images (24, 25).

Two image filters were applied to the original MR images before extracting radiomic features: the Laplacian of Gaussian (LoG) filter with a kernel size dimension of 0.4 mm and the intensity-based (IB) image filter, with a step of 20%: additional information about the use of these filters can be found in (26, 27).

Radiomic analysis led to the extraction of four feature families: morphological features were extracted from the raw images, statistical and textural features were extracted from the MR images preprocessed using the LOG filter, fractal features were extracted from the images processed with the IB filter (27, 28). A diagrammatic representation of the whole radiomic process is reported in **Figure 1**.

As regards the textural features, three gray-level matrices were considered: run length (rlm), co-occurrence (cm), and size zone (szm) matrices. The complete list of the radiomic features extracted is reported in the Supplementary Materials, with similar experiences dealing with this topic (15, 29).

Fractal features were instead calculated on the images preprocessed using the IB filter, which consists in normalizing the pixel values within GTV using the first and 99th percentiles of the gray-level GTV histogram as extremes and then identifying pixel clusters based on different threshold levels defined as the percentage of the maximum intensity (27, 30).

Once the images were processed, fractal dimension (FD) was calculated slice by slice using the Box counting algorithm, and minimum, maximum, median, and mean values were calculated and considered as fractal features (27).

Statistical Analysis

Statistical analysis was performed separately for the cohort of patients treated with (OXA-based) and without oxaliplatin

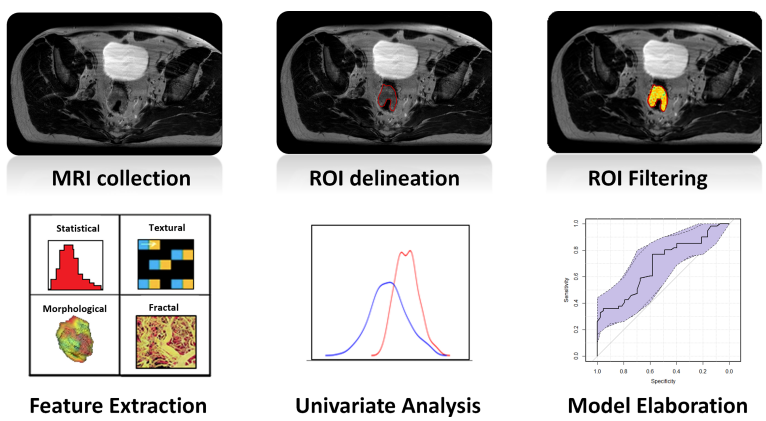

FIGURE 1 | Diagrammatic representation of the whole radiomic process: once MR images were collected, GTV was delineated on each MRI. Images were filtered, and four types of radiomic features (statistical, textural, morphological, and fractal) were extracted. The ability of every single feature in predicting the outcome was evaluated in terms of the Wilcoxon–Mann–Whitney test, and a logistic regression was calculated considering the most significant feature. The last two steps were repeated separately for the two cohorts of patients of the study (OXA and no-OXA). GTV, gross tumor volume; OXA, oxaliplatin.

(no-OXA-based), considering that the DFS reached 5 years from the date of surgery (5yDFS) as a dichotomic outcome.

Figure 2 reports the number of patients showing metastases or tumor recurrence as a function of the years from the date of surgery: the time of 5 years was chosen as the optimal cutoff between the number of events that occurred and the number of patients with valid follow-up at that time.

The ability of every single radiomic feature in predicting 5yDFS at the univariate analysis was assessed by considering the Wilcoxon–Mann–Whitney (WMW) test or the t-test, depending on the normality of data distribution, which was previously evaluated using the Shapiro–Wilk test (31).

Clinical information such as initial tumor staging, GTV volume, sex, and age at diagnosis was considered as an additional variable. The radiomic feature showing the highest level of significance in both the patient cohorts was considered as the best predictor, and two logistic regression models were developed, one for each cohort.

The predictive performance of the two predictive models was evaluated using the area under the receiver operating characteristic (ROC) curve (AUC), with the 95% CIs calculated using the bootstrap method with 2,000 iterations (32).

The best cutoff threshold was identified maximizing Youden's index (J), and the sensitivity and specificity values at the best threshold were calculated for each model (33).

With the use of the elaborated models, the probability of 5yDFS at different values of the radiomic parameter was calculated to identify different ranges in which a CT regimen can be considered of higher value, ensuring a higher probability of 5yDFS.

The robustness of the two developed models was evaluated by means of a threefold cross-validation analysis with five iterations, as an independent external validation dataset was not available (30).

The whole statistical analysis was performed using R software (version 3.6.1, Wien Austria) and dedicated packages (34).

RESULTS

A total of 240 patients were considered for this study, but only 188 cases met the inclusion criteria: 125 (66%) were treated with oxaliplatin CT and 63 (34%) without oxaliplatin CT. The clinical characteristics of the patients included in the study are summarized in **Table 1**.

The median follow-up time was 96 months, with a range of 9–156 months, and with a 5yDFS of 84.8% and 87.3% for OXA- and no-OXA-based CT, respectively.

A total of 176 image features (92 radiomic and 84 fractal features) were extracted for each patient: among the radiomic

TABLE 1 | Clinical characteristics of patients enrolled and treated with and without oxaliplatin.

Clinical characteristics	OXA-based regimen n = 125	No-OXA-based regimen n = 63
Age (range)	61 (26–81)	64 (32–83)
Sex		
Male	83 (66%)	38 (58%)
Female	42 (34%)	25 (42%)
Clinical tumoral stage		
cT2	3 (2%)	9 (14%)
cT3	72 (58%)	45 (72%)
cT4	49 (40%)	9 (14%)
Clinical nodal stage		
cN0	3 (2%)	10 (16%)
cN1–2	122 (88%)	53 (84%)
MRF involvement		
Positive	47 (38%)	50 (79%)
Negative	78 (62%)	13 (21%)
GTV (cm^3) (range)		
Pre	47.92 (30.21–210.53)	25.28 (24.02–76.22)
Post	18.16 (7.47–120.49)	8.74 (4.47–64.40)

Categorical variables are reported with the percentage of evidence, continuous variable with mean values, and corresponding range.
OXA, oxaliplatin; GTV, gross tumor volume; MRF+, mesorectal fascia involvement.

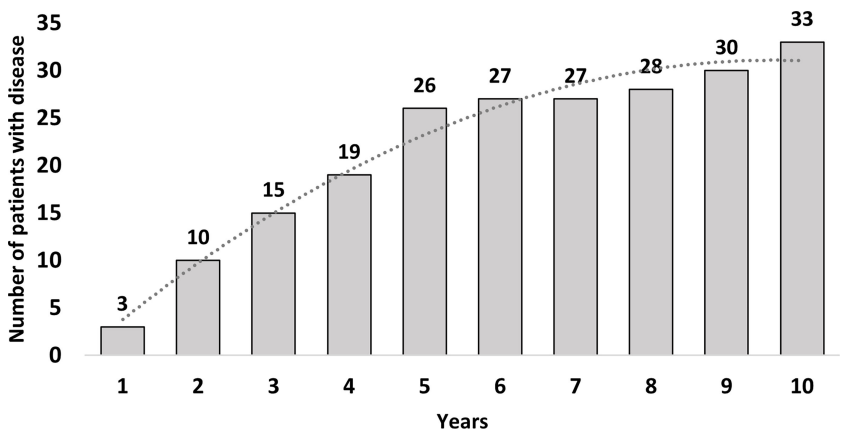

FIGURE 2 | Number of patients showing metastases in relation to the years after the end of surgery.

features, 14 were based on morphology, 22 on gray-level histogram analysis (1st-order features), and 46 on the textural analysis (16 szm, 18 rlm, and 22 cm).

At the univariate analysis, the only feature that showed statistically significant ability in predicting 5yDFS in both patient cohorts was the maximum FD of the subpopulation identified considering 30% and 50% as threshold levels ($maxFD_{30-50}$), with a p-value of 0.018 in the cohort treated with oxaliplatin and 0.019 in the one treated without oxaliplatin. The values of the parameters and coefficients characterizing the two models developed are reported in **Table 2**.

Figure 3 reports the ROC curves with the corresponding 95% CIs obtained for the two logistic regression models created using $maxFD_{30-50}$ as variable and 5yDFS as the outcome.

For the OXA-based cohort, the predictive model reports an AUC of 0.67 (95% CI ranging from 0.57 to 0.77); for the no-OXA-based cohort, the model shows an AUC of 0.75 (95% CI ranging from 0.56 to 0.95). The best cutoff threshold was 0.88 (corresponding to a J index of 0.44) for patients on OXA-based regimen, 0.80 (J = 0.42) for patients in no-OXA-based regimen. At the best threshold value, the sensitivity was 44.3% for patients treated with an OXA-based regimen and 80% for patients treated with no-OXA regimen, while the specificity was 100% and 62.5%, respectively. The robustness analysis performed using the threefold cross-validation reported an AUC of 0.67 with an SD of 0.06 for the oxaliplatin cohort and an AUC of 0.75 with SD equal to 0.15 for the no-oxaliplatin cohort.

Applying the two models developed, the probability of achieving 5yDFS when oxaliplatin is or is not administered can be calculated. **Figure 4** summarizes the values obtained in terms of 5yDFS probability to varying $maxFD_{30-50}$ values.

Figure 5 reports a visual representation of the meaning of FD: such parameter can be considered as a metric indicator of the tumor aggressiveness, as higher FD values describe tumor structures characterized by a more complex spatial arrangement. In particular, the higher value of $maxFD_{30-50}$ is correlated with a lower probability of 5yDFS.

DISCUSSION

During recent years, the number of radiomic applications has exponentially grown, demonstrating that the image-based biomarkers can play a significant role in the context of the omics-based predictive models, at the same level as more advanced disciplines such as genomics, proteomics, and transcriptomics (35–37).

This work represents one of the first experiences that aim to identify the role of radiomics in the definition of a more intensive schedule of concomitant CT at the time of diagnosis, in order to reduce the rate of local and distant metastases at 5 years.

For rectal cancer, indeed, the majority of the experiences are focused on predicting early surrogate endpoints, such as the pCR, because these data are more quickly available in a clinical

TABLE 2 | Covariates and coefficients of the linear logistic regression models elaborated to predict 5yDFS from the analysis of T2-w MR staging images.

Regimen	Covariate	Coefficient	Sigma coefficient	p-Value
OXA-based	Intercept	19.43	7.57	0.01
	$maxFD_{30-50}$	−10.91	4.62	0.02
No-OXA-based	Intercept	22.15	10.15	0.03
	$maxFD_{30-50}$	−12.67	6.25	0.04

5yDFS, 5-year disease-free survival; T2-w, T2-weighted; OXA, oxaliplatin.

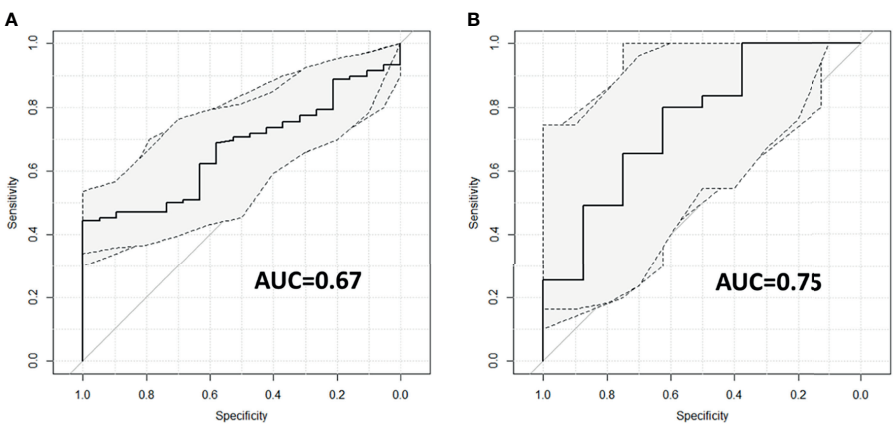

FIGURE 3 | ROC curves with corresponding 95% CIs for patients treated with **(A)** and without **(B)** oxaliplatin. ROC, receiver operating characteristic.

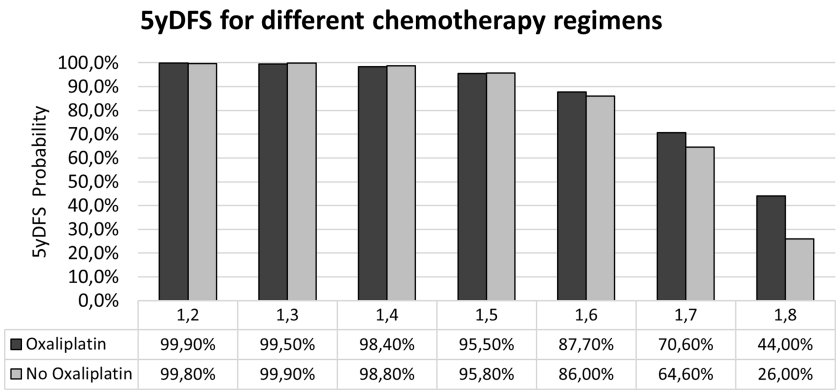

	1,2	1,3	1,4	1,5	1,6	1,7	1,8
Oxaliplatin	99,90%	99,50%	98,40%	95,50%	87,70%	70,60%	44,00%
No Oxaliplatin	99,80%	99,90%	98,80%	95,80%	86,00%	64,60%	26,00%

FIGURE 4 | Probability of 5yDFS to varying of the $maxFD_{30-50}$ extracted from the T2-w staging MR images in the case of the two treatment regimens. 5yDFS, 5-year disease-free survival; T2-w, T2-weighted.

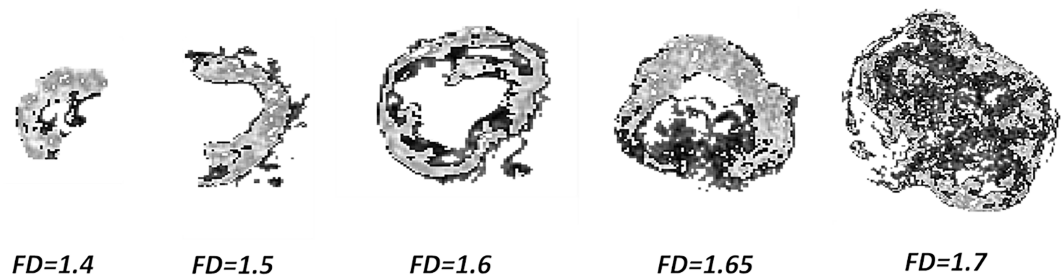

FIGURE 5 | Complexity of GTV to increasing $maxFD_{30-50}$ values: pixels in light gray indicating the subpopulation between 30% and 50% of the maximum intensity. GTV, gross tumor volume.

setting and allow a faster analysis of the radiomic potentialities (30, 38, 39).

Developing models that can predict long-term outcomes is much more challenging, as it requires a very precise and time-consuming follow-up analysis: one of the strengths of this experience is that it is based on the analysis of patients with a very long follow-up (median of 96 months).

Interestingly, an innovative methodology was proposed in this experience, with the aim of identifying the optimal CT regimen for every single patient, based on initial staging MRI analysis.

Patients were divided into two cohorts, and the features able to predict 5yDFS with statistical significance in both the cohorts were analyzed: the only one showing predictive ability in both the cohorts was the FD, which is an interesting point, as previous experiences in rectal cancer had demonstrated the fractal potentialities in predicting pCR from staging MRI analysis (27, 30).

In the idea of applying the proposed model in clinical reality, the therapeutic choice would be based on the $maxFD_{30-50}$ value: an oxaliplatin-based regimen should be preferred in cases of $maxFD_{30-50}$ >1.6, as it ensures a higher 5yDFS probability (70.6% vs. 64.6% in case of FD = 1.7; 44% vs. 26% in cases of FD = 1.8), while the two CT regimens can be considered equivalent in terms of 5yDFS for $maxFD_{30-50}$ ≤1.6.

Obviously, the findings of this study are still not mature enough to be considered ready for clinical applications, as they are not supported by an external validation: to partially compensate for such absence, internal cross-validation was performed, which had confirmed the results observed in the training set.

Furthermore, the 95% CI values of the ROC curves elaborated are still quite large, mainly due to the small number of events analyzed: a more comprehensive study including larger patient cohorts is recommended to verify the potential of FD as an image-based biomarker in rectal cancer.

In conclusion, this study proved the feasibility of establishing the optimal regimen of CT combined with nCRT for stage III LARC cancer patients based on information extracted from the analysis of T2-w MR images. In particular, by providing an indication of the spatial heterogeneity of GTV at staging, $maxFD_{30-50}$ is able to predict with statistical significance the probability of 5yDFS. New studies including a larger cohort of patients and external validation sets are recommended to verify the results of this hypothesis-generating study.

DATA AVAILABILITY STATEMENT

The raw data supporting the conclusions of this article will be made available by the authors, without undue reservation.

ETHICS STATEMENT

The studies involving human participants were reviewed and approved by Gemelli. The patients/participants provided their written informed consent to participate in this study. Written informed consent was obtained from the individual(s) for the publication of any potentially identifiable images or data included in this article.

AUTHOR CONTRIBUTIONS

All authors contributed to the article and approved the submitted version.

REFERENCES

1. Berardi R, Maccaroni E, Onofri A, Morgese F, Torniai M, Tiberi M, et al. Locally Advanced Rectal Cancer: The Importance of a Multidisciplinary Approach. *World J Gastroenterol* (2014) 20:17279–87. doi: 10.3748/wjg.v20.i46.17279
2. Feeney G, Sehgal R, Sheehan M, Hogan A, Regan M, Joyce M, et al. Neoadjuvant Radiotherapy for Rectal Cancer Management. *World J Gastroenterol* (2019) 25:4850–69. doi: 10.3748/wjg.v25.i33.4850
3. Habr-Gama A, Gama-Rodrigues J, São Julião GP, Proscurshim I, Sabbagh C, Lynn PB, et al. Local Recurrence After Complete Clinical Response and Watch and Wait in Rectal Cancer After Neoadjuvant Chemoradiation: Impact of Salvage Therapy on Local Disease Control. *Int J Radiat Oncol Biol Phys* (2014) 88:822–8. doi: 10.1016/j.ijrobp.2013.12.012
4. Valentini V, van Stiphout RGPM, Lammering G, Gambacorta MA, Barba MC, Bebenek M, et al. Selection of Appropriate End-Points (pCR vs 2ydfs) for Tailoring Treatments With Prediction Models in Locally Advanced Rectal Cancer. *Radiother Oncol* (2015) 114:302–9. doi: 10.1016/j.radonc.2015.02.001
5. van Gijn W, Marijnen CAM, Nagtegaal ID, Kranenbarg EM-K, Putter H, Wiggers T, et al. Preoperative Radiotherapy Combined With Total Mesorectal Excision for Resectable Rectal Cancer: 12-Year Follow-Up of the Multicentre, Randomised Controlled TME Trial. *Lancet Oncol* (2011) 12:575–82. doi: 10.1016/S1470-2045(11)70097-3
6. Gérard J-P, Azria D, Gourgou-Bourgade S, Martel-Laffay I, Hennequin C, Etienne P-L, et al. Comparison of Two Neoadjuvant Chemoradiotherapy Regimens for Locally Advanced Rectal Cancer: Results of the Phase III Trial ACCORD 12/0405-Prodige 2. *J Clin Oncol* (2010) 28:1638–44. doi: 10.1200/JCO.2009.25.8376
7. Allegra CJ, Yothers G, O'Connell MJ, Beart RW, Wozniak TF, Pitot HC, et al. Neoadjuvant 5-FU or Capecitabine Plus Radiation With or Without Oxaliplatin in Rectal Cancer Patients: A Phase III Randomized Clinical Trial. *J Natl Cancer Inst* (2015) 107:djv248. doi: 10.1093/jnci/djv248
8. Aschele C, Cionini L, Lonardi S, Pinto C, Cordio S, Rosati G, et al. Primary Tumor Response to Preoperative Chemoradiation With or Without Oxaliplatin in Locally Advanced Rectal Cancer: Pathologic Results of the STAR-01 Randomized Phase III Trial. *J Clin Oncol* (2011) 29:2773–80. doi: 10.1200/JCO.2010.34.4911
9. Schmoll H-J, Stein A, Van Cutsem E, Price T, Hofheinz RD, Nordlinger B, et al. Pre- and Postoperative Capecitabine Without or With Oxaliplatin in Locally Advanced Rectal Cancer: PETACC 6 Trial by EORTC GITCG and ROG, AIO, AGITG, BGDO, and FFCD. *JCO* (2021) 39:17–29. doi: 10.1200/JCO.20.01740
10. Deng Y, Chi P, Lan P, Wang L, Chen W, Cui L, et al. Modified FOLFOX6 With or Without Radiation Versus Fluorouracil and Leucovorin With Radiation in Neoadjuvant Treatment of Locally Advanced Rectal Cancer: Initial Results of the Chinese FOWARC Multicenter, Open-Label, Randomized Three-Arm Phase III Trial. *J Clin Oncol* (2016) 34:3300–7. doi: 10.1200/JCO.2016.66.6198
11. Jiao D, Zhang R, Gong Z, Liu F, Chen Y, Yu Q, et al. Fluorouracil-Based Preoperative Chemoradiotherapy With or Without Oxaliplatin for Stage II/III Rectal Cancer: A 3-Year Follow-Up Study. *Chin J Cancer Res* (2015) 27:588–96. doi: 10.3978/j.issn.1000-9604.2015.12.05
12. Liu Z, Zhang X-Y, Shi Y-J, Wang L, Zhu H-T, Tang Z, et al. Radiomics Analysis for Evaluation of Pathological Complete Response to Neoadjuvant Chemoradiotherapy in Locally Advanced Rectal Cancer. *Clin Cancer Res* (2017) 23:7253–62. doi: 10.1158/1078-0432.CCR-17-1038
13. Kumar V, Gu Y, Basu S, Berglund A, Eschrich SA, Schabath MB, et al. Radiomics: The Process and the Challenges. *Magn Reson Imaging* (2012) 30:1234–48. doi: 10.1016/j.mri.2012.06.010
14. Fokas E, Glynne-Jones R, Appelt A, Beets-Tan R, Beets G, Haustermans K, et al. Outcome Measures in Multimodal Rectal Cancer Trials. *Lancet Oncol* (2020) 21:e252–64. doi: 10.1016/S1470-2045(20)30024-3
15. Cusumano D, Boldrini L, Yadav P, Yu G, Musurunu B, Chiloiro G, et al. External Validation of Early Regression Index (ERITCP) as Predictor of Pathologic Complete Response in Rectal Cancer Using Magnetic Resonance-Guided Radiation Therapy. *Int J Radiat Oncol Biol Phys* (2020) 108:1347–56. doi: 10.1016/j.ijrobp.2020.07.2323
16. Fiorino C, Gumina C, Passoni P, Palmisano A, Broggi S, Cattaneo GM, et al. A TCP-Based Early Regression Index Predicts the Pathological Response in Neo-Adjuvant Radio-Chemotherapy of Rectal Cancer. *Radiother Oncol* (2018) 128:564–8. doi: 10.1016/j.radonc.2018.06.019
17. Chiloiro G, Rodriguez-Carnero P, Lenkowicz J, Casà C, Masciocchi C, Boldrini L, et al. Delta Radiomics Can Predict Distant Metastasis in Locally Advanced Rectal Cancer: The Challenge to Personalize the Cure. *Front Oncol* (2020) 10:595012. doi: 10.3389/fonc.2020.595012
18. Liu Z, Meng X, Zhang H, Li Z, Liu J, Sun K, et al. Predicting Distant Metastasis and Chemotherapy Benefit in Locally Advanced Rectal Cancer. *Nat Commun* (2020) 11:4308. doi: 10.1038/s41467-020-18162-9
19. Brierley JD, Gospodarowicz MK, Wittekind C. *TNM Classification of Malignant Tumours*. Bridgewater, NJ 08807: John Wiley & Sons (2017).
20. Valentini V, Gambacorta MA, Barbaro B, Chiloiro G, Coco C, Das P, et al. International Consensus Guidelines on Clinical Target Volume Delineation in Rectal Cancer. *Radiother Oncol* (2016) 120:195–201. doi: 10.1016/j.radonc.2016.07.017
21. Suárez J, Vera R, Balén E, Gómez M, Arias F, Lera JM, et al. Pathologic Response Assessed by Mandard Grade Is a Better Prognostic Factor Than Down Staging for Disease-Free Survival After Preoperative Radiochemotherapy for Advanced Rectal Cancer. *Colorectal Dis* (2008) 10:563–8. doi: 10.1111/j.1463-1318.2007.01424.x
22. Barbaro B, Fiorucci C, Tebala C, Valentini V, Gambacorta MA, Vecchio FM, et al. Locally Advanced Rectal Cancer: MR Imaging in Prediction of Response After Preoperative Chemotherapy and Radiation Therapy. *Radiology* (2009) 250:730–9. doi: 10.1148/radiol.2503080310
23. Hodapp N. [The ICRU Report 83: Prescribing, Recording and Reporting Photon-Beam Intensity-Modulated Radiation Therapy (IMRT)]. *Strahlenther Onkol* (2012) 188:97–9. doi: 10.1007/s00066-011-0015-x
24. Gatta R, Vallati M, Dinapoli N, Masciocchi C, Lenkowicz J, Cusumano D, et al. Towards a Modular Decision Support System for Radiomics: A Case Study on Rectal Cancer. *Artif Intell Med* (2018) 96:145–53. doi: 10.1016/j.artmed.2018.09.003
25. Dinapoli N, Alitto AR, Vallati M, Gatta R, Autorino R, Boldrini L, et al. Moddicom: A Complete and Easily Accessible Library for Prognostic Evaluations Relying on Image Features. *Conf Proc IEEE Eng Med Biol Soc* (2015) 2015:771–4. doi: 10.1109/EMBC.2015.7318476

26. Dinapoli N, Barbaro B, Gatta R, Chiloiro G, Casà C, Masciocchi C, et al. Magnetic Resonance, Vendor-Independent, Intensity Histogram Analysis Predicting Pathologic Complete Response After Radiochemotherapy of Rectal Cancer. *Int J Radiat Oncol Biol Phys* (2018) 102(4):765–74. doi: 10.1016/j.ijrobp.2018.04.065
27. Cusumano D, Dinapoli N, Boldrini L, Chiloiro G, Gatta R, Masciocchi C, et al. Fractal-Based Radiomic Approach to Predict Complete Pathological Response After Chemo-Radiotherapy in Rectal Cancer. *Radiol Med* (2018) 123:286–95. doi: 10.1007/s11547-017-0838-3
28. Zwanenburg A, Vallières M, Abdalah MA, Aerts HJWL, Andrearczyk V, Apte A, et al. The Image Biomarker Standardization Initiative: Standardized Quantitative Radiomics for High-Throughput Image-Based Phenotyping. *Radiology* (2020) 295:328–38. doi: 10.1148/radiol.2020191145
29. Cusumano D, Boldrini L, Yadav P, Gao Y, Chiloiro G, Musurunu B, et al. Delta Radiomics for Rectal Cancer Response Prediction Using Low Field Magnetic Resonance Guided Radiotherapy: An External Validation. *Phys Med* (2021) 84:186-191. doi: 10.1016/j.ejmp.2021.03.038
30. Cusumano D, Meijer G, Lenkowicz J, Chiloiro G, Boldrini L, Masciocchi C, et al. A Field Strength Independent MR Radiomics Model to Predict Pathological Complete Response in Locally Advanced Rectal Cancer. *Radiol Med* (2020) 126(3):421–9. doi: 10.1007/s11547-020-01266-z
31. Taylor J. *Introduction to Error Analysis, the Study of Uncertainties in Physical Measurements* (1997). 648 Broadway, Suite 902, New York, NY 10012, 1997: Published by University Science Books. Available at: http://adsabs.harvard.edu/abs/1997ieas.book (Accessed June 4, 2020).
32. International Commissioning on Radiation Units and Measurements. Receiver Operating Characteristic (ROC) Analysis in Medical Imaging. *ICRU Rep 79* (2008) 8:1-62. doi: 10.1093/jicru/ndn018
33. Ruopp MD, Perkins NJ, Whitcomb BW, Schisterman EF. Youden Index and Optimal Cut-Point Estimated From Observations Affected by a Lower Limit of Detection. *Biometrical J Biometrische Z* (2008) 50:419. doi: 10.1002/bimj.200710415
34. Robin X, Turck N, Hainard A, Tiberti N, Lisacek F, Sanchez J-C, et al. pROC: An Open-Source Package for R and S+ to Analyze and Compare ROC Curves. *BMC Bioinf* (2011) 12:77. doi: 10.1186/1471-2105-12-77
35. Scott JG, Berglund A, Schell MJ, Mihaylov I, Fulp WJ, Yue B, et al. A Genome-Based Model for Adjusting Radiotherapy Dose (GARD): A Retrospective, Cohort-Based Study. *Lancet Oncol* (2017) 18:202–11. doi: 10.1016/S1470-2045(16)30648-9
36. Gillies RJ, Kinahan PE, Hricak H. Radiomics: Images Are More Than Pictures, They Are Data. *Radiology* (2016) 278:563–77. doi: 10.1148/radiol.2015151169
37. Lambin P, Leijenaar RTH, Deist TM, Peerlings J, de Jong EEC, van Timmeren J, et al. Radiomics: The Bridge Between Medical Imaging and Personalized Medicine. *Nat Rev Clin Oncol* (2017) 14:749–62. doi: 10.1038/nrclinonc.2017.141
38. Horvat N, Veeraraghavan H, Khan M, Blazic I, Zheng J, Capanu M, et al. MR Imaging of Rectal Cancer: Radiomics Analysis to Assess Treatment Response After Neoadjuvant Therapy. *Radiology* (2018) 287:833–43. doi: 10.1148/radiol.2018172300
39. Boldrini L, Cusumano D, Chiloiro G, Casà C, Masciocchi C, Dinapoli N, et al. Delta Radiomics for Rectal Cancer Response Prediction With Hybrid 0.35 T Magnetic Resonance Guided Radiotherapy (MRgRT) : A Hypothesis Generating Study for an Innovative Personalized Medicine Approach. *La Radiol Med* (2018) 124:145–53. doi: 10.1007/s11547-018-0951-y

Conflict of Interest: The authors declare that the research was conducted in the absence of any commercial or financial relationships that could be construed as a potential conflict of interest.

Publisher's Note: All claims expressed in this article are solely those of the authors and do not necessarily represent those of their affiliated organizations, or those of the publisher, the editors and the reviewers. Any product that may be evaluated in this article, or claim that may be made by its manufacturer, is not guaranteed or endorsed by the publisher.

frontiers in Oncology

ORIGINAL RESEARCH
published: 03 January 2022
doi: 10.3389/fonc.2021.783544

Amide Proton Transfer Weighted and Intravoxel Incoherent Motion Imaging in Evaluation of Prognostic Factors for Rectal Adenocarcinoma

Juan Li[1], *Liangjie Lin*[2], *Xuemei Gao*[1], *Shenglei Li*[3]* and *Jingliang Cheng*[1]*

[1] Department of Magnetic Resonance Imaging (MRI), The First Affiliated Hospital of Zhengzhou University, Zhengzhou, China, [2] Advanced Technical Support, Philips Healthcare, Beijing, China, [3] Department of Pathology, The First Affiliated Hospital of Zhengzhou University, Zhengzhou, China

OPEN ACCESS

Edited by:
Pierfrancesco Franco, University of Eastern Piedmont, Italy

Reviewed by:
Yee Kai Tee, Tunku Abdul Rahman University, Malaysia
Carlos Perez-Torres, Purdue University, United States

***Correspondence:**
Jingliang Cheng
fccchengjl@zzu.edu.cn
Shenglei Li
shenglei_lsl3@163.com

Specialty section:
This article was submitted to Cancer Imaging and Image-directed Interventions, a section of the journal Frontiers in Oncology

Received: *26 September 2021*
Accepted: *06 December 2021*
Published: *03 January 2022*

Citation:
Li J, Lin L, Gao X, Li S and Cheng J (2022) Amide Proton Transfer Weighted and Intravoxel Incoherent Motion Imaging in Evaluation of Prognostic Factors for Rectal Adenocarcinoma. Front. Oncol. 11:783544. doi: 10.3389/fonc.2021.783544

Objectives: To analyze the value of amide proton transfer (APT) weighted and intravoxel incoherent motion (IVIM) imaging in evaluation of prognostic factors for rectal adenocarcinoma, compared with diffusion weighted imaging (DWI).

Materials and Methods: Preoperative pelvic MRI data of 110 patients with surgical pathologically confirmed diagnosis of rectal adenocarcinoma were retrospectively evaluated. All patients underwent high-resolution T_2-weighted imaging (T_2WI), APT, IVIM, and DWI. Parameters including APT signal intensity (APT SI), pure diffusion coefficient (D), pseudo-diffusion coefficient (D*), perfusion fraction (f), and apparent diffusion coefficient (ADC) were measured in different histopathologic types, grades, stages, and structure invasion statuses. Receiver operating characteristic (ROC) curves were used to evaluate the diagnostic efficacy, and the corresponding area under the curves (AUCs) were calculated.

Results: APT SI, D and ADC values of rectal mucinous adenocarcinoma (MC) were significantly higher than those of rectal common adenocarcinoma (AC) ([3.192 ± 0.661%] *vs*. [2.333 ± 0.471%], [1.153 ± 0.238×10^{-3} mm^2/s] *vs*. [0.792 ± 0.173×10^{-3} mm^2/s], and [1.535 ± 0.203×10^{-3} mm^2/s] *vs*. [0.986 ± 0.124×10^{-3} mm^2/s], respectively; all $P<0.001$). In AC group, the APT SI and D values showed significant differences between low- and high-grade tumors ([2.226 ± 0.347%] *vs*. [2.668 ± 0.638%], and [0.842 ± 0.148×10^{-3} mm^2/s] *vs*. [0.777 ± 0.178×10^{-3} mm^2/s], respectively, both $P<0.05$). The D value had significant difference between positive and negative extramural vascular invasion (EMVI) tumors ([0.771 ± 0.175×10^{-3} mm^2/s] *vs*. [0.858 ± 0.151×10^{-3} mm^2/s], $P<0.05$). No significant difference of APT SI, D, D*, f or ADC was observed in different T stages, N stages, perineural and lymphovascular invasions (all $P>0.05$). The ROC curves showed that the AUCs of APT SI, D and ADC values for distinguishing MC from AC were 0.921, 0.893 and 0.995, respectively. The AUCs of APT SI and D values in distinguishing low- from high-grade AC were 0.737 and 0.663, respectively. The AUC of the D value for evaluating EMVI involvement was 0.646.

Conclusion: APT and IVIM were helpful to assess the prognostic factors related to rectal adenocarcinoma, including histopathological type, tumor grade and the EMVI status.

Keywords: APT, IVIM, rectal neoplasms, adenocarcinoma, magnetic resonance imaging

INTRODUCTION

Colorectal cancer is a common malignancy of the digestive system, 30-35% are occurred in the rectum, and 90% are classified as adenocarcinoma (1, 2). Many factors are associated with therapeutic schedule and prognosis of rectal cancer, including tumor location, histological type, tumor grade, T stage, N stage, and related imaging indicators based on MRI, such as circumferential resection margin (CRM), and extramural vascular invasion (EMVI) statuses (3, 4). Rectal mucinous adenocarcinoma (MC) is a common subtype of rectal adenocarcinomas, which has a poor prognosis, and it is not sensitive to neoadjuvant chemoradiotherapy (5, 6). The selection of individualized treatment options for rectal cancer is based on accurate imaging evaluation.

Magnetic resonance imaging (MRI) is the most accurate test for preoperative assessment of rectal cancer. Conventional high-resolution MRI imaging, especially the small-field-of-view and thin-layer T_2 weighted imaging (T_2WI), not only clearly distinguishes the various layers of the rectal wall, but also displays the mesorectal fascia and EMVI (7, 8). Functional MRI has become increasingly widespread in recent years. Diffusion weighted imaging (DWI) is an example of functional MRI that reflects changes in tissue microenvironments by measuring the diffusion of water molecules in tissues. It has been applied in tumor TN stage, grading, and prognosis of rectal cancer in previous studies. However, the results were lack of consistency (9). Zhu et al. found the ADC values of low-grade adenocarcinoma were higher than those of high-grade adenocarcinoma, but the difference was not statistically significant (10). Several new MRI techniques have been used to evaluate the pathological features of rectal cancer, including intravoxel incoherent motion (IVIM), diffusion kurtosis imaging (DKI), and dynamic contrast-enhanced (DCE) imaging (11, 12). IVIM provides diffusion and perfusion information within tissue through the biexponential modelling of images acquired by multiple b values (13). Previous studies showed the ability of IVIM for the differential diagnosis of malignant and benign tumors, as well as reflect the biological behavior and predict prognosis (14–16). Amide proton transfer (APT) weighted imaging is a noninvasive molecular imaging technique based on chemical exchange saturation transfer (CEST). It measures the endogenous moving proteins and peptides by detecting the reduction in bulk water intensity, which indirectly reflects changes of the internal metabolism (17, 18). APT weighted imaging has been applied in studies of various cancers, it exhibits an excellent ability in tumor differentiation, grading, and discrimination of treatment related necrosis from recurrence (19–21). Li et al. suggested the utility of APT and IVIM may be a useful technique in the diagnosis and predicting the differentiation of squamous cell carcinoma (22). Jia et al. found a prediction model incorporating APT and IVIM in the tumor may be useful for predicting the response of hepatocellular carcinoma (HCC) to transarterial chemoembolization (TACE) pretreatment (23). There are few studies using APT on research of rectal cancer. Nishie et al. observed APT weighted imaging can predict the tumor response to neoadjuvant chemotherapy in patients with locally advanced rectal cancer (24). Previous studies have reported that tumors with high-grade, more advanced T stage, and lymph node metastasis had higher APT signal intensity (APT SI) (25–27). However, the previous studies were commonly with limited sample sizes, without involvement of the histopathologic type, perineural invasion and lymphovascular invasion, and without comparison to IVIM.

This study aims to investigate the ability of APT and IVIM in evaluation of prognostic factors for rectal adenocarcinoma, thereby to evaluate its reference value for assessing the malignant degree and predicting tumor aggressiveness, compared with results by conventional DWI.

MATERIALS AND METHODS

Participants

Preoperative pelvic MRI data of 158 patients with pathologically confirmed rectal cancer at our hospital were collected between July 2020 and August 2021. The inclusion criteria were as follows: pathologically proven rectal adenocarcinoma; patients did not undergo surgery, chemical, or radiation therapy before MRI examination; surgery and pathology was confirmed within one week after MRI examination. The exclusion criteria were as follows: patients received neoadjuvant therapy (n=35); patients had poor compliance or poor image quality (n=7); rectal neuroendocrine tumor, lymphomas, and other rare tumors (n=6). Finally, 110 patients were enrolled in this study (**Figure 1**).

MR Imaging Protocols

MRI were performed on a 3T scanner (Ingenia CX, Philips Healthcare, Best, the Netherlands) with a 32-channel phase array coil. Patients were instructed to empty the rectum before examination. To suppress intestinal movement artifacts, 20 mg raceanisodamine hydrochloride injection (Suicheng Pharmaceutical Co, Ltd.) was given intramuscularly 5-10 min before examination. The scanning sequences included T_2WI, T_1-weighted imaging (T_1WI), DWI, APT, IVIM, and dynamic contrast-enhanced T_1WI. The oblique axial was positioned perpendicular to the long axis of the lesion. Detailed parameters for the sequences were listed in **Table 1**.

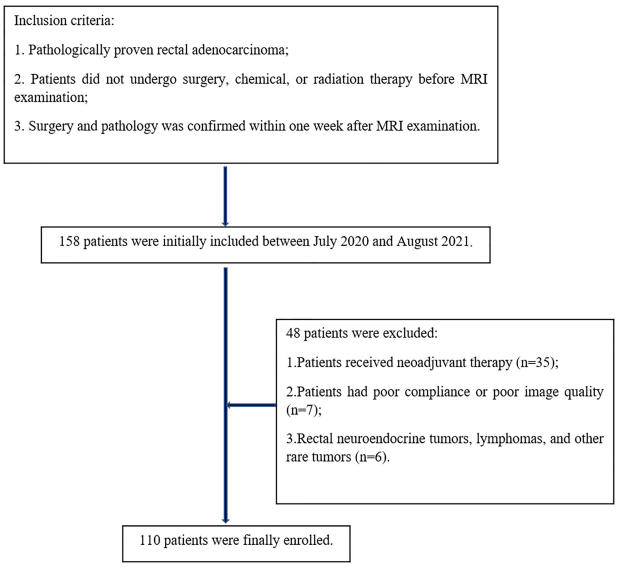

FIGURE 1 | Flowchart of patient selection.

TABLE 1 | MRI acquisition parameters.

Parameters	APT	IVIM	DWI	T_2WI
Sequence	TSE	EPI	EPI	TSE
TR/TE (ms)	6540/8.3	4888/90	4421/77	3000/100
Field of view (mm^2)	230×181	240×240	200×129	180×180
Slice thickness (mm)	5	5	4	4
No. of slices	9	24	24	24
Matrix	116×90	72×67	80×52	300×235
Spatial resolution (mm^3)	2×2×5	3.3×3.58×5	2.5×2.46×4	0.6×0.7×4
b-values (s/mm^2)	N/A	0,10,20,50,100,200,400,800,1200	0,800	N/A
Bandwidth (Hz/pixel)	647.2	2977.8	2365.9	254.1
TSE factor	174	N/A	N/A	15
Fat suppression	Yes	No	No	N0
Acquisition time	6min0s	4min53s	2min26s	2min54s

T_2WI, T_2-weighted imaging; TSE, turbo spin echo; EPI, echo-planar imaging; TR, repetition time; TE, echo time; N/A, not applicable.

High-resolution T_2WI was helpful for estimating tumor location, the relationship with peritoneal reflection, tumor size, bowel circumferential involvement, CRM, and EMVI statuses. APT weighted images were acquired by using a 3D turbo spin echo (TSE) sequence for optimized signal-to-noise ratio. The continuous RF saturation for a duration of 2 seconds (each RF coil was turned on and off for 500 msec to generate four block RF pulses at 2 μT amplitude) (20). For convenience, the water frequency (around 4.75 ppm in the proton MR spectrum) is placed at 0 ppm of the Z-spectrum, in which the water signal saturation is measured as a function of saturation frequency. Data were acquired with seven different saturation frequency offsets with respect to the water resonance (± 3.5, ± 3.42, ± 3.58, −1560 ppm). A B_0 map was derived from three echo acquisitions at +3.5 ppm for B_0 correction (28). IVIM (with b values of 0, 10, 20, 50, 100, 200, 400, 800, 1200 s/mm^2) were performed in the oblique axial plane using a single-shot echo planar imaging (ss-EPI) sequence with comparable parameters. The diffusion gradients were applied simultaneously along with three orthogonal directions. DWI (with b values of 0, 800 s/mm^2) was also performed using the ss-EPI sequence.

Data Processing and Analysis

APT weighted images were automatically generated on the console at the time of scan completion. After MR scans, all images were uploaded to the IntelliSpace Portal (ISP v10, Philips Healthcare) workstation for post processing or quantitative measurements. The MTR_{asym} (magnetization transfer ratio asymmetry) value at the frequency offset of +3.5 ppm was displayed as percent level (relative to S_0) in the final APT images, and referred as APT SI:

$$\text{APT SI} = MTRasym\ [\Delta\omega = +3.5ppm]\ (\%)$$

The IVIM data were processed by the application of advanced diffusion analysis (ADA) on the workstation with maps of the pure diffusion coefficient (D), pseudo-diffusion coefficient (D*) and perfusion fraction (f) generated. The linear fitting equation is as follows:

$$S_b/S_0 = (1-f)\exp(-b \times D) + f \exp(-b \times D*)$$

where S_b is the MR signal intensity with diffusion gradient; S_0 is the MR signal intensity without diffusion gradient. The ADC maps were generated immediately after DWI data acquisition.

MRI images were analyzed by two radiologists experienced in gastrointestinal diseases diagnosis. Regions of interest (ROIs) on APT SI, D, D*, f and ADC images were manually selected for analysis, according to T_2WI and pathology results. The ROIs of APT SI were drawn on APT-T2 merged images, then the same ROIs were copied to the ADC images for measuring values. The ROIs of D were drawn on D images, then the same ROIs were showed on the D* and f images for quantitative measurements. The ROIs were drawn at the level of the maximum extent of the tumor and the levels above and below it, and the averaged values were taken. Necrotic, cystic, and hemorrhagic regions were avoided.

Pathologic Analyses

Pathological reports of rectal cancer were referred to standardized templates, including surgical procedures, gross and histological types, tumor grade, pathological stage, perineural invasion, lymphovascular invasion, cut edge infringement, and immunohistochemistry. According to world health organization (WHO) grading criteria, rectal common adenocarcinoma (AC) was classified as grade 1 (G1, well differentiated, >95% gland forming), grade 2 (G2, moderately differentiated, 50-95% gland forming), or grade 3 (G3, poorly differentiated, 0-49% gland forming). According to two-tiered grading system of WHO criteria, G1 and G2 tumors were classified as low-grade tumors, G3 tumors were classified as high-grade tumors. The staging criteria were evaluated according to the American Joint Committee on Cancer (AJCC) 8th edition. T staging was classified as pT1-2 and pT3-4 stage based on depth of tumor invasion. pT1-2 stage cancer was defined as disease confined to the muscularis propria, including pT1 and pT2 stage, and pT3-4 stage cancer was defined as disease extending beyond the muscularis propria, including pT3 and pT4 stage. Lymph node staging was performed based on results of postoperative pathology including pN0 stage: lack of regional lymph node metastasis, pN1 stage: less than 3 regional lymph node metastasis, and pN2 stage: 4 or more regional lymph node metastasis. Perineural invasion, lymphovascular invasion, and EMVI statuses were classified into positive and negative groups.

Statistical Analysis

SPSS 22.0 software (IBM, Armonk, NY) was used for statistical analysis. The Kolmogorov-Smirnov test was performed for analyzing normality. Data conforming to the normal distribution were expressed as mean ± standard deviation (SD). The intraclass correlation coefficient (ICC) was used to evaluate the interobserver consistency of the measured parameters. ICC values of less than 0.40, 0.41–0.75, and greater than 0.75 were considered to indicate poor, fair, and good agreement, respectively. The t-test for independent samples was used to compare APT SI, D, D*, f and ADC parameters between pathological types (MC *vs*. AC), WHO grades (low- *vs*. high-grade), pT stages (pT1-2 *vs*. pT3-4), pN stages (pN1-2 *vs*. pN0), perineural invasion (positive *vs*. negative), lymphovascular invasion (positive *vs*. negative), and EMVI statuses (positive *vs*. negative). For parameters with significant differences between groups, the receiver operating characteristic (ROC) curve was used to analyze their diagnostic efficacy using the software of MedCalc v. 20.0 (MedCalc Software, Ostend, Belgium). DeLong test was used to compare the differences of area under ROC curves (AUCs). The forward model of binary logistic regression was applied for parameter fusion. Differences with $P<0.05$ were considered statistically significant.

RESULTS

The Pathological Results of Rectal Adenocarcinomas

Among 110 rectal adenocarcinomas, 17 cases were MC and 93 cases were AC. The mean age was 60.31 ± 10.84 years (age range 33–83 years). Within the AC group, 69 and 24 cases were low-grade and high-grade adenocarcinomas, respectively (**Figures 2**–**4**); 38 and 55 cases were pT1-2 stage and pT3-4 stage, respectively; 64 and 29 cases were pN0 stage and pN1-2 stage, respectively; 23 and 70 cases were positive and negative perineural invasion, respectively; 26 and 67 cases were positive and negative lymphovascular invasion, respectively; 25 and 68 cases were positive and negative EMVI, respectively; 90 and 3 cases were positive and negative CRM, respectively. Clinical features, histopathologic characteristics were summarized in **Table 2**.

Interobserver Agreement

The intraclass correlation coefficient were 0.942 (95% CI 0.831–0.967) for APT SI; 0.862 (95% CI, 0.714–0.913) for D; 0.762 (95% CI, 0.632–0.825) for D*; 0.859 (95% CI, 0.697–0.912) for f; and 0.916 (95% CI, 0.850–0.933) for ADC, respectively. There were good agreements between two observers for measurements of APT SI, D, D*, f, and ADC values.

Comparison of the Parameters in Different Groups of Rectal Adenocarcinomas

Detailed results were showed in **Tables 3**, **4** and **Figure 5**. The APT SI, D and ADC values of MC were significantly higher than those of AC (all $P<0.001$). Within the AC group, the APT SIs were significantly lower, and the D values were higher in low-grade adenocarcinomas than in high-grade ones ($P=0.001$ and 0.025; respectively). The D values were significantly lower in positive than in negative EMVI tumors ($P=0.045$). No significant difference of APT SI, D, D*, f or ADC observed in other groups (all $P>0.05$).

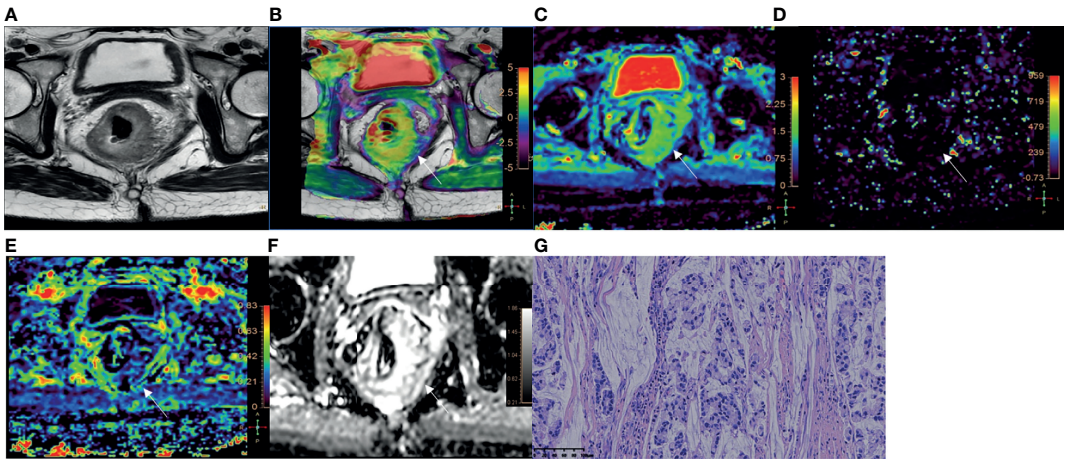

FIGURE 2 | A 51-year-old female with MC. **(A)** Oblique axial T_2-weighted image showed a mass with high intensity in the rectum. **(B)** APT-T2 merged image showed the mass with a mean APT SI of 3.4%. **(C–E)** D, D* and f maps showed the mass with values of 1.42×10^{-3} mm^2/s, 5.00×10^{-3} mm^2/s and 0.22, respectively. **(F)** The mass showed high intensity ($1.87\times10^{-3}mm^2/s$) on the ADC map. **(G)** HE staining revealed mucinous adenocarcinoma. (×200).

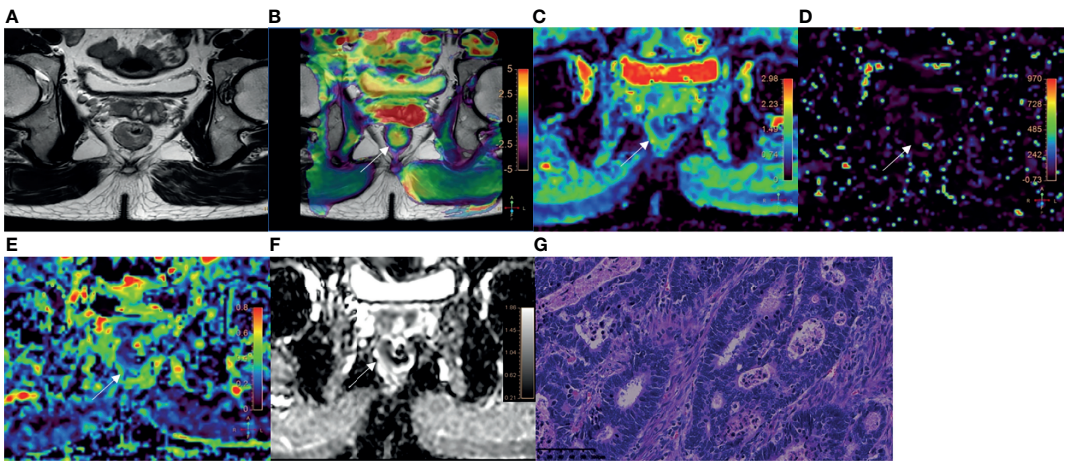

FIGURE 3 | A 52-year-old male with AC of grade 2. **(A)** Oblique axial T_2-weighted image showed a mass with slightly high intensity in the rectum. **(B)** APT-T2 merged image showed the mass with a mean APT SI of 2.1%. **(C–E)** D, D* and f maps showed the mass with values of 0.81×10^{-3} mm^2/s, 7.74×10^{-3} mm^2/s and 0.19, respectively. **(F)** The mass showed low intensity (1.03×10^{-3} mm^2/s) on the ADC map. **(G)** HE staining revealed moderately differentiated adenocarcinoma. (×200).

Comparison of ROC Curves for Distinguishing MC From AC, Low- From High-Grade AC, and Distinguishing EMVI Status

ROC curves of APT SI, D, and ADC values between MC and AC, low- and high-grade AC, positive and negative EMVI were listed in **Figure 6**. The ROC curves for distinguishing MC from AC were shown in **Figure 6A** using the APT SI, D and ADC values with the AUCs of 0.921, 0.893, 0.995, respectively. The comparison among these AUCs showed no significant difference (APT SI *vs*. D: Z=2.457, P=0.140; APT SI *vs*. ADC: Z=2.457, P=0.140; and D *vs*. ADC: Z=1.607, P=0.108; respectively). The AUCs for distinguishing low- from high-grade AC using the APT SI and D values were 0.737 and 0.663, respectively (**Figure 6B**), without significant difference (Z=0.748, P=0.455). The AUC was increased to 0.806 through the combination of APT SI and D values (**Figure 6B**). The comparison of AUCs showed significant differences between the combined parameter and APT SI (Z=1.962, P=0.049) or D values (Z=2.040, P=0.041). The AUC for distinguishing positive EMVI from negative EMVI using the D value was 0.646 (**Figure 6C**). The diagnostic performance and optimal diagnostic threshold of parameters were listed in **Table 5**.

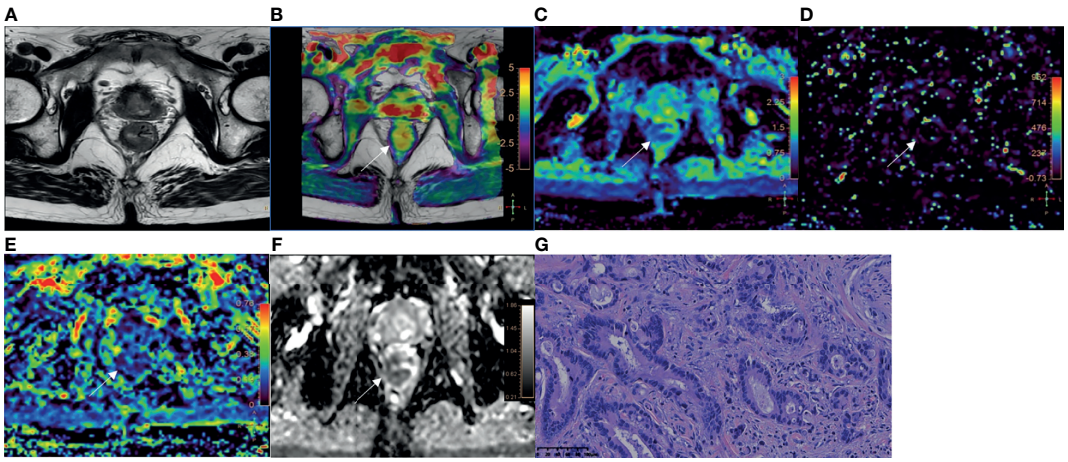

FIGURE 4 | A 78-year-old male with AC of grade 3. **(A)** Oblique axial T_2-weighted image showed a mass with slightly high intensity in the rectum. **(B)** APT-T2 merged image showed the mass with a mean APT SI of 2.8%. **(C–E)** D, D* and f maps showed the mass with values of $0.79\times10^{-3}mm^2/s$, $9.40\times10^{-3}mm^2/s$ and 0.17, respectively. **(F)** The mass showed low intensity ($0.93\times10^{-3}mm^2/s$) on the ADC map. **(G)** HE staining revealed poorly differentiated adenocarcinoma. (×200).

TABLE 2 | Clinical and pathological characteristics.

Category	Gender (Male/Female)	Relationship with peritoneal reflection (Above/Across/Below)	Tumor location (Upper/Middle/Lower)	Tumor longitudinal diameter (≥50mm/<50mm)	Tumor transverse diameter (≥10mm/<10mm)	Bowel circumferential involvement (≥1/2/<1/2)
Pathological type						
MC (n=17)	9/8	3/6/8	5/7/5	10/7	14/3	15/2
AC (n=93)	60/33	15/28/50	32/41/20	36/57	70/23	74/19
WHO grade(AC)						
G1 (n=2)	1/1	0/1/1	1/1/0	0/2	0/2	0/2
G2 (n=67)	46/21	10/18/39	13/41/13	22/45	50/17	57/10
G3 (n=24)	17/7	3/7/14	4/15/5	10/14	21/3	21/3
T stage(AC)						
pT1 (n=5)	3/2	0/0/5	0/2/3	2/3	3/2	3/2
pT2 (n=33)	25/8	3/8/22	4/24/5	17/16	25/8	24/9
pT3 (n=47)	32/15	11/13/23	14/19/14	16/31	39/8	42/5
pT4 (n=8)	3/5	0/5/3	2/4/2	5/3	7/1	8/0
N stage(AC)						
pN0 (n=64)	40/24	10/14/40	11/39/14	33/31	53/11	54/10
pN1 (n=17)	12/5	1/8/8	3/9/5	11/6	13/4	15/2
pN2 (n=12)	7/5	2/5/5	4/7/1	7/5	9/3	11/1
Perineural invasion (AC)						
Positive (n=23)	14/9	1/5/17	3/13/7	12/11	20/3	21/2
Negative (n=70)	49/21	12/21/37	15/41/14	35/35	52/18	58/12
Lymphovascular invasion(AC)						
Positive (n=26)	15/11	4/9/13	5/13/8	16/10	20/6	21/5
Negative (n=67)	47/20	10/17/40	13/42/12	33/34	53/14	57/10
EMVI(AC)						
Positive (n=25)	14/11	3/8/14	7/12/6	14/11	23/2	25/0
Negative (n=68)	49/19	10/18/40	10/43/15	33/35	51/17	54/14

MC, mucinous adenocarcinoma; AC, common adenocarcinoma.

DISCUSSION

The histopathologic type, tumor grade, T stage, N stage, perineural invasion, lymphovascular invasion, and EMVI statuses are important prognostic factors for rectal cancer. In our study, we performed a comprehensive investigation of correlations of APT and IVIM parameters with rectal cancer prognostic factors, in comparison with results by DWI. Results

TABLE 3 | The comparison of APT SI, D, D*, f and ADC values in different groups of types.

Groups	APT SI (%)	D ($\times10^{-3}mm^2/s$)	D* ($\times10^{-3}mm^2/s$)	f	ADC ($\times10^{-3}mm^2/s$)
Gross types					
Ulcerated (n=73)	2.578 ± 0.241	0.965 ± 0.217	6.307 ± 2.135	0.163 ± 0.068	0.956 ± 0.127
Elevated (n=37)	2.612 ± 0.325	0.942 ± 0.228	6.791 ± 2.139	0.184 ± 0.045	0.911 ± 0.130
P value	0.185	0.107	0.218	0.195	0.136
Histological types					
MC (n=17)	3.192 ± 0.661	1.153 ± 0.238	7.017 ± 2.579	0.150 ± 0.073	1.535 ± 0.203
AC (n=93)	2.333 ± 0.471	0.792 ± 0.173	6.989 ± 2.711	0.212 ± 0.033	0.986 ± 0.124
P value	0.000	0.000	0.267	0.106	0.000

ADC, apparent diffusion coefficient.

TABLE 4 | The comparison of APT SI, D, D*, f and ADC values in different groups of AC.

Groups	APT SI (%)	D ($\times10^{-3}mm^2/s$)	D* ($\times10^{-3}mm^2/s$)	f	ADC ($\times10^{-3}mm^2/s$)
WHO grade					
Low-grade (n=69)	2.226 ± 0.347	0.842 ± 0.148	7.193 ± 2.913	0.225 ± 0.141	1.004 ± 0.129
High-grade (n=24)	2.668 ± 0.438	0.777 ± 0.178	6.361 ± 1.877	0.171 ± 0.100	0.929 ± 0.085
P value	0.001	0.025	0.420	0.124	0.155
T stage					
pT1-2 (n=38)	2.417 ± 0.318	0.772 ± 0.193	6.837 ± 2.502	0.214 ± 0.158	0.983 ± 0.129
pT3-4 (n=55)	2.276 ± 0.335	0.806 ± 0.158	7.094 ± 2.865	0.211 ± 0.116	0.989 ± 0.121
P value	0.399	0.447	0.778	0.775	0.795
N stage					
pN1-2 (n=29)	2.279 ± 0.366	0.770 ± 0.175	6.689 ± 2.015	0.189 ± 0.090	0.952 ± 0.110
pN0 (n=64)	2.236 ± 0.413	0.841 ± 0.160	7.127 ± 2.575	0.222 ± 0.149	1.002 ± 0.127
P value	0.692	0.157	0.163	0.359	0.074
Perineural invasion					
Positive (n=23)	2.325 ± 0.409	0.778 ± 0.186	5.986 ± 1.399	0.203 ± 0.085	0.946 ± 0.184
Negative (n=70)	2.335 ± 0.491	0.841 ± 0.111	7.294 ± 2.938	0.215 ± 0.145	0.998 ± 0.131
P value	0.609	0.098	0.064	0.830	0.123
Lymphovascular invasion					
Positive (n=26)	2.354 ± 0.443	0.787 ± 0.169	6.660 ± 2.092	0.201 ± 0.081	0.968 ± 0.101
Negative (n=67)	2.324 ± 0.485	0.805 ± 0.185	7.117 ± 2.921	0.217 ± 0.149	0.993 ± 0.131
P value	0.294	0.799	0.689	0.847	0.389
EMVI					
Positive (n=25)	2.416 ± 0.288	0.771 ± 0.175	6.929 ± 2.115	0.201 ± 0.114	0.979 ± 0.114
Negative (n=68)	2.306 ± 0.315	0.858 ± 0.151	7.009 ± 2.891	0.216 ± 0.140	0.988 ± 0.127
P value	0.139	0.045	0.665	0.654	0.901

indicated that APT, IVIM, and DWI all can be used in differentiating between AC and MC. APT and IVIM can be used in differentiating grades of AC, and the combination of APT with IVIM could improve the diagnostic performance. DWI can't be used in differentiating grades of AC.

We observed that APT SIs were significantly higher in MC than AC. According to the literature, APT SI was mainly contributed by the endogenous cellular proteins and peptides and affected by intercellular pH environment. Otherwise, cell density, mucin and angiogenesis also have significant effects on APT SI (17, 29). MC is characterized by tumor cell hypersecretion, with more than 50% of mucus content in the tumor parenchyma (5), which may have contributed to the higher APT SIs. D is the pure diffusion coefficient representing pure molecular diffusion, D* is the pseudo-diffusion coefficient representing microperfusion related diffusion, while f is the perfusion fraction related to microcirculation. Our study also found that D and ADC values of MC were significantly higher than those of AC, which was in accordance with previous research (30). Mucinous adenocarcinoma cells float on a layer of mucus in a relatively loose arrangement, which may decrease the cellularity and facilitate water molecule movement (31). The D* and f values showed no significant difference for distinguishing MC from AC, which may indicate the similar microperfusion component in these two types of lesions.

The histologic grade is an important prognostic factor for rectal adenocarcinoma. We demonstrated that the APT SIs of low-grade adenocarcinomas were significantly lower compared to those of high-grade adenocarcinomas, which was consistent with previous studies (25, 26). Therefore, APT weighted imaging may be helpful to identify the pathological grade of rectal cancer. Similar results have been reported in other tumors. For example, Sotirios et al. found that APT could differentiate low- from high-grade gliomas and predict the histopathological grade potentially (32). A study by Yin et al. demonstrated that APT SIs were significantly higher in prostate cancer than in benign prostatic hyperplasia and showed a strong correlation with the Gleason score (33). All these studies indicated that malignant tumors

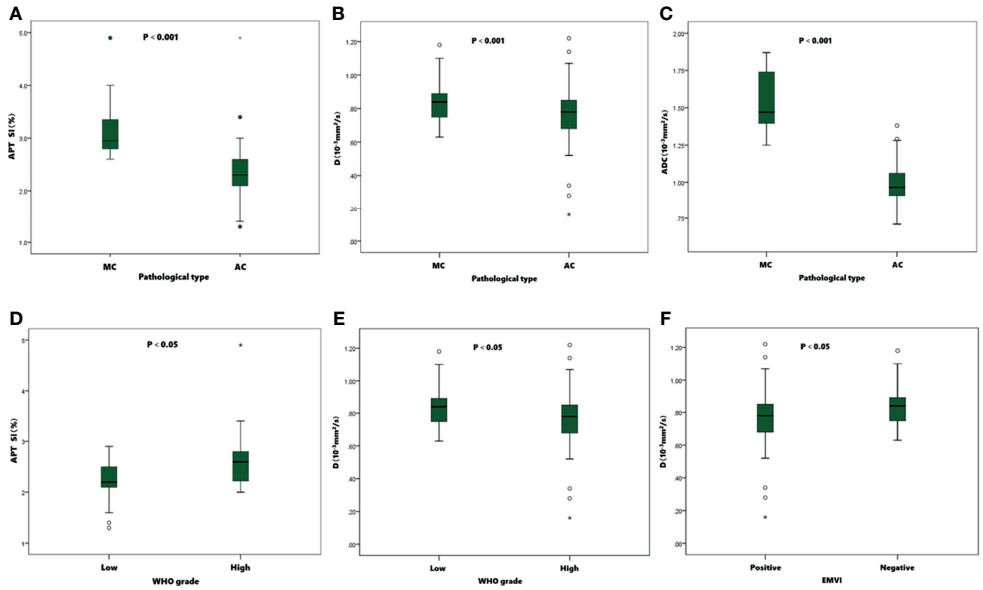

FIGURE 5 | Boxplots of APT SI, D and ADC values in different pathological types, WHO grades, and EMVI statuses of tumors. The APT SIs **(A)**、D **(B)** and ADC **(C)** values were significantly higher in MC than in AC. In AC group, the APT SIs **(D)** were significantly lower in low-grade than in high-grade group, and the D values **(E)** were significantly higher than in high-grade group. The D values **(F)** were significantly lower in positive EMVI than negative EMVI.

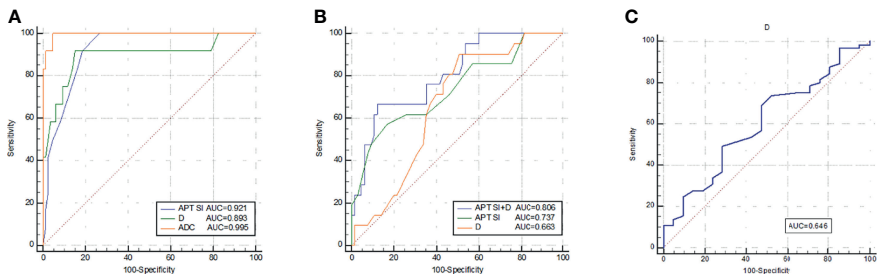

FIGURE 6 | ROC curves of APT SI, D, and ADC for discrimination between MC and AC **(A)**; ROC curves of APT SI, D, and APT SI combined with D for discrimination between low- and high-grade AC **(B)**; and the ROC curve of D for discrimination between positive EMVI and negative EMVI **(C)**. All parameters were with significant differences between the groups.

TABLE 5 | Diagnostic performance of APT SI, D and ADC values with significant difference between groups.

Category	*P* value	AUC (95% CI)	Threshold	Sensitivity (%)	Specificity (%)
MC *vs*. AC					
APT SI	0.000	0.921(0.895-0.978)	2.650%	91.7	81.6
D	0.000	0.893(0.767-1.000)	$0.930\times10^{-3}mm^2/s$	91.7	84.9
ADC	0.000	0.995(0.986-1.000)	$1.230\times10^{-3}mm^2/s$	100	95.4
Low- *vs*. high grade AC					
APT SI	0.001	0.737 (0.607-0.867)	2.550%	57.1	81.8
D	0.025	0.663(0.544-0.782)	$0.851\times10^{-3}mm^2/s$	48.5	80.5
APT SI + D	0.000	0.806(0.702-0.910)	N/A	76.7	87.7
EMVI (+) *vs*. (-) AC					
D	0.045	0.646(0.511-0.780)	$0.785\times10^{-3}mm^2/s$	76.2	76.9

AUC, area under the curve; CI, confidence interval; APT SI +D, APT SI combined with D values.

commonly have significantly higher APT SIs compared to those of the benign or normal tissues, and the APT SI tends to increase as the pathological grade advanced (34, 35). The higher APT SIs in high-grade tumors can be due to the abundant proteins production, rapid cell proliferation and angiogenesis. Previous studies suggested that IVIM was helpful to assess tumor grades of intracranial tumors, solid soft-tissue tumors, HCC, and prostate cancer etc., and the D value was observed to be inversely correlated with the tumor grade (36–39). In present study, lower D values were observed in high-grade than those of low-grade rectal adenocarcinomas, which was in agreement with previous results (11, 40, 41). The D value, that represents the pure diffusion of free water molecules, was decreased with the increasing cellularity, tight cellular structure in high-grade tumors. The AUCs of APT and D for distinguishing low- from high-grade adenocarcinomas were 0.737 and 0.663 respectively, with moderate diagnostic performance. The AUC was raised to 0.806 by the combination of APT SI and D values, with 76.7% sensitivity and 87.7% specificity. The D* and f values showed a trend of decreasing with increased tumor grades in our study but without statistically significance. Furthermore, previous studies showed D* or f was negative correlated with tumor grade in rectal cancer (11, 30, 40, 41). A possible explanation is that tumor cells grow rapidly in high-grade tumor, leading to immature vascular structure and reduced microcirculation perfusion thus lower perfusion-related parameters, such as D* and f values. The ADC values showed no significant differences for distinguishing tumor grade of AC in present study, which may be caused by the integrated effects of both diffusion and microperfusion.

Tumor stage is closely related to prognosis for rectal adenocarcinoma. In present study, postoperative pathological stage was used to retrospectively analyze the correlation of APT and IVIM parameters with tumor stages. Parameters derived from APT and IVIM showed no significant differences between pT1-2 and pT3-4 stages, or between pN1-2 and pN0 stages. These results were inconsistent with previous studies which showed that APT SIs were higher in advanced T stage and lymph node metastasis (25, 26). However, T1 or T4 stage cases were absent in previous studies, and the positive rate of lymph node metastasis was higher in previous studies than our study, which may cause the selection bias of the sample. Sun et al. observed that D and D* showed a trend of decreasing with the increasing of tumor clinical stages and lymph node metastasis in rectal cancer (40). The parameters derived from APT and IVIM might exhibit more aggressive biologic behavior, further study is needed to evaluate the significance.

EMVI refers to the presence of tumor infiltration in the vessels outside the muscularis propria, and it is an independent prognostic factor of rectal cancer. Positive EMVI exhibits more local recurrence, more distant metastasis, and more tumor-related death (42). Although Chen et al. suggested that APT SIs were higher in EMVI-positive than in EMVI-negative cases (26), our study showed no significant difference of APT SI in EMVI involvement. We considered that the inconsistent results might be related to the different positive rate of EMVI status (26.9% in present study while 50.8% in the previous study). In addition, the D value was observed to be lower in the positive EMVI group than in the negative group in this study, while Wei et al. identified that D value was lower in microvascular invasion (MVI)-positive than in MVI-negative HCCs (43). The decreased D value may be because tumor emboli or clusters of cancer cells restrict the diffusion of water molecules. The AUC for distinguishing EMVI involvement using the D value was 0.646 with moderate diagnostic significance. The high-resolution T_2WI images should be combined to improve the diagnosis accuracy of EMVI, which was considered positive if vessel wall irregularity, abnormal extension, suspected the empty signal was replaced by tumor tissue with intermediate signal intensity. Additionally, perineural invasion and lymphovascular invasion are prognostic factors for rectal cancer associated with recurrence, metastasis, and postoperative adjuvant therapy. No significant difference of parameters derived from APT and IVIM were found in groups with and without different types of structure invasion in our study, which may be because the tumor microenvironment reflected by APT or IVIM parameters is insufficient to cause significant changes in perineural and lymphovascular invasion.

The present study has some limitations. First, patients with locally advanced rectal cancer received neoadjuvant therapy were excluded, potentially causing selection bias. Second, only 2 types of rectal adenocarcinomas were collected, and further studies with abundant cases are needed to be explored. Third, the choice of different ROIs may also lead to differences in results due to tumor heterogeneity. Furthermore, this study did not analyze the correlation of APT and IVIM parameters with immuno-histochemical indicators or gene expression. In the future, collection of complete data for more in-depth research is needed.

CONCLUSION

APT SI and D values can be used in discriminating between MC and AC, slightly inferior to ADC. The APT SI and D values were helpful to differentiate the low- and high-grade of AC, and the combination of APT SI with D values could improve the diagnostic performance. The D value can help determine EMVI status for AC patients. However, it is still debatable whether APT or IVIM can help distinguish stage, perineural invasion, and lymphovascular invasion. In conclusion, APT and IVIM were helpful to assess the prognostic factors related to rectal adenocarcinoma, including histopathological type, tumor grade and EMVI status.

DATA AVAILABILITY STATEMENT

The raw data supporting the conclusions of this article will be made available by the authors, without undue reservation.

ETHICS STATEMENT

Written informed consent was obtained from the individual(s) for the publication of any potentially identifiable images or data included in this article.

AUTHOR CONTRIBUTIONS

JL: manuscript preparation, literature research, data acquisition, statistical analysis, and manuscript editing. LL: study design, manuscript preparation, data analysis, and manuscript revising. XG: manuscript preparation and literature research. SL and JC: study conception and design, manuscript review, and guarantor of integrity of the entire study. All authors contributed to the article and approved the submitted version.

REFERENCES

1. Siegel RL, Miller KD, Goding Sauer A, Fedewa SA, Butterly LF, Anderson JC, et al. Colorectal Cancer Statistics,2020. *CA Cancer J Clin* (2020) 70:145–64. doi: 10.3322/caac.21601
2. Wong MCS, Huang J, Lok V, Wang J, Fung F, Ding H, et al. Differences in Incidence and Mortality Trends of Colorectal Cancer Worldwide Based on Sex, Age, and Anatomic Location. *Clin Gastroenterol Hepatol* (2021) 19:955–966.e61. doi: 10.1016/j.cgh.2020.02.026
3. Glynne-Jones R, Wyrwicz L, Tiret E, Brown G, Rödel C, Cervantes A, et al. Rectal Cancer: ESMO Clinical Practice Guidelines for Diagnosis, Treatment and Follow-Up. *Ann Oncol* (2017) 28:22–40. doi: 10.1093/annonc/mdx224
4. Wilkinson N. Management of Rectal Cancer. *Surg Clin North Am* (2020) 100:615–28. doi: 10.1016/j.suc.2020.02.014
5. Reynolds IS, O'Connell E, Fichtner M, McNamara DA, Kay EW, Prehn JHM, et al. Mucinous Adenocarcinoma of the Colon and Rectum: A Genomic Analysis. *J Surg Oncol* (2019) 120:1427–35. doi: 10.1002/jso.25764
6. McCawley N, Clancy C, O'Neill BD, Deasy J, McNamara DA, Burke JP. Mucinous Rectal Adenocarcinoma Is Associated With a Poor Response to Neoadjuvant Chemoradiotherapy: A Systematic Review and Meta-Analysis. *Dis Colon Rectum* (2016) 59:1200–8. doi: 10.1097/DCR.0000000000000635
7. Nougaret S, Reinhold C, Mikhael HW, Rouanet P, Bibeau F, Brown G. The Use of MR Imaging in Treatment Planning for Patients With Rectal Carcinoma: Have You Checked the "DISTANCE"? *Radiology* (2013) 268:330–44. doi: 10.1148/radiol.13121361
8. Horvat N, Carlos Tavares Rocha C, Clemente Oliveira B, Petkovska I, Gollub MJ. MRI of Rectal Cancer: Tumor Staging, Imaging Techniques, and Management. *Radiographics* (2019) 39:367–87. doi: 10.1148/rg.2019180114
9. Schurink NW, Lambregts DMJ, Beets-Tan RGH. Diffusion-Weighted Imaging in Rectal Cancer: Current Applications and Future Perspectives. *Br J Radiol* (2019) 92:20180655. doi: 10.1259/bjr.20180655
10. Zhu L, Pan Z, Ma Q, Yang W, Shi H, Fu C, et al. Diffusion Kurtosis Imaging Study of Rectal Adenocarcinoma Associated With Histopathologic Prognostic Factors: Preliminary Findings. *Radiology* (2017) 284:66–76. doi: 10.1148/radiol.2016160094
11. Geng Z, Zhang Y, Yin S, Lian S, He H, Li H, et al. Preoperatively Grading Rectal Cancer With the Combination of Intravoxel Incoherent Motions Imaging and Diffusion Kurtosis Imaging. *Contrast Media Mol Imaging* (2020) 2020:2164509. doi: 10.1155/2020/2164509
12. Bakke KM, Grøvik E, Meltzer S, Negård A, Holmedal SH, Mikalsen LTG, et al. Comparison of Intravoxel Incoherent Motion Imaging and Multiecho Dynamic Contrast-Based MRI in Rectal Cancer. *J Magn Reson Imaging* (2019) 50:1114–24. doi: 10.1002/jmri.26740
13. Le Bihan D. What Can We See With IVIM MRI? *Neuroimage* (2019) 187:56–67. doi: 10.1016/j.neuroimage.2017.12.062
14. Ma G, Xu XQ, Zhu LN, Jiang JS, Su GY, Hu H, et al. Intravoxel Incoherent Motion Magnetic Resonance Imaging for Assessing Parotid Gland Tumors: Correlation and Comparison With Arterial Spin Labeling Imaging. *Korean J Radiol* (2021) 22:243–52. doi: 10.3348/kjr.2020.0290
15. Song XL, Wang L, Ren H, Wei R, Ren JL, Niu J. Intravoxel Incoherent Motion Imaging in Differentiation Borderline From Malignant Ovarian Epithelial Tumors: Correlation With Histological Cell Proliferation and Vessel Characteristics. *J Magn Reson Imaging* (2020) 51:928–35. doi: 10.1002/jmri.26885
16. Lecler A, Duron L, Zmuda M, Zuber K, Bergès O, Putterman M, et al. Intravoxel Incoherent Motion (IVIM) 3 T MRI for Orbital Lesion Characterization. *Eur Radiol* (2021) 31:14–23. doi: 10.1007/s00330-020-07103-1
17. Zhou J, Heo HY, Knutsson L, van Zijl PCM, Jiang S. APT-Weighted MRI: Techniques, Current Neuro Applications, and Challenging Issues. *J Magn Reson Imaging* (2019) 50:347–64. doi: 10.1002/jmri.26645
18. Wu Y, Chen Y, Zhao Y, Yang S, Zhao J, Zhou J, et al. Direct Radiofrequency Saturation Corrected Amide Proton Transfer Tumor MRI at 3T. *Magn Reson Med* (2019) 81:2710–9. doi: 10.1002/mrm.27562
19. Law BKH, King AD, Ai QY, Poon DMC, Chen W, Bhatia KS, et al. Head and Neck Tumors: Amide Proton Transfer MRI. *Radiology* (2018) 288:782–90. doi: 10.1148/radiol.2018171528
20. He YL, Li Y, Lin CY, Qi YF, Wang X, Zhou HL, et al. Three-Dimensional Turbo-Spin-Echo Amide Proton Transfer-Weighted Mri for Cervical Cancer: A Preliminary Study. *J Magn Reson Imaging* (2019) 50:1318–25. doi: 10.1002/jmri.26710
21. Qamar S, King AD, Ai QH, Mo FKF, Chen W, Poon DMC, et al. Pre-Treatment Amide Proton Transfer Imaging Predicts Treatment Outcome in Nasopharyngeal Carcinoma. *Eur Radiol* (2020) 30:6339–47. doi: 10.1007/s00330-020-06985-5
22. Li B, Sun H, Zhang S, Wang X, Guo Q. The Utility of APT and IVIM in the Diagnosis and Differentiation of Squamous Cell Carcinoma of the Cervix: A Pilot Study. *Magn Reson Imaging* (2019) 63:105–13. doi: 10.1016/j.mri.2019.08.020
23. Jia F, Wu B, Yan R, Li L, Wang K, Han D. Prediction Model for Intermediate-Stage Hepatocellular Carcinoma Response to Transarterial Chemoembolization. *J Magn Reson Imaging* (2020) 52:1657–67. doi: 10.1002/jmri.27189
24. Nishie A, Asayama Y, Ishigami K, Ushijima Y, Takayama Y, Okamoto D, et al. Amide Proton Transfer Imaging to Predict Tumor Response to Neoadjuvant Chemotherapy in Locally Advanced Rectal Cancer. *J Gastroenterol Hepatol* (2019) 34:140–6. doi: 10.1111/jgh.14315
25. Li L, Chen W, Yan Z, Feng J, Hu S, Liu B, et al. Comparative Analysis of Amide Proton Transfer MRI and Diffusion-Weighted Imaging in Assessing P53 and Ki-67 Expression of Rectal Adenocarcinoma. *J Magn Reson Imaging* (2020) 52:1487–96. doi: 10.1002/jmri.27212
26. Chen W, Li L, Yan Z, Hu S, Feng J, Liu G, et al. Three-Dimension Amide Proton Transfer MRI of Rectal Adenocarcinoma: Correlation With Pathologic Prognostic Factors and Comparison With Diffusion Kurtosis Imaging. *Eur Radiol* (2021) 31:3286–96. doi: 10.1007/s00330-020-07397-1
27. Nishie A, Takayama Y, Asayama Y, Ishigami K, Ushijima Y, Okamoto D, et al. Amide Proton Transfer Imaging Can Predict Tumor Grade in Rectal Cancer. *Magn Reson Imaging* (2018) 51:96–103. doi: 10.1016/j.mri.2018.04.017
28. Togao O, Keupp J, Hiwatashi A, Yamashita K, Kikuchi K, Yoneyama M, et al. Amide Proton Transfer Imaging of Brain Tumors Using a Self-Corrected 3d Fast Spin-Echo Dixon Method: Comparison With Separate B0 Correction. *Magn Reson Med* (2017) 77:2272–9. doi: 10.1002/mrm.26322
29. Ray KJ, Simard MA, Larkin JR, Coates J, Kinchesh P, Smart SC, et al. Tumor pH and Protein Concentration Contribute to the Signal of Amide Proton Transfer Magnetic Resonance Imaging. *Cancer Res* (2019) 79:1343–52. doi: 10.1158/0008-5472.CAN-18-2168
30. Lu B, Yang X, Xiao X, Chen Y, Yan X, Yu S. Intravoxel Incoherent Motion Diffusion-Weighted Imaging of Primary Rectal Carcinoma: Correlation With Histopathology. *Med Sci Monit* (2018) 24:2429–36. doi: 10.12659/msm.908574
31. Wen Z, Chen Y, Yang X, Lu B, Liu Y, Shen B, et al. Application of Magnetic Resonance Diffusion Kurtosis Imaging for Distinguishing Histopathologic Subtypes and Grades of Rectal Carcinoma. *Cancer Imaging* (2019) 19:8. doi: 10.1186/s40644-019-0192-x
32. Sotirios B, Demetriou E, Topriceanu CC, Zakrzewska Z. The Role of APT Imaging in Gliomas Grading: A Systematic Review and Meta-Analysis. *Eur J Radiol* (2020) 133:109353. doi: 10.1016/j.ejrad.2020.109353

33. Yin H, Wang D, Yan R, Jin X, Hu Y, Zhai Z, et al. Comparison of Diffusion Kurtosis Imaging and Amide Proton Transfer Imaging in the Diagnosis and Risk Assessment of Prostate Cancer. *Front Oncol* (2021) 11:640906. doi: 10.3389/fonc.2021.640906
34. Kamitani T, Sagiyama K, Togao O, Yamasaki Y, Hida T, Matsuura Y, et al. Amide Proton Transfer (APT) Imaging of Parotid Tumors: Differentiation of Malignant and Benign Tumors. *Eur J Radiol* (2020) 129:109047. doi: 10.1016/j.ejrad.2020.109047
35. Xu Z, Ke C, Liu J, Xu S, Han L, Yang Y, et al. Diagnostic Performance Between MR Amide Proton Transfer (APT) and Diffusion Kurtosis Imaging (DKI) in Glioma Grading and IDH Mutation Status Prediction at 3 T. *Eur J Radiol* (2021) 134:109466. doi: 10.1016/j.ejrad.2020.109466
36. Wu H, Zhang S, Liang C, Liu H, Liu Y, Mei Y, et al. Intravoxel Incoherent Motion MRI for the Differentiation of Benign, Intermediate, and Malignant Solid Soft-Tissue Tumors. *J Magn Reson Imaging* (2017) 46:1611–8. doi: 10.1002/jmri.25733
37. Kikuchi K, Hiwatashi A, Togao O, Yamashita K, Kamei R, Momosaka D, et al. Intravoxel Incoherent Motion MR Imaging of Pediatric Intracranial Tumors: Correlation With Histology and Diagnostic Utility. *Am J Neuroradiol* (2019) 40:878–84. doi: 10.3174/ajnr.A6052
38. Sokmen BK, Sabet S, Oz A, Server S, Namal E, Dayangac M, et al. Value of Intravoxel Incoherent Motion for Hepatocellular Carcinoma Grading. *Transplant Proc* (2019) 51:1861–6. doi: 10.1016/j.transproceed.2019.02.027
39. Cui Y, Li C, Liu Y, Jiang Y, Yu L, Liu M, et al. Differentiation of Prostate Cancer and Benign Prostatic Hyperplasia: Comparisons of the Histogram Analysis of Intravoxel Incoherent Motion and Monoexponential Model With in-Bore MR-Guided Biopsy as Pathological Reference. *Abdom Radiol (NY)* (2020) 45:3265–77. doi: 10.1007/s00261-019-02227-5
40. Sun H, Xu Y, Song A, Shi K, Wang W. Intravoxel Incoherent Motion MRI of Rectal Cancer: Correlation of Diffusion and Perfusion Characteristics With Prognostic Tumor Markers. *Am J Roentgenol* (2018) 210:W139–47. doi: 10.2214/AJR.17.18342
41. Cheng Y, Jiang H, Wang H, Tang Q, Liu T. Application of Field-Of-View Optimized and Constrained Undistorted Single Shot (FOCUS) With Intravoxel Incoherent Motion (IVIM) in 3T in Locally Advanced Rectal Cancer. *Dis Markers* (2021) 2021:5565902. doi: 10.1155/2021/5565902
42. Zhang XY, Wang S, Li XT, Wang YP, Shi YJ, Wang L, et al. MRI of Extramural Venous Invasion in Locally Advanced Rectal Cancer: Relationship to Tumor Recurrence and Overall Survival. *Radiology* (2018) 289:677–85. doi: 10.1148/radiol.2018172889
43. Wei Y, Huang Z, Tang H, Deng L, Yuan Y, Li J, et al. IVIM Improves Preoperative Assessment of Microvascular Invasion in HCC. *Eur Radiol* (2019) 29:5403–14. doi: 10.1007/s00330-019-06088-w

Conflict of Interest: Author LL was employed by Philips Healthcare.

The remaining authors declare that the research was conducted in the absence of any commercial or financial relationships that could be construed as a potential conflict of interest.

Publisher's Note: All claims expressed in this article are solely those of the authors and do not necessarily represent those of their affiliated organizations, or those of the publisher, the editors and the reviewers. Any product that may be evaluated in this article, or claim that may be made by its manufacturer, is not guaranteed or endorsed by the publisher.

frontiers in Oncology

ORIGINAL RESEARCH
published: 24 January 2022
doi: 10.3389/fonc.2021.785788

OPEN ACCESS

Edited by:
Letizia Deantonio, Oncology Institute of Southern Switzerland (IOSI), Switzerland

Reviewed by:
Juliane Hoerner-Rieber, Heidelberg University Hospital, Germany
Chen Liu, Army Medical University, China

***Correspondence:**
Tsung-Ying Ho
tyho@cgmh.org.tw
Dakai Jin
dakai.jin@gmail.com
Senxiang Yan
yansenxiang@zju.edu.cn

†These authors have contributed equally to this work

‡These authors share senior authorship

Specialty section:
This article was submitted to Cancer Imaging and Image-directed Interventions, a section of the journal Frontiers in Oncology

Received: *29 September 2021*
Accepted: *22 December 2021*
Published: *24 January 2022*

Citation:
Ye X, Guo D, Tseng C-K, Ge J, Hung T-M, Pai P-C, Ren Y, Zheng L, Zhu X, Peng L, Chen Y, Chen X, Chou C-Y, Chen D, Yu J, Chen Y, Jiao F, Xin Y, Huang L, Xie G, Xiao J, Lu L, Yan S, Jin D and Ho T-Y (2022) Multi-Institutional Validation of Two-Streamed Deep Learning Method for Automated Delineation of Esophageal Gross Tumor Volume Using Planning CT and FDG-PET/CT. Front. Oncol. 11:785788. doi: 10.3389/fonc.2021.785788

Multi-Institutional Validation of Two-Streamed Deep Learning Method for Automated Delineation of Esophageal Gross Tumor Volume Using Planning CT and FDG-PET/CT

Xianghua Ye[1†], Dazhou Guo[2†], Chen-Kan Tseng[3], Jia Ge[1], Tsung-Min Hung[3], Ping-Ching Pai[3], Yanping Ren[4], Lu Zheng[5], Xinli Zhu[1], Ling Peng[6], Ying Chen[1], Xiaohua Chen[7], Chen-Yu Chou[3], Danni Chen[1], Jiaze Yu[8], Yuzhen Chen[9], Feiran Jiao[10], Yi Xin[11], Lingyun Huang[11], Guotong Xie[11], Jing Xiao[11], Le Lu[2], Senxiang Yan[1*‡], Dakai Jin[2*‡] and Tsung-Ying Ho[9*‡]

[1] Department of Radiation Oncology, The First Affiliated Hospital Zhejiang University, Hangzhou, China, [2] PAII Inc., Bethesda, MD, United States, [3] Department of Radiation Oncology, Chang Gung Memorial Hospital, Linkou, Taiwan, [4] Department of Radiation Oncology, Huadong Hospital Affiliated to Fudan University, Shanghai, China, [5] Department of Radiation Oncology, Lihuili Hospital, Ningbo Medical Center, Ningbo, China, [6] Department of Respiratory Disease, Zhejiang Provincial People's Hospital, Hangzhou, China, [7] Department of Radiation Oncology, The First Hospital of Lanzhou University, Lanzhou, China, [8] Department of Radiation Oncology, Haining People's Hospital, Jiaxing, China, [9] Department of Nuclear Medicine, Chang Gung Memorial Hospital, Linkou, Taiwan, [10] Independent Researcher, Silver Spring, MD, United States, [11] Ping An Technology, Shenzhen, China

Background: The current clinical workflow for esophageal gross tumor volume (GTV) contouring relies on manual delineation with high labor costs and inter-user variability.

Purpose: To validate the clinical applicability of a deep learning multimodality esophageal GTV contouring model, developed at one institution whereas tested at multiple institutions.

Materials and Methods: We collected 606 patients with esophageal cancer retrospectively from four institutions. Among them, 252 patients from institution 1 contained both a treatment planning CT (pCT) and a pair of diagnostic FDG-PET/CT; 354 patients from three other institutions had only pCT scans under different staging protocols or lacking PET scanners. A two-streamed deep learning model for GTV segmentation was developed using pCT and PET/CT scans of a subset (148 patients) from institution 1. This built model had the flexibility of segmenting GTVs *via* only pCT or pCT+PET/CT combined when available. For independent evaluation, the remaining 104 patients from institution 1 behaved as an unseen internal testing, and 354 patients from the other three institutions were used for external testing. Degrees of manual revision were further evaluated by human experts to assess the contour-editing effort. Furthermore, the

deep model's performance was compared against four radiation oncologists in a multi-user study using 20 randomly chosen external patients. Contouring accuracy and time were recorded for the pre- and post-deep learning-assisted delineation process.

Keywords: deep learning, PET/CT (18)F-FDG, radiotherapy, segmentation, delineation, esophageal cancer

INTRODUCTION

Gross tumor volume (GTV) contouring is an essential task in radiotherapy planning. GTV refers to the demonstrable gross tumor region. Accurate contouring improves patient prognosis and serves as the basis for further clinical target volume delineation (1). For precise GTV delineation, radiation oncologists often need to consider multimodality imaging of MRI, FDG-PET, contrast-enhanced CT, and radiology reports and other relevant clinical information. This manual process is both labor-intensive and highly variable.

For esophageal cancer, neoadjuvant concurrent chemoradiation therapy is the recommended primary treatment for locally advanced disease in our institution, as relatively fewer patients are first diagnosed at asymptomatic early stages eligible for esophagostomy. Compared to other types of cancers, esophageal GTV contouring has its unique challenges: 1) The esophagus possesses a long cranial to caudal anatomical range, where tumors may appear at any location along this tubular organ. Multifocal tumors are also not uncommon (2, 3). Accurately identifying the tumor location needs significant efforts and expertise from radiation oncologists by referring to multiple examinations, such as panendoscopy, contrast esophagography, or FDG-PET/CT. 2) Assessing the longitudinal esophageal tumor extension is difficult on CT, even with additional information from PET. This leads to considerable GTV contouring variations at the cranial-caudal border (4, 5). 3) Treatment planning CT (pCT) exhibits poor contrast between the esophageal tumor and surrounding tissues. This limitation is addressed by frequently manually referring to adjacent slices to delineate GTV's radial borders, further increasing the manual burden and time. Therefore, current manual esophageal GTV contouring is labor-intensive and requires extensive experiences of radiation oncologists, otherwise leading to inconsistent delineation. Accurate and automated GTV contouring is of evidently great benefits.

Deep learning methods have been demonstrated as potentially clinically relevant and useful tools in many medical image analysis tasks (6–10). The deep learning-based target volume and organ at risk contouring were also increasingly studied recently (11–17). Nevertheless, for esophageal GTV, the clinical applicability of deep learning-based auto-contouring is still unclear under a multi-institutional evaluation setup.

In this study, we developed and validated a two-streamed three-dimensional (3D) deep learning esophageal GTV segmentation model, which had the flexibility to segment the GTV using only pCT or pCT and PET/CT combined when available. The deep model was developed using 148 patients with pCT and PET/CT imaging from institution 1 and independently validated using 104 unseen patients from institution 1 and 354 patients from three external institutions. Furthermore, using 20 randomly selected patients from external institutions, the deep model performance was compared under a multi-user setting with four board-certified radiation oncologists experienced in esophageal cancer treatment.

MATERIALS AND METHODS

Datasets

A total of 606 patients with esophageal cancer from four institutions were collected in this retrospective study under each institutional review board approval. Requirements to obtain informed consent were waived. All patients had undergone concurrent chemoradiation therapy before surgery between 2015 and 2020. The exclusion criteria are shown in **Figure 1**. All patients had available pCT scans and the corresponding manual GTV contours used for clinical treatment. According to the availability of PET scanner and the staging protocol of different institutions, patients from institution 1 (252 patients total) received additional diagnostic FDG-PET/CT scan, whereas 354 patients from other institutions collected only pCT. Imaging details are described in **Appendix**. A subset of 148 patients from institution 1 was used as the training/validation cohort, while the remaining 104 patients from institution 1 and 354 patients from the other three institutions were treated as unseen internal and external testing cohorts, respectively (**Figure 1**). One hundred forty-eight (institution 1) of the 606 patients were previously reported (18). This prior work dealt with segmentation method developments, whereas in this article, we constructed the deep model using a different implementation (**Appendix**) and evaluated the performance on 458 unseen multi-institutional patients (104 from institution 1; 354 from the other three institutions).

Model Development

We implemented a two-streamed 3D esophageal GTV segmentation method based on the process described in Jin et al. (18, 19), which consisted of a pCT stream to segment GTVs using only pCT input (denoted pCT model) and a pCT +PET stream using an early fusion module followed by a late fusion module to segment GTVs leveraging the joint information in pCT and PET multimodalities (denoted pCT+PET model). The overall segmentation flowchart is illustrated in **Figure 2**. In the pCT+PET stream, PET was aligned to pCT by first registering the diagnostic CT (accompanying the PET) to pCT and applying the deformation field to map PET to pCT. For

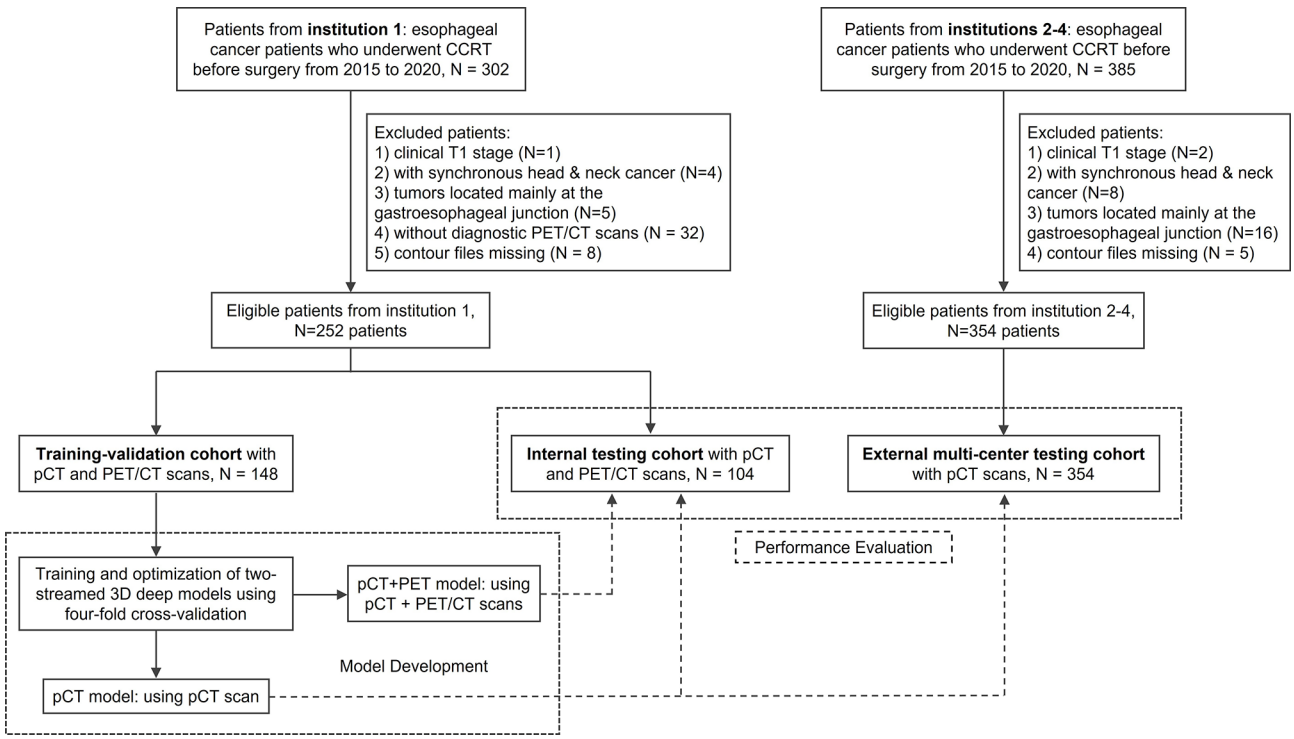

FIGURE 1 | Study flow diagram of esophageal gross tumor volume (GTV) segmentation in a multi-institutional setup. CCRT, concurrent chemoradiation therapy; pCT, treatment planning CT.

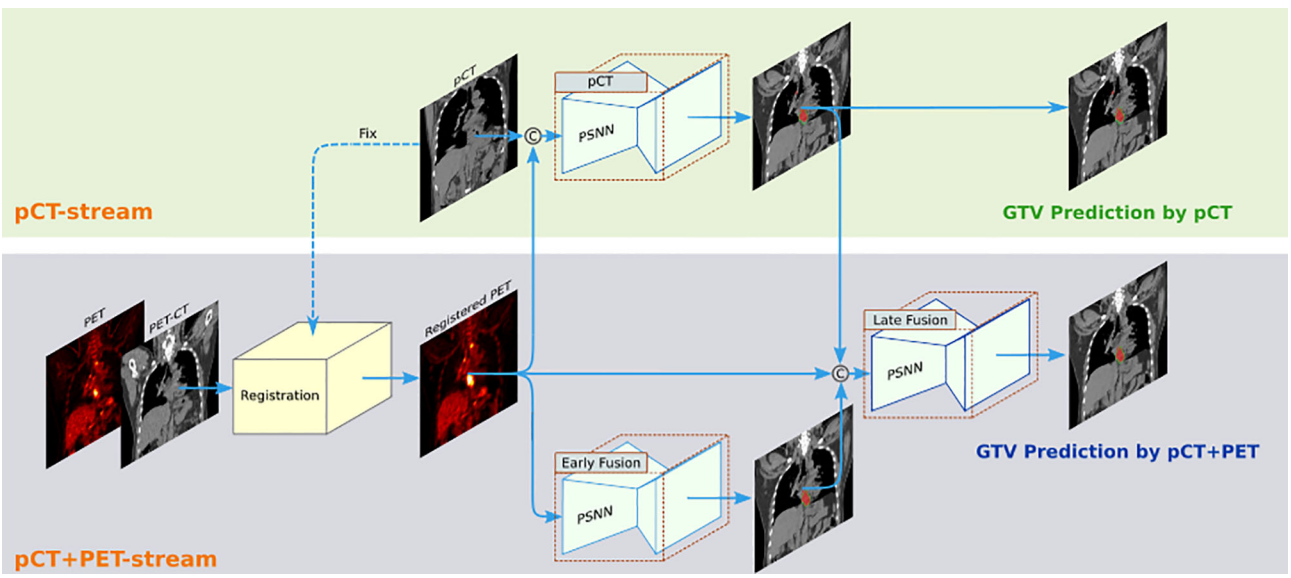

FIGURE 2 | The two-streamed 3D deep learning model for esophageal gross tumor volume (GTV) segmentation using treatment planning CT (pCT) and FDG-PET/CT scans. pCT stream takes the pCT as input and produces the GTV segmentation prediction. The pCT+PET stream takes both pCT and PET/CT scans as input. It first aligns the PET to pCT by registering diagnostic CT (accompanying PET scan) to pCT and applying the deformation field to further map PET to pCT. Then, it uses an early fusion module followed by a late fusion module to segment the esophageal GTV using the complementary information in pCT and PET. This workflow can accommodate to the availability of PET scans in different institutions. Although 3D inputs are used, we depict 2D images for clarity.

segmentation backbone, 3D progressive semantically nested network (18) was adopted. Details of the registration, two-streamed formulation, and network architecture are included in **Appendix**.

To obtain the final models for testing, we conducted 4-fold cross-validation (split at the patient level) on the 148 training-validation patients from institution 1. Thereby, 148 patients were randomly partitioned into four equal-size subgroups (25% of patients). Of the four subgroups, a single subgroup was retained as the validation data for model selection, while the remaining three subgroups were used for training. The cross-validation process was repeated four times/4-fold, with each of the four subgroups used once as the validation data. Finally, four deep models were obtained from the four rounds of training. They were ensembled to predict the final GTV contours in all the unseen testing data.

Quantitative Evaluation of Contour Accuracy

The contouring accuracy was quantitatively evaluated using three common segmentation metrics (11, 12), i.e., Dice similarity coefficient (DSC), 95% Hausdorff distance (HD95), and average surface distance (ASD). For the internal testing, the performance of pCT or pCT+PET model was separately computed. During external testing, the pCT model performance was reported. We also explored the comparison of these metrics in subgroups with different characteristics: clinical T stages and different tumor locations [cervical and upper, middle, and lower third of esophagus according to Japan Esophageal Society (20)].

Additionally, the performance of our two-streamed models was compared with the previous state-of-the-art method (21) using a 3D denseUnet (22, 23) for pCT-based esophageal GTV segmentation. For the model development of Yousefi et al. (21), the same 4-fold cross-validation protocol was applied to ensure a neutral comparison.

Human Experts' Assessment of Contour Accuracy

An assessment experiment by human experts was further conducted to evaluate the contour editing efforts required for deep model predictions to be clinically accepted. Specifically, deep learning predictions of 354 patients from three external multi-institutions were distributed to two experts (both >15 years of experience) to assess the degree of manual revision that was defined as the percentage of GTV slices that needed modification for clinical acceptance. Five categories were designated as no revision required, revision required in <10% slices, revision required in 10%–30% slices, revision required in 30%–60% slices, and unacceptable (revision required in >60% slices or prediction completely missed the tumor). We analyzed the correlations between different quantitative metrics and degrees of manual revision.

Note that esophageal GTV may appear at any esophageal location spanning an extensive longitudinal range, which is different from the more spatially constrained anatomical location such as head and neck or prostate (11, 12). Hence, automated esophageal GTV segmentation may identify wrong tumor locations. These scenarios could lead to large or undefined distance errors. Therefore, for the quantitative evaluation, we additionally report the number of patients identified as unacceptable by clinical experts and calculated the DSC, HD95, and ASD metrics using the remaining patients.

Multi-User Evaluation

We further conducted a multi-user study involving four board-certified radiation oncologists (3–6 years' experience in treating esophageal cancer) from 4 different institutions. First, pCT of 20 randomly selected patients in the external testing cohort along with their clinical, radiological, and panendoscopy reports and any other useful information were extracted and provided to these four radiation oncologists for manual contouring. Next, after a minimum interval of 1 month, deep model-predicted GTV contours were distributed to these four radiation oncologists for editing along with previously available information. All radiation oncologists were blinded to the ground truth contours and their first-time contours. Accuracy of our deep model predictions was compared to the multi-user performance in terms of DSC, HD95, and ASD. Similar to Lin et al. (11), interobserver variations were assessed using multi-user DSC and volume coefficient of variation (the ratio between standard deviation and mean). Times used for the pre- and post-deep learning-assisted contouring were recorded.

Statistical Analysis

The Wilcoxon matched-pairs signed rank test was used to compare 1) DSC, HD95, and ASD scores between the pCT model and pCT+PET model in the internal testing set and between the proposed model and 3D DenseUNet method in the external testing set; 2) DSC, HD95, ASD, and time taken of pre- *vs.* post-deep learning-assisted contouring in multi-user evaluation. Mann–Whitney U test was used to compare DSC, HD95, and ASD at different clinical T stages. Multiple linear regression with stepwise model selection was used to compare the metrics at different tumor locations, since a large tumor may locate across multiple esophagus regions. Spearman correlation coefficients were assessed for mean DSC, HD95, and ASD vs. degrees of manual revision, respectively. The χ^2 test was used to compare the difference in degrees of manual revision between subgroups. All analyses were performed by using R (24). Statistical significance was set at two-tailed $p < 0.05$.

RESULTS

A total of 606 esophageal cancer patients were included. **Table 1** summarizes the main characteristics of the entire cohort, and the separated training-validation, internal testing, and external testing cohorts. Characteristics of the 20 randomly selected

TABLE 1 | Subject and imaging characteristics.

Characteristics	Entire cohort Institutions 1–4 (n = 606)	Training-validation Institution 1 (n = 148)	Internal testing Institution 1 (n = 104)	External testing Institutions 2–4 (n = 354)
Sex	…	…	…	…
Male	537 (89%)	135 (91%)	98 (94%)	304 (86%)
Female	69 (11%)	13 (9%)	6 (6%)	50 (14%)
Diagnostic age	65 [57–72]	55 [50–61]	56 [50–62]	67 [61–75]
Clinical T stage	…	…	…	…
cT2	116 (19%)	24 (16%)	18 (17%)	74 (21%)
cT3	306 (51%)	71 (48%)	58 (56%)	177 (50%)
cT4	184 (30%)	53 (36%)	28 (27%)	103 (29%)
Tumor location	…	…	…	…
Cervical	81 (13%)	11 (7%)	10 (10%)	60 (17%)
Upper third	204 (34%)	26 (18%)	35 (34%)	143 (40%)
Middle third	325 (54%)	84 (57%)	63 (61%)	178 (50%)
Lower third	174 (29%)	69 (47%)	35 (34%)	70 (20%)
BMI	…	…	…	…
<18.5	121 (20%)	22 (15%)	15 (14%)	84 (24%)
18.5–23.9	393 (65%)	94 (63%)	59 (57%)	240 (68%)
>24	92 (15%)	32 (22%)	30 (29%)	30 (8%)
Imaging available	…	…	…	…
pCT	606 (100%)	148 (100%)	104 (100%)	354 (100%)
PET/CT	252 (42%)	148 (100%)	104 (100%)	0 (0%)

Patients may have tumors located across multiple esophagus regions; hence, total numbers summed at various tumor locations for the entire and sub-institution cohorts are greater than the corresponding total patient numbers. Age is presented as median and [interquartile range].
cT2, clinical T stage 2; cT3, clinical T stage 3; cT4, clinical T stage 4; BMI, body mass index; pCT, treatment planning CT.

patients used in multi-user evaluation are presented in Appendix Table A1.

Performance in the Internal Testing Set

Quantitative performance of our deep model in the internal testing set is summarized in **Tables 2**, **3**. For the pCT model, we observed the mean and 95% confidence interval of DSC, HD95, and ASD as 0.81 (0.79, 0.83), 11.5 (9.2, 13.7) mm, and 2.7 (2.2, 3.3) mm, respectively. In the subgroup analysis (**Appendix Figures A3, A4**), the pCT model achieved a significantly higher mean DSC for advanced T stage patients (cT3, cT4) than those in the early cT2 patients (0.82 and 0.82 vs. 0.76, $p < 0.05$). The tumor locations exhibited no significant performance differences. With additional PET scans, the pCT+PET model significantly increased the performance to 0.83 (0.81, 0.84), 9.5 (8.0, 10.9) mm, and 2.2 (1.9, 2.5) mm with $p < 0.01$ in DSC, HD95, and ASD, respectively. **Figure 4A** shows several qualitative examples for GTV segmentation in the internal testing set.

Performance in the External Testing Set

In the external multi-institutional testing, we observed the mean and 95% CI of DSC, HD95, and ASD as 0.80 (0.78, 0.81), 11.8 (10.1, 13.4) mm, and 2.8 (2.4, 3.2) mm, respectively, using the pCT model (**Table 4**). These values did not show significant differences compared to those during the internal testing. Our pCT-based GTV segmentation model generalized well to patients of three other institutions. In the subgroup analysis, a similar trend was observed as internal testing: deep model obtained markedly improved DSC and HD95 in advanced cT3 and cT4 patients vs. early cT2 patients (mean DSC 0.81 and 0.82 vs. 0.71, $p < 0.001$; mean HD95 11.4 and 11.4 mm vs. 13.8 mm, $p \leq 0.001$).

TABLE 2 | Quantitative results of esophageal GTV segmentation by the pCT model in the unseen internal testing data.

	Institution 1 (Unseen Internal Testing) Using pCT Model			
	Unacceptable Number (percentage)	DSC mean (95% CI)	HD95 (mm) Mean (95% CI)	ASD (mm) Mean (95% CI)
Total patients (n = 104)	8 (8%)	0.81 (0.79, 0.83)	11.5 (9.2, 13.7)	2.7 (2.2, 3.3)
Clinical T stage				
cT2 (n = 18)	4 (22%)	0.76 (0.67, 0.86)	12.0 (5.5, 18.4)	3.0 (1.0, 5.1)
cT3 (n = 58)	3 (5%)	0.82 (0.80, 0.84)	10.7 (7.9, 13.5)	2.5 (1.9, 3.2)
cT4 (n = 28)	1 (4%)	0.82 (0.79, 0.85)	12.8 (7.9, 17.7)	3.0 (2.0, 4.0)
Tumor location				
Cervical (n = 10)	1 (10%)	0.82 (0.75, 0.89)	9.2 (6.5, 12.0)	2.2 (1.5, 2.8)
Upper third (n = 35)	1 (3%)	0.83 (0.81, 0.85)	9.6 (7.4, 11.9)	2.2 (1.8, 2.5)
Middle third (n = 63)	5 (8%)	0.80 (0.78, 0.83)	12.0 (8.9, 15.0)	2.9 (2.2, 3.6)
Lower third (n = 35)	2 (6%)	0.81 (0.77, 0.85)	13.3 (8.6, 18.0)	3.3 (2.1, 4.5)

GTV, gross tumor volume; CI, confidence interval; DSC, Dice similarity coefficient; HD95, 95% Hausdorff distance; ASD, average surface distance; cT2, clinical T stage 2; cT3, clinical T stage 3; cT4, clinical T stage 4; pCT, treatment planning CT.

TABLE 3 | Quantitative results of esophageal GTV segmentation by the pCT+PET model in the unseen internal testing data.

	Institution 1 (Unseen Internal Testing) Using pCT+PET Model			
	Unacceptable Number (percentage)	**DSC Mean (95% CI)**	**HD95 (mm) Mean (95% CI)**	**ASD (mm) Mean (95% CI)**
Total patients (n = 104)	4 (4%)	0.83 (0.81, 0.84)	9.5 (8.0, 10.9)	2.2 (1.9, 2.5)
Clinical T stage				
cT2 (n = 18)	3 (17%)	0.77 (0.69, 0.85)	11.4 (6.3, 16.6)	2.7 (1.3, 4.2)
cT3 (n = 58)	0 (0%)	0.84 (0.82, 0.85)	9.0 (7.0, 11.0)	2.0 (1.7, 2.4)
cT4 (n = 28)	1 (4%)	0.84 (0.82, 0.86)	9.3 (7.3, 11.4)	2.3 (1.9, 2.6)
Tumor location				
Cervical (n = 10)	1 (10%)	0.83 (0.78, 0.89)	9.4 (6.2, 12.7)	2.0 (1.5, 2.5)
Upper third (n = 35)	0 (0%)	0.84 (0.82, 0.86)	8.1 (6.2, 10.0)	1.9 (1.6, 2.2)
Middle third (n = 63)	3 (5%)	0.83 (0.81, 0.84)	9.5 (8.0, 11.1)	2.2 (1.9, 2.5)
Lower third (n = 35)	0 (0%)	0.83 (0.79, 0.86)	10.8 (7.5, 14.0)	2.6 (1.9, 3.3)

GTV, gross tumor volume; CI, confidence interval; DSC, Dice similarity coefficient; HD95, 95% Hausdorff distance; ASD, average surface distance; cT2, clinical T stage 2; cT3, clinical T stage 3; cT4, clinical T stage 4; pCT, treatment planning CT.

TABLE 4 | Quantitative results of esophageal GTV segmentation by the pCT model in the multi-institutional external testing data.

	Institutions 2–4 (External Multi-Institutional Testing) Using pCT Model			
	Unacceptable Number (percentage)	**DSC Mean (95% CI)**	**HD95 (mm) Mean (95% CI)**	**ASD (mm) Mean (95% CI)**
Total patients (n = 354)	33 (9%)	0.80 (0.78, 0.81)	11.8 (10.1, 13.4)	2.8 (2.4, 3.2)
Clinical T stage				
cT2 (n = 74)	23 (31%)	0.71 (0.66, 0.76)	13.8 (10.0, 17.5)	3.6 (2.5, 4.8)
cT3 (n = 177)	5 (3%)	0.81 (0.80, 0.82)	11.4 (8.8, 13.9)	2.6 (2.1, 3.2)
cT4 (n = 103)	5 (5%)	0.82 (0.80, 0.83)	11.4 (9.3, 13.6)	2.7 (2.1, 3.3)
Tumor location				
Cervical (n = 60)	4 (6%)	0.80 (0.78, 0.82)	11.7 (8.6, 14.8)	2.5 (1.7, 3.3)
Upper third (n = 143)	11 (8%)	0.79 (0.77, 0.81)	12.6 (10.4, 14.9)	3.0 (2.4, 3.7)
Middle third (n = 178)	14 (8%)	0.80 (0.78, 0.81)	11.5 (9.3, 13.5)	2.9 (2.4, 3.5)
Lower third (n = 70)	5 (7%)	0.80 (0.78, 0.82)	15.4 (9.3, 21.5)	3.3 (2.1, 4.5)

GTV, gross tumor volume; CI, confidence interval; DSC, Dice similarity coefficient; HD95, 95% Hausdorff distance; ASD, average surface distance; cT2, clinical T stage 2; cT3, clinical T stage 3; cT4, clinical T stage 4; pCT, treatment planning CT.

When compared with the previous leading 3D DenseUNet (21), its DSC, HD95, and ASD scores were all inferior to our model performance, e.g., mean DSC 0.75 vs. 0.80, $p < 0.001$ (**Appendix Table A2**).

Human Experts' Assessment

Human experts' assessment showed that the majority (311 of 354, 88%) of deep learning predictions in the external testing set were clinically accepted or required only minor editing (no revision, n = 220; 0%–30% revision, n = 91). Ten (3%) patients had contouring errors in 30%–60% slices, and 33 (9%) patients had unacceptable predictions that required substantial editing efforts. **Figure 3** details the assessment results. The mean DSC, HD95, and ASD were correlated to the degrees of manual revision (DSC: R = -0.58, $p < 0.001$; HD95: R = 0.60, $p < 0.001$; ASD: R = 0.60, $p < 0.001$). These results indicated the reliability of using DSC, HD95, and ASD as contouring accuracy evaluation criteria, consistent with the contour editing effort necessitated in actual clinical practice. Thirty-three (9%) patients had unacceptable predictions where our model failed to accurately locate the tumor, leading to small dice and large distance errors. Among 33 unaccepted cases, 23 (70%) patients had cT2 tumors. Other cases often exhibited relatively uncommon scanning position or anatomies (see the rightmost column in **Figure 4B**). In the subgroup analysis (**Appendix Table A3**), a significantly smaller percentage of patients required major revision (>30% slice revision) in advanced cT3 and cT4 stages as compared to that in early cT2 stage (5% and 8% vs. 35%, $p < 0.01$). Tumor locations did not significantly impact the degrees of manual revision.

Multi-User Evaluation

Performance evaluation of our pCT model with four board-certified radiation oncologists is shown in **Figure 5** and **Appendix Table A4**. Among 20 testing cases, our model performed comparably to these four radiation oncologists in terms of DSC and ASD (mean DSC: 0.82 vs. 0.82, 0.83, 0.79, 0.82; mean ASD: 2.0 mm vs. 1.9, 1.8, 2.6, 2.0 mm). For HD95, our model achieved the lowest mean HD95 errors among all results (significantly smaller than R3, mean HD95 7.9 mm vs. 12.0 mm, $p = 0.01$).

Next, we examined if the accuracy of manual contouring could be improved with assistance of deep model predictions. It is observed that when editing upon deep model predictions, 2 out of 4 radiation oncologists' performance had been significantly improved in DSC and HD95 (**Figure 5** and **Appendix Table A5**). The inter-user variation was also reduced (**Figure 6**). Mean multi-user DSC was improved from 0.82 to 0.84 ($p < 0.001$), and mean volume coefficient of variation was reduced by 37.6%

Evaluation Metrics	Institution 2-4 (external multi-institutional testing) using pCT model		
	DSC mean (95% CI)	HD95 (mm) mean (95% CI)	ASD (mm) mean (95% CI)
Total (354)	0.80 (0.78, 0.81)	11.8 (10.1, 13.4)	2.8 (2.4, 3.2)
Degree of revision			
No revision (220, 62%)	0.83 (0.82, 0.84)	7.8 (7.1, 8.6)	1.9 (1.7, 2.0)
>0-10% (49, 14%)	0.78 (0.75 0.81)	11.7 (8.2, 15.2)	2.9 (2.1, 3.7)
>10-30% (42, 12%)	0.71 (0.67, 0.76)	22.5 (18.2, 26.9)	5.0 (3.8, 6.3)
>30-60% (10, 3%)	0.54 (0.35, 0.73)	53.7 (18.8, 88.6)	14.1 (6.9, 21.3)
Unacceptable (33, 9%)	0.05 (0.01, 0.09)	96.3 (75.9, 116.6)	70.4 (50.9, 89.9)

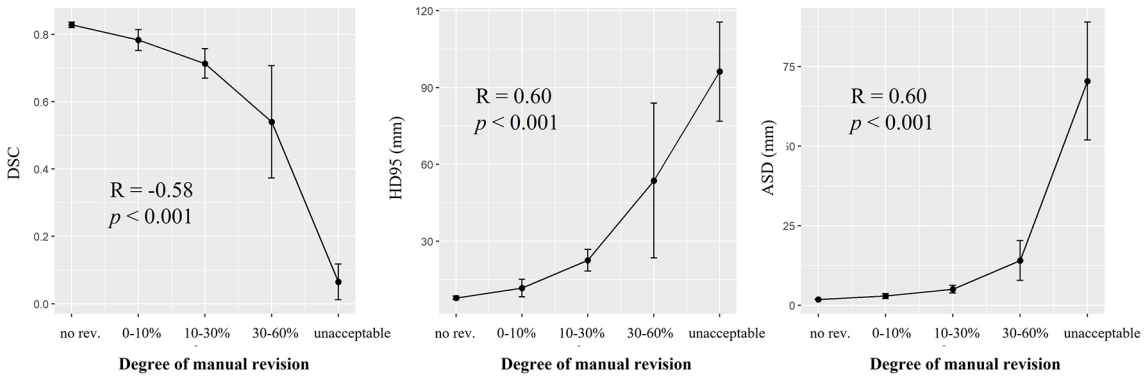

FIGURE 3 | Expert assessment of manual revision degree of the deep model-predicted contours. Table in the top row summarized the mean and 95% confidence interval (CI) of Dice similarity coefficient (DSC), 95% Hausdorff distance (HD95), and average surface distance (ASD) stratified by different degrees of manual revision. The correlations between the mean of DSC, HD95, ASD, and the degree of manual revision were plotted in the bottom row. Spearman correlation coefficient showed that DSC and degree of manual revision were correlated (R = -0.58, $p < 0.001$). Same correlation was observed for the HD95 and ASD (HD95: R = 0.60, $p < 0.001$; ASD: R = 0.60, $p < 0.001$). Degree of manual revision was defined as the percentage of gross tumor volume (GTV) slices that needed modification for clinical acceptance. pCT, treatment planning CT.

(from 0.14 to 0.09, $p = 0.03$). Furthermore, the contouring time had been reduced by an average of 48.0% (from 10.2 to 5.3 min). Our pCT model takes an average of 20 s to predict one patient.

DISCUSSION

In this multi-institutional study, we developed a two-streamed 3D deep learning model to segment esophageal GTV trained on 148 patients with both treatment planning CT (pCT) and PET/CT scans from institution 1. The performance was extensively evaluated using 104 unseen institution 1 patients and 354 external multi-institutional patients. Our pCT model achieved mean DSC and ASD of 0.81 and 2.7 mm in the internal testing and generalized well to the external testing with mean DSC and ASD of 0.80 and 2.8 mm. Adding PET scans, the pCT+PET model further boosted DSC and ASD to 0.83 and 2.2 mm for the internal testing. From a multi-user study, the pCT model performed favorably when compared against four board-certified radiation oncologists in metrics of DSC and ASD while achieving the smallest HD95 errors. By allowing radiation oncologists to edit the deep model predictions, the overall accuracy was improved, and inter-observer variation and contouring time were reduced by 37.6% and 48.0%, respectively.

Accurate GTV delineation improves patient's prognosis (1). Manual contouring of esophageal GTV on pCT highly relies on the expertise and experiences of radiation oncologists, leading to substantial inter-user variations (4, 5, 25). In clinical practice, radiation oncologists almost always need to refer to other information such as panendoscopy report to determine the tumor range, which is not trivial, requiring the "virtual fusion" of panendoscopy information with pCT image in their minds. In this context, our deep model could benefit radiation oncologists by improving their contouring accuracy and consistency and reducing time spent.

Previous works showed potential clinical applicability of deep learning for the GTV contouring in head and neck and prostate cancers (11, 12). However, for esophageal cancer, studies often collected limited single-institution data for both training and testing (18, 21, 26). For example, a 73% Dice score was achieved when trained and tested on a total of 49 patients (21). In this work, with our deep model developed using 148 patients from

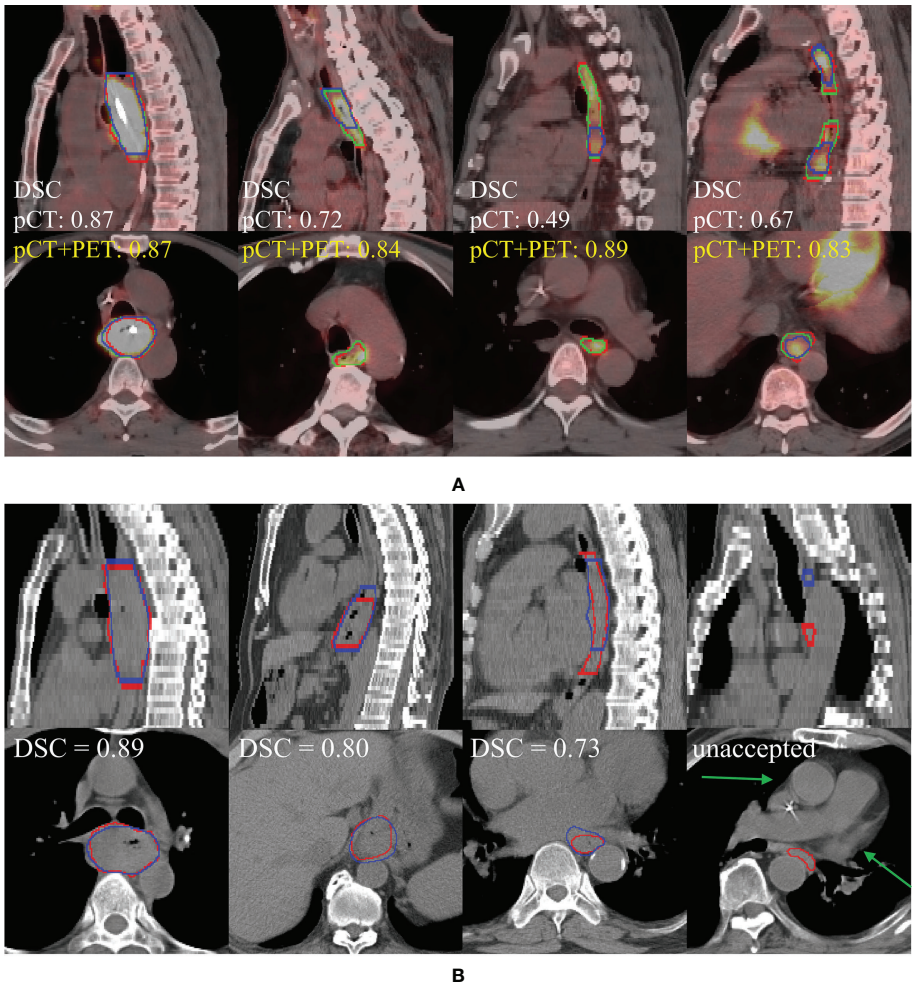

FIGURE 4 | **(A)** Performance comparison of pCT model and pCT+PET in the internal testing set (left to right: cT4, cT3, cT3, multifocal cT2). Red, green, and blue show the contours of ground truth reference, pCT+PET model prediction, and pCT model prediction, respectively. **(B)** Performance examples of pCT model in the external testing set according to the degree of manual revision (left to right): no revision, >0%–30%, >30%–60%, and unacceptable. Red and blue show the contours of ground truth reference and pCT model prediction, respectively. Green arrow points to the uncommon anatomy for the unacceptable case in the rightmost column. pCT, treatment planning CT; DSC, Dice similarity coefficient.

the internal institution 1, we extensively evaluated the GTV segmentation performance using 104 unseen internal patients and 354 external multi-institutional patients. Robust performance generalizability to the external multi-institutional testing data was observed despite variations of CT scanner types, imaging protocols, and patient populations.

Generalizability of deep learning models was often the bottleneck for successful clinical deployment. As shown in Zhang et al. (27), direct deployment of well-trained MRI-based prostate and left arterial segmentation models to the unseen data from different centers led to averaged >10% DSC decrease. Good generalizability of our model may come from the following: 1) relative standardized imaging protocols for pCT from various institutions despite different pCT scanner vendors; 2) physically well-calibrated HU values in CT; 3) the 148 training patients from institution 1 are relatively sufficient for covering different CT characteristics of esophageal tumors; and 4) we have effectively trained our two-streamed deep GTV networks.

The developed two-streamed model has demonstrated the flexibility of segmenting esophageal GTV according to the availability of PET/CT scans. For institutions where PET/CT scans are not included as a standardized staging protocol, our pCT model already achieved high accuracy comparable to the inter-user agreement. When PET/CT scans were available, the pCT+PET model could further improve the performance (mean DSC of pCT vs. pCT+PET: 0.81 vs. 0.83, $p = 0.01$).

This study has a few limitations. First, patients in the external test set do not have PET/CT scans because PET is either not available or not required for esophageal cancer staging in three external institutions. Hence, we have not directly validated the performance of our pCT+PET model in the external data. However, considering that tumor contrast in PET is often prominent and can

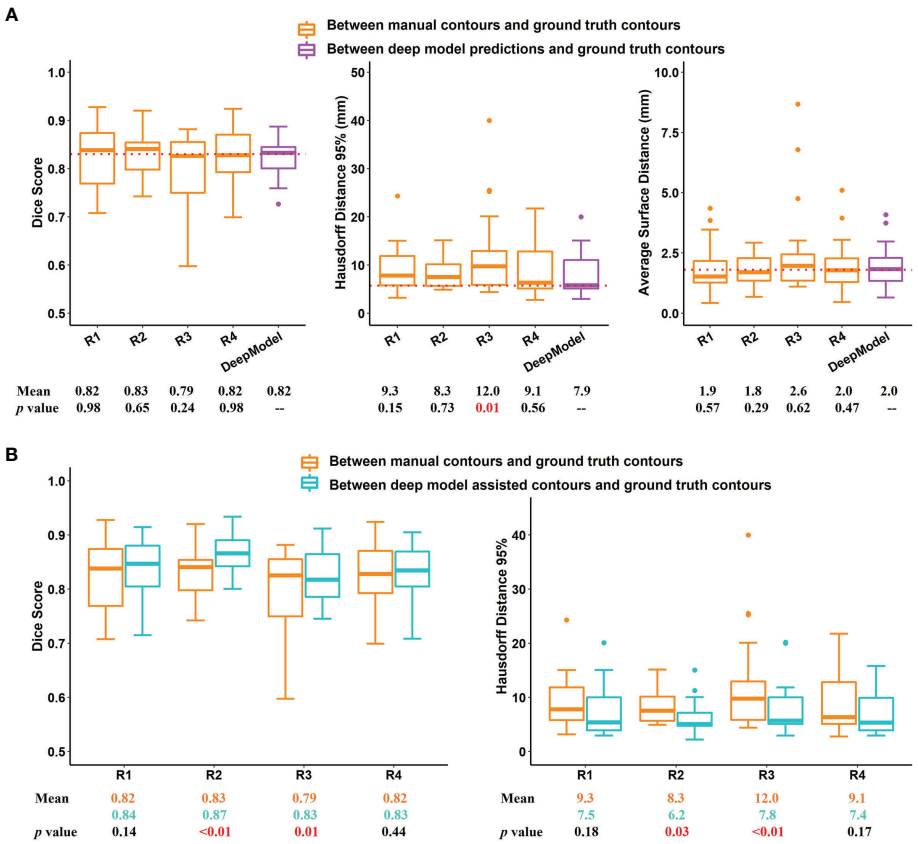

FIGURE 5 | Results of multi-user evaluation. **(A)** Boxplot of Dice similarity coefficient (DSC), 95% Hausdorff distance (HD95), and average surface distance (ASD) for the comparison of manual contours of four radiation oncologists with our treatment planning CT (pCT)-based deep model-predicted contours. Dotted lines indicate the median DSC, HD95, and ASD of our pCT model performance. **(B)** Comparison of DSC and HD95 between second-time deep learning-assisted contours with those of first-time manual contours. R1 to R4 represent the 4 radiation oncologists involved in the multi-user evaluation. DeepModel is our pCT model.

be assessed as a semiquantitative standard uptake value (SUV), we believe that it would not significantly impact our pCT+PET model performance when applied to external patients. Second, the pCT model obtained lower performance for patients of cT2 as compared to those of advanced clinical T stages. This may be because cT2 tumors often exhibited less prominent imaging features in CT. After adding PET, this phenomenon was less evident. Another potential solution might be combining the panendoscopy report information with a deep learning model, which could be optimized by restricting longitudinal ranges. Third, we excluded patients with the primary tumor at gastroesophageal junction, since they were relatively rare (<2%) in our study population and some were treated by surgery. Further investigation of developing the deep learning model on this subpopulation would be of clinical interest. Lastly, we did not include GTV of lymph nodes (GTV_{LN}) and clinical target volume (CTV) that are essential for a comprehensive esophageal cancer target contouring tool in this proposed model. GTV_{LN} is a vital part in treating esophageal cancer. However, in this work, our deep model only includes the main esophageal tumor and focuses on the multi-institutional clinical evaluation of tumor GTV auto-contouring because metastatic lymph node identification is a non-trivial problem itself. For example, detecting and subsequently segmenting the metastatic regional lymph nodes, which may spread to a long longitudinal range along the esophagus, would require the development of dedicated deep learning models (28). Note that we have developed recent state-of-the-art technical solutions along this line of work on finding and segmenting GTV_{LN} (29–31). Nevertheless, GTV_{LN} identification is highly challenging, so further technical improvement is needed to achieve clinically applicable performance. We leave the thorough clinical evaluation of GTV_{LN} auto-contouring as our next step of future work. In addition, CTV is another indispensable volume to be delineated in esophageal cancer radiotherapy. We have developed a deep learning-based technical solution to incorporate the 3D spatial context of tumors and lymph nodes for CTV auto-contouring (32). The current main roadblock is on the auto-contouring of GTV_{LN}. Once we solve the lymph node problem, we are ready to implement and conduct a large-scale clinical evaluation on the esophageal CTV auto-contouring task.

To conclude, we developed and clinically validated an effective two-streamed 3D deep model that can reliably segment the esophageal GTV using two protocols of pCT alone or pCT+PET/CT. Predicted GTV contours for 88% of patients were in close agreement with the ground truth and

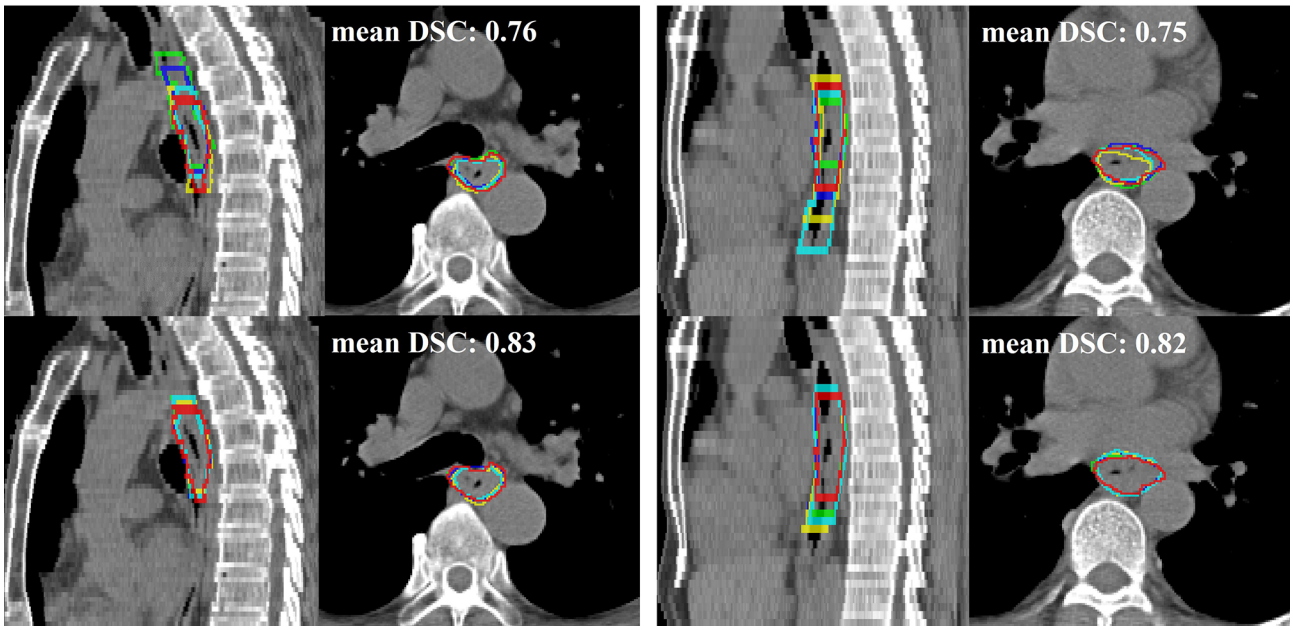

FIGURE 6 | Two qualitative examples (left and right) in sagittal and axial views of comparison between the first-time manual contour (top row) and second-time deep learning-assisted contours (bottom row). Red is the ground truth contour, while green, blue, yellow, and cyan represent the other four radiation oncologists' contours. The average Dice similarity coefficient (DSC) of 4 radiation oncologists for their first-time manual contour is 0.76 and 0.75 to the two examples, respectively. The DSC performance improved to 0.83 and 0.82 for their second-time contour with assistance from the deep learning predictions.

could be implemented and adopted clinically where only minor or no editing efforts are required.

DATA AVAILABILITY STATEMENT

The data analyzed in this study is subject to the following licenses/restrictions: The dataset may be available upon request and application for the institutional research boards' approval of each participating institution. Requests to access these datasets should be directed to T-YH, albertyho@gmail.com.

ETHICS STATEMENT

Patients from the four institutions were collected in this retrospective study under each institutional review board approval. Requirements to obtain informed consent were waived.

AUTHOR CONTRIBUTIONS

First co-authors: XY helped collect the external data, review and modify contours from external institutions, and coordinated multi-user study. DG was responsible for the data cleaning, deep learning model development, and internal and external evaluation. They both designed the experiments and drafted the article. C-KT, P-CP, and T-MH approved the contours for training and validation of the internal institution. JG, YR, and LZ helped collect and organized the external data. XZ, LP, YC, XC, DC, and JY carried out the contouring experiments before and after assistance of deep learning. C-YC and YZC collected and organized internal data. YX, LH, GX, and JX contributed to the design and implementation of the research. LL interpreted the results and drafted the article. DJ was responsible for conception and design of the experiment, development of the deep learning model, and overseeing the evaluation process. SY was responsible for coordinating the external institutions and reviewing and modifying the contours from external institutions, and he also provided guidance and consulting in multi-user study. FJ conducted the statistical analysis and aided in interpreting the results. DJ and T-YH conceived the study, were in charge of overall direction and planning, and drafted the article.

FUNDING

This work is partially supported by Maintenance Project of the Center for Artificial Intelligence in Medicine (Grant CLRPG3H0012, CMRPG3K1091, SMRPG3I0011) at Chang Gung Memorial Hospital.

SUPPLEMENTARY MATERIAL

The Supplementary Material for this article can be found online at: https://www.frontiersin.org/articles/10.3389/fonc.2021.785788/full#supplementary-material

REFERENCES

1. Burnet NG, Thomas SJ, Burton KE, Jefferies SJ. Defining the Tumour and Target Volumes for Radiotherapy. *Cancer Imaging* (2004) 4(2):153–61. doi: 10.1102/1470-7330.2004.0054
2. Kanamoto A, Yamaguchi H, Nakanishi Y, Tachimori Y, Kato H, Watanabe H. Clinicopathological Study of Multiple Superficial Oesophageal Carcinoma. *Br J Surg* (2000) 87(12):1712–5. doi: 10.1046/j.1365-2168.2000.01588.x
3. Altorki NK, Lee PC, Liss Y, Meherally D, Korst RJ, Christos P, et al. Multifocal Neoplasia and Nodal Metastases in T1 Esophageal Carcinoma: Implications for Endoscopic Treatment. *Ann Surg* (2008) 247(3):434–9. doi: 10.1097/SLA.0b013e318163a2ff
4. Nowee ME, Voncken FE, Kotte A, Goense L, van Rossum P, van Lier A, et al. Gross Tumour Delineation on Computed Tomography and Positron Emission Tomography-Computed Tomography in Oesophageal Cancer: A Nationwide Study. *Clin Trans Radiat Oncol* (2019) 14:33–9. doi: 10.1016/j.ctro.2018.10.003
5. Vesprini D, Ung Y, Dinniwell R, Breen S, Cheung F, Grabarz D, et al. Improving Observer Variability in Target Delineation for Gastro-Oesophageal Cancer—the Role of 18Ffluoro-2-Deoxy-D-Glucose Positron Emission Tomography/Computed Tomography. *Clin Oncol* (2008) 20(8):631–8. doi: 10.1016/j.clon.2008.06.004
6. Nikolov S, Blackwell S, Mendes R, De Fauw J, Meyer C, Hughes C, et al. Deep Learning to Achieve Clinically Applicable Segmentation of Head and Neck Anatomy for Radiotherapy. *arXiv preprint arXiv* (2018) 180904430.
7. De Fauw J, Ledsam JR, Romera-Paredes B, Nikolov S, Tomasev N, Blackwell S, et al. Clinically Applicable Deep Learning for Diagnosis and Referral in Retinal Disease. *Nat Med* (2018) 24(9):1342–50. doi: 10.1038/s41591-018-0107-6
8. Kickingereder P, Isensee F, Tursunova I, Petersen J, Neuberger U, Bonekamp D, et al. Automated Quantitative Tumour Response Assessment of MRI in Neuro-Oncology With Artificial Neural Networks: A Multicentre, Retrospective Study. *Lancet Oncol* (2019) 20(5):728–40. doi: 10.1016/S1470-2045(19)30098-1
9. Cheng CT, Wang Y, Chen HW, Hsiao PM, Yeh CN, Hsieh CH, et al. A Scalable Physician-Level Deep Learning Algorithm Detects Universal Trauma on Pelvic Radiographs. *Nat Commun* (2021) 12(1):1066. doi: 10.1038/s41467-021-21311-3
10. Hsieh C-I, Zheng K, Lin C, Mei L, Lu L, Li W, et al. Automated Bone Mineral Density Prediction and Fracture Risk Assessment Using Plain Radiographs *via* Deep Learning. *Nat Commun* (2021) 12(1):1–9. doi: 10.1038/s41467-021-25779-x
11. Lin L, Dou Q, Jin Y-M, Zhou G-Q, Tang Y-Q, Chen W-L, et al. Deep Learning for Automated Contouring of Primary Tumor Volumes by MRI for Nasopharyngeal Carcinoma. *Radiology* (2019) 291(3):677–86. doi: 10.1148/radiol.2019182012
12. Liu C, Gardner SJ, Wen N, Elshaikh MA, Siddiqui F, Movsas B, et al. Automatic Segmentation of the Prostate on CT Images Using Deep Neural Networks (DNN). *Int J Radiat Oncol Biol Phys* (2019) 104(4):924–32. doi: 10.1016/j.ijrobp.2019.03.017
13. Tang H, Chen X, Liu Y, Lu Z, You J, Yang M, et al. Clinically Applicable Deep Learning Framework for Organs at Risk Delineation in CT Images. *Nat Mach Intell* (2019) 1(10):480–91. doi: 10.1038/s42256-019-0099-z
14. Cardenas CE, McCarroll RE, Court LE, Elgohari BA, Elhalawani H, Fuller CD, et al. Deep Learning Algorithm for Auto-Delineation of High-Risk Oropharyngeal Clinical Target Volumes With Built-in Dice Similarity Coefficient Parameter Optimization Function. *Int J Radiat Oncol Biol Phys* (2018) 101(2):468–78. doi: 10.1016/j.ijrobp.2018.01.114
15. Ibragimov B, Xing L. Segmentation of Organs-at-Risks in Head and Neck CT Images Using Convolutional Neural Networks. *Med Phys* (2017) 44(2):547–57. doi: 10.1002/mp.12045
16. Guo D, Jin D, Zhu Z, Ho T-Y, Harrison AP, Chao C-H, et al. Organ at Risk Segmentation for Head and Neck Cancer Using Stratified Learning and Neural Architecture Search. *Proc IEEE/CVF Conf Comput Vision Pattern Recognit* (2020) 2020:4222-31. doi: 10.1109/CVPR42600.2020.00428
17. Guo D, Ge J, Ye X, Yan S, Xin Y, Song Y, et al. Comprehensive and Clinically Accurate Head and Neck Organs at Risk Delineation *via* Stratified Deep Learning: A Large-Scale Multi-Institutional Study. *arXiv preprint arXiv* (2021) 211101544. doi: 10.21203/rs.3.rs-1039673/v1
18. Jin D, Guo D, Ho TY, Harrison AP, Xiao J, Tseng CK, et al. DeepTarget: Gross Tumor and Clinical Target Volume Segmentation in Esophageal Cancer Radiotherapy. *Med Image Anal* (2021) 68:101909. doi: 10.1016/j.media.2020.101909
19. Jin D, Guo D, Ho T-Y, Harrison AP, Xiao J, Tseng C-K, et al. Accurate Esophageal Gross Tumor Volume Segmentation in Pet/Ct Using Two-Stream Chained 3d Deep Network Fusion. In: *International Conference on Medical Image Computing and Computer-Assisted Intervention*. Cambridge, United States: Springer (2019).
20. Japan Esophageal Society. Japanese Classification of Esophageal Cancer: Part I. *Esophagus* (2017) 14:1–36. doi: 10.1007/s10388-016-0551-7
21. Yousefi S, Sokooti H, Elmahdy MS, Peters FP, Shalmani MTM, Zinkstok RT, et al. Esophageal Gross Tumor Volume Segmentation Using a 3D Convolutional Neural Network. In: *International Conference on Medical Image Computing and Computer-Assisted Intervention*. Springer (2018).
22. Çiçek Ö, Abdulkadir A, Lienkamp SS, Brox T, Ronneberger O. 3d U-Net: Learning Dense Volumetric Segmentation From Sparse Annotation. In: *International Conference on Medical Image Computing and Computer-Assisted Intervention*. Springer (2016).
23. Huang G, Liu Z, van der Maaten L, Weinberger KQ. Densely Connected Convolutional Networks. In: *Proceedings of the IEEE Conference on Computer Vision and Pattern Recognition* (2017).
24. Team RC. *R: A Language and Environment for Statistical Computing*. (2013).
25. Machiels M, Jin P, van Hooft JE, Gurney-Champion OJ, Jelvehgaran P, Geijsen ED, et al. Reduced Inter-Observer and Intra-Observer Delineation Variation in Esophageal Cancer Radiotherapy by Use of Fiducial Markers. *Acta Oncol* (2019) 58(6):943–50. doi: 10.1080/0284186X.2019.1588991
26. Chen S, Yang H, Fu J, Mei W, Ren S, Liu Y, et al. U-Net Plus: Deep Semantic Segmentation for Esophagus and Esophageal Cancer in Computed Tomography Images. *IEEE Access* (2019) 7:82867–77. doi: 10.1109/ACCESS.2019.2923760
27. Zhang L, Wang X, Yang D, Sanford T, Harmon S, Turkbey B, et al. Generalizing Deep Learning for Medical Image Segmentation to Unseen Domains *via* Deep Stacked Transformation. *IEEE Trans Med Imaging* (2020) 39(7):2531–40. doi: 10.1109/TMI.2020.2973595
28. Roth HR, Lu L, Seff A, Cherry KM, Hoffman J, Wang S, et al. A New 2.5 D Representation for Lymph Node Detection Using Random Sets of Deep Convolutional Neural Network Observations. In: *International Conference on Medical Image Computing and Computer-Assisted Intervention*. Cambridge, United States: Springer (2014).
29. Zhu Z, Jin D, Yan K, Ho T-Y, Ye X, Guo D, et al. Lymph Node Gross Tumor Volume Detection and Segmentation *via* Distance-Based Gating Using 3d Ct/Pet Imaging in Radiotherapy. In: *International Conference on Medical Image Computing and Computer-Assisted Intervention*. Lima, Peru: Springer (2020).
30. Chao C-H, Zhu Z, Guo D, Yan K, Ho T-Y, Cai J, et al. Lymph Node Gross Tumor Volume Detection in Oncology Imaging *via* Relationship Learning Using Graph Neural Network. In: *International Conference on Medical Image Computing and Computer-Assisted Intervention*. Lima, Peru: Springer (2020).
31. Guo D, Ye X, Ge J, Di X, Lu L, Huang L, et al. DeepStationing: Thoracic Lymph Node Station Parsing in CT Scans Using Anatomical Context Encoding and Key Organ Auto-Search. In: *International Conference on Medical Image Computing and Computer-Assisted Intervention*. Strasbourg, France: Springer (2021).
32. Jin D, Guo D, Ho T-Y, Harrison AP, Xiao J, Tseng C-K, et al. Deep Esophageal Clinical Target Volume Delineation Using Encoded 3d Spatial Context of Tumors, Lymph Nodes, and Organs at Risk. In: *International Conference on Medical Image Computing and Computer-Assisted Intervention*. Shenzhen, China: Springer (2019).

Conflict of Interest: DG, LL, and DJ were employed by PAII Inc. YX, LH, GX, and JX are employed by Ping An Technology.

The remaining authors declare that the research was conducted in the absence of any commercial or financial relationships that could be construed as a potential conflict of interest.

the publisher, the editors and the reviewers. Any product that may be evaluated in this article, or claim that may be made by its manufacturer, is not guaranteed or endorsed by the publisher.

frontiers in Oncology

SYSTEMATIC REVIEW
published: 09 March 2022
doi: 10.3389/fonc.2022.844390

Updated Evaluation of the Diagnostic Performance of Double Contrast-Enhanced Ultrasonography in the Preoperative T Staging of Gastric Cancer: A Meta-Analysis and Systematic Review

Xin Zhang[1†], *Jun Yao*[1†], *Yu Zhang*[1†], *Xin Huang*[1], *Weijun Wang*[1*] *and Hejing Huang*[2*]

[1] *Department of Gastrointestinal Surgery, Second Affiliated Hospital of Naval Medical University, Shanghai, China,*
[2] *Department of Ultrasound, Second Affiliated Hospital of Naval Medical University, Shanghai, China*

Objective: This study aimed to systematically evaluate the diagnostic performance of double contrast-enhanced ultrasonography (DCEUS) in the preoperative T staging of gastric cancer (GC).

Methods: Literature searches for eligible studies were performed using MEDLINE, EMBASE, and Cochrane Library. The pooled sensitivity, specificity, positive likelihood ratio, negative likelihood ratio, diagnostic odds ratio, and area under the summary receiver operating characteristic curve of DCEUS in the diagnosis of each T stage tumor were calculated. Meta-analyses were performed to obtain the pooled effects of risk ratio (RR) with 95% confidence interval (CI) in the comparison of DCEUS with CT/endoscopic ultrasound (EUS).

Results: A total of 8 studies including 1,232 patients were identified for inclusion in this meta-analysis. The pooled sensitivity and specificity were 0.78 (95% CI = 0.64–0.88) and 0.98 (95% CI = 0.96–0.99) for T1, 0.81 (95% CI = 0.76–0.86) and 0.96 (95% CI = 0.91–0.98) for T2, 0.88 (95% CI = 0.84–0.91) and 0.85 (95% CI = 0.79–0.90) for T3, and 0.81 (95% CI = 0.69–0.89) and 0.96 (95% CI = 0.93–0.97) for T4. Moreover, DCEUS demonstrated significant superiority to CT in diagnosing T1 (RR = 1.57, 95% CI = 1.20–2.05, $p = 0.001$) and T2 (RR = 1.41, 95% CI = 1.16–1.71, $p = 0.001$) and to EUS in diagnosing T3 (RR = 1.24, 95% CI = 1.08–1.42, $p = 0.003$) and T4 (RR = 1.40, 95% CI = 1.09–1.79, $p = 0.008$). However, it showed a lower diagnostic accuracy than EUS in T1 tumors (RR = 0.77, 95% CI = 0.62–0.94, $p = 0.013$).

Conclusions: DCEUS is a feasible complementary diagnostic tool for clinical T staging of GC. However, it is still far from a definitive conclusion for DCEUS to be proposed for use in routine clinical practice.

Keywords: double contrast-enhanced ultrasonography, gastric cancer, preoperative evaluation, tumor staging, diagnostic performance

OPEN ACCESS

Edited by:
Pierfrancesco Franco,
University of Eastern Piedmont, Italy

Reviewed by:
Bogdan Silviu Ungureanu,
University of Medicine and Pharmacy of Craiova, Romania
Rinaldo Pellicano,
Molinette Hospital, Italy
Irina Cazacu,
Fundeni Clinical Institute, Romania

***Correspondence:**
Weijun Wang
wangweijun@smmu.edu.cn
Hejing Huang
huanghejinga@163.com

[†]*These authors have contributed equally to this work*

Specialty section:
This article was submitted to Cancer Imaging and Image-directed Interventions, a section of the journal Frontiers in Oncology

Received: *28 December 2021*
Accepted: *08 February 2022*
Published: *09 March 2022*

Citation:
Zhang X, Yao J, Zhang Y, Huang X, Wang W and Huang H (2022) Updated Evaluation of the Diagnostic Performance of Double Contrast-Enhanced Ultrasonography in the Preoperative T Staging of Gastric Cancer: A Meta-Analysis and Systematic Review. Front. Oncol. 12:844390. doi: 10.3389/fonc.2022.844390

INTRODUCTION

Gastric cancer (GC) represents one of the most common causes of cancer death worldwide (1). As a shift toward a more individualized, stage-dependent treatment of GC has been advocated, accurate preoperative staging is essential for appropriate treatment (2). In particular, the depth of primary tumor invasion, namely, T stage, is both an important indicator for predicting prognosis and a major factor for the determination of an optimal therapeutic strategy (3, 4). Therefore, it is important to explore reliable and effective techniques for preoperative T staging of GC.

Many imaging modalities, such as computed tomography (CT), magnetic resonance imaging (MRI), and endoscopic ultrasound (EUS), have been utilized clinically for evaluating the T stage of GC (5, 6). Particularly, multi-detector row CT (MDCT) with multi-planar reformatted views is believed to be a powerful tool, but its sensitivity in T staging for early GC is low (7). Moreover, it carries a burden on ionizing radiation, which may be an obvious disadvantage. MRI seems to have better performance for high resolution, but the relatively expensive fees and longer scanning time also limit its extensive application in the staging of GC (6). EUS is regularly applied to stage GC due to its high sensitivity (8, 9). However, overstaging of T2 lesions appears to be a frequent problem (10), and EUS could not avoid bringing about some discomfort.

Double contrast-enhanced ultrasonography (DCEUS) refers to the combination of oral contrast agent and intravenous contrast agent for ultrasound examination (11). It has been explored as an innovative modality to screen diseases of the gastrointestinal tract (12). SonoVue is an intravenous contrast agent of sulfur hexafluoride microbubbles, and DCEUS provides a feasible way to make an accurate T staging by using ultrasonic oral contrast agent alongside SonoVue in patients with GC (13). Although there have been some studies that estimated the diagnostic performance of DCEUS in the preoperative T staging of GC (14, 15), only a small number of patients were included in each study. In addition, the only one previously published meta-analysis on the diagnostic accuracy of DCEUS in the T staging of GC is scarce and not robust to reach definitive conclusions (16). Therefore, we aim to provide an updated and revised version of the meta-analysis to determine the diagnostic performance of DCEUS for T staging in patients with GC.

METHODS

Literature Search

Databases including MEDLINE, EMBASE, and the Cochrane Library were searched up to December 23, 2021 to identify pertinent citations. The following search strategies were employed: (double contrast-enhanced ultrasonography OR double contrast-enhanced ultrasound) AND (stomach OR gastric) AND (cancer OR carcinoma OR neoplasia OR tumor OR adenocarcinoma). For unpublished data, trial registries including clinical trial.gov, the national research register, and current controlled trials were searched. Additionally, a manual search was performed by checking the reference lists in recent important publications. This review involved only the secondary use of anonymous information or anonymous biological materials and thus was exempted from research ethics board review.

Study Selection

Both prospective and retrospective studies examining the diagnostic performance of DCEUS for the preoperative T staging of GC were included, namely, (1) gastric carcinoma as proven by endoscopic biopsy; (2) without history of chemotherapy, radiotherapy, targeted therapy, immunotherapy, or other cancer-related treatment; (3) the patients were examined by DCEUS not more than one week before the surgical resections; and (4) no age or gender restrictions. Studies were included regardless of the publication date, publication status, and language. The exclusion criteria were as follows: (1) unresectable lesions with metastasis detected on preoperative evaluation, (2) patients medically unfit for surgery, (3) letters to the editor, case reports, editorials, and review articles, (4) studies that did not provide sufficient data to determine at least one of the preoperative staging performance measures (sensitivity, specificity, or accuracy), and (5) studies that did not use the TNM classification system.

The title and the abstract of each article were screened and assessed independently against the predetermined inclusion criteria by two reviewers (XZ and HH). A third party was involved in the discussion and decision-making. A reason must be given for excluding any article.

Quality Assessment

Two authors (XZ and JY) independently evaluated the overall quality of the included studies by using the Quality Assessment of Studies of Diagnostic Accuracy-2 (17). This method has four domains, namely, patient selection, index test, reference standard, and flow and timing. Each domain was assessed considering the risk of bias, and the first three domains were assessed to confirm the applicability. Each domain contains three judgments, namely, "low", "high", and "unclear". Discrepancies between the two authors were resolved by a discussion. The final results were reviewed by the other authors. The quality assessment of the included study was performed using RevMan 5.3 (Cochrane Collaboration).

Statistical Analysis

A bivariate model was used to pool the sensitivity, specificity, positive likelihood ratio (PLR), negative likelihood ratio (NLR), and diagnostic odds ratio (DOR) of the included studies (18). A summary receiver operating characteristic (SROC) curve was generated, and the area under the curve (AUC) was calculated to determine the overall diagnostic accuracy of DCEUS (19). Deeks' test was applied to assess the potential publication bias (20). Fagan graph was plotted to estimate the posttest probability. Heterogeneity across all eligible studies was estimated by using Q-test and I^2 statistics (21). Statistical analyses were performed using STATA 16.0 (StataCorp, College Station, TX, USA) and Meta-DiSc (version 1.4).

RESULTS

Description of the Studies

A total of 65 citations from database searching were initially identified, of which 20 duplicates were excluded. Seventeen papers were retrieved for full-text review after excluding 25 articles on the basis of the titles and the abstracts, two case reports, and one review article. Nine studies concerning the application of DCEUS irrelevant of preoperative T staging of GC were also further excluded. A total of 8 studies (13–15, 22–26) including 1,232 patients were finally included in this meta-analysis. Of these, seven studies were retrospective, and 1 study was prospective. The publication year ranged from 2010 to 2021. The publication language was English in 6 studies and Chinese in 2 studies. The specific flow chart in identifying eligible studies is shown in **Figure 1**. The main characteristics of the included studies are shown in **Table 1**. The overall quality of the included studies was moderate to high, and the results of the methodological quality assessment (bias risk and applicability) are shown in **Figure 2**.

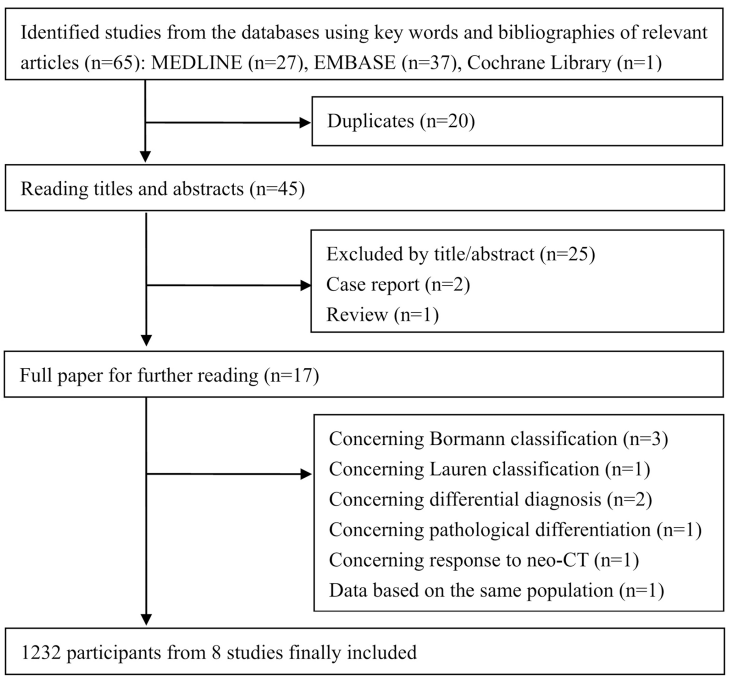

FIGURE 1 | Flow of studies through the review process. neo-CT, neoadjuvant chemotherapy.

TABLE 1 | Characteristics of the studies included.

Author	Region	Gold standard	PL*	Study type	Number	Gender (F/M)	Age, years	TNM edition	Histopathological composition	UOCA volume, ml	Equipment
Wang (22)	China	Pathology	E	R	206	95/111	59.7 ± 11.3	AJCC, 8th	NS	NS	Acuson Sequoia-512
Shen (23)	China	Pathology	C	R	59	14/45	51.4 ± 10.7	NS	NS	500–800	NS
Li (14)	China	Pathology	E	R	100	42/58	62.3 ± 2.6	AJCC, 8th	Well, 10; moderately, 21; poorly, 66	500–800	NS
Wang (15)	China	Pathology	E	R	158	52/106	59.5 ± 10.6	NS	Well, 22; moderately, 33; poorly, 65; signet ring, 16; mucinous, 8; squamous carcinoma, 1	500	Acuson Sequoia-512
He (13)	China	Pathology	E	R	54	18/36	61.0 ± 9.7	AJCC, 7th	NS	500–800	Philips iU22
Li (24)	China	Pathology	E	P	350	105/245	63.6 ± 11.8	AJCC, 6th	NS	500	Acuson Sequoia-512
Zheng (25)	China	Pathology	E	R	162	35/127	58.3 ± 11.3	NS	Well, 34; moderately, 31; poorly, 68; signet ring, 29	500	Acuson Sequoia-512
Chen (26)	China	Pathology	C	R	143	54/89	56.0 ± 11.4	NS	NS	600	Acuson Sequoia-512

**PL, publication language; C, Chinese; E, English; P, prospective; R, retrospective; UOCA, ultrasonic oral contrast agent; NS, not specified.*

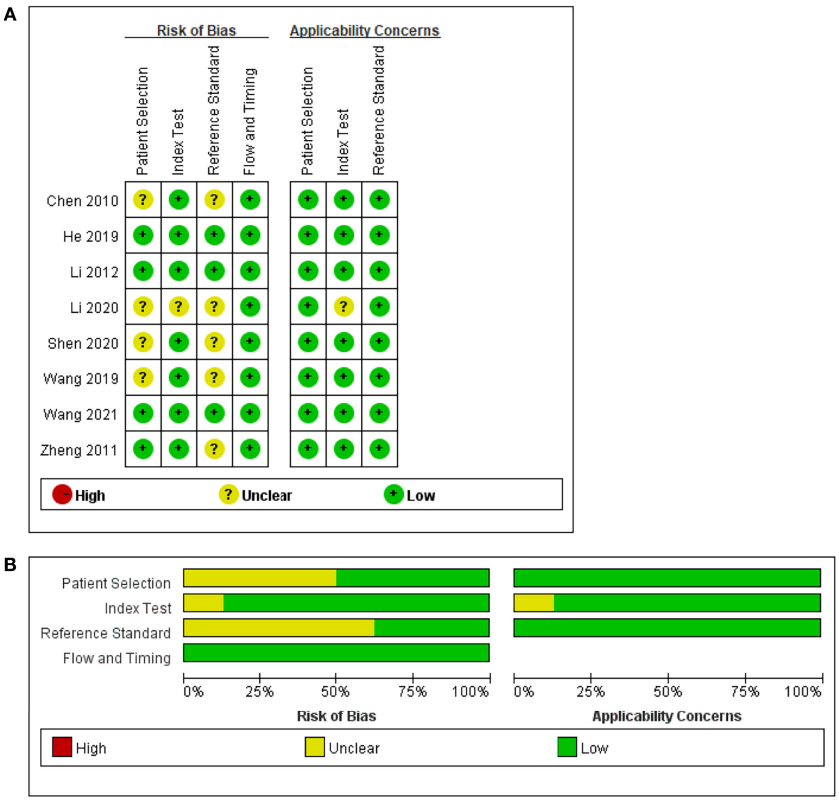

FIGURE 2 | Risk of bias and applicability concerns. **(A)** Summary: review authors' judgments about each domain for each included study. **(B)** Review authors' judgments about each domain presented as percentages across the included studies.

Descriptive Diagnostic Performance of DCEUS

The pooled sensitivity, specificity, PLR, NLR, and DOR of DCEUS in diagnosing each T stage tumor were calculated. The pooled sensitivity and specificity were 0.78 (95% CI = 0.64–0.88) and 0.98 (95% CI = 0.96–0.99) for T1 tumors (**Supplementary Figure S1**), 0.81 (95% CI = 0.76–0.86) and 0.96 (95% CI = 0.91–0.98) for T2 tumors (**Supplementary Figure S2**), 0.88 (95% CI = 0.84–0.91) and 0.85 (95% CI = 0.79–0.90) for T3 tumors (**Supplementary Figure S3**), and 0.81 (95% CI = 0.69–0.89) and 0.96 (95% CI = 0.93–0.97) for T4 tumors (**Supplementary Figure S4**). For each outcome, the pooled PLR, NLR, and DOR are listed in **Table 2**.

Between-study heterogeneity was high in the pooled sensitivity in T1 ($I^2 = 65.7\%$, $p = 0.01$) and T4 ($I^2 = 71.1\%$, $p < 0.001$) and in the pooled specificity in T2 ($I^2 = 85.2\%$, $p < 0.001$) and T3 ($I^2 = 66.5\%$, $p < 0.001$). Interestingly, heterogeneity was obviously reduced when the study by He et al. (13) was excluded from the pooled analyses.

The sensitivity analyses were implemented by omitting the included studies one by one. With the sequential removal of each individual study, the overall results were essentially unchanged, indicating the robustness of these findings (**Supplementary Figure S5**).

Threshold Effect and SROC of DCEUS

No typical "shoulder arm" was observed in the SROC curve plane graphs for the test of T1, T2, T3, or T4 (**Figure 3**). The

TABLE 2 | Descriptive diagnostic performance of DCEUS.

	T1	T2	T3	T4
Sen	0.78 (0.64–0.88)	0.81 (0.76–0.86)	0.88 (0.84–0.91)	0.81 (0.69–0.89)
Spe	0.98 (0.96–0.99)	0.96 (0.91–0.98)	0.85 (0.79–0.90)	0.96 (0.93–0.97)
PLR	46.3 (17.5–123.0)	21.1 (8.6–51.4)	5.9 (4.2–8.4)	19.1 (12.1–30.0)
NLR	0.22 (0.12–0.39)	0.19 (0.15–0.25)	0.14 (0.11–0.18)	0.20 (0.12–0.34)
DOR	210 (54–813)	109 (39–309)	41 (26–67)	95 (43–208)

Data are shown as mean (95% confidence limits).

DCEUS, double contrast-enhanced ultrasonography; Sen, sensitivity; Spe, specificity; PLR, positive likelihood ratio; NLR, negative likelihood ratio; DOR, diagnostic odds ratio.

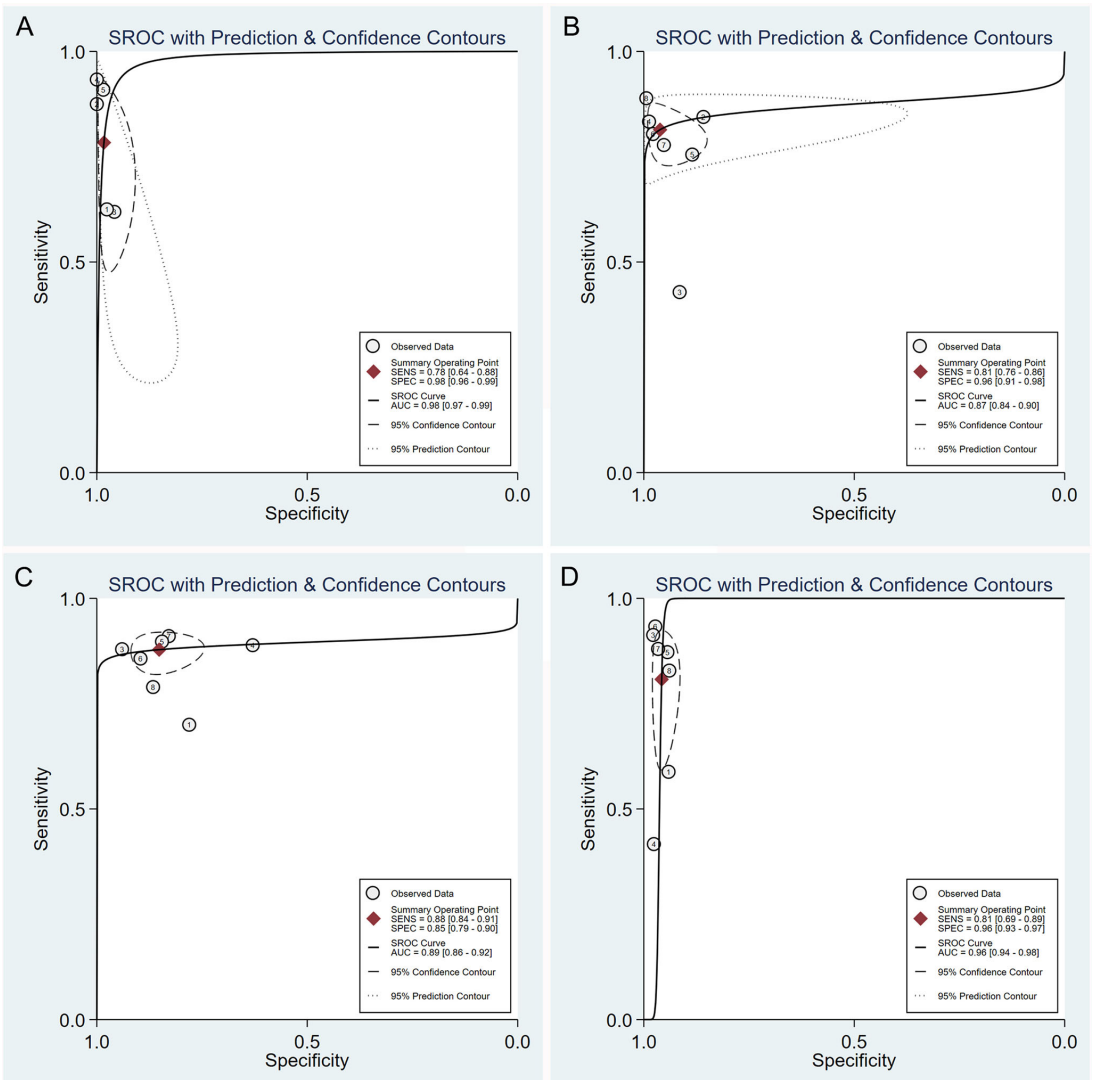

FIGURE 3 | Summary receiver operating characteristic plot of studies assessing the accuracy of double contrast-enhanced ultrasonography in diagnosing T1 **(A)**, T2 **(B)**, T3 **(C)**, and T4 **(D)** gastric tumors. Each study sensitivity/specificity value is represented by an empty circle. The summary point for sensitivity/specificity is represented by a black-filled circle. Dotted closed line, 95% confidence interval of the summary point; dashed closed line, 95% prediction region.

correlation coefficients of the sensitivity logarithm were -0.600, -0.429, 0.143, and -0.357, and the corresponding *p*-values were 0.285, 0.337, 0.760, and 0.432 for the test of T1, T2, T3, and T4, respectively. These results indicate that the threshold effects were not significant.

The AUCs of the SROC curve were 0.98 (95% CI = 0.97–0.99) for T1, 0.87 (95% CI = 0.84–0.90) for T2, 0.89 (95% CI = 0.86–0.92) for T3, and 0.96 (95% CI = 0.94–0.98) for T4. The SROC curve along with the summary point and the 95% confidence and prediction contours is shown in **Figure 3**.

Clinical Utility of DCEUS

The Fagan graph was plotted to show the relationship among the pretest probability, the likelihood ratio, and the posttest probability. When the pretest probability was set at 50%, the posttest probability was 98% if the results were positive and 18% if the results were negative for T1 tumors (**Figure 4A**). The posttest probability was 95% if the results were positive and 16% if the results were negative for T2 tumors (**Figure 4B**). The posttest probability was 86% if the results were positive and 13% if the results were negative for T3 tumors (**Figure 4C**). The posttest probability was 95% if the results were positive and 17% if the results were negative for T4 tumors (**Figure 4D**).

The likelihood ratio scatter plots demonstrated that the summary point of the probability ratio fell in the upper right quadrant for T1, T2, and T4, indicating that DCEUS was effective for T1, T2, and T4 confirmation but not effective for T1, T2, or T4 exclusion (**Figures 5A, B, D**). In addition, the summary point

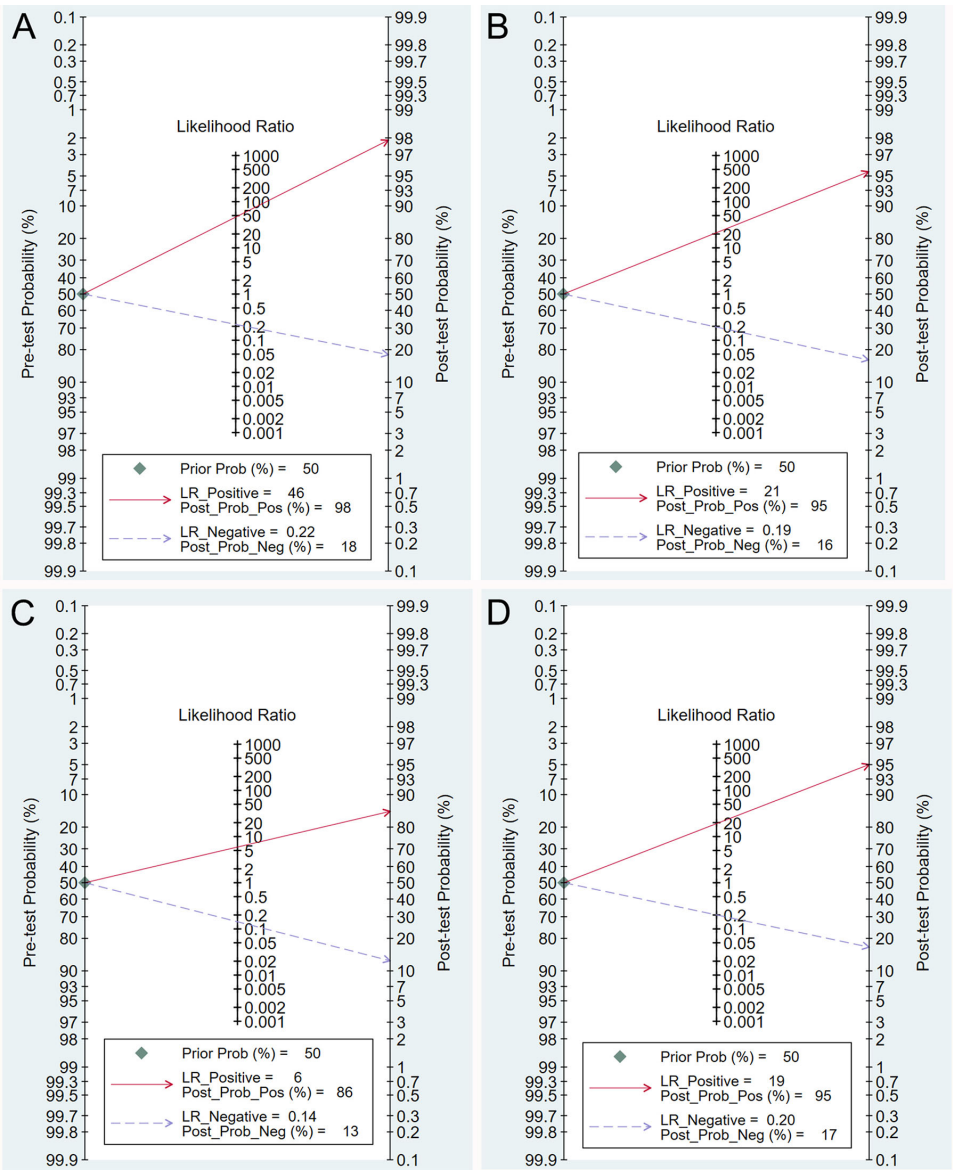

FIGURE 4 | Fagan plot estimating how much the result of double contrast-enhanced ultrasonography changes the probability that a patient has a T1 **(A)**, T2 **(B)**, T3 **(C)**, or T4 **(D)** gastric cancer, considering a given pre-test probability (here the mean pre-test probability found in eligible studies is shown as an example).

of the probability ratio fell in the lower right quadrant for T3, indicating that the utility of DCEUS was limited for T3 evaluation (**Figure 5C**).

Comparison of DCEUS *vs.* CT

Data were available in 4 studies on the comparison of the diagnostic accuracy in determining the T stage of GC between DCEUS and CT. The pooled analysis failed to show a statistically significant difference between the two examinations in T1 (RR = 1.43, 95% CI = 0.91–2.24, $p = 0.119$, **Figure 6A**), T2 (RR = 1.22, 95% CI = 0.91–1.63, $p = 0.177$, **Figure 6B**), T3 (RR = 1.11, 95% CI = 0.82–1.49, $p = 0.498$, **Figure 6C**), or T4 (RR = 1.05, 95% CI = 0.70–1.57, $p = 0.822$, **Figure 6D**). Heterogeneity was detected in the pooled analyses in each T stage tumor (T1: $I^2 = 84.7\%$, $p < 0.001$; T2: $I^2 = 75.3\%$, $p = 0.007$; T3: $I^2 = 61.3\%$, $p = 0.051$; and T4: $I^2 = 90.4\%$, $p < 0.001$, **Figure 6**).

Sensitivity analyses were implemented to explore the heterogeneity by omitting the included studies one by one. Interestingly, when the study by He et al. (13) was excluded from the pooled analyses, DCEUS demonstrated significant superiority to CT in diagnosing T1 (RR = 1.57, 95% CI = 1.20–2.05, $p = 0.001$, **Figure 7A**) and T2 (RR = 1.41, 95% CI = 1.16–1.71, $p = 0.001$, **Figure 7B**) with homogeneity.

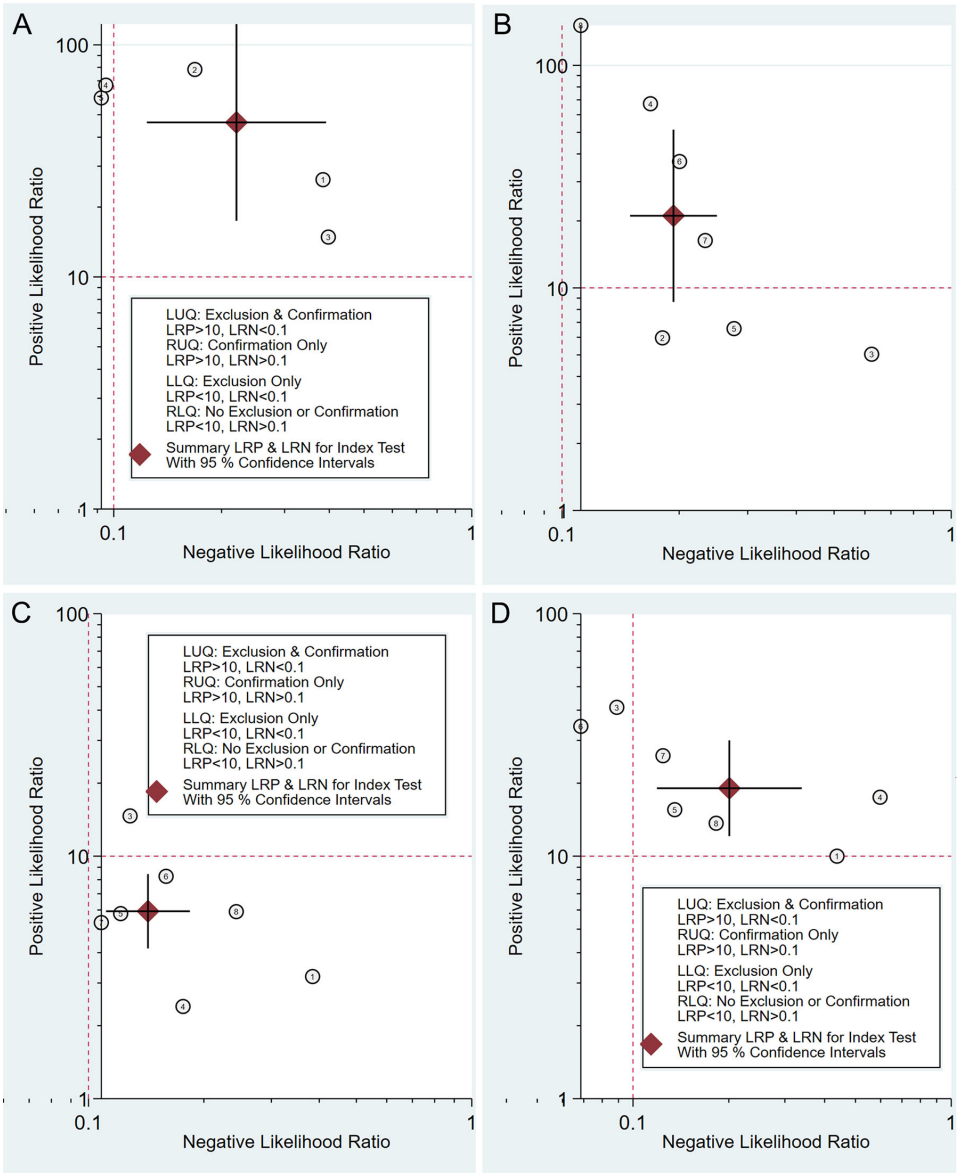

FIGURE 5 | Double contrast-enhanced ultrasonography performance to diagnose T1 **(A)**, T2 **(B)**, T3 **(C)**, and T4 **(D)** gastric cancer. Likelihood ratio (LR) scattergram defining the quadrants of informativeness based on desirable thresholds (positive LR > 10, negative LR < 0.1): left upper quadrant (test suitable both for diagnosis exclusion and confirmation), right upper quadrant (confirmation only), left lower quadrant (exclusion only), and right lower quadrant (neither confirmation nor exclusion).

Comparison of DCEUS *vs*. EUS

Data were available in 2 studies on the comparison of the diagnostic accuracy in determining the T stage of GC between DCEUS and EUS. The pooled analysis showed that DCEUS had a lower diagnostic accuracy than EUS in T1 tumors (RR = 0.77, 95% CI = 0.62–0.94, p = 0.013, **Figure 8A**) but had a higher accuracy in T3 (RR = 1.24, 95% CI = 1.08–1.42, p = 0.003, **Figure 8C**) and T4 tumors (RR = 1.40, 95% CI = 1.09–1.79, p = 0.008, **Figure 8D**). No significant difference was detected in the T2 tumors between the two examinations (RR = 0.94, 95% CI = 0.81–1.08, p = 0.370, **Figure 8B**).

Publication Bias

Deeks' test was applied to assess the publication bias. The p-value was 0.015, 0.325, 0.111, and 0.987 for T1, T2, T3, and T4, respectively, indicating the presence of publication bias.

DISCUSSION

Precise preoperative staging is greatly essential for proper stage-dependent patient management (27). It is utilized to select patients who may benefit from less invasive diagnostic

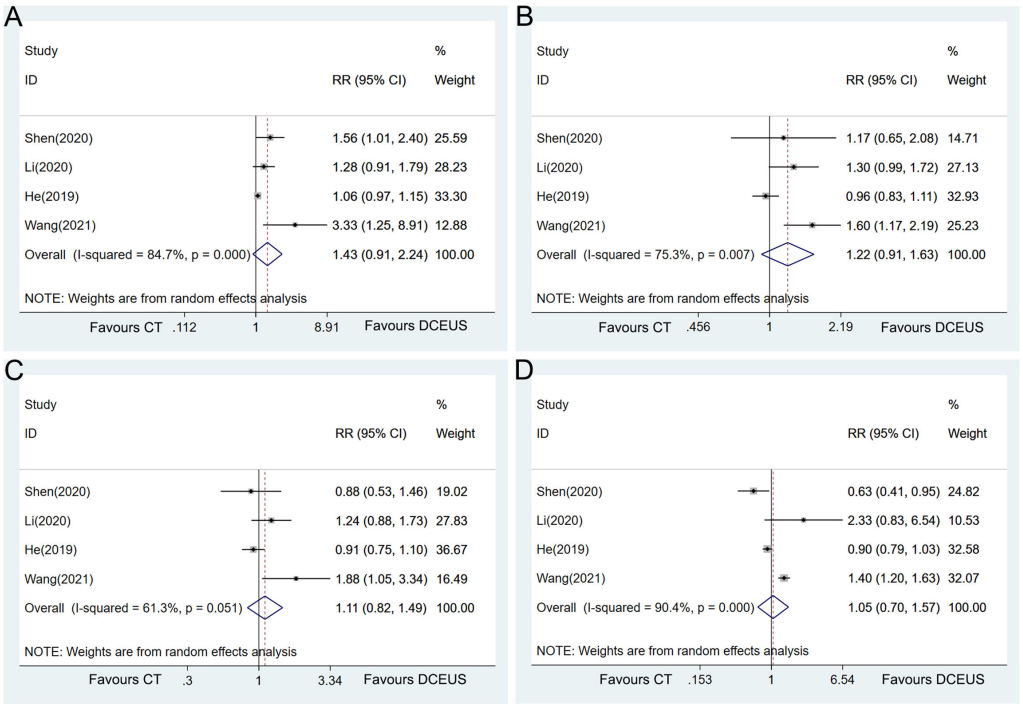

FIGURE 6 | Forest plot showing the pooled effects of diagnostic performance of double contrast-enhanced ultrasonography compared with CT in diagnosing T1 **(A)**, T2 **(B)**, T3 **(C)**, and T4 **(D)** gastric cancer.

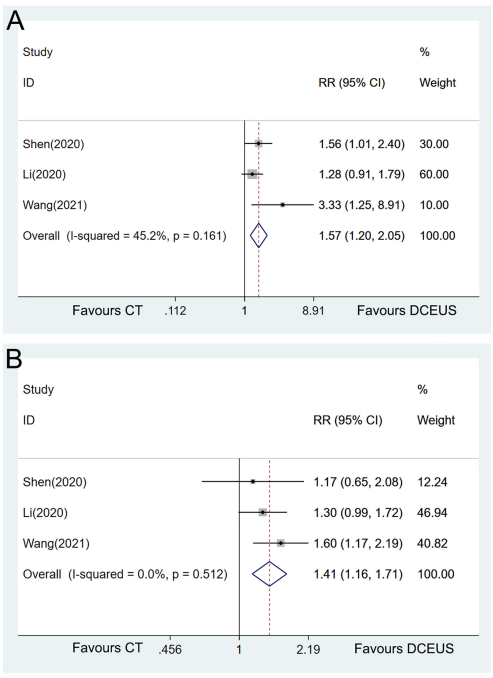

FIGURE 7 | Forest plot showing the pooled effects of diagnostic performance of double contrast-enhanced ultrasonography compared with CT in diagnosing T1 **(A)** and T2 **(B)** with only homogeneous studies included.

procedures and those who may benefit from multimodal treatment (28). This systematic review provides an overview of current evidence on the diagnostic performance of DCEUS for preoperative T staging in patients with GC. On the whole, the sensitivity, specificity, and AUC of DCEUS in the diagnosis of each T stage of GC are relatively high. This information enables clinicians to get a precise sense of the risk of making errors, in terms of both false-positive and false-negative predictions. More importantly, DCEUS shows a superiority to CT in the diagnosis of stages T1 and T2 tumors and to EUS in stages T3 and T4 tumors. Therefore, DCEUS could serve as a feasible complementary diagnostic tool for the clinical T staging of GC.

Currently, MDCT is the most commonly used imaging method for staging GC, which can provide visualization of the depth of the primary tumor invasion and an estimate of the lymph node involvement (29). However, the diagnostic performance of CT for T staging is limited, especially for early GC (30). DCEUS was developed as a novel method to complement existing modalities in the staging of GC. It is based on oral gastric window contrast-enhanced ultrasonography and further uses ultrasound venography to analyze the blood flow perfusion of the lesion. The diagnostic method zywas based on the characteristics of "positive imaging" in the arterial phase and "negative imaging" in the venous phase and T staging were performed according to the range of these two areas (31). In the present meta-analysis, DCEUS reveals superiority to CT in the diagnosis of T1 and T2 stage of GC, and such difference reaches statistical significance in the study by He et al. (13), which

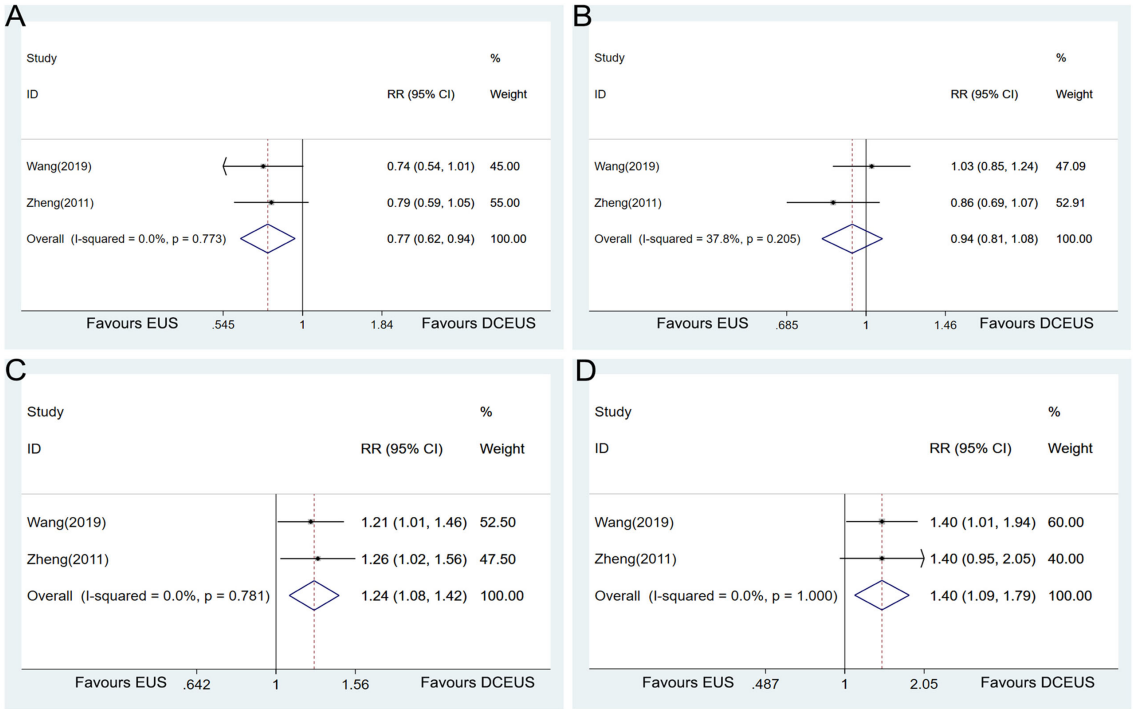

FIGURE 8 | Forest plot showing the pooled effects of the diagnostic performance of double contrast-enhanced ultrasonography compared with endoscopic ultrasound in diagnosing T1 **(A)**, T2 **(B)**, T3 **(C)**, and T4 **(D)** gastric cancer.

contributes to the heterogeneity, and is excluded from the pooled analysis. These results were consistent with the previous meta-analysis by Xu et al. (16). Since only a small number of patients are included, these inspiring results would trigger more clinical studies to further elucidate the diagnostic performance of DCEUS.

EUS is routinely used in the preoperative staging of GC since remarkably different echogenic appearances could be displayed between the adjacent structural layers of the stomach (32). All available guidelines on GC recommend EUS as the main method to assess the T stage (33). The diagnostic accuracy of EUS for overall T staging varied from 56.9 to 87.7%, and the accuracy values for T1, T2, T3, and T4 stages were 14 to 100%, 24 to 90%, 50 to 100%, and 25 to 100%, respectively (34–37). In the present meta-analysis, two original studies (15, 25) reported the head-to-head comparison results between DCEUS and EUS in the diagnosis of T staging of GC. DCEUS yields a better consistency with postoperative pathological results than EUS in T3 and T4 tumors, and EUS seems to have a higher accuracy in diagnosing T1 tumors than DCEUS. Despite the inspiring results, DCEUS should only be considered as a research method, an alternative tool, and may not be used as a routine procedure for GC staging.

There was a meta-analysis by Xu et al. published previously on the diagnostic accuracy of DCEUS in clarifying the tumor depth of GC (16). In that publication, a total of 926 patients from 6 studies were included, and the pooled sensitivity and specificity of DCEUS were 0.67 and 0.98 for T1 stage, 0.81 and 0.95 for T2 stage, 0.89 and 0.86 for T3 stage, and 0.87 and 0.96 for T4 stage, respectively. However, some defects exist in that meta-analysis. Data from the studies by Chen et al. (26) and Wang et al. (38) were based on the overlapping population, and three most recently published relevant studies were not included, which makes the pooled results less convincing. More importantly, they did not provide the pooled comparison of the diagnostic performance between DCEUS and other tools (CT or EUS). Therefore, our present meta-analysis may serve as an updated and revised version.

Despite these favorable findings, some critical issues need to be emphasized to correctly appreciate the limitations of DCEUS. Firstly, the remarkable heterogeneity of results across eligible studies casts some doubts on the reliability and reproducibility of DCEUS in the tumor staging of GC. Since the study by He et al. contributed a great amount to the heterogeneity, it seems that the ultrasonography equipment utilized and the differences in the experience levels of the doctors performing the ultrasound examination might be the factors that brought about the heterogeneity. However, we could not explore the effect of other potential sources of heterogeneity due to the lack of data. Secondly, all the included studies were conducted among Chinese populations, and no data derived from Caucasians or black people are available. As the thickness of abdominal fat in Chinese patients is thinner than those in people from Western countries, it may be beneficial to obtain clear images when performing the DCEUS examination. Therefore, the generalizability of the findings to a population with different races, ethnicity, or geographical environments may be limited. Finally, since only a small

number of studies and patients are available to make a pooled analysis, these findings should be interpreted with caution. More restrictedly designed studies are still warranted to make a direct comparison of DCEUS with CT or EUS to further confirm the clinical utility value of DCEUS.

CONCLUSIONS

The findings obtained from the present meta-analysis provide evidence for the utility of DCEUS in the preoperative tumor staging of GC. DCEUS showed a superiority to CT in the diagnosis of stage of T1 and T2 tumors and to EUS in the staging of T3 and T4 tumors. Therefore, DCEUS could serve as a feasible complementary diagnostic tool for clinical T staging of GC. However, it is still far from a definitive conclusion for DCEUS to be proposed for use in routine clinical practice.

DATA AVAILABILITY STATEMENT

The original contributions presented in the study are included in the article/**Supplementary Materials**. Further inquiries can be directed to the corresponding authors.

AUTHOR CONTRIBUTIONS

WW and HH designed this study. XZ, JY, and YZ acquired and analyzed the data. XZ and XH wrote and edited the manuscript. All authors contributed to the article and approved the submitted version.

FUNDING

This study was supported by grants from the National Natural Science Foundation of China (81773049, 81402359, and 81602617).

SUPPLEMENTARY MATERIAL

The Supplementary Material for this article can be found online at: https://www.frontiersin.org/articles/10.3389/fonc.2022.844390/full#supplementary-material

Supplementary Figure S1 | Forest plot to show the pooled effects of diagnostic performance of DCEUS in diagnosing stage T1 gastric cancer.

Supplementary Figure S2 | Forest plot to show the pooled effects of diagnostic performance of DCEUS in diagnosing stage T2 gastric cancer.

Supplementary Figure S3 | Forest plot to show the pooled effects of diagnostic performance of DCEUS in diagnosing stage T3 gastric cancer.

Supplementary Figure S4 | Forest plot to show the pooled effects of diagnostic performance of DCEUS in diagnosing stage T4 gastric cancer.

Supplementary Figure S5 | Results of the sensitivity analysis of the pooled effects of diagnostic performance of DCEUS in diagnosing stage T1 **(A)**, T2 **(B)**, T3 **(C)**, and T4 **(D)** gastric cancer by removing each study one by one.

REFERENCES

1. Joshi SS, Badgwell BD. Current Treatment and Recent Progress in Gastric Cancer. *CA Cancer J Clin* (2021) 71:264–79. doi: 10.3322/caac.21657
2. Smyth EC, Nilsson M, Grabsch HI, van Grieken NC, Lordick F. Gastric Cancer. *Lancet* (2020) 396:635–48. doi: 10.1016/S0140-6736(20)31288-5
3. Reim D, Loos M, Vogl F, Novotny A, Schuster T, Langer R, et al. Prognostic Implications of the Seventh Edition of the International Union Against Cancer Classification for Patients With Gastric Cancer: The Western Experience of Patients Treated in a Single-Center European Institution. *J Clin Oncol* (2013) 31:263–71. doi: 10.1200/JCO.2012.44.4315
4. Tate DJ, Klein A, Sidhu M, Desomer L, Awadie H, Lee EYT, et al. Endoscopic Submucosal Dissection for Suspected Early Gastric Cancer: Absolute Versus Expanded Criteria in a Large Western Cohort (With Video). *Gastrointest Endosc* (2019) 90:467–79.e4. doi: 10.1016/j.gie.2019.04.242
5. Ungureanu BS, Sacerdotianu VM, Turcu-Stiolica A, Cazacu IM, Saftoiu A. Endoscopic Ultrasound vs. Computed Tomography for Gastric Cancer Staging: A Network Meta-Analysis. *Diagn (Basel)* (2021) 11. doi: 10.3390/diagnostics11010134
6. Renzulli M, Clemente A, Spinelli D, Ierardi AM, Marasco G, Farina D, et al. Gastric Cancer Staging: Is It Time for Magnetic Resonance Imaging? *Cancers (Basel)* (2020) 12. doi: 10.3390/cancers12061402
7. Cimavilla Roman M, de la Serna Higuera C, Loza Vargas LA, Benito Fernandez C, Barrio Andres J, Madrigal Rubiales B, et al. Endoscopic Ultrasound Versus Multidetector Computed Tomography in Preoperative Gastric Cancer Staging. *Rev Esp Enferm Dig* (2017) 109:761–7. doi: 10.17235/reed.2017.4638/2016
8. Zhang K, Park S, Chen L. Editorial: Emerging Diagnostic and Therapeutic Approaches for Gastric Cancer. *Front Oncol* (2020) 10:554960. doi: 10.3389/fonc.2020.554960
9. Pellicano R, Bruno M, Fagoonee S, Ribaldone DG, Fasulo R, De Angelis C. Endoscopic Ultrasound in the Preoperative Staging of Gastric Cancer: Key Messages for Surgeons. *Minerva Chir* (2015) 70:417–27.
10. Kutup A, Vashist YK, Groth S, Vettorazzi E, Yekebas EF, Soehendra N, et al. Endoscopic Ultrasound Staging in Gastric Cancer: Does It Help Management Decisions in the Era of Neoadjuvant Treatment? *Endoscopy* (2012) 44:572–6. doi: 10.1055/s-0032-1308950
11. Wang L, Wang X, Kou H, He H, Lu M, Zhou L, et al. Comparing Single Oral Contrast-Enhanced Ultrasonography and Double Contrast-Enhanced Ultrasonography in the Preoperative Borrmann Classification of Advanced Gastric Cancer. *Oncotarget* (2018) 9:8716–24. doi: 10.18632/oncotarget.23819
12. Zhuang H, Yang ZG, Chen HJ, Peng YL, Li L. Time-Intensity Curve Parameters in Colorectal Tumours Measured Using Double Contrast-Enhanced Ultrasound: Correlations With Tumour Angiogenesis. *Colorectal Dis* (2012) 14:181–7. doi: 10.1111/j.1463-1318.2011.02546.x
13. He P, Miao LY, Ge HY, Wang TL, Ye JX, Meng LM, et al. Preoperative Tumor Staging of Gastric Cancer: Comparison of Double Contrast-Enhanced Ultrasound and Multidetector Computed Tomography. *J Ultrasound Med* (2019) 38:3203–9. doi: 10.1002/jum.15028
14. Li X, Liang H, Luo Q, Wang J. Application Value of CT and Double Contrast-Enhanced Ultrasound in TNM Staging of Gastric Cancer Patients Before Operation. *Acta Med Mediterr* (2020) 36:3479–84. doi: 10.19193/0393-6384_2020_6_549
15. Wang L, Liu Z, Kou H, He H, Zheng B, Zhou L, et al. Double Contrast-Enhanced Ultrasonography in Preoperative T Staging of Gastric Cancer: A Comparison With Endoscopic Ultrasonography. *Front Oncol* (2019) 9:66. doi: 10.3389/fonc.2019.00066
16. Xu L, Wang X, Wu W, Li Y. Diagnostic Accuracy of Double Contrast-Enhanced Ultrasonography in Clarifying Tumor Depth (T Stage) of Gastric

Cancer: Meta-Analysis. *Ultrasound Med Biol* (2021) 47:2483–93. doi: 10.1016/j.ultrasmedbio.2021.05.017
17. Whiting PF, Rutjes AW, Westwood ME, Mallett S, Deeks JJ, Reitsma JB, et al. QUADAS-2: A Revised Tool for the Quality Assessment of Diagnostic Accuracy Studies. *Ann Intern Med* (2011) 155:529–36. doi: 10.7326/0003-4819-155-8-201110180-00009
18. Reitsma JB, Glas AS, Rutjes AW, Scholten RJ, Bossuyt PM, Zwinderman AH. Bivariate Analysis of Sensitivity and Specificity Produces Informative Summary Measures in Diagnostic Reviews. *J Clin Epidemiol* (2005) 58:982–90. doi: 10.1016/j.jclinepi.2005.02.022
19. Walter SD. Properties of the Summary Receiver Operating Characteristic (SROC) Curve for Diagnostic Test Data. *Stat Med* (2002) 21:1237–56. doi: 10.1002/sim.1099
20. Deeks JJ, Macaskill P, Irwig L. The Performance of Tests of Publication Bias and Other Sample Size Effects in Systematic Reviews of Diagnostic Test Accuracy Was Assessed. *J Clin Epidemiol* (2005) 58:882–93. doi: 10.1016/j.jclinepi.2005.01.016
21. Higgins JP, Thompson SG, Deeks JJ, Altman DG. Measuring Inconsistency in Meta-Analyses. *BMJ* (2003) 327:557–60. doi: 10.1136/bmj.327.7414.557
22. Wang J, Li X, Zhang Z, Jing C, Li J. Clinical Research of Combined Application of DCEUS and Dynamic Contrast-Enhanced MSCT in Preoperative cT Staging of Gastric Cancer. *J Oncol* (2021) 2021:9868585. doi: 10.1155/2021/9868585
23. Shen WF, Zhou HL, Li Y. Contrast-Enhanced CT vs Double Contrast-Enhanced Ultrasound for Preoperative Evaluation of T Stage of Gastric Cancer. *World Chin J Digestol* (2020) 28:1042–7. doi: 10.11569/wcjd.v28.i20.1042
24. Li S, Huang P, Wang Z, Chen J, Xu H, Wang L, et al. Preoperative T Staging of Advanced Gastric Cancer Using Double Contrast-Enhanced Ultrasound. *Ultraschall Med* (2012) 33:E218–E24. doi: 10.1055/s-0032-1312958
25. Zheng Z, Yu Y, Lu M, Sun W, Wang F, Li P, et al. Double Contrast-Enhanced Ultrasonography for the Preoperative Evaluation of Gastric Cancer: A Comparison to Endoscopic Ultrasonography With Respect to Histopathology. *Am J Surg* (2011) 202:605–11. doi: 10.1016/j.amjsurg.2010.09.033
26. Chen RJ, Huang PT, Li YP, Zheng ZQ, Zhao YP, Huang FG, et al. Comparison of Preoperative T Staging by Oral Contrast Enhanced Ultrasonography and Double Contrast Enhanced Ultrasonography in Advanced Gastric Carcinoma. *Zhonghua Zhong Liu Za Zhi* (2010) 32:551–4.
27. Okada K, Fujisaki J, Kasuga A, Omae M, Yoshimoto K, Hirasawa T, et al. Endoscopic Ultrasonography Is Valuable for Identifying Early Gastric Cancers Meeting Expanded-Indication Criteria for Endoscopic Submucosal Dissection. *Surg Endosc* (2011) 25:841–8. doi: 10.1007/s00464-010-1279-4
28. Borgstein ABJ, van Berge Henegouwen MI, Lameris W, Eshuis WJ, Gisbertz SS, Dutch Upper GICA. Staging Laparoscopy in Gastric Cancer Surgery. A Population-Based Cohort Study in Patients Undergoing Gastrectomy With Curative Intent. *Eur J Surg Oncol* (2021) 47:1441–8. doi: 10.1016/j.ejso.2020.11.011
29. Wang ZL, Li YL, Tang L, Li XT, Bu ZD, Sun YS. Utility of the Gastric Window in Computed Tomography for Differentiation of Early Gastric Cancer (T1 Stage) From Muscularis Involvement (T2 Stage). *Abdom Radiol (NY)* (2021) 46:1478–86. doi: 10.1007/s00261-020-02785-z
30. Bai L, Liu W, Di S, Xu C. Clinical Study of CT Enhanced Scan in Preoperative TNM Staging of Advanced Gastric Cancer and the Effect of Misdiagnosis Rate. *Panminerva Med* (2021) 42:1431–40. doi: 10.23736/S0031-0808.21.04372-X
31. Yan C, Bao X, Shentu W, Chen J, Liu C, Ye Q, et al. Preoperative Gross Classification of Gastric Adenocarcinoma: Comparison of Double Contrast-Enhanced Ultrasound and Multi-Detector Row CT. *Ultrasound Med Biol* (2016) 42:1431–40. doi: 10.1016/j.ultrasmedbio.2016.01.030
32. Lee KG, Shin CI, Kim SG, Choi J, Oh SY, Son YG, et al. Can Endoscopic Ultrasonography (EUS) Improve the Accuracy of Clinical T Staging by Computed Tomography (CT) for Gastric Cancer? *Eur J Surg Oncol* (2021) 47:1969–75. doi: 10.1016/j.ejso.2021.02.031
33. *National Comprehensive Cancer Network Clinical Practice Guidelines in Oncology: Gastric Cancer. Version 1* (2021). Available at: https://www.nccn.org/.
34. Spolverato G, Ejaz A, Kim Y, Squires MH, Poultsides GA, Fields RC, et al. Use of Endoscopic Ultrasound in the Preoperative Staging of Gastric Cancer: A Multi-Institutional Study of the US Gastric Cancer Collaborative. *J Am Coll Surg* (2015) 220:48–56. doi: 10.1016/j.jamcollsurg.2014.06.023
35. Cardoso R, Coburn N, Seevaratnam R, Sutradhar R, Lourenco LG, Mahar A, et al. A Systematic Review and Meta-Analysis of the Utility of EUS for Preoperative Staging for Gastric Cancer. *Gastric Cancer* (2012) 15 Suppl 1: S19–26. doi: 10.1007/s10120-011-0115-4
36. Cho JW. The Role of Endosonography in the Staging of Gastrointestinal Cancers. *Clin Endosc* (2015) 48:297–301. doi: 10.5946/ce.2015.48.4.297
37. Li X, Zhu M, Wang Y, Niu Y, Ji M, Li P, et al. Diagnostic Efficacy and Decision-Making Role of Preoperative Endoscopic Ultrasonography in Early Gastric Cancer. *Front Med (Lausanne)* (2021) 8:761295. doi: 10.3389/fmed.2021.761295
38. Wang CL, Yang YM, Cui J, Ouyang H, Wang ZM, Ye HS, et al. Diagnostic Value of Double Contrast-Enhanced Ultrasonography in Preoperative Staging of Gastric Cancer. *Zhonghua Zhong Liu Za Zhi* (2009) 31:701–4.

Conflict of Interest: The authors declare that the research was conducted in the absence of any commercial or financial relationships that could be construed as a potential conflict of interest.

frontiers in Oncology

SYSTEMATIC REVIEW
published: 15 March 2022
doi: 10.3389/fonc.2022.861638

18F-FDG PET Radiomics as Predictor of Treatment Response in Oesophageal Cancer: A Systematic Review and Meta-Analysis

Letizia Deantonio[1,2], Maria Luisa Garo[3], Gaetano Paone[4], Maria Carla Valli[1], Stefano Cappio[5], Davide La Regina[6,2], Marco Cefali[7], Maria Celeste Palmarocchi[7], Alberto Vannelli[8†] and Sara De Dosso[2,7†]*

[1] Radiation Oncology Clinic, Oncology Institute of Southern Switzerland (IOSI), Bellinzona, Switzerland, [2] University of Southern Switzerland, Faculty of Biomedical Sciences, Lugano, Switzerland, [3] Mathsly Research, Brescia, Italy, [4] Clinic for Nuclear Medicine and Molecular Imaging, Imaging Institute of Southern Switzerland, Ente Ospedaliero Cantonale, Bellinzona, Switzerland, [5] Clinic for Radiology, Imaging Institute of Southern Switzerland, Ente Ospedaliero Cantonale, Bellinzona, Switzerland, [6] Department of Surgery, Ente Ospedaliero Cantonale, Bellinzona, Switzerland, [7] Department of Medical Oncology, Oncology Institute of Southern Switzerland (IOSI), Bellinzona, Switzerland, [8] Department of General Surgery, Ospedale Valduce, Como, Italy

OPEN ACCESS

Edited by:
Chen Liu,
Army Medical University, China

Reviewed by:
Xiaoping Yi,
Central South University, China
Chenbin Liu,
Chinese Academy of Medical Sciences and Peking Union Medical College, China

***Correspondence:**
Sara De Dosso
sara.dedosso@eoc.ch

[†]These authors share senior authorship

Specialty section:
This article was submitted to Cancer Imaging and Image-directed Interventions, a section of the journal Frontiers in Oncology

Received: *24 January 2022*
Accepted: *16 February 2022*
Published: *15 March 2022*

Citation:
Deantonio L, Garo ML, Paone G, Valli MC, Cappio S, La Regina D, Cefali M, Palmarocchi MC, Vannelli A and De Dosso S (2022) 18F-FDG PET Radiomics as Predictor of Treatment Response in Oesophageal Cancer: A Systematic Review and Meta-Analysis. Front. Oncol. 12:861638. doi: 10.3389/fonc.2022.861638

The best treatment strategy for oesophageal cancer patients achieving a complete clinical response after neoadjuvant chemoradiation is a burning topic. The available diagnostic tools, such as 18F-FDG PET/CT performed routinely, cannot accurately evaluate the presence or absence of the residual tumour. The emerging field of radiomics may encounter the critical challenge of personalised treatment. Radiomics is based on medical image analysis, executed by extracting information from many image features; it has been shown to provide valuable information for predicting treatment responses in oesophageal cancer. This systematic review with a meta-analysis aims to provide current evidence of 18F-FDG PET-based radiomics in predicting response treatments following neoadjuvant chemoradiotherapy in oesophageal cancer. A comprehensive literature review identified 1160 studies, of which five were finally included in the study. Our findings provided that pooled Area Under the Curve (AUC) of the five selected studies was relatively high at 0.821 (95% CI: 0.737–0.904) and not influenced by the sample size of the studies. Radiomics models exhibited a good performance in predicting pathological complete responses (pCRs). This review further strengthens the great potential of 18F-FDG PET-based radiomics to predict pCRs in oesophageal cancer patients who underwent neoadjuvant chemoradiotherapy. Additionally, our review imparts additional support to prospective studies on 18F-FDG PET radiomics for a tailored treatment strategy of oesophageal cancer patients.

Systematic Review Registration: https://www.crd.york.ac.uk/prospero/, identifier CRD42021274636.

Keywords: oesophageal cancer, radiomics, 18F-FDG PET, complete clinical response, pathological complete response, neoadjuvant chemoradiotherapy

INTRODUCTION

Globally, oesophageal carcinoma is the seventh most frequently diagnosed cancer and sixth leading cause of cancer-related death (1). In 2020, about 604.100 new cases were estimated, resulting in nearly 544.000 deaths (2). To date, neoadjuvant chemoradiotherapy followed by surgery is considered the standard care for patients with resectable locally advanced oesophageal and gastro-oesophageal junction cancer, and 25–42% of patients achieved a pathological complete response (pCR) following such treatment (3, 4). More in detail, between 20 and 30% of patients with adenocarcinoma and 40% with squamous cell histology are expected to achieve a pCR following a multimodal therapy (4)

Despite the survival benefits of this combined approach, oesophagectomy is considered a highly invasive procedure with a significant rate of morbidity and mortality, potentially affecting long-term quality of life. Consequently, the active surveillance strategy in case of clinical complete response (cCR) following chemoradiotherapy is a debatable topic (5–7). This strategy appears appealing and should be based on the risk of relapse, quality of life, and morbidity due to the multimodality treatment approach, along with survival expectancy. Consequently, the reliability of non-operative diagnostic tools, which identify complete clinical response, is crucial. However, one of the practical obstacles in selecting patients for immediate surgery or close observation is poor ability to predict a pCR before surgery with the currently available imaging tools.

On the other hand, persistent disease after chemoradiotherapy is usually associated with poorer long-term prognosis, which may suggest more aggressive and resistant tumour biology requiring an immediate and aggressive surgical approach. The early identification of tumours not responding to chemoradiotherapy is clearly another significant area for future investigation on the optimal timing of the treatment sequence.

Endoscopy/endoscopic ultrasound and 18F-fluorodeoxyglucose positron emission tomography/computed tomography (18F-FDG PET/CT) are the current diagnostic tools for baseline staging as well as the evaluation of treatment responses. Although endoscopy and ultrasound have an accuracy assessment of around 70%, and 18-FDG PET/CT identified a complete response in 71–88% of cases, no current procedure can accurately predict the treatment response (8).

To perform a personalised approach of combined treatment or surveillance after neoadjuvant radiochemotherapy, an accurate patient stratification is the main issue. In this regard, physicians perceive radiomics with great interest, and the opportunity to offer a personalised treatment to our patients seems to be closer than before.

Radiomics involves the automatic extraction of a range of quantitative features from radiologic images (i.e., 18F-FDG PET/CT, CT, and magnetic resonance imaging (MRI)) to arrive at a comprehensive quantification of tumour phenotypes for the prediction of the treatment response and outcome (9). This emerging field is rapidly gaining scientific interest for its potential clinical implications (9–11). In this regard, the concept of precision medicine could be supported by radiomics. Its findings can be applied to individual patients, although the relationship between radiomics and outcomes are derived from populations. Furthermore, radiomics analysis commits to increase accuracy in diagnosis, evaluation of prognosis, and prediction of therapy response (12).

Preliminary data for oesophageal and gastro-oesophageal cancer suggest a potential for radiomics approaches in improving patient stratification for therapy (13).

To date, the published studies are based on several radiologic images (i.e 18F-FDG PET, CT, and MRI) and systematic reviews and meta-analysis based their conclusions on radiomics findings of both morphologic and metabolic diagnostic images (14).

18F-FDG PET-based radiomics seems promising for the management of oesophageal cancer patients concerning the prediction of the treatment response in addition to orienting tailored treatments (15). However, the power of the current 18F-FDG PET/CT radiomics algorithms to predict a pCR in oesophageal cancer in patients who underwent neoadjuvant chemoradiotherapy is an unmet need. The present systematic review and meta-analysis aimed to collect the current evidence of 18F-FDG PET-based radiomics in predicting the response treatment following neoadjuvant chemoradiotherapy in oesophageal cancer. The findings can lead to build future PET-based radiomics prospective trials for predicting pCR in oesophageal and gastro-oesophageal junction cancer.

METHODS

Preferred Reporting Items for Systematic Reviews and Meta-Analysis (PRISMA) guidelines were employed in conducting this study (16). The methodology was previously registered in the International Prospective Register of Systematic Reviews (PROSPERO) database under the protocol number CRD42021274636.

Data Sources and Search Strategy

A comprehensive search strategy, used on PubMed, Scopus, Web of Science, and EMBASE to identify all relevant studies irrespective of language or publication status, was performed until 15 November 2021. Duplicates were manually removed. After a comprehensive selection process, the reference lists of all the identified studies were checked.

PubMed Search Strategy

The search strategy was (Oesophageal OR esophageal OR oesophagogastric OR esophagogastric OR gastro-oesophageal OR gastro-esophageal) AND (cancer OR neoplasia) AND (radiomics OR radiomics features OR radiomic) AND (response OR remission OR outcome OR prognostic OR predictive OR predicting OR prediction)

Inclusion Criteria and Study Selection

Studies were included if they strictly met the following criteria: 1) Patients with oesophageal and gastro-oesophageal cancer who had received neoadjuvant chemoradiation; 2) 18F-FDG PET/CT imaging was performed; 3) Radiomics was used to predict a pCR; 4) Area Under the Curve (AUC) was determined; 5) Any models/algorithm applied to predict the pathological response.

Studies that did not report results in AUC, accuracy, sensitivity, and specificity, lacked proof of validation, or had insufficient detail regarding algorithm development and extraction of diagnostic accuracy were excluded.

Implementation of Search

Two reviewers independently screened the identified articles based on their titles and abstracts (LD and SDD), which were considered in constructing a list of all potentially relevant papers. The full-text versions of potentially eligible studies were assessed against the eligibility criteria. The authors planned to solve disagreements concerning study selection or quality assessment by consensus or discussion with a third member of the review team (AV) and reported this in the final review. However, no disagreement was present, and consequently, the kappa statistic was not determined.

Outcome Measures and Data Extraction

The primary endpoint was set as the highest AUC in the validation set (training set). When external validation was not present, we chose internal validation results. If the internal validation was not reported, the result from the training set was chosen. In the absence of the AUC, the C-index was used.

Two authors (LD and SDD) independently extracted the following information:

1. General study characteristics (authors, year, country)
2. Study population (source of data and sample size)
3. Clinical outcomes (pathological response)
4. Treatment schedule
5. Algorithm used for the outcome prediction
6. Dimensionality reduction methods
7. Results: highest AUC and standard error

If the standard error was not indicated, we determined it through Hanley and McNeil's formula (17). On the other hand, we determine the standard error using the conventional procedure if the standard deviation was reported.

Quality Assessment

Two authors (LD and SDD) assessed the study quality through the Radiomics Quality Score (RQS) (18), ranging from a minimum score of -5 to a maximum score of 36 points.

Risk of Bias

The researchers planned to assess the risk of bias using a funnel plot, however, as the number of studies was lower than 10, we did not report this following the Cochrane Handbook (19).

Data Synthesis

After extracting the highest AUC and Standard Error, the random-effects model was used to calculate the pooled AUC. Heterogeneity was assessed using the Cochrane Q-test and I^2 statistic, where a p-value < 0.05 indicated statistically significant heterogeneity. Accordingly, I^2 scores are divided into the following: moderate heterogeneity (30–60%), substantial heterogeneity (50–90%), or considerable heterogeneity (75–100%). The meta-analysis was executed by MedCalc Statistical Software version 19.2.6 (MedCalc Software bv, Ostend, Belgium; https://www.medcalc.org; 2020).

RESULTS

Study Selection

A flow diagram of the search strategy results is presented in **Figure 1**. After removing 56 duplicates and 953 articles in different medical fields, 151 articles were obtained – all in English, from which 80 studies were excluded after examining their titles and abstracts. Subsequently, 71 studies were selected for full-text reading. Of these, 66 were excluded as they did not match the inclusion criteria or had an overlapping population. Finally, five studies were included in the present systematic review.

Quality Assessment

Radiomics Quality Score (RQS) for each of the five included studies is reported in **Table 1**. RQS ranged between 5 (21) to 16 points (20). None of them reported a phantom study, imaging at multiple time points, biological correlates, cost-effectiveness analysis, nor a prospective study. All studies adequately recorded the feature reduction on adjustment for multiple testing and potential clinical utilities. The remaining items illustrated a strong level of heterogeneity among the selected group.

Review of Type of Radiomics Feature and Other Features in Selected Studies

According to the International Symposium on Biomedical Imaging (ISBI) standards, the radiomics features are divided

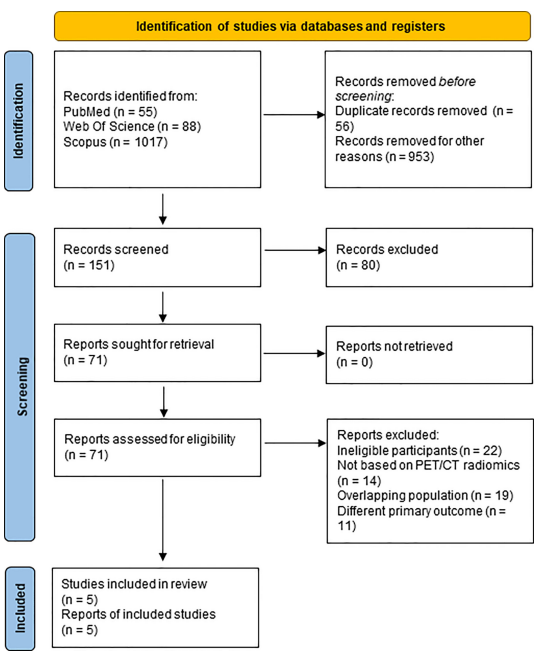

FIGURE 1 | PRISMA Flow-chart.

TABLE 1 | Quality assessment – Radiomics Quality Score (RQS).

Criteria/Study	van Rossum, 2016 (20)	Yip, 2016 (21)	Beukinga, 2017 (22)	Rishi, 2020 (23)	Murakami, 2021 (24)
Image protocol quality	1	1	2	2	0
Multiple segmentation	1	0	1	1	1
Phantom study	0	0	0	0	0
Imaging at multiple time points	0	0	0	0	0
Feature reduction on adjustment for multiple testing	3	3	3	3	3
Multivariable analysis	1	0	1	0	0
Biological correlates	0	0	0	0	0
Cut-off analysis	0	1	0	1	1
Discrimination statistics	2	1	2	2	2
Calibration statistics	2	0	2	0	0
Prospective study	0	0	0	0	0
Validation	2	-5	2	-5	2
Comparison to 'gold standard'	2	2	0	2	0
Potential clinical utility	2	2	2	2	2
Cost-effectiveness analysis	0	0	0	0	0
Opens science and data	0	0	0	0	3
Total Score (max 36 points)	**16**	**5**	**15**	**8**	**14**

into morphology class (e.g., shape-based), first-order class (e.g., histogram-based), and second-order class (e.g., texture-based).

One study used the morphology class feature (20) while three studies employed (21, 22, 24) the second-order class including different grey-level matrix (i.e., grey-level run-length matrix, grey-level co-occurrence matrix, grey-level size-zone matrix, grey-level dependence matrix); lastly, Rishi et al. (23) used both the first-order (i.e., intensity and shape) and second-order classes.

Four out of five studies used features selection methods for dimensionality reduction (19–22), while the fifth study identified six textures according to clinical values in prognostic and treatment response assessment after extracting textural features through complex mathematical models (18).

Among studies that adopted features selection methods, three adopted wrapper methods (20–22). In particular, Beukinga et al., after pre-selecting 144 of the 147 features, identified, through a univariable logistic regression analysis, 24 significant variables, subsequently used to develop six different models (21). Murakami et al. starting from 4250 features and adding 22 more features selected through the LASSO analysis and one chosen from the original image features, compared performances of five neural network models generated in 5-fold cross-validation steps (20). Rishi et al. determined the predictive model after building and validating four models using leave-one-out cross-validation on a total of 126 features and some composite features (22). Instead, Van Rossum et al., after using a univariable analysis from which many potential predictors were identified, used a filter approach based on a standardized pre-selection variables method according to the following three inclusion rules: (1) variables with $p \leq 0.25$ in the univariable analysis; (2) variable with the lowest p-value in case of highly correlated pairs of variables; (3) features with an ICC ≤ 0.70 in the test-retest analysis.

Study Characteristics

The authors provided a descriptive summary of the characteristics of the studies in **Table 2**.

We included a total of five studies: three carried out in the USA (20, 21, 23), one in the Netherlands (22), and one in Japan (24).

One study included more than 200 patients (20), whereas four studies had less than 100 patients (21–24).

Altogether, 534 patients were included in this study (458 males and 76 females). The patients' median age ranged between 35 years (24) and more than 80 years (23). Two of the selected papers did not report the patients' histology, while the other three were primarily focused on adenocarcinoma patients (20–22).

All patients were treated with external beam radiation therapy and concurrent chemotherapy. A total radiation dose ranging from 40 to 50.4 Gy was delivered in daily fractions of 1.8–2Gy. Among the 534 patients analysed in the 5 studies, in the vast majority of cases RT was delivered with three-dimensional conformal radiation therapy (3D-CRT) and intensity-modulated radiation therapy (IMRT) (18–22), in a minority of cases (12%) proton therapy was performed (19). Concomitant chemotherapy generally consisted of a platinum compound with fluoropyrimidine or taxane.

Meta-Analysis

The pooled AUC for the five studies was 0.821 (95% CI: 0.737–0.904), according to the results from **Table 3** and **Figure 2A**. The I^2 was 96.46% (95% CI: 94.00–97.92%) (Cochrane Q = 113.09, $p < 0.0001$), displaying a substantial heterogeneity among studies. After excluding the small studies (e.g., studies with less than 70 patients), AUC was 0.829 (95% CI: 0.719–0.938) (**Figure 2B**). The sensitivity analysis (fixed-effect model) depicted no significant differences from the previously reported results.

DISCUSSION

To the best of our knowledge, this is the first meta-analysis exclusively analysing the power of 18F-FDG PET-based radiomics

TABLE 2 | Studies' Characteristics.

Author	Country	Data Source	Patients	Gender (Females/ Males)	Age	Histology	Localisation	nCRT	Training Set	External Validation	Highest AUC	SE	Pathological response	Model
van Rossum (20**) (2016)**	USA	Single-institution	217	15/202	PathCR: 58.8 ± 12.3; No pathCR: 60.1 ± 9.9	AC	Middle third: 3; Distal third: 195; GEJ: 19	45-50.4 Gy + 5FU with either a platinum compound or taxane	217	No	0.77	0.030	CR = 59 No CR = 158	Multivariable Logistic regression with stepwise backward elimination
Yip (21) **(2016)**	USA	Single-institution	54	10/44	65 yr	AC: 50; SCC: 4	NR	45-50.4 Gy + a platinum compound with either 5FU or taxane	45	No	0.65	0.100	CR=8 No CR = 37	Kaplan – Meier with the log-rank test
Beukinga (22) **(2017)**	Netherland	Single-institution database	97	15/82	< 70 yr: 78; ≥ 70 yr: 19	AC: 88; SCC: 9	Mid: 4; Distal: 62; GEJ: 31	41.4 Gy + carboplatin /paclitaxel	97	No	0.74	0.050	CR: 19 – No CR: 78	Logistic regression with LASSO
Rishi (23) **(2020)**	USA	Single Institution	68	21/47	65.3 yr (43–82)	NR	Upper: 3; Mid: 7; Distal: 34; GEJ: 24	45-56Gy+ 5FU and cisplatin	68	No	0.87	0.010	CR: 34	Kaplan- Meier
Murakami (24) **(2021)**	Japan	NR	98	15/83	66 yr (35–78)	NR	Upper: 22; Middle: 46; Lower GEJ: 30	40Gy + 5FU and cisplatin	98	Yes	0.95	0.004	CR: 44	Neural Network Classifier

CR, complete response; AC, Adenocarcinoma; SCC, Squamous Cell Carcinoma; nCRT, neoadjuvant chemoradiotherapy.

to predict the pCR after neoadjuvant chemoradiotherapy in oesophageal and gastro-oesophageal junction cancer.

In oesophageal cancer, 18F-FDG PET/CT is part of the initial work-up improving the accuracy of the clinical staging and better assessing distant metastatic disease and is frequently incorporated into radiotherapy planning (25). Moreover, the prognostic value of 18-F-FDG PET in assessing pCR after neoadjuvant radiochemotherapy showed contrasting results (26). To predict treatment outcome is crucial in oesophageal and gastro-oesophageal junction cancer in order to select patients more likely to escalate or de-escalate therapy. Radiomics is an appealing field of research and is deeply under investigation.

Radiomics is an advanced method to extract imaging features and thereby quantify tumour phenotype from medical images (16). Using radiomics, a single medical image shows more information, and extraction and analysis of hundreds of imaging features can be obtained. In general, radiomics features are classified into morphological features (size and shape), first-, second-, and higher-order textures. As reported by Gillies et al., first-order statistics describe the distribution of values of individual voxels without concern for spatial relationships and are generally histogram-based methods. Second-order statistical descriptors generally are described as "texture" features and provide a measure of intratumoral heterogeneity. Higher-order statistical methods impose filter grids on the image to extract repetitive or non-repetitive patterns (12).

Among them, texture analyses depicting and objectively quantifying tumour heterogeneity seem to be of great interest in order to identify potentially responders and non-responders (9, 18). Moreover, these imaging features can be used in predictive modelling alone or with other patient-related data (e.g. clinical data, pathological data, and genomic data). This could lead to tailored and potentially most effective treatment for each patient (12, 18).

In this regard, among the studies here analysed only one reported the influence of clinical parameters on the probability of pCR. In particular, smaller tumour length based on endoscopic

TABLE 3 | Summary Table Meta-Analysis.

Study	ROC Area	Standard Error	95% CI	z	P	Weight (%)	
						Fixed	Random
van Rossum (2016) (20)	0.770	0.030	0.711 to 0.829			1.21	22.02
Yip (2016) (21)	0.650	0.100	0.454 to 0.846			0.11	10.51
Beukinga (2017) (22)	0.740	0.050	0.642 to 0.838			0.44	18.46
Rishi (2020) (23)	0.870	0.0100	0.850 to 0.890			10.92	24.36
Murakami (2021) (24)	0.950	0.0035	0.943 to 0.957			87.33	24.65
Total (fixed effects)	0.938	0.0033	0.931 to 0.944	283.859	<0.001	100.00	100.00
Total (random effects)	0.821	0.0428	0.737 to 0.904	19.186	<0.001	100.00	100.00

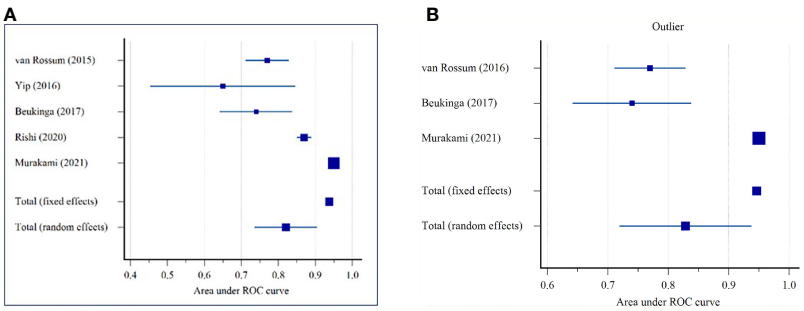

FIGURE 2 | Forest plot for the area under the receiver operating characteristics (ROC) curve for predicting the pathological response in patients with oesophageal cancer: **(A)** All Sample (n = 5 studies); **(B)** Without small studies (n = 3 studies).

ultrasound and lower T stage (i.e. T2 *vs* T3) and negative post-treatment endoscopic biopsy significantly influence the probability of pCR (19).

Moving to our meta-analysis, our findings provided that the pooled AUC of the five selected studies was quite high at 0.821 (95% CI: 0.737–0.904) and not influenced by the studies' sample size. Moreover, the I^2 score was 96.46% (95% CI: 94.00–97.92%, $p < 0.0001$). Thus, substantial heterogeneity existed among the studies: this is explained by different image scanners and imaging elaboration, which influenced radiomics features (27).

The dissected studies' RQS ranged from 5 (21) to 16 (20) – considered a poor-quality level because some items are not present. Although RQS is widely used in the quality assessment of radiomics studies, the low methodological quality is their main limit and comparable to most systematic reviews in other tumour sites (15, 28, 29). Although the quality was not always as desired, all studies included in this analysis deliver the most complete overview of the existing literature.

Overall, none of the analysed studies performed a cost-effectiveness analysis; they were not prospective, did not perform a phantom study or imaging at multiple time points, or had a biological correlation. Similarly, in a recent systematic review on nasopharyngeal tumours using MRI radiomics features, none of the included studies executed neither a phantom study nor a cost-effectiveness analysis (28). Conversely, all the studies addressed their potential clinical utility and used a feature reduction or adjustment for multiple testing. In a recent meta-analysis of renal cancer, most of the 57 studies reported a potential clinical utility, and only 51% employed a feature reduction (30).

In the future, the RQS principles should be considered before planning radiomics studies to ensure satisfactory quality. Although a high- or low-quality range was not stated in the RQS guidelines (18), a cut-off score of 30% should be planned as suggested by Wesdorp et al. (14).

Among the five studies included in our analysis, three enrolled a majority of adenocarcinoma 335/368 (20–22), while the remaining two (23, 24) did not report the histology of their 166 patients. Therefore, due to this heterogeneity, a stratification for histology (adenocarcinoma *vs.* squamous cell cancer) could not be performed in the present meta-analysis.

Neoadjuvant chemoradiotherapy followed by surgery is a well-established approach in oesophageal squamous cell carcinoma and gastro-oesophageal adenocarcinoma (4, 31), while definitive chemoradiotherapy is often preferred in cervical oesophageal cancer (32). The tide of active surveillance in cervical oesophageal cancer was also applied to thoracic oesophageal squamous cell carcinoma, providing a salvage surgery for persistent or recurrence disease (7, 33). This approach is also currently under investigation in gastro-oesophageal adenocarcinoma (5, 6). Future radiomics studies stratifying patients between squamous cell tumours and adenocarcinoma could be of great interest and grant further evidence for choosing optimal care.

The articles included in this review suggest that first- and second-order features contributed to the response assessment, predominantly in predicting pCR. Tumours with low heterogeneity were more likely to reach a pCR. In detail, van Rossum et al. developed a prediction model adding four comprehensive 18F-FDG PET texture/geometry features (i.e., baseline cluster shade, change in run percentage, change in co-occurrence matrix entropy, and post-radiation roundness) and improved the AUC to 0.77 instead of the 0.67 obtained with clinical models (20). A tumour exhibiting a heterogeneous 18F-FDG PET distribution – baseline cluster shade – was less likely to reach pCR in their analysis on 217 oesophageal adenocarcinoma cancer patients (19). Beukinga et al. depicted a model that combined the clinical T-stage and 18F-FDG PET-derived textural feature long run low gray-level emphasis. After internal validation, the model provided high accuracy in predicting pCR with an AUC score of 0.74 (22). However, both authors concluded that their results did not translate into a clinically relevant benefit. In Yip et al., the change in the run-length and size-zone matrix textures significantly differentiated non-responders from partial and complete responders (AUC = 0.65) (21).

More recently, Murakami et al. constructed a predictive model with a good AUC score of 0.95, extracting 22 second-order radiomics features (24). Lastly, Rishi et al. illustrated that a composite model (based on PET and CT) improved pCR predicting power with an AUC score of 0.87 (23).

As reported in literature and in our findings, tumour heterogeneity seems to have impact on tumour response, since

tumours with greater intratumoral heterogeneity are often assumed to have an aggressive biology (34). However, these results are not definitive due to the lack of standardized methodology in extracting and analysing radiomics features. Among the studies here analysed, Beukinga et al. showed that the most predictive textural features were LRLGLe-PET and RP-CT. Both were higher in complete responders, corresponding to homogeneous 18F-FDG uptake. A possible explanation of homogeneity and heterogeneity is hypoxia and necrosis (21).

Overall, radiomics features could objectively and quantitatively describe distinctive tumour "radio-phenotypes". In future, all these radio-phenotypes could potentially substitute a "real biopsy" and explain treatment sensibility or resistance describing and identifying metabolic activity, proliferation grade, angiogenesis as well as genomic stability or instability (22).

Remarkably, we discovered that the pooled AUC after excluding two small studies with less than 70 patients remains pretty high at 0.829 (95% CI: 0.719–0.938). A recent review underlined the relevance of the sample size to allow high dimensional models and machine learning approaches to be statistically robust considering an adequate cut-off > 100 or > 200 patients. The performance of the existing algorithm would be applied to new large datasets (35). In the present review, one study enrolled more than 200 patients (20), whereas two approached 100 (22, 24).

A machine-learning algorithm was used in four out of the five studies (20, 22–24). In the last few years, the machine learning approach has been widely used. Interestingly, the most recent study by Murakami et al. used a neural network classifier to construct their prediction model (24). Deep learning is a subfield of machine learning, rapidly gaining interest among the radiation-oncology community; it may offer a better model complexity; however, the published literature on tumour response prediction is relatively scarce and requires a much larger sample size (15, 36).

Despite the encouraging findings of the present meta-analysis in using 18F-FDG PET/CT radiomics to predict treatment responses in oesophageal cancer, some limits should be underlined. First, few studies were included; thus, publication bias analysis was not performed because it was not appropriate. Second, all included studies were retrospective and performed in a monocentric setting. Third, demographic heterogeneities were observed among studies due to different race ethnicity. Furthermore, they used different PET scanners, and the selection of the features was based on different methodologies, distinct methods of tumour volume segmentation (manual delineation and semi-automatic segmentation), and often on differing in-house software. An additional limitation of these studies is that their authors focused on different feature sets, and the data analysis and interpretation were based on several approaches. Moreover, only one study (19) reported clinical characteristics between pCR and non pCR groups. Lastly, they differed in treatment schedules in terms of radiation dose and chemotherapy schedule. Among the five studies, only Beukinga et al. analysed patients who underwent the CROSS schedule, considered the standard of care in a neoadjuvant setting (21).

Based on these results, we conclude that 18F-FDG PET/CT-based radiomics images have a high accuracy in predicting pCR to neoadjuvant chemoradiotherapy. Overall, the main concern is reaching higher data quality in oesophageal and gastro-oesophageal junction cancer. Next step is to plan studies incorporating quality control. Future research should focus on developing predictive models, through well-designed and appropriately powered prospective studies, with the aim to complement the current clinical findings with radiomics, and further stratify and personalise oncologic treatment.

DATA AVAILABILITY STATEMENT

The original contributions presented in the study are included in the article/supplementary material. Further inquiries can be directed to the corresponding author.

AUTHOR CONTRIBUTIONS

LD, MG, and SD contributed to conception and design of the study. MG performed the statistical analysis. LD and MG wrote the first draft of the manuscript. SD and AV wrote the discussion. GP and SC helped collect literature and participated in discussions. DL, MV, DLR, MC, and MCP examined and verified the results. All authors read and approved the final manuscript.

REFERENCES

1. Uhlenhopp DJ, Then EO, Sunkara T, Gaduputi V. Epidemiology of Esophageal Cancer: Update in Global Trends, Etiology and Risk Factors. *Clin J Gastroenterol* (2020) 13(6):1010–21. doi: 10.1007/s12328-020-01237-x
2. Sung H, Ferlay J, Siegel RL, Laversanne M, Soerjomataram I, Jemal A, et al. Global Cancer Statistics 2020: GLOBOCAN Estimates of Incidence and Mortality Worldwide for 36 Cancers in 185 Countries. *CA Cancer J Clin* (2021) 71(3):209–49. doi: 10.3322/caac.21660
3. Shapiro J, van Lanschot JJB, Hulshof M, van Hagen P, van Berge Henegouwen MI, Wijnhoven BPL, et al. Neoadjuvant Chemoradiotherapy Plus Surgery Versus Surgery Alone for Oesophageal or Junctional Cancer (CROSS): Long-Term Results of a Randomised Controlled Trial. *Lancet Oncol* (2015) 16 (9):1090–8. doi: 10.1016/S1470-2045(15)00040-6
4. van Hagen P, Hulshof MC, van Lanschot JJ, Steyerberg EW, van Berge Henegouwen MI, Wijnhoven BP, et al. Preoperative Chemoradiotherapy for Esophageal or Junctional Cancer. *N Engl J Med* (2012) 366(22):2074–84. doi: 10.1056/NEJMoa1112088
5. Ito Y, Takeuchi H, Ogawa G, Kato K, Onozawa M, Minashi K, et al. Final Analysis of Single-Arm Confirmatory Study of Definitive Chemoradiotherapy Including Salvage Treatment in Patients With Clinical Stage II/III Esophageal Carcinoma: JCOG0909. *J Clin Oncol* (2020) 38(15_suppl):4545–. doi: 10.1200/JCO.2020.38.15_suppl.4545
6. Dijon C. Comparison of Systematic Surgery Versus Surveillance and Rescue Surgery in Operable Oesophageal Cancer With a Complete Clinical Response to

Radiochemotherapy (Esostrate). *ClinicalTrials.gov* (2015) ClinicalTrials.gov Identifier: NCT02551458.
7. Markar S, Gronnier C, Duhamel A, Pasquer A, Thereaux J, du Rieu MC, et al. Salvage Surgery After Chemoradiotherapy in the Management of Esophageal Cancer: Is It a Viable Therapeutic Option? *J Clin Oncol* (2015) 33(33):3866–73. doi: 10.1200/JCO.2014.59.9092
8. Semenkovich TR, Meyers BF. Surveillance Versus Esophagectomy in Esophageal Cancer Patients With a Clinical Complete Response After Induction Chemoradiation. *Ann Transl Med* (2018) 6(4):81. doi: 10.21037/atm.2018.01.31
9. Traverso A, Wee L, Dekker A, Gillies R. Repeatability and Reproducibility of Radiomic Features: A Systematic Review. *Int J Radiat Oncol Biol Phys* (2018) 102(4):1143–58. doi: 10.1016/j.ijrobp.2018.05.053
10. Alfieri S, Romano R, Bologna M, Calareso G, Corino V, Mirabile A, et al. Prognostic Role of Pre-Treatment Magnetic Resonance Imaging (MRI)-Based Radiomic Analysis in Effectively Cured Head and Neck Squamous Cell Carcinoma (HNSCC) Patients. *Acta Oncol* (2021) 60(9):1192–200. doi: 10.1080/0284186X.2021.1924401
11. Bosetti DG, Ruinelli L, Piliero MA, van der Gaag LC, Pesce GA, Valli M, et al. Cone-Beam Computed Tomography-Based Radiomics in Prostate Cancer: A Mono-Institutional Study. *Strahlenther Onkol* (2020) 196(10):943–51. doi: 10.1007/s00066-020-01677-x
12. Gillies RJ, Kinahan PE, Hricak H. Radiomics: Images Are More Than Pictures, They Are Data. *Radiology* (2016) 278(2):563–77. doi: 10.1148/radiol.2015151169
13. Sah BR, Owczarczyk K, Siddique M, Cook GJR, Goh V. Radiomics in Esophageal and Gastric Cancer. *Abdom Radiol (NY)* (2019) 44(6):2048–58. doi: 10.1007/s00261-018-1724-8
14. Wesdorp NJ, Hellingman T, Jansma EP, van Waesberghe JTM, Boellaard R, Punt CJA, et al. Advanced Analytics and Artificial Intelligence in Gastrointestinal Cancer: A Systematic Review of Radiomics Predicting Response to Treatment. *Eur J Nucl Med Mol Imaging* (2021) 48(6):1785–94. doi: 10.1007/s00259-020-05142-w
15. Kao YS, Hsu Y. A Meta-Analysis for Using Radiomics to Predict Complete Pathological Response in Esophageal Cancer Patients Receiving Neoadjuvant Chemoradiation. *In Vivo* (2021) 35(3):1857–63. doi: 10.21873/invivo.12448
16. Moher D, Liberati A, Tetzlaff J, Altman DG, Group P. Preferred Reporting Items for Systematic Reviews and Meta-Analyses: The PRISMA Statement. *PloS Med* (2009) 6(7):e1000097. doi: 10.1371/journal.pmed.1000097
17. Hanley JA, McNeil BJ. The Meaning and Use of the Area Under a Receiver Operating Characteristic (ROC) Curve. *Radiology* (1982) 143(1):29–36. doi: 10.1148/radiology.143.1.7063747
18. Lambin P, Leijenaar RTH, Deist TM, Peerlings J, de Jong EEC, van Timmeren J, et al. Radiomics: The Bridge Between Medical Imaging and Personalized Medicine. *Nat Rev Clin Oncol* (2017) 14(12):749–62. doi: 10.1038/nrclinonc.2017.141
19. Page HJ, Higgins JPT, Sterne JAC. Chapter 13: Assessing Risk of Bias Due to Missing Results in a Synthesis. In: Higgins JPT, Thomas J, Chandler J, Cumpston M, Li T, Page MJ, Welch VA (editors). *Cochrane Handbook for Systematic Reviews of Interventions version 6.3 (updated February 2022)*. Cochrane (2022). Available from www.training.cochrane.org/handbook
20. van Rossum PS, Fried DV, Zhang L, Hofstetter WL, van Vulpen M, Meijer GJ, et al. The Incremental Value of Subjective and Quantitative Assessment of 18F-FDG PET for the Prediction of Pathologic Complete Response to Preoperative Chemoradiotherapy in Esophageal Cancer. *J Nucl Med* (2016) 57(5):691–700. doi: 10.2967/jnumed.115.163766
21. Yip SS, Coroller TP, Sanford NN, Mamon H, Aerts HJ, Berbeco RI. Relationship Between the Temporal Changes in Positron-Emission-Tomography-Imaging-Based Textural Features and Pathologic Response and Survival in Esophageal Cancer Patients. *Front Oncol* (2016) 6:72. doi: 10.3389/fonc.2016.00072
22. Beukinga RJ, Hulshoff JB, van Dijk LV, Muijs CT, Burgerhof JGM, Kats-Ugurlu G, et al. Predicting Response to Neoadjuvant Chemoradiotherapy in Esophageal Cancer With Textural Features Derived From Pretreatment (18)F-FDG PET/CT Imaging. *J Nucl Med* (2017) 58(5):723–9. doi: 10.2967/jnumed.116.180299
23. Rishi A, Zhang GG, Yuan Z, Sim AJ, Song EY, Moros EG, et al. Pretreatment CT and (18) F-FDG PET-Based Radiomic Model Predicting Pathological Complete Response and Loco-Regional Control Following Neoadjuvant Chemoradiation in Oesophageal Cancer. *J Med Imaging Radiat Oncol* (2021) 65(1):102–11. doi: 10.1111/1754-9485.13128
24. Murakami Y, Kawahara D, Tani S, Kubo K, Katsuta T, Imano N, et al. Predicting the Local Response of Esophageal Squamous Cell Carcinoma to Neoadjuvant Chemoradiotherapy by Radiomics With a Machine Learning Method Using (18)F-FDG PET Images. *Diagn (Basel)* (2021) 11(6):1049. doi: 10.3390/diagnostics11061049
25. Chatterton BE, Ho Shon I, Baldey A, Lenzo N, Patrikeos A, Kelley B, et al. Positron Emission Tomography Changes Management and Prognostic Stratification in Patients With Oesophageal Cancer: Results of a Multicentre Prospective Study. *Eur J Nucl Med Mol Imaging* (2009) 36(3):354–61. doi: 10.1007/s00259-008-0959-y
26. Duong CP, Hicks RJ, Weih L, Drummond E, Leong T, Michael M, et al. FDG-PET Status Following Chemoradiotherapy Provides High Management Impact and Powerful Prognostic Stratification in Oesophageal Cancer. *Eur J Nucl Med Mol Imaging* (2006) 33(7):770–8. doi: 10.1007/s00259-005-0040-z
27. Park CM. Can Artificial Intelligence Fix the Reproducibility Problem of Radiomics? *Radiology* (2019) 292(2):374–5. doi: 10.1148/radiol.2019191154
28. Spadarella G, Calareso G, Garanzini E, Ugga L, Cuocolo A, Cuocolo R. MRI Based Radiomics in Nasopharyngeal Cancer: Systematic Review and Perspectives Using Radiomic Quality Score (RQS) Assessment. *Eur J Radiol* (2021) 140:109744. doi: 10.1016/j.ejrad.2021.109744
29. Staal FCR, van der Reijd DJ, Taghavi M, Lambregts DMJ, Beets-Tan RGH, Maas M. Radiomics for the Prediction of Treatment Outcome and Survival in Patients With Colorectal Cancer: A Systematic Review. *Clin Colorectal Cancer* (2021) 20(1):52–71. doi: 10.1016/j.clcc.2020.11.001
30. Ursprung S, Beer L, Bruining A, Woitek R, Stewart GD, Gallagher FA, et al. Radiomics of Computed Tomography and Magnetic Resonance Imaging in Renal Cell Carcinoma-a Systematic Review and Meta-Analysis. *Eur Radiol* (2020) 30(6):3558–66. doi: 10.1007/s00330-020-06666-3
31. Lordick F, Mariette C, Haustermans K, Obermannova R, Arnold D, Committee EG. Oesophageal Cancer: ESMO Clinical Practice Guidelines for Diagnosis, Treatment and Follow-Up. *Ann Oncol* (2016) 27(suppl 5):v50–v7. doi: 10.1093/annonc/mdw329
32. Cao J, Zhang S. Multiple Comparison Procedures. *JAMA* (2014) 312(5):543–4. doi: 10.1001/jama.2014.9440
33. Bedenne L, Michel P, Bouche O, Milan C, Mariette C, Conroy T, et al. Chemoradiation Followed by Surgery Compared With Chemoradiation Alone in Squamous Cancer of the Esophagus: FFCD 9102. *J Clin Oncol* (2007) 25 (10):1160–8. doi: 10.1200/JCO.2005.04.7118
34. Morris LG, Riaz N, Desrichard A, Senbabaoglu Y, Hakimi AA, Makarov V, et al. Pan-Cancer Analysis of Intratumor Heterogeneity as a Prognostic Determinant of Survival. *Oncotarget* (2016) 7(9):10051–63. doi: 10.18632/oncotarget.7067
35. Dercle L, Lu L, Schwartz LH, Qian M, Tejpar S, Eggleton P, et al. Radiomics Response Signature for Identification of Metastatic Colorectal Cancer Sensitive to Therapies Targeting EGFR Pathway. *J Natl Cancer Inst* (2020) 112(9):902–12. doi: 10.1093/jnci/djaa017
36. Appelt AL, Elhaminia B, Gooya A, Gilbert A, Nix M. Deep Learning for Radiotherapy Outcome Prediction Using Dose Data - A Review. *Clin Oncol (R Coll Radiol)* (2022) 34(2):e87–e96. doi: 10.1016/j.clon.2021.12.002

Conflict of Interest: The authors declare that the research was conducted in the absence of any commercial or financial relationships that could be construed as a potential conflict of interest.

frontiers in Oncology

ORIGINAL RESEARCH
published: 29 March 2022
doi: 10.3389/fonc.2022.841460

Quantitative Dynamic-Enhanced MRI and Intravoxel Incoherent Motion Diffusion–Weighted Imaging for Prediction of the Pathological Response to Neoadjuvant Chemotherapy and the Prognosis in Locally Advanced Gastric Cancer

*Yongjian Zhu[1], Zhichao Jiang[2], Bingzhi Wang[3], Ying Li[1], Jun Jiang[1], Yuxin Zhong[4], Sicong Wang[5] and Liming Jiang[1]**

[1] Department of Diagnostic Radiology, National Cancer Center/National Clinical Research Center for Cancer/Cancer Hospital, Chinese Academy of Medical Sciences and Peking Union Medical College, Beijing, China, [2] Department of Medical Oncology, National Cancer Center/National Clinical Research Center for Cancer/Cancer Hospital, Chinese Academy of Medical Sciences and Peking Union Medical College, Beijing, China, [3] Department of Pathology, National Cancer Center/National Clinical Research Center for Cancer/Cancer Hospital, Chinese Academy of Medical Sciences and Peking Union Medical College, Beijing, China, [4] Department of Pancreatic and Gastric Surgery, National Cancer Center/National Clinical Research Center for Cancer/Cancer Hospital, Chinese Academy of Medical Sciences and Peking Union Medical College, Beijing, China, [5] Pharmaceutical Diagnostic Team, GE Healthcare, Life Sciences, Beijing, China

Background: This study aimed to explore the predictive value of quantitative dynamic contrast-enhanced MRI (DCE-MRI) and intravoxel incoherent motion diffusion-weighted imaging (IVIM-DWI) quantitative parameters for the response to neoadjuvant chemotherapy (NCT) in locally advanced gastric cancer (LAGC) patients, and the relationship between the prediction results and patients' prognosis, so as to provide a basis for clinical individualized precision treatment.

Methods: One hundred twenty-nine newly diagnosed LAGC patients who underwent IVIM-DWI and DCE-MRI pretreatment were enrolled in this study. Pathological tumor regression grade (TRG) served as the reference standard of NCT response evaluation. The differences in DCE-MRI and IVIM-DWI parameters between pathological responders (pR) and pathological non-responders (pNR) groups were analyzed. Univariate and multivariate logistic regressions were used to identify independent predictive parameters for NCT response. Prediction models were built with statistically significant quantitative parameters and their combinations. The performance of these quantitative parameters and models was evaluated using receiver operating characteristic (ROC) analysis. Clinicopathological variables, DCE-MRI and IVIM-DWI derived parameters, as well as the prediction model were analyzed in relation to 2-year recurrence-free survival

OPEN ACCESS

Edited by:
Berardino De Bari,
Hospital Neuchâtelois, Switzerland

Reviewed by:
Nguyen Minh Duc,
Pham Ngoc Thach University of Medicine, Vietnam
Luciana Caravatta,
SS Annunziata Polyclinic Hospital, Chieti, Italy
Carlos Perez-Torres,
Virginia Tech, United States

***Correspondence:**
Liming Jiang
dr_jiangliming@126.com

Specialty section:
This article was submitted to Cancer Imaging and Image-directed Interventions, a section of the journal Frontiers in Oncology

Received: 22 December 2021
Accepted: 28 February 2022
Published: 29 March 2022

Citation:
Zhu Y, Jiang Z, Wang B, Li Y, Jiang J, Zhong Y, Wang S and Jiang L (2022) Quantitative Dynamic-Enhanced MRI and Intravoxel Incoherent Motion Diffusion–Weighted Imaging for Prediction of the Pathological Response to Neoadjuvant Chemotherapy and the Prognosis in Locally Advanced Gastric Cancer. Front. Oncol. 12:841460. doi: 10.3389/fonc.2022.841460

(RFS) by using Cox proportional hazards model. RFS was compared using the Kaplan–Meier method and the log-rank test.

Results: Sixty-nine patients were classified as pR and 60 were pNR. K^{trans}, k_{ep}, and v_e values in the pR group were significantly higher, while $ADC_{standard}$ and D values were significantly lower than those in the pNR group. Multivariate logistic regression analysis demonstrated that K^{trans}, k_{ep}, v_e, and D values were independent predictors for NCT response. The combined predictive model, which consisted of DCE-MRI and IVIM-DWI, showed the best prediction performance with an area under the curve (AUC) of 0.922. Multivariate Cox regression analysis showed that ypStage III and NCT response predicted by the IVIM-DWI model were independent predictors of poor RFS. The IVIM-DWI model could significantly stratify median RFS (52 vs. 15 months) and 2-year RFS rate (72.3% vs. 21.8%) of LAGC.

Conclusion: Pretreatment DCE-MRI quantitative parameters K^{trans}, k_{ep}, v_e, and IVIM-DWI parameter D value were independent predictors of NCT response for LAGC patients. The regression model based on baseline DCE-MRI, IVIM-DWI, and their combination could help RFS stratification of LAGC patients.

Keywords: gastric cancer, neoadjuvant chemotherapy, magnetic resonance imaging, intravoxel incoherent motion diffusion-weighted imaging, dynamic contrast-enhanced magnetic resonance imaging, tumor regression grade, response prediction, prognosis

INTRODUCTION

Gastric cancer (GC) represents the fifth most frequent cancer worldwide with 1,089,103 new cases (5.6%) and the fourth leading cause of cancer-related death (7.7%) with 768,793 deaths each year in 2020, according to global cancer statistics (1). In particular, gastric cancer has a high incidence in East Asia, which accounts for about 60% newly diagnosed cases worldwide (1, 2).

In China, about 70%–80% of GC patients were staged as locally advanced gastric cancer (LAGC) at the time of diagnosis (3), which was defined as a tumor invading the muscularis propria or deeper layer of the gastric wall without distant metastasis, often with a high rate of lymph node metastasis and poor clinical prognosis. The current treatment strategy for LAGC includes radical surgical resection through a multidisciplinary team (MDT) discussion, but the recurrence rate after radical resection is still up to 40%–60%, and the overall 5-year survival rate is only 20%–40% (4, 5). Several large international clinical trials (MAGIC and FFCD trials) showed that neoadjuvant chemotherapy (NCT) could significantly improve the R0 resection rate of LAGC patients, and the 5-year overall survival (OS) rate could be increased 10%–15% compared with the surgery alone group (6). NCT has been recognized as the standard treatment strategy for LAGC based on the National Comprehensive Cancer Network (NCCN) and Chinese Society of Clinical Oncology (CSCO) guidelines for gastric cancer (7, 8).

However, the therapeutic response of LAGC to NCT is highly heterogeneous, and the prognosis of patients who have good responses is significantly better than that of patients with poor responses (9). Patients with poor treatment response could not benefit from NCT, and NCT might increase treatment-related adverse reactions and medical cost, delay the optimal timing of surgery, or lead to tumor progression, resulting in poor prognosis (10). Currently, tumor regression grade (TRG) is widely used as an objective indicator for evaluating the NCT response in LAGC (11), but it can only be obtained through postoperative pathological examination. Therefore, an accurate prediction of the response to NCT in LAGC patients before surgery would be of great clinical significance, through which could screen patients who might benefit from NCT and further make an appropriate and personalized treatment plan.

Quantitative dynamic contrast-enhanced MRI (DCE-MRI) and intravoxel incoherent motion diffusion-weighted imaging (IVIM-DWI) are commonly used as functional MRI imaging techniques. DCE-MRI could obtain quantitative parameters of hemodynamics non-invasively through the pharmacokinetic model (12). IVIM-DWI proposed by Le Bihan et al. (13) used a biexponential model with multiple *b* values to obtain multiple parameters, which can distinguish pure molecular diffusion and microcirculatory perfusion in the capillary networks, compared with conventional DWI (14). Previous studies have found that quantitative parameters of DCE-MRI and IVIM-DWI can be used as an imaging biomarker of clinical, histopathological, and prognostic factors in different tumors (15–17). However, due to respiratory movement and gastrointestinal motility, these functional MRI techniques are rarely used in gastric research. There have been also no reports on the prediction of NCT response and prognosis in LAGC using DCE-MRI and IVIM-DWI.

Therefore, the purpose of this study is to explore the predictive value of DCE-MRI and IVIM-DWI quantitative parameters for the pathological treatment response of NCT in LAGC patients, and the relationship between the prediction

results and patient prognosis, to provide a basis for clinical individualized precision treatment.

MATERIALS AND METHODS

This prospective study was conducted in accordance with the Declaration of Helsinki and approved by the Independent Ethics Committee of the Cancer Hospital, Chinese Academy of Medical Sciences (Beijing, China), and written informed consent was acquired from each subject before inclusion.

Patients

A total of 167 consecutive patients with newly diagnosed resectable LAGC who underwent gastric MRI in National Cancer Center/Cancer Hospital, Chinese Academy of Medical Sciences, and Peking Union Medical College from January 2016 to December 2018 were initially enrolled. Patients were included according to the following criteria: 1) pathologically confirmed gastric adenocarcinoma on gastroscopy; 2) no contraindication to MR examinations; 3) locally advanced stage (cT3-4aN1-3M0) according to the American Joint Committee on Cancer (AJCC) TNM staging system (8th edition) (18) as determined by pretreatment CT, MRI, or endoscopic ultrasonography; 4) no previous treatment before MRI examination; 5) NCT performed within 1 week after MR examination; 6) R0 radical gastrectomy within 30 days after the completion of NCT; and 7) regular follow-up after surgery.

The enrolment flowchart of the study cohort is summarized in **Figure 1**. Thirty-eight patients were excluded for the following reasons: 1) low quality of MR images due to obvious respiratory movement or gastrointestinal motility artifact or significant image distortion (n = 7); 2) maximum tumor diameter (MTD) <1.0 cm (n = 5); 3) NCT not completed due to severe adverse reactions (n = 8); 4) refused surgery after complete NCT (n = 10); and 5) lost to follow-up postoperatively (n = 8). Finally, a total of 129 patients were included in this study, including 107 men and 22 women, with a median age of 60 years (range from 28 to 76 years).

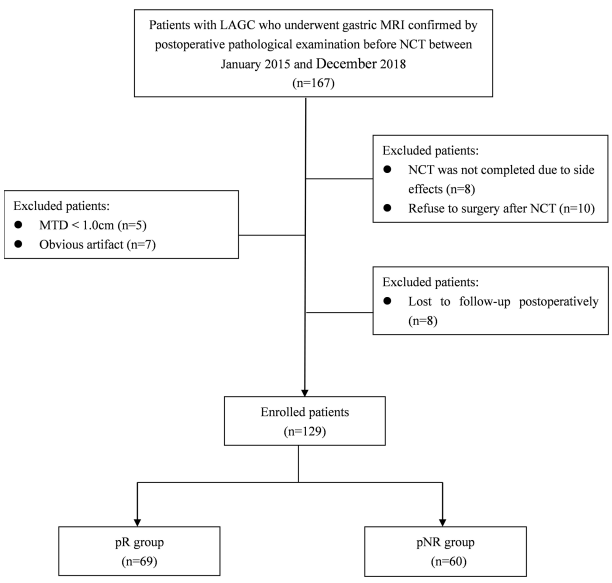

FIGURE 1 | Diagram showing the recruitment of the study population and exclusion criteria. LAGC, locally advanced gastric cancer; NCT, neoadjuvant chemotherapy; MTD, maximum tumor diameter; pR, pathological responders; pNR, pathological non-responders.

MRI Data Acquisitions

Patients were asked to fast for 6–8 h prior to MR examinations to empty the gastrointestinal tract and underwent breath-holding training. In order to avoid the artifact of gastrointestinal peristalsis, patients without contraindications (i.e., glaucoma, prostate hypertrophy, asthma, or severe heart disease) were injected with 10 mg of anisodamine hydrobromide (Hangzhou Minsheng Pharmaceutical Co., Ltd., Hangzhou, China) intramuscularly, followed by drinking 800–1,000 ml of water to dilate the stomach wall before MRI.

All examinations were performed with a whole-body 3.0-T MR scanner (Discovery MR750; GE Healthcare, Milwaukee, WI, USA) equipped with an 8-channel, phased-array body coil. The conventional MRI protocols used for standardized gastric imaging at our institution include the following sequence: 1) axial three-dimensional (3D) spoiled-gradient recalled-echo sequences for liver acquisition with volume acceleration flexible (LAVA-Flex) sequence in one breath-hold; 2) respiratory-triggered axial PROPELLER T2-weighted imaging (T2WI) with fat suppression; 3) axial, coronal, and sagittal single-shot fast spin-echo T2WI in breath-hold; and 4) respiratory-triggered axial DWI sequence included two b values (b = 0 and 800 s/mm^2).

IVIM-DWI was performed by using a respiratory-triggered single-shot echo-planar imaging sequence in the transverse plane with diffusion in three orthogonal directions, and the parallel imaging using the array spatial-sensitivity encoding technique (ASSET) was used to shorten the scanning time and reduce image distortion. Ten b values from 0 to 1200 s/mm^2 (0, 10, 20, 40, 100, 200, 400, 800, 1,000, and 1,200) were applied. Quantitative DCE-MRI was performed by using multiphase axial 3D spoiled-gradient recalled-echo sequences for liver acquisition with volume acceleration-extended volume (LAVA-XV) sequence with breath-hold. According to our previous study (19), pre-contrast T1 mapping with four different flip angles (3°, 6°, 9°, and 12°) was acquired before dynamic scanning for the determination of pre-contrast T1 values. Then a dynamic scan with 42 consecutive phases was performed, which shared the scanning parameters and range as T1 mapping, with a flip angle of 15° and temporal resolution of 6 s/phase. A bolus of gadopentetate dimeglumine (Magnevist, Bayer Schering, Berlin, Germany) at a constant dose of 0.1 mmol/kg was power injected, followed by a 20-ml saline flush at a rate of 2.5 ml/s for all patients. The acquisition time was 18 s for each of the three consecutive phases with an interval of 5–10 s; the total scanning time for DCE-MRI was 5–6 min. The detailed acquisition parameters of sequences are shown in **Supplementary Table 1**.

Imaging Analysis

Two radiologists (YJZ and YL, with 9 and 17 years of experience in gastrointestinal abdominal imaging, respectively) who were blinded to the patients' clinical and histopathological data independently reviewed the MR imaging and measured the DCE-MRI and IVIM-DWI parameters at the largest section of the tumor with good image quality. The mean values of quantitative parameters were used for subsequent analysis, and the interobserver agreement was also assessed according to the intraclass correlation coefficient (ICC). In order to ensure data repeatability, all parameters were measured twice with a month interval to assess the intraobserver agreement.

The region of interest (ROI) drawing principles were as follows: the slide containing the largest tumor diameter was selected for further analysis. The ROI was manually traced slightly along the borders of the tumor to include the entire tumor, while avoiding visible blood vessels, necrotic areas, and cystic areas, on DCE-MRI and IVIM-DWI.

The IVIM images were transferred to GE ADW 4.6 workstation and analyzed by MADC software in the FuncTool software package. ROI of the tumor was manually delineated on the IVIM-DWI with a b value of 800 s/mm^2 using axial T2WI as a reference. $ADC_{standard}$ value was calculated by the monoexponential model using the total available b values according to the following equation:

$$S_b/S_0 = \exp(-b \cdot ADC_{standard})$$

The IVIM parameters were calculated by biexponential fitting according to the following equation, suggested by Le Bihan et al. (13):

$$S_b/S_0 = f\exp(-b \cdot D^*) + (1 - f)\exp(-b \cdot D)$$

where S_b is the signal intensity with diffusion gradient b and S_0 is the signal intensity without diffusion gradient. D is the true diffusion coefficient as reflected by pure water molecular diffusion, D* is the pseudo-diffusion coefficient representing perfusion-related incoherent microcirculation, and f is the perfusion fraction related to the microvascular volume fraction. The parameter maps of IVIM were generated automatically by the MADC software, and the $ADC_{standard}$, D, D*, and f values in the ROIs were obtained

Quantitative DCE-MRI parameters were calculated using an in-house-developed image-processing workstation, OmniKinetics 2.0.10 (GE Healthcare, Beijing, China). The signal intensity on MRI was converted into an equivalent concentration of contrast material using the variable flip angles method. The pharmacokinetic parameters including volume transfer constant (K^{trans}), reverse reflux rate constant (k_{ep}), extracellular extravascular volume fraction (v_e), and plasma volume fraction (v_p), which were derived from DCE-MRI, were calculated using the two-compartment extended Tofts model as described in our previous study and report (19, 20).

Clinical Treatment

All 129 patients were treated with 4 to 6 cycles of oxaliplatin-based NCT as recommended in CSCO guideline (7), in which 76 patients receiving oxaliplatin and S-1 (SOX) regimen, 32 patients receiving capecitabine and oxaliplatin (XELOX) regimen, and 21 patients receiving docetaxel oxaliplatin and S-1 (DOS) regimen. D2 radical gastrectomy was performed within 30 days after the completion of NCT. The surgical procedures were in accordance with CSCO guidelines for gastric cancer (7). Adjuvant chemotherapy was routinely started 3–4 weeks after surgery, and the oncologist decided on both regimens and cycles based on the clinical and pathological responses.

Histopathological Examination and Tumor Regression Grade Evaluation

Patient records and original histopathological slides were independently re-evaluated by 2 pathologists with over 10 years' experience in gastrointestinal pathology. The pathologists were blinded to the routine diagnoses and patient outcomes. Response to chemotherapy was assessed according to the Mandard TRG system (21), which divided the residual tumor into grades 1–5, based on the amount of fibrosis and/or necrosis over the remaining viable tumor cells. To ensure consistency of the evaluation criteria, the 2 pathologists were trained prior to the evaluation. In case of disagreement, a consensus diagnosis would be reached through joint re-review and discussion on a multi-headed microscope. Patients were divided into two groups: pathological responders (pR) (TRG 1–3) and pathological non-responders (pNR) (TRG 4 and 5).

Histopathological variables were also recorded, including histopathological type, tumor differentiation, Lauren classification, lymphovascular invasion (LVI), perineural invasion (PNI), and immunohistochemical assays of HER2, EGFR, and c-MET. For patients with no residual remaining tumor after NCT, a preoperative biopsy specimen was used for analysis. TNM stage was assessed according to the 8th edition of the AJCC staging system. HER2, EGFR, and c-MET expression were detected according to the HER2 detection guideline from the College of American Pathologists (22) and a previous study (23).

Follow-Up

After radical gastrectomy, all patients were followed up every 3 months for the first year and every 6–12 months afterward. Follow-up consisted of physical examination, tumor marker assessment, CT scan, and endoscopic examination. Recurrence-free survival (RFS) was recorded and was defined as the interval between the date of surgery and the first date of identified local and/or distant recurrence or the last follow-up date without recurrence. Tumor recurrence was defined as local recurrence, distant metastasis, or death caused by gastric cancer, detected by imaging or pathology. All patients were observed until recurrence or the final follow-up date of December 31, 2020. Patients were censored if they were recurrence-free and alive at the last follow-up.

Statistical Analysis

All statistical analyses were performed with SPSS (version 21.0; SPSS Inc., Chicago, IL, USA). The intraobserver and interobserver reliability in the measurements of IVIM-DWI and DCE-MRI parameters was estimated with ICC, which was defined in previous studies (24).

Quantitative data were expressed as the median and interquartile range (IQR) and were compared using the Mann–Whitney U-test.

Categorical data were expressed as number (percentage) and were compared using the χ^2 test or Fisher's exact test, as appropriate. Differences in clinicopathological features, IVIM-DWI, and quantitative DCE-MRI parameters between the pR and pNR were compared. Those variables with a significant difference, as determined by the univariate logistic regression analysis, were chosen for multivariate logistic regression analysis to identify significant independent predictive parameters for NCT response.

Multivariate logistic regression was used to build a combined prediction model with the statistically significant parameters. The prediction performance of the quantitative parameters and models was evaluated by receiver operating characteristic (ROC) curve, quantified by the area under the curve (AUC), overall accuracy (ACC), sensitivity, specificity, negative predictive value (NPV), and positive predictive value (PPV). The optimal cutoff value was calculated at the maximum value of Youden's index (sensitivity + specificity − 1).

The quantitative parameters and prediction probabilities were converted into binary variables according to the diagnostic threshold, that is, the predicted treatment response group and non-response group. The RFS was assessed using the Kaplan–Meier method, and differences between predicted groups were assessed by log-rank test. Univariable and multivariable Cox proportional hazards analyses were used to determine independent prognostic factors for tumor recurrence among clinicopathological factors, quantitative parameters, and prediction models. $p < 0.05$ was considered to be statistically significant.

RESULTS

The Clinicopathological Findings

After the NCT and radical gastrectomy, the complete histopathologic regression of the LAGC (TRG 1) was achieved in 12/129 patients (9.3%); TRG 2 was recorded in 12/129 patients (9.3%), TRG 3 in 45/129 patients (34.9%), TRG 4 in 43/129 patients (33.3%), and TRG 5 in 17/129 (13.2%). According to TRG results, patients were divided into the pR group (n = 69) (**Figure 2**) and the pNR group (n = 60) (**Figure 3**).

There were significant differences in LVI, PNI, and postoperative pathological stage (ypStage) between the pR and pNR groups (all $p < 0.001$). No significant differences were found for gender, age, MTD, tumor site, surgical approach, histopathological type, differentiation, Lauren's classification, HER2 expression, EGFR expression, and C-MET expression between the two groups (all $p > 0.05$) (**Table 1**).

Intraobserver and Interobserver Agreement Assessments for Quantitative Analysis

The interobserver and intraobserver agreement for the assessments of quantitative parameters by the two radiologists is shown in **Supplementary Table 2**. ICCs for interobserver and intraobserver were all above 0.80 (95% CI, 0.837–0.975, and 0.845–0.966, respectively), which indicated excellent agreement. Therefore, the mean values of the first measurement by the two radiologists were used for subsequent analysis.

Comparison of Dynamic Contrast-Enhanced MRI and Intravoxel Incoherent Motion Diffusion-Weighted Imaging Quantitative Parameters Between Pathological Response and Pathological Non-Response Groups

Among the 129 patients, quantitative DCE-MRI parameters in the primary lesion of K^{trans}, k_{ep}, v_e, and v_p were 0.103 (0.073, 0.161) min^{-1}, 0.592 (0.452, 0.813) min^{-1}, 0.229 (0.170, 0.351), and 0.019 (0.007, 0.037); IVIM parameters of $ADC_{standard}$, D, D*, and *f* value were 1.380 (1.250, 1.650) × 10^{-3} mm^2/s, 1.050 (0.920, 1.255) × 10^{-3} mm^2/s, 15.400 (6.405, 34.300) × 10^{-3} mm^2/s, and 41.700% (35.550%, 53.550%). The comparisons of quantitative DCE-MRI and IVIM-DWI parameters between the pR and pNR groups are summarized in **Table 2**. The results showed that K^{trans}, k_{ep}, and v_e values in the pR group were significantly higher than those in the pNR group (all $p < 0.001$), while $ADC_{standard}$ and D values were significantly lower than those in the pNR group ($p = 0.011$ and $p < 0.001$). D* value and *f* value in the pR group were slightly higher than those in pNR, but there were no significant differences (*p*-value was 0.233 and 0.105, respectively). v_p value showed no significant difference between the two groups ($p = 0.470$). Box and whisker plot graphs for parameters derived from DCE-MRI and IVIM-DWI in the pR and pNR groups are given in **Figure 4**.

Clinical Factors and MRI Quantitative Parameters for Predicting Neoadjuvant Chemotherapy Response

With the univariate analysis, none of the clinical factors showed significant correlation with pathology response of NCT (all $p > 0.05$). Meanwhile, higher pretreatment baseline K^{trans} (OR = 9.334; 95% CI, 3.531–24.672), k_{ep} (OR = 4.442; 95% CI, 2.297–8.589), and v_e values (OR = 3.221; 95% CI, 1.837–5.646) and lower $ADC_{standard}$ (OR = 0.673; 95% CI, 0.465–0.973) and D values (OR = 0.221; 95% CI, 0.127–0.384) were more likely to be responsive to NCT (all $p < 0.05$).

Multivariate logistic regression analysis demonstrated that K^{trans} (OR = 5.300; 95% CI, 1.470–19.104), k_{ep} (OR = 3.918; 95% CI, 1.484–10.345), v_e values (OR = 2.926; 95% CI, 1.437–5.961), and D values (OR = 0.266; 95% CI, 0.138–0.515) were independently associated with the response to NCT. The univariate and multivariate logistic regression results are summarized in **Supplementary Table 3**.

Prediction Efficiency of Response to Neoadjuvant Chemotherapy Using Dynamic Contrast-Enhanced MRI and Intravoxel Incoherent Motion Diffusion-Weighted Imaging Quantitative Parameters

Multivariate logistic regression analysis was conducted to build prediction models for response to NCT, using K^{trans}, k_{ep}, and v_e for DCE-MRI model; D for the IVIM-DWI model; and K^{trans}, k_{ep}, v_e, and D for the DCE+IVIM model. The results are summarized in **Table 3**.

ROC curve analysis results of MRI quantitative parameters and combined model for predicting pathological treatment response are presented in **Table 4** and **Figure 5**. D value was

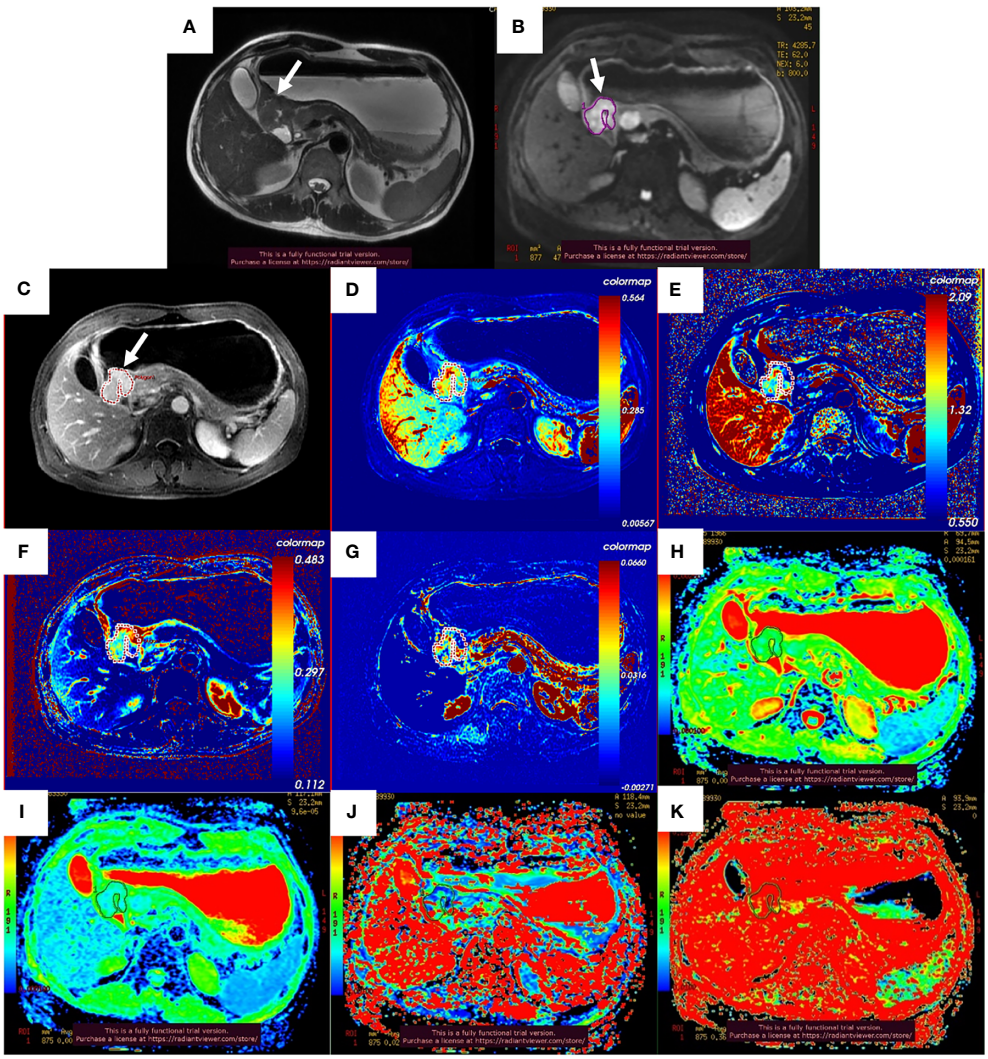

FIGURE 2 | Images of a 51-year-old man with gastric adenocarcinoma in the antrum of the stomach who had response to NCT. In T2WI **(A)**, IVIM-DWI **(B)**, and contrast-enhanced imaging **(C)**, the gastric wall was irregularly thickened with high signal intensity, diffusion restricted, and heterogeneously enhanced (white arrows). The pseudo-colorized K^{trans} maps **(D)**, k_{ep} map **(E)**, v_e map **(F)**, v_p map **(G)**, $ADC_{standard}$ map **(H)**, D map **(I)**, D* map **(J)**, and *f* map **(K)** show mixed red, green, and blue colors in the corresponding tumor with a K^{trans} of 0.298 min^{-1}, k_{ep} of 1.086 min^{-1}, v_e of 0.303, v_p of 0.027, $ADC_{standard}$ of 1.330 × 10^{-3} mm^2/s, D of 0.893 × 10^{-3} mm^2/s, D* of 24.000 × 10^{-3} mm^2/s, and *f* of 36.6%. NCT, neoadjuvant chemotherapy; T2WI, T2-weighted imaging; IVIM-DWI, intravoxel incoherent motion diffusion-weighted imaging.

the single parameter with the highest predictive efficiency, of which AUC was 0.812. The combination of DCE-MRI and IVIM-DWI displayed the highest AUC of 0.922.

Prognostic Value of MRI Quantitative Parameters and Its Association With Recurrence-Free Survival

The median follow-up period for all patients was 15.0 months (IQR, 9.0–21.0 months). Of the 129 patients, 54 patients (41.9%) developed tumor recurrence by the last follow-up day. The median RFS time was 24.0 months (95% CI: 17.2–30.8), and the 2-year RFS rate was 49.9% months.

Univariate Cox proportional hazards analysis with clinicopathological factors, MRI quantitative parameters, and prediction models showed that signet ring cell, LVI, PNI, ypStage III, pathological response, K^{trans} value, k_{ep} value, v_e value, D value, DCE model, IVIM model, and DCE+IVIM model were significantly associated with RFS. Multivariate Cox regression analysis showed that ypStage III (hazard ratio [HR] = 6.197; 95% CI, 2.132–18.014) and no response predicted by IVIM model (HR = 2.240; 95% CI, 1.231–4.075) were independent predictors of poor RFS (**Table 5**).

The Kaplan–Meier survival analysis based on clinicopathological factors, MRI quantitative parameters, and prediction model, which were identified from Cox regression analysis, are summarized in

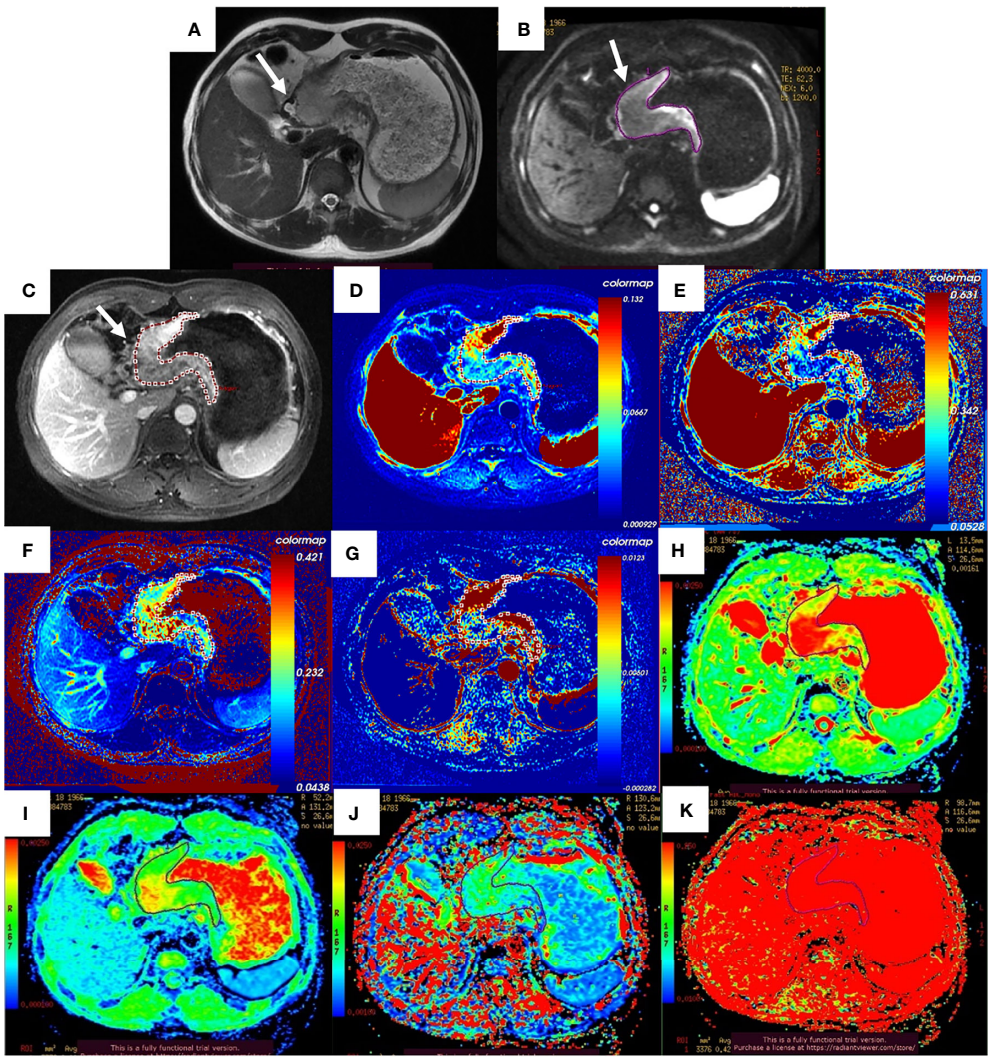

FIGURE 3 | Images of a 52-year-old man with gastric adenocarcinoma in the body of the stomach who had non-response to NCT. In T2WI **(A)**, IVIM-DWI **(B)**, and contrast-enhanced imaging **(C)**, the gastric wall was irregularly thickened with high signal intensity, diffusion restricted, and heterogeneously enhanced (white arrows). The pseudo-colorized K^{trans} maps **(D)**, k_{ep} map **(E)**, v_e map **(F)**, v_p map **(G)**, $ADC_{standard}$ map **(H)**, D map **(I)**, D* map **(J)**, and *f* map **(K)** show mixed red, green, and blue colors in the corresponding tumor with a K^{trans} of 0.072 min^{-1}, k_{ep} of 0.335 min^{-1}, v_e of 0.271, v_p of 0.015, $ADC_{standard}$ of 2.140 × 10^{-3} mm^2/s, D of 1.500 × 10^{-3} mm^2/s, D* of 10.700 × 10^{-3} mm^2/s, and *f* of 42.2%. NCT, neoadjuvant chemotherapy; T2WI, T2-weighted imaging; IVIM-DWI, intravoxel incoherent motion diffusion-weighted imaging.

Tables 6, **7**. These features significantly stratified in 2-year RFS rate are demonstrated in **Figures 6**, **7** according to the log-rank test (all log-rank $p < 0.05$).

Further subgroup analysis showed that in ypStage II/III, LVI-positive and PNI-positive groups, and 2-year RFS rate between different groups of pathological treatment response and prediction models were also significantly different (all log-rank $p < 0.05$) (**Table 8** and **Supplementary Figure 1**).

DISCUSSION

In this study, DCE-MRI and IVIM-DWI quantitative parameters were used to construct a prediction model for NCT pathological treatment response of LAGC patients, and the relationship between predicted results and RFS was explored for the first time. The results showed that K^{trans}, k_{ep}, and v_e values of DCE-MRI and D values of IVIM-DWI were independent predictors of pathological response to NCT. The prediction models showed good predictive efficacy for NCT response, and RFS could be stratified based on the prediction result.

CSCO guideline of gastric cancer recommends NCT for patients with resectable GC with clinical-stage ≥ cT3-4N1-3M0 (Evidence 1B) (7), which is an important part of the multidisciplinary management for LAGC. At present, morphology-based Response Evaluation Criteria in Solid Tumors (RECIST) can only evaluate and monitor the

TABLE 1 | Clinical and histopathological characteristics of 129 patients in pR and pNR groups.

Characteristic	All patients (n = 129)	pR (n = 69)	pNR (n = 60)	*p*-Value
Gender				0.407*
Male	107 (82.9)	59 (85.5)	48 (80.0)	
Female	22 (17.1)	10 (14.5)	12 (20.0)	
Age, years	60.00 (52.00, 64.50)	60.00 (52.00, 64.00)	61.00 (48.25, 67.75)	0.806**
MTD, cm	4.80 (3.90, 5.80)	4.70 (3.75, 5.95)	5.00 (3.93, 5.58)	0.923**
Location				0.804*
EGJ	43 (33.3)	22 (31.9)	21 (35.0)	
Fundus	7 (5.4)	5 (7.3)	1 (1.7)	
Body	27 (20.9)	13 (18.8)	14 (23.3)	
Antrum	35 (27.1)	21 (30.4)	14 (23.3)	
Whole stomach	17 (13.3)	8 (11.6)	10 (16.7)	
Surgical approach				0.834*
Esophagogastrectomy	29 (22.5)	15 (21.7)	14 (23.3)	
Proximal gastrectomy	14 (10.9)	7 (10.1)	7 (11.7)	
Distal gastrectomy	44 (34.1)	26 (37.7)	18 (30.0)	
Total gastrectomy	42 (32.6)	21 (30.4)	21 (35.0)	
Histopathological type				0.576***
Adenocarcinoma	104 (80.6)	58 (84.1)	46 (76.7)	
Mucinous	7 (5.4)	3 (4.3)	4 (6.7)	
Signet-ring cell	18 (14.0)	8 (11.6)	10 (16.6)	
Differentiation				0.937***
Well	3 (2.3)	2 (2.9)	1 (1.7)	
Moderate	36 (27.9)	20 (29.0)	16 (26.7)	
Poor	90 (69.8)	47 (68.1)	43 (71.6)	
Lauren classification				0.165*
Intestinal	51 (39.5)	27 (39.1)	24 (40.0)	
Diffuse	43 (33.3)	19 (27.5)	24 (40.0)	
Mixed	35 (27.2)	23 (33.4)	12 (20.0)	
Lymphovascular invasion				<0.001*
Positive	59 (45.7)	18 (26.1)	41 (68.3)	
Negative	70 (54.3)	51 (73.9)	19 (31.7)	
Perineural invasion				<0.001*
Positive	72 (55.8)	25 (36.2)	47 (78.3)	
Negative	57 (44.2)	44 (63.8)	13 (21.7)	
HER2 expression				0.514***
–/1+	101 (78.3)	53 (76.8)	48 (80.0)	
2+	20 (15.5)	10 (14.5)	10 (16.7)	
3+	8 (6.2)	6 (8.7)	2 (3.3)	
EGFR expression				0.423*
–/1+	81 (62.8)	46 (66.7)	35 (58.3)	
2+	37 (28.7)	19 (27.5)	18 (30.0)	
3+	11 (8.5)	4 (5.8)	7 (11.7)	
c-MET expression				0.881***
–/1+	92 (71.3)	48 (69.6)	44 (73.3)	
2+	33 (25.6)	19 (27.5)	14 (23.4)	
3+	4 (3.1)	2 (2.9)	2 (3.3)	
ypStage				<0.001*
0/I	33 (25.6)	30 (43.5)	3 (5.0)	
II	43 (33.3)	24 (34.8)	19 (31.7)	
III	53 (41.1)	15 (21.7)	38 (63.3)	

Data are given as n (%) or median (IQR).

pR, pathological responders; pNR, pathological non-responders; MTD, maximum tumor diameter; EGJ, esophagogastric junction.

**p-Values were calculated using χ^2 test.*

***p-Values were calculated using Mann–Whitney U-test.*

****p-Values were calculated using Fisher's exact test.*

treatment response through tumor size changes but cannot predict the efficacy of NCT before treatment.

The pathological staging of gastric cancer is an important factor affecting the prognosis of gastric cancer (25); LVI, PNI, and signet-ring cell carcinoma are also indicators for poor prognosis (26, 27). In this study, it was concluded that higher ypStage, LVI positive, PNI positive, and signet ring cell carcinoma were risk factors for poor prognosis of RFS. However, multivariate Cox regression analysis showed that only ypStage and the IVIM-DWI model were independent predictors for RFS, possibly because tumor stage and the IVIM-DWI model had stronger effects on prognosis.

Quantitative DCE-MRI reflects the exchange of contrast agents in tumor blood vessels and extravascular extracellular

TABLE 2 | Comparison of DCE-MRI and IVIM quantitative parameters between pR and pNR groups.

Parameter	pR (n = 69)	pNR (n = 60)	Z	*p*-Value
K^{trans} (min^{-1})	0.135 (0.097, 0.226)	0.081 (0.066, 0.111)	–5.227	<0.001*
k_{ep} (min^{-1})	0.772 (0.532, 0.987)	0.475 (0.383, 0.614)	–5.241	<0.001*
v_e	0.305 (0.205, 0.428)	0.189 (0.158, 0.248)	–4.835	<0.001*
v_p	0.019 (0.008, 0.037)	0.019 (0.004, 0.038)	–0.722	0.470*
$ADC_{standard}$ (10^{-3} mm^2/s)	1.340 (1.230, 1.525)	1.495 (1.333, 1.745)	–2.541	0.011*
D (10^{-3} mm^2/s)	0.950 (0.845, 1.065)	1.230 (1.058, 1.330)	7.330	<0.001*
D* (10^{-3} mm^2/s)	15.900 (8.200, 34.800)	12.650 (5.240, 34.900)	–1.192	0.233*
f (%)	44.200 (35.650, 55.550)	40.450 (35.475, 48.575)	–1.724	0.105*

Data were expressed as the median (IQR).

K^{trans}, volume transfer constant; k_{ep}, reflux rate; v_e, volume fraction of the extravascular extracellular matrix; v_p, plasma volume fraction; $ADC_{standard}$, standard apparent diffusion coefficient; D, true diffusion coefficient; D, pseudo-diffusion coefficient; f, microvascular volume fraction; DCE-MRI, dynamic contrast-enhanced MRI; IVIM, intravoxel incoherent motion; pR, pathological responders; pNR, pathological non-responders.*

**p-Values were calculated using the Mann–Whitney U-test.*

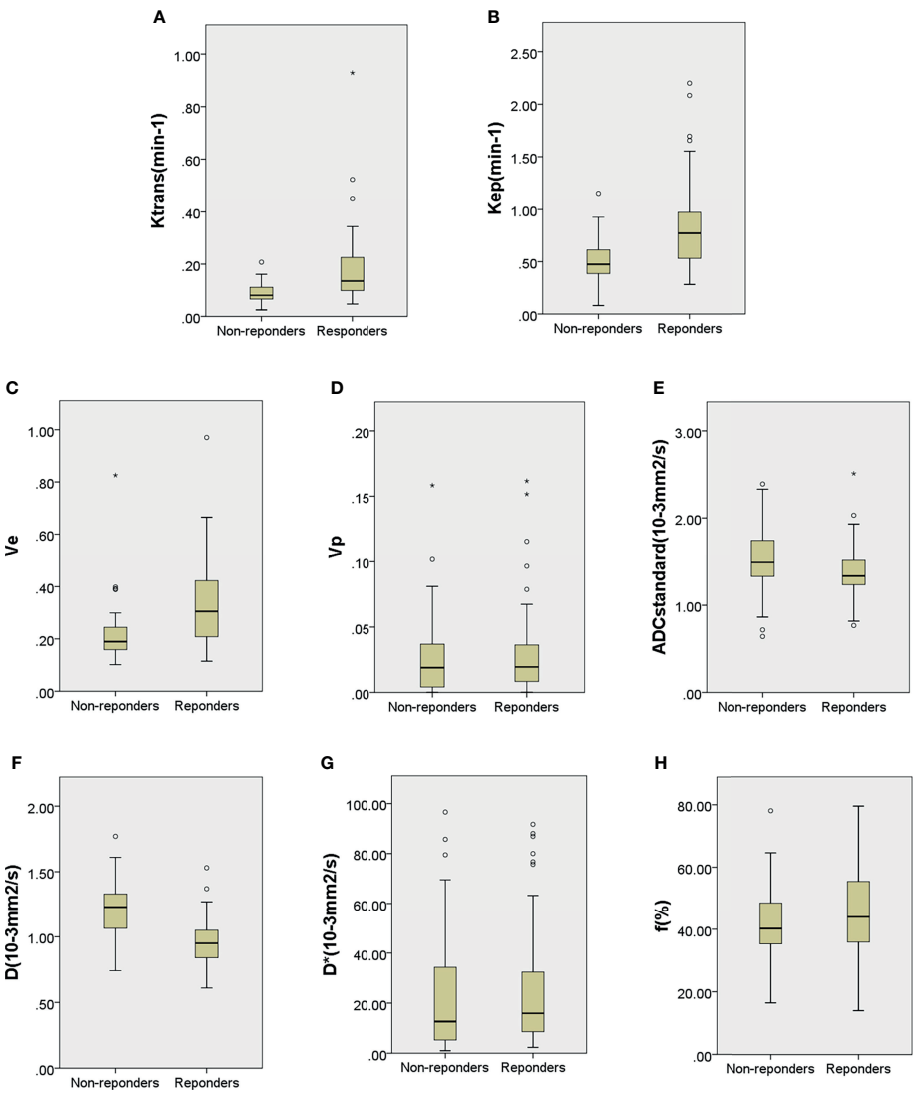

FIGURE 4 | Boxplots for K^{trans} **(A)**, k_{ep} **(B)**, v_e **(C)**, v_p **(D)**, $ADC_{standard}$ **(E)**, D **(F)**, D* **(G)**, and *f* **(H)** of locally advanced gastric cancer in the pathological responder and non-responder groups. The top and bottom of the boxes are the 25th and 75th percentiles, respectively. The mid lines and bars indicate the medians and the 5th–95th percentiles, respectively. Circles indicate outliers, stars represent extreme values.

TABLE 3 | Model of DCE-MRI and IVIM-DWI quantitative parameters and their combination in predictive impact on response to NCT by multivariate logistic regression analysis.

Model*	Coefficients	Std. error	Wald	OR	95% CI	*p*-Value
DCE-MRI						
K^{trans}	1.744	0.587	8.816	5.722	1.809–18.096	0.003
k_{ep}	1.258	0.413	9.272	3.517	1.565–7.902	0.002
v_e	1.257	0.359	12.240	3.516	1.738–7.111	<0.001
Constant	0.852	0.306	7.727	2.344		0.005
IVIM-DWI						
D	–1.509	0.281	28.760	0.221	0.127–0.384	<0.001
Constant	0.156	0.212	0.538	0.463	1.168	
Combined						
K^{trans}	1.668	0.654	6.499	5.300	1.470, 19.104	0.011
k_{ep}	1.365	0.495	7.596	3.918	1,484, 10.345	0.006
v_e	1.074	0.363	8.752	2.926	1.437, 5.961	0.003
D	–1.323	0.336	15.472	0.266	0.138, 0.515	<0.001
Constant	0.966	0.353	7.476	2.627		0.006

OR, odds ratio; K^{trans}, volume transfer constant; k_{ep}, reflux rate; v_e, volume fraction of the extravascular extracellular matrix; D, true diffusion coefficient; DCE-MRI, dynamic contrast-enhanced MRI; IVIM-DWI, intravoxel incoherent motion diffusion-weighted imaging; NCT, neoadjuvant chemotherapy.

**Forward stepwise, likelihood ratio method was adapted in multivariate logistic regression analysis, with probability <0.05 for stepwise entry and 0.1 for removal.*

TABLE 4 | Diagnostic performance of DCE-MRI and IVIM-DWI quantitative parameters and their combinations in discriminating treatment response to NCT in LAGC patients.

Parameters or model	Cutoff value	AUC	Sensitivity	Specificity	Accuracy	PPV	NPV	*p*
K^{trans} (min^{-1})	0.134	0.767 (0.687–0.848)	52.2	93.3	71.3	90.0	62.9	<0.001
k_{ep} (min^{-1})	0.661	0.768 (0.688–0.848)	60.9	83.3	71.3	80.8	64.9	<0.001
v_e	0.300	0.747 (0.662–0.832)	52.2	93.3	71.3	90.0	62.9	<0.001
v_p	0.002	0.537 (0.436–0.638)	95.7	21.7	61.2	58.4	81.3	0.470
$ADC_{standard}$ (10^{-3} mm^2/s)	1.440	0.630 (0.531–0.728)	71.0	55.0	55.0	64.5	62.3	0.011
D (10^{-3} mm^2/s)	1.200	0.812 (0.736–0.889)	92.8	60.0	77.5	72.7	87.8	<0.001
D* (10^{-3} mm^2/s)	10.650	0.561 (0.460–0.662)	72.5	46.7	60.5	63.6	59.6	0.233
f (%)	50.900	0.583 (0.485–0.681)	36.2	81.7	57.4	69.4	52.7	0.105
DCE*	0.613	0.875 (0.816–0.934)	71.0	91.7	80.6	90.7	73.3	<0.001
IVIM*	0.462	0.818 (0.743–0.894)	84.1	70.0	77.5	76.3	79.2	<0.001
DCE+IVIM*	0.481	0.922 (0.877–0.966)	87.0	85.0	86.0	87.0	85.0	<0.001

Data in parentheses are 95% CI.

AUC, area under the curve; PPV, positive predictive value; NPV, negative predictive value; K^{trans}, volume transfer constant; k_{ep}, reflux rate; v_e, volume fraction of the extravascular extracellular matrix; v_p, plasma volume fraction; $ADC_{standard}$, standard apparent diffusion coefficient; D, true diffusion coefficient; D, pseudo-diffusion coefficient; f, microvascular volume fraction; DCE-MRI, dynamic contrast-enhanced MRI; IVIM-DWI, intravoxel incoherent motion diffusion-weighted imaging; NCT, neoadjuvant chemotherapy; LAGC, locally advanced gastric cancer.*

**Cutpoint is probability.*

space through certain pharmacokinetic models (20) and evaluates tumor microvascular structure, capillary permeability, and tissue perfusion. IVIM-DWI uses the biexponential model to quantitatively separate the Brownian motion of water molecules in tissues (diffusion) from the movement of blood in the microvasculature (perfusion) (14), which can reflect the tissue diffusion and microcirculation perfusion more accurately and comprehensively. Studies have shown that perfusion of tumor tissue might be a key factor affecting the sensitivity of some chemotherapy drugs (28, 29). Quantitative DCE-MRI and IVIM-DWI have been widely applied to predict and evaluate the therapeutic response of chemotherapy, radiotherapy, and targeted therapy for a variety of tumors (16, 30, 31). At present, studies on quantitative DCE-MRI and IVIM-DWI mostly focus on head and neck, breast, and pelvic tumors. As gastric MRI is susceptible to artifacts caused by respiratory movement and gastrointestinal peristalsis, the application in the stomach is limited. Studies on NCT response prediction of gastric cancer using quantitative DCE-MRI and IVIM-DWI have not been reported.

The present study showed that the values of K^{trans}, k_{ep}, and v_e in the pR group were significantly higher than in the pNR group before treatment (all $p < 0.001$). K^{trans} reflects the exchangeability of contrast agents in the plasma and extracellular space of tumor tissue, while k_{ep} reflects the flux rate of contrast agent diffusion back into the blood vessels, both of which are important markers of vascular permeability. v_e and v_p reflect the volume of extravascular extracellular space and plasma in unit voxel, respectively (20). Tong et al. (32) found in a study of rectal cancer that K^{trans}, k_{ep}, and v_e before NCT were significantly higher in the pathological complete response (pCR) group than in the non-pCR group, while these parameters showed no significant difference after treatment. Tang et al. (33) also found that K^{trans} and k_{ep} in the response group were significantly higher than in the non-response group in pancreatic cancer. In addition,

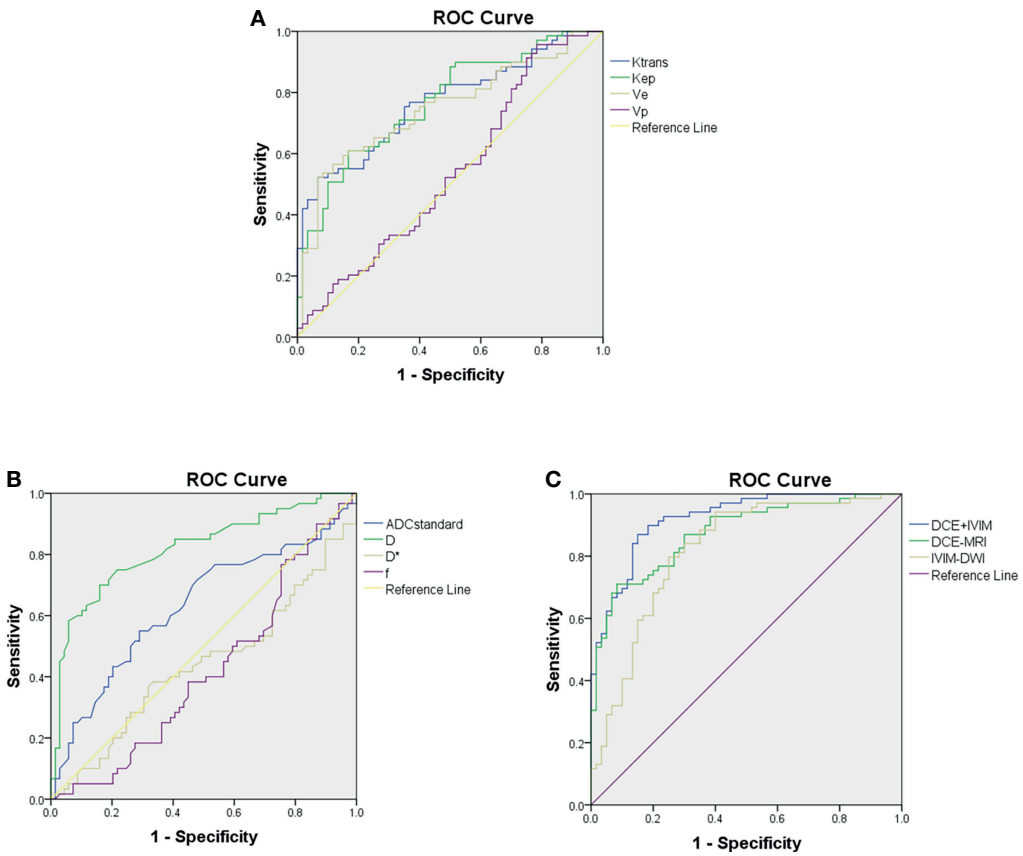

FIGURE 5 | Receiver operating characteristic curves for predicting treatment response to neoadjuvant therapy. **(A)** Comparison of diagnostic performance using dynamic contrast-enhanced (DCE) MRI parameters. **(B)** Comparison of diagnostic performance using intravoxel incoherent motion (IVIM) parameters. **(C)** Comparison of diagnostic performance using combined model of DCE-MRI and IVIM-DWI.

K^{trans} and v_e were found to be significantly correlated with 3-year progression-free and OS of oropharyngeal and hypopharyngeal squamous cell carcinoma (34). These results are consistent with the findings of our study. High K^{trans} and k_{ep} values reflect higher permeability and perfusion of tumor tissue due to tumor neoangiogenesis, which could make chemotherapy drugs penetrate easier into tumor tissues and kill tumor cells. An increased v_e indicates an elevated fraction in the extracellular extravascular space, which might be caused by increasing immature incompetent vessel leakage, which could provide wider distribution space for chemotherapy drugs and more oxygen distribution for tissues to avoid the occurrence of hypoxia, thus increasing the sensitivity of chemotherapy drugs. In a study of glioma, Kim et al. (35) found that v_p in the progression group was higher, suggesting that it may be related to the destruction of the blood–brain barrier and tumor angiogenesis. However, our study did not find a significant relationship between NCT treatment response and RFS. We speculate that there might be more influence factors to v_p, and gastric cancer is not a tumor of rich blood supply. Therefore, the significance of v_p in the prediction of NCT treatment response and prognosis of gastric cancer needs to be further clarified.

IVIM-DWI has been widely applied in the diagnosis, treatment response evaluation, and prognosis prediction of various tumors, and its quantitative parameter has been found to be predictive for the prognosis of many cancers (31, 36, 37). In this study, the $ADC_{standard}$ and D values of the pR group were significantly lower than those of the pNR group (both $p < 0.05$), and the multivariate logistic regression revealed that D was an independent predictor for NCT response with an OR of 0.266, indicating that patients with low D values were more likely to respond to NCT. Similar results were also found in the study on response prediction of neoadjuvant therapy for locally advanced rectal cancer (36). Compared with the non-pCR group, the pCR group showed lower pretreatment ADC_{mean}, D value, and higher *f* value, and D value was the best predictor of treatment response. The study conducted by Zheng et al. (37) also demonstrated that the residual tumor group had higher ADC value and D value as compared with the non-residual tumor group, and multivariate analysis showed that the pretreatment D value was an independent prognostic factor for cervical cancer. The reason might be that a lower ADC or D value indicated more restriction of water molecule diffusion in tumor tissues, higher cellular density, and richer

TABLE 5 | Univariate and multivariate Cox proportional hazards prediction analyses of recurrence-free survival according to responder and non-responder groups determined by baseline DCE-MRI and IVIM-DWI quantitative parameters and their combination models.

Parameters	Univariate analysis			Multivariate analysis		
	Hazard ratio	95% CI	*p*	Hazard ratio	95% CI	*p*
Clinical factors						
Gender						
Male	1 (reference)					
Female	1.436	0.755–2.733	0.270			
Age, years	0.982	0.959–1.005	0.121			
MTD, cm	1.125	0.941–1.345	0.196			
Location						
EGJ	1 (reference)					
Fundus	2.536	0.843–7.624	0.098			
Body	1.161	0.553–2.434	0.694			
Antrum	0.728	0.336–1.579	0.421			
Whole stomach	1.571	0.712–3.467	0.264			
Pathological factors						
Histopathological type						
Adenocarcinoma	1 (reference)					
Mucinous	0.900	0.217–3.745	0.885			NS
Signet-ring cell	2.396	1.227–4.680	0.010**			NS
Differentiation						
Well	1 (reference)					
Moderate	1.447	0.190–10.989	0.721			
Poor	1.529	0.209–11.157	0.676			
Lauren classification						
Intestinal	1 (reference)					
Diffuse	1.398	0.767–2.549	0.274			
Mixed	0.704	0.337–1.471	0.350			
Lymphovascular invasion						
Negative	1 (reference)					
Positive	3.051	1.738–5.356	<0.001**			NS
Perineural invasion						
Negative	1 (reference)					
Positive	2.639	1.435–4.854	0.002**			NS
HER2 expression						
–/1+	1 (reference)					
2+	0.877	0.411–1.869	0.733			
3+	1.094	0.392–3.054	0.863			
EGFR expression						
–/1+	1 (reference)					
2+	0.617	0.321–1.185	0.147			
3+	0.965	0.379–2.460	0.941			
c-MET expression						
–/1+	1 (reference)					
2+	0.570	0.286–1.138	0.111			
3+	1.621	0.390–6.736	0.506			
ypStage						
0/I	1 (reference)			1 (reference)		
II	2.220	0.715–6.892	0.168	1.930	0.618-6.026	0.257
III	8.834	3.145–24.812	<0.001**	6.197	2.132-18.014	0.001
Pathological response						
Responder	1 (reference)					
Non-responder	2.887	1.637–5.092	<0.001**			NS
Multiparametric MRI						
K^{trans} (min^{-1})						
Responder (>0.134)	1 (reference)					
Non-responder (≤0.134)	3.125	1.473–6.631	0.003**			NS
k_{ep} (min^{-1})						
Responder (>0.661)	1 (reference)					
Non-responder (≤0.661)	2.624	1.381–4.986	0.003**			NS
v_e						
Responder (>0.300)	1 (reference)					NS
Non-responder (≤0.300)	2.369	1.191–4.714	0.014**			

(Continued)

TABLE 5 | Continued

Parameters	Univariate analysis			Multivariate analysis		
	Hazard ratio	95% CI	*p*	Hazard ratio	95% CI	*p*
v_p						
Responder (>0.002)	1 (reference)					
Non-responder (≤0.002)	1.442	0.704–2.955	0.317			
$ADC_{standard}$ ($\times10^{-3}$ mm^2/s)						
Responder (<1.440)	1 (reference)					
Non-responder (≥1.440)	1.593	0.933–2.720	0.088			
D ($\times10^{-3}$ mm^2/s)						
Responder (<1.200)	1 (reference)					
Non-responder (≥1.200)	3.746	2.171–6.462	<0.001**			NS
D* ($\times10^{-3}$ mm^2/s)						
Responder (>10.650)	1 (reference)					
Non-responder (≤10.650)	1.434	0.838–2.456	0.188			
f (%)						
Responder (>50.900)	1 (reference)					
Non-responder (≤50.900)	1.266	0.678–2.364	0.459			
DCE*						
Responder (>0.613)	1 (reference)					
Non-responder (≤0.613)	2.522	1.351–4.707	0.004**			NS
IVIM*						
Responder (>0.462)	1 (reference)			1 (reference)		
Non-responder (≤0.462)	3.646	2.065–6.438	<0.001**	2.240	1.231-4.075	0.008
DCE+IVIM*						
Responder (>0.481)	1 (reference)					
Non-responder (≤0.481)	2.789	1.582–4.916	<0.001**			NS

NS, not significant; K^{trans}, volume transfer constant; k_{ep}, reflux rate; v_e, volume fraction of the extravascular extracellular matrix; v_p, plasma volume fraction; $ADC_{standard}$, standard apparent diffusion coefficient; D, true diffusion coefficient; D, pseudo-diffusion coefficient; f, microvascular volume fraction; DCE-MRI, dynamic contrast-enhanced MRI; IVIM-DWI, intravoxel incoherent motion diffusion-weighted imaging; MTD, maximum tumor diameter; EGJ, esophagogastric junction.*

**The predictive probability of the combined model was used.*

***Data are statistically from the univariate Cox proportional hazards analyses.*

TABLE 6 | Kaplan–Meier survival analysis according to pathological factors for predictors of RFS.

Pathological factors	N = 129	Median RFS (95% CI)	2-year RFS rate	Log-rank *p*
Histopathological type				0.007
Signet-ring cell	16	14 (9.431–18.569)	18.6 ± 11.5	
Non-signet-ring cell	113	28 (21.011–34.989)	54.4 ± 5.9	
Lymphovascular invasion				<0.001
Positive	59	16 (13.501–18.499)	24.5 ± 7.4	
Negative	70	52*	70.5 ± 6.3	
Perineural invasion				0.001
Positive	72	18 (14.793–21.207)	35.0 ± 6.8	
Negative	57	52*	70.8 ± 7.5	
ypStage				<0.001
0/I	33	39*	85.4 ± 7.1	
II	43	52*	64.5 ± 9.1	
III	53	12 (7.719–16.281)	19.8 ± 6.6	
Pathological response				<0.001
Responder	69	49*	69.4 ± 7.2	
Non-responder	60	16 (12.221–19.779)	29.2 ± 7.0	

RFS, recurrence-free survival.

**Cumulative survival probability was above the follow-up.*

blood supply. On the contrary, an increased ADC or D value reflects a decrease in cell density of tumor tissue due to necrosis, inflammation, or fibrosis and then affects the penetration and distribution of antitumor drugs as a result of decreased blood supply, ultimately leading to chemotherapy or radiotherapy resistance and poor prognosis. Perfusion-related parameters D* and *f* values have also been found to be possible predictors of tumor treatment response in some studies (37–39). However, in this study, although D* and *f* values in the pR group were higher than those in the pNR group, no significant difference was observed, which may be related to the small sample size or different pathological types of tumors.

TABLE 7 | Kaplan–Meier survival analysis according to cutoff values for predictors of RFS.

Parameters	Above cutoff			Below cutoff			Log-rank *p*
	Median parameter (25%, 75% quartile)	Median RFS (n)**	2-year RFS rate	Median parameter (25%, 75% quartile)	Median RFS (n)	2-year RFS rate	
DCE-MRI parameters							
K^{trans}	0.212 (0.163, 0.266)	42*** (40)	75.7 ± 9.3	0.086 (0.066, 0.104)	19 (89)	38.8 ± 6.3	0.002
k_{ep}	0.869 (0.774, 1.068)	49*** (52)	66.0 ± 9.4	0.467 (0.379, 0.573)	19 (77)	40.6 ± 6.5	0.002
v_e	0.410 (0.361, 0.490)	42*** (40)	63.9 ± 10.5	0.189 (0.160, 0.235)	20 (89)	43.4 ± 6.4	0.010
v_p	0.026 (0.012, 0.400)	28 (113)	53.4 ± 5.9	0.001 (0.000, 0.002)	18 (16)	26.7 ± 13.1	0.308
IVIM-DWI parameters							
$ADC_{standard}$	1.680 (1.550, 1.895)	18 (53)	38.7 ± 7.6	1.270 (1.150, 1.360)	28 (76)	58.6 ± 7.7	0.081
D	1.310 (1.265, 1.395)	16 (41)	14.1 ± 6.5	0.955 (0.850, 1.058)	52*** (88)	70.4 ± 6.1	<0.001
D*	28.300 (16.200, 52.925)	52*** (82)	57.8 ± 6.3	5.300 (3.370, 7.290)	20 (47)	39.3 ± 9.1	0.180
f	56.750 (54.725, 63.375)	28 (36)	63.7 ± 9.1	37.500 (32.800, 43.650)	22 (93)	45.6 ± 6.4	0.452
Response prediction model*							
DCE	0.941 (0.762, 0.990)	42*** (54)	65.5 ± 9.1	0.239 (0.154, 0.449)	19 (75)	39.7 ± 6.6	0.002
IVIM	0.755 (0.615, 0.854)	52*** (76)	72.3 ± 6.7	0.224 (0.158, 0.358)	15 (53)	21.8 ± 6.8	<0.001
DCE+IVIM	0.910 (0.722, 0.994)	49*** (69)	69.3 ± 7.3	0.140 (0.059, 0.258)	18 (60)	30.2 ± 7.1	<0.001

RFS, recurrence-free survival; K^{trans}, volume transfer constant; k_{ep}, reflux rate; v_e, volume fraction of the extravascular extracellular matrix; v_p, plasma volume fraction; $ADC_{standard}$, standard apparent diffusion coefficient; D, true diffusion coefficient; D, pseudo-diffusion coefficient; f, microvascular volume fraction; DCE-MRI, dynamic contrast-enhanced MRI; IVIM-DWI, intravoxel incoherent motion diffusion-weighted imaging.*

**The predictive probabilities of combined parameters for NCT response derived from multivariate logistic regression analysis previously were used as new parameters.*

***Data in parentheses are number of patients.*

****Cumulative survival probability was above the follow-up.*

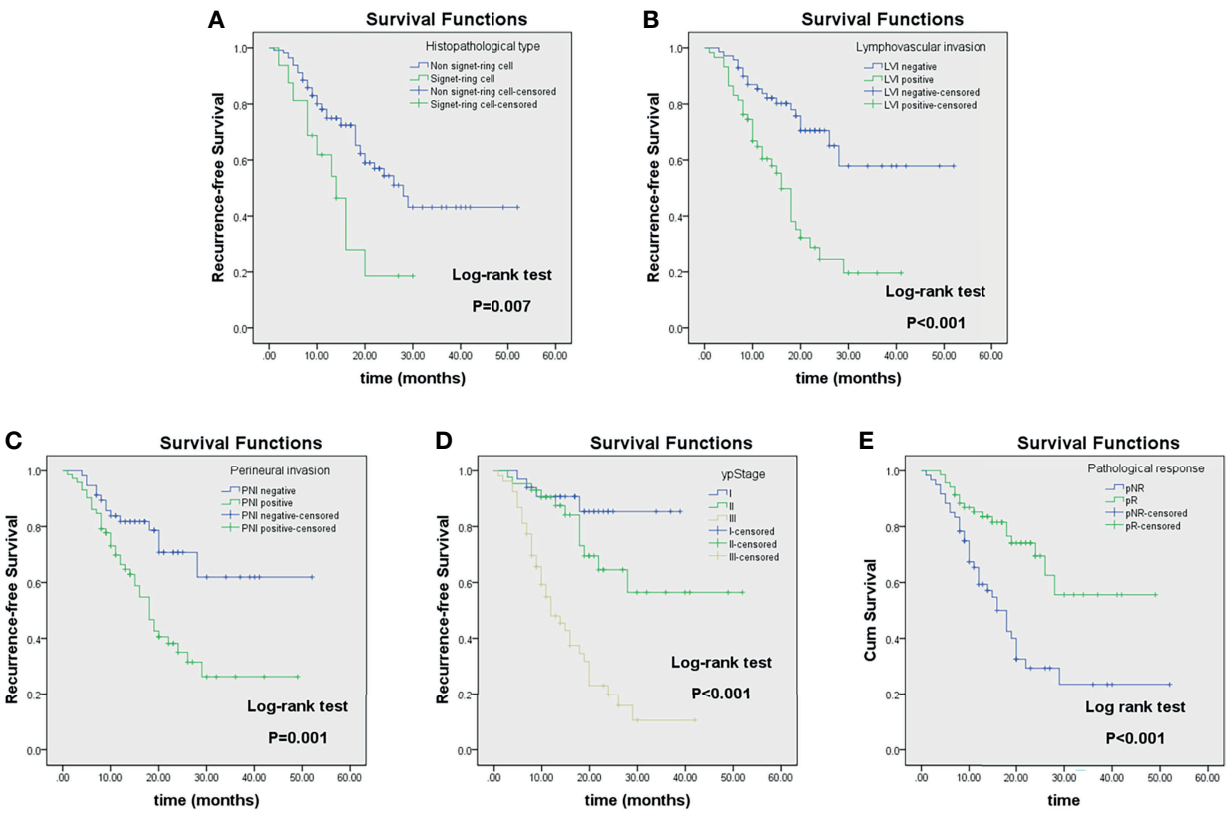

FIGURE 6 | Kaplan–Meier analyses of recurrence-free survival (RFS) in locally advanced gastric cancer (LAGC) patients (n = 129) stratified by category: histopathological type **(A)**, lymphovascular invasion **(B)**, perineural invasion **(C)**, ypStage **(D)**, and pathological response **(E)**.

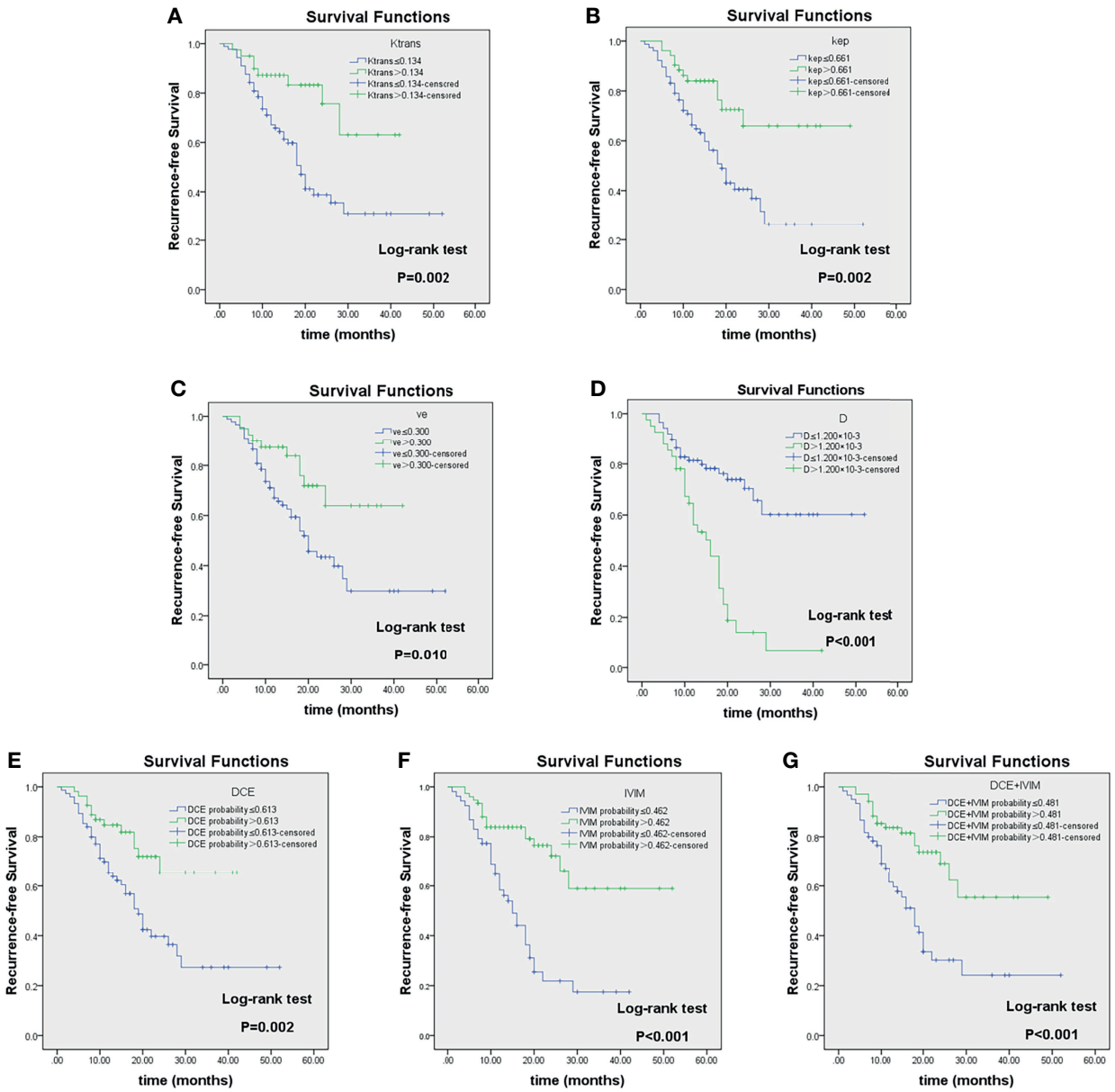

FIGURE 7 | Kaplan–Meier analyses of recurrence-free survival (RFS) in LAGC patients (n = 129) stratified by category: responders and non-responders as classified according to imaging parameter cutoff values of K^{trans} **(A)**, k_{ep} **(B)**, v_e **(C)**, D **(D)**, DCE-MRI **(E)**, IVIM-DWI **(F)**, and their combinations **(G)**. Reported in **Table 4**. LAGC, locally advanced gastric cancer; DCE-MRI, dynamic contrast-enhanced MRI; IVIM-DWI, intravoxel incoherent motion diffusion-weighted imaging.

The present study combined DCE-MRI and IVIM-DWI quantitative parameters for the first time, to build the prediction model for NCT response in LAGC through multivariate logistic regression. ROC analysis showed that combination DCE-MRI and IVIM-DWI exhibited the highest predictive efficiency, with AUC, sensitivity, and specificity of 0.922, 87.0%, and 85.0%, respectively. To further verify the relationship between MRI quantitative parameters and patient prognosis, Cox regression analysis was performed, and the results showed that the IVIM-DWI model was an independent predictor of RFS. Kaplan–Meier survival analysis showed that low K^{trans}, k_{ep}, and v_e and high D value groups had shorter RFS (all $p < 0.05$). The RFS of different groups based on DCE, IVIM, and DCE+IVIM prediction models was significantly different (all log-rank $p < 0.05$). The same conclusion was reached in further subgroup analysis in the ypStage II/III, LVI positive, and PNI positive groups. Different studies (40, 41) have shown that pathological TRG grade was a predictor of OS and RFS in LAGC patients. Patients with good response had obvious tumor tissue fibrosis, less tumor residual, and down-staging, which were correlated with better prognosis. DCE-MRI and IVIM-DWI make it

TABLE 8 | Subgroup Kaplan–Meier survival analysis of RFS according to response grouped by pathology and prediction models.

Subgroup	R		NR		Log-rank *p*
	Median RFS (n)*	2-year RFS rate	Median RFS (n)	2-year RFS rate	
ypStage II/III					
Pathological response	28 (39)	59.8 ± 10.0	16 (57)	25.6 ± 6.9	0.006
DCE	42** (35)	57.5 ± 12.1	16 (61)	29.6 ± 6.7	0.004
IVIM	28 (49)	64.2 ± 8.7	15 (47)	17.1 ± 6.4	<0.001
DCE+IVIM	28 (44)	60.1 ± 9.8	16 (52)	25.0 ± 6.8	0.005
LVI positive					
Pathological response	41** (18)	51.3 ± 16.3	14 (41)	15.9 ± 7.2	0.012
DCE	41** (18)	54.3 ± 17.0	14 (41)	15.5 ± 7.1	0.005
IVIM	41** (26)	53.8 ± 15.2	12 (33)	9.9 ± 6.1	0.002
DCE+IVIM	41** (22)	50.6 ± 15.9	14 (37)	15.5 ± 7.1	0.008
PNI positive					
Pathological response	24 (25)	53.2 ± 12.4	16 (47)	24.5 ± 7.6	0.041
DCE	24 (23)	47.2 ± 14.6	16 (49)	29.8 ± 7.4	0.041
IVIM	26 (29)	60.4 ± 12.1	15 (43)	18.8 ± 7.0	0.008
DCE+IVIM	26 (29)	50.4 ± 11.9	16 (43)	25.4 ± 7.9	0.049

R, responders; NR, non-responders; RFS, recurrence-free survival; DCE, dynamic contrast enhanced; IVIM, intravoxel incoherent motion.
**Data in parentheses are number of patients.*
***Cumulative survival probability was above the follow-up.*

possible to predict NCT response before treatment, which can provide a basis for the selection of individualized treatment plans for LAGC patients.

The present study also has several limitations. First, the sample size is relatively small, which requires more cases to be verified, so as to be applied in clinical practice. Second, manually drawing ROI in the slices at the greatest diameter might introduce certain subjectivity of measurement, while 3D voxel-by-voxel analyses might have yielded more reliable and repeatable results for biological tumor heterogeneity. Third, a total of seven patients were excluded due to the inferior image quality. Therefore, the stability of MRI image quality in gastric cancer needs to be further improved. Fourth, the follow-up time was comparatively short (median follow-up time 15.0 months), and the clinical endpoints were not evaluated as OS rate. These limitations need to be addressed in future studies.

CONCLUSION

In conclusion, this study demonstrated that pretreatment DCE-MRI quantitative parameters K^{trans}, k_{ep}, v_e, and IVIM-DWI parameter D value were independent predictors of NCT response for LAGC. The regression models based on baseline DCE-MRI, IVIM-DWI, and their combination could predict the RFS of patients. This is of great value for clinicians to choose the most appropriate and individualized treatment strategy for LAGC patients.

DATA AVAILABILITY STATEMENT

The original contributions presented in the study are included in the article/**Supplementary Material**. Further inquiries can be directed to the corresponding author.

ETHICS STATEMENT

The studies involving human participants were reviewed and approved by the Independent Ethics Committee of the Cancer Hospital, Chinese Academy of Medical Sciences (Beijing, China). The patients/participants provided their written informed consent to participate in this study.

AUTHOR CONTRIBUTIONS

YJZ and LJ contributed to the conception and design of the study. YJZ, ZJ, BW, and YXZ contributed to the enrollment of the patients. YJZ, ZJ, and BW collected the clinical data and performed followed-ups. YL and JJ performed the MRI examination. YJZ and SW performed the data analysis and interpretation. YJZ wrote the first draft of the manuscript. SW and LJ revised the language and reviewed the manuscript. All authors contributed to the article and approved the submitted version of the manuscript.

FUNDING

This work was supported by the Beijing Hope Run Special Fund (No. LC2016A06). The funders played no role in data collection and analysis, design, decision to publish, or preparation of the manuscript.

SUPPLEMENTARY MATERIAL

The Supplementary Material for this article can be found online at: https://www.frontiersin.org/articles/10.3389/fonc.2022.841460/full#supplementary-material

REFERENCES

1. Sung H, Ferlay J, Siegel RL, Laversanne M, Soerjomataram I, Jemal A, et al. Global Cancer Statistics 2020: GLOBOCAN Estimates of Incidence and Mortality Worldwide for 36 Cancers in 185 Countries. *CA Cancer J Clin* (2021) 71:209–49. doi: 10.3322/caac.21660
2. Sekiguchi M, Oda I, Matsuda T, Saito Y. Epidemiological Trends and Future Perspectives of Gastric Cancer in Eastern Asia. *Digestion* (2021) 7:1–7. doi: 10.1159/000518483
3. Fang C, Wang W, Deng JY, Sun Z, Seeruttun SR, Wang ZN, et al. Proposal and Validation of a Modified Staging System to Improve the Prognosis Predictive Performance of the 8th AJCC/UICC pTNM Staging System for Gastric Adenocarcinoma: A Multicenter Study With External Validation. *Cancer Commun (Lond)* (2018) 38:67. doi: 10.1186/s40880-018-0337-5
4. Catalano V, Labianca R, Beretta GD, Gatta G, de Braud F, Van Cutsem E. Gastric Cancer. *Crit Rev Oncol Hematol* (2005) 54:209–41. doi: 10.1016/j.critrevonc.2005.01.002
5. Allemani C, Matsuda T, Di Carlo V, Harewood R, Matz M, Nikšić M, et al. Global Surveillance of Trends in Cancer Survival 2000-14 (CONCORD-3): Analysis of Individual Records for 37 513 025 Patients Diagnosed With One of 18 Cancers From 322 Population-Based Registries in 71 Countries. *Lancet* (2018) 391:1023–75. doi: 10.1016/S0140-6736(17)33326-3
6. Smyth EC, Nilsson M, Grabsch HI, van Grieken NC, Lordick F. Gastric Cancer. *Lancet* (2020) 396:635–48. doi: 10.1016/S0140-6736(20)31288-5
7. Wang FH, Zhang XT, Li YF, Tang L, Qu XJ, Ying JE, et al. The Chinese Society of Clinical Oncology (CSCO): Clinical Guidelines for the Diagnosis and Treatment of Gastric Cancer, 2021. *Cancer Commun (Lond)* (2021) 41:747–95. doi: 10.1002/cac2.12193
8. National Comprehensive Cancer Network. *NCCN Clinical Practice Guidelines in Oncology: Gastric Cancer, Version 5* (2021). Available at: https://www.nccn.org/professionals/physician_ gls/pdf/gastric.pdf.
9. Derieux S, Svrcek M, Manela S, Lagorce-Pages C, Berger A, André T, et al. Evaluation of the Prognostic Impact of Pathologic Response to Preoperative Chemotherapy Using Mandard's Tumor Regression Grade (TRG) in Gastric Adenocarcinoma. *Dig Liver Dis* (2020) 52:107–14. doi: 10.1016/j.dld.2019.07.010
10. Robb WB, Mariette C. Predicting the Response to Chemotherapy in Gastric Adenocarcinoma: Who Benefits From Neoadjuvant Chemotherapy? *Recent Results Cancer Res* (2012) 196:241–68. doi: 10.1007/978-3-642-31629-6_17
11. Neves Filho EH, de Sant'Ana RO, Nunes LV, Pires AP, da Cunha MD. Histopathological Regression of Gastric Adenocarcinoma After Neoadjuvant Therapy: A Critical Review. *APMIS* (2017) 125(2):79–84. doi: 10.1111/apm.12642
12. García-Figueiras R, Padhani AR, Beer AJ, Baleato-González S, Vilanova JC, Luna A, et al. Imaging of Tumor Angiogenesis for Radiologists–Part 1: Biological and Technical Basis. *Curr Probl Diagn Radiol* (2015) 44:407–24. doi: 10.1067/j.cpradiol.2015.02.010
13. Le Bihan D, Breton E, Lallemand D, Aubin ML, Vignaud J, Laval-Jeantet M. Separation of Diffusion and Perfusion in Intravoxel Incoherent Motion MR Imaging. *Radiology* (1988) 168:497–505. doi: 10.1148/radiology.168.2.3393671
14. Federau C. Measuring Perfusion: Intravoxel Incoherent Motion MR Imaging. *Magn Reson Imaging Clin N Am* (2021) 29:233–42. doi: 10.1016/j.mric.2021.01.003
15. You SH, Choi SH, Kim TM, Park CK, Park SH, Won JK, et al. Differentiation of High-Grade From Low-Grade Astrocytoma: Improvement in Diagnostic Accuracy and Reliability of Pharmacokinetic Parameters From DCE MR Imaging by Using Arterial Input Functions Obtained From DSC MR Imaging. *Radiology* (2018) 286:981–91. doi: 10.1148/radiol.2017170764
16. Hao Y, An R, Xue Y, Li F, Wang H, Zheng J, et al. Prognostic Value of Tumoral and Peritumoral Magnetic Resonance Parameters in Osteosarcoma Patients for Monitoring Chemotherapy Response. *Eur Radiol* (2021) 31:3518–29. doi: 10.1007/s00330-020-07338-y
17. Zeng Q, Hong Y, Cheng J, Cai W, Zhuo H, Hou J, et al. Quantitative Study of Preoperative Staging of Gastric Cancer Using Intravoxel Incoherent Motion Diffusion-Weighted Imaging as a Potential Clinical Index. *Eur J Radiol* (2021) 141:109627. doi: 10.1016/j.ejrad.2021.109627
18. Amin MB, Edge S, Greene F, Byrd DR, Brookland RK, Washington MK, et al. (2018).
19. Zhu Y, Zhou Y, Zhang W, Xue L, Li Y, Jiang J, et al. Value of Quantitative Dynamic Contrast-Enhanced and Diffusion-Weighted Magnetic Resonance Imaging in Predicting Extramural Venous Invasion in Locally Advanced Gastric Cancer and Prognostic Significance. *Quant Imaging Med Surg* (2021) 11:328–40. doi: 10.21037/qims-20-246
20. Koh TS, Bisdas S, Koh DM, Thng CH. Fundamentals of Tracer Kinetics for Dynamic Contrast-Enhanced MRI. *J Magn Reson Imaging* (2011) 34:1262–76. doi: 10.1002/jmri.22795
21. Mandard AM, Dalibard F, Mandard JC, Marnay J, Henry-Amar M, Petiot JF, et al. Pathologic Assessment of Tumor Regression After Preoperative Chemoradiotherapy of Esophageal Carcinoma. Clinicopathologic Correlations. *Cancer* (1994) 73:2680–6. doi: 10.1002/1097-0142(19940601)73:11<2680::aid-cncr2820731105>3.0.co;2-c
22. Bartley AN, Washington MK, Colasacco C, Ventura CB, Ismaila N, Benson AB3rd, et al. HER2 Testing and Clinical Decision Making in Gastroesophageal Adenocarcinoma: Guideline From the College of American Pathologists, American Society for Clinical Pathology, and the American Society of Clinical Oncology. *J Clin Oncol* (2017) 35(4):446–64. doi: 10.1200/JCO.2016.69.4836
23. Fuse N, Kuboki Y, Kuwata T, Nishina T, Kadowaki S, Shinozaki E, et al. Prognostic Impact of HER2, EGFR, and C-MET Status on Overall Survival of Advanced Gastric Cancer Patients. *Gastric Cancer* (2016) 19(1):183–91. doi: 10.1007/s10120-015-0471-6
24. Koo TK, Li MY. A Guideline of Selecting and Reporting Intraclass Correlation Coefficients for Reliability Research. *J Chiropr Med* (2016) 15:155–63. doi: 10.1016/j.jcm.2016.02.012
25. In H, Solsky I, Palis B, Langdon-Embry M, Ajani J, Sano T. Validation of the 8th Edition of the AJCC TNM Staging System for Gastric Cancer Using the National Cancer Database. *Ann Surg Oncol* (2017) 24:3683–91. doi: 10.1245/s10434-017-6078-x
26. Blumenthaler AN, Newhook TE, Ikoma N, Estrella JS, Blum Murphy M, Das P, et al. Concurrent Lymphovascular and Perineural Invasion After Preoperative Therapy for Gastric Adenocarcinoma Is Associated With Decreased Survival. *J Surg Oncol* (2021) 123:911–22. doi: 10.1002/jso.26367
27. Khan N, Donohoe CL, Phillips AW, Griffin SM, Reynolds JV. Signet Ring Gastric and Esophageal Adenocarcinomas: Characteristics and Prognostic Implications. *Dis Esophagus* (2020) 33:doaa016. doi: 10.1093/dote/doaa016
28. Sung YS, Park B, Choi Y, Lim HS, Woo DC, Kim KW, et al. Dynamic Contrast-Enhanced MRI for Oncology Drug Development. *J Magn Reson Imaging* (2016) 44:251–64. doi: 10.1002/jmri.25173
29. Li SP, Padhani AR. Tumor Response Assessments With Diffusion and Perfusion MRI. *J Magn Reson Imaging* (2012) 35:745–63. doi: 10.1002/jmri.22838
30. Jalaguier-Coudray A, Villard-Mahjoub R, Delouche A, Delarbre B, Lambaudie E, Houvenaeghel G, et al. Value of Dynamic Contrast-Enhanced and Diffusion-Weighted MR Imaging in the Detection of Pathologic Complete Response in Cervical Cancer After Neoadjuvant Therapy: A Retrospective Observational Study. *Radiology* (2017) 284:432–42. doi: 10.1148/radiol.2017161299
31. Song T, Yao Q, Qu J, Zhang H, Zhao Y, Qin J, et al. The Value of Intravoxel Incoherent Motion Diffusion-Weighted Imaging in Predicting the Pathologic Response to Neoadjuvant Chemotherapy in Locally Advanced Esophageal Squamous Cell Carcinoma. *Eur Radiol* (2021) 31:1391–400. doi: 10.1007/s00330-020-07248-z
32. Tong T, Sun Y, Gollub MJ, Peng W, Cai S, Zhang Z, et al. Dynamic Contrast-Enhanced MRI: Use in Predicting Pathological Complete Response to Neoadjuvant Chemoradiation in Locally Advanced Rectal Cancer. *J Magn Reson Imaging* (2015) 42:673–80. doi: 10.1002/jmri.24835
33. Tang W, Liu W, Li HM, Wang QF, Fu CX, Wang XH, et al. Quantitative Dynamic Contrast-Enhanced MR Imaging for the Preliminary Prediction of the Response to Gemcitabine-Based Chemotherapy in Advanced Pancreatic Ductal Carcinoma. *Eur J Radiol* (2019) 121:108734. doi: 10.1016/j.ejrad.2019.108734
34. Ng SH, Liao CT, Lin CY, Chan SC, Lin YC, Yen TC, et al. Dynamic Contrast-Enhanced MRI, Diffusion-Weighted MRI and 18F-FDG PET/CT for the Prediction of Survival in Oropharyngeal or Hypopharyngeal Squamous Cell Carcinoma Treated With Chemoradiation. *Eur Radiol* (2016) 26:4162–72. doi: 10.1007/s00330-016-4276-8

35. Kim R, Choi SH, Yun TJ, Lee ST, Park CK, Kim TM, et al. Prognosis Prediction of Non-Enhancing T2 High Signal Intensity Lesions in Glioblastoma Patients After Standard Treatment: Application of Dynamic Contrast-Enhanced MR Imaging. *Eur Radiol* (2017) 27:1176–85. doi: 10.1007/s00330-016-4464-6
36. Xu Q, Xu Y, Sun H, Chan Q, Shi K, Song A, et al. Quantitative Intravoxel Incoherent Motion Parameters Derived From Whole-Tumor Volume for Assessing Pathological Complete Response to Neoadjuvant Chemotherapy in Locally Advanced Rectal Cancer. *J Magn Reson Imaging* (2018) 48:248–58. doi: 10.1002/jmri.25931
37. Zheng X, Guo W, Dong J, Qian L. Prediction of Early Response to Concurrent Chemoradiotherapy in Cervical Cancer: Value of Multi-Parameter MRI Combined With Clinical Prognostic Factors. *Magn Reson Imaging* (2020) 72:159–66. doi: 10.1016/j.mri.2020.06.014
38. Perucho JAU, Wang M, Vardhanabhuti V, Tse KY, Chan KKL, Lee EYP. Association Between IVIM Parameters and Treatment Response in Locally Advanced Squamous Cell Cervical Cancer Treated by Chemoradiotherapy. *Eur Radiol* (2021) 31:7845–54. doi: 10.1007/s00330-021-07817-w
39. Guo B, Ouyang F, Ouyang L, Huang X, Guo T, Lin S, et al. Intravoxel Incoherent Motion Magnetic Resonance Imaging for Prediction of Induction Chemotherapy Response in Locally Advanced Hypopharyngeal Carcinoma: Comparison With Model-Free Dynamic Contrast-Enhanced Magnetic Resonance Imaging. *J Magn Reson Imaging* (2021) 54:91–100. doi: 10.1002/jmri.27537
40. Xie JW, Lu J, Xu BB, Zheng CH, Li P, Wang JB, et al. Prognostic Value of Tumor Regression Grading in Patients Treated With Neoadjuvant Chemotherapy Plus Surgery for Gastric Cancer. *Front Oncol* (2021) 11:587856. doi: 10.3389/fonc.2021.587856
41. Lombardi PM, Mazzola M, Achilli P, Aquilano MC, De Martini P, Curaba A, et al. Prognostic Value of Pathological Tumor Regression Grade in Locally Advanced Gastric Cancer: New Perspectives From a Single-Center Experience. *J Surg Oncol* (2021) 123:923–31. doi: 10.1002/jso.26391

Conflict of Interest: Author SW was employed by GE Healthcare, Life Sciences.

The remaining authors declare that the research was conducted in the absence of any commercial or financial relationships that could be construed as a potential conflict of interest.

Publisher's Note: All claims expressed in this article are solely those of the authors and do not necessarily represent those of their affiliated organizations, or those of the publisher, the editors and the reviewers. Any product that may be evaluated in this article, or claim that may be made by its manufacturer, is not guaranteed or endorsed by the publisher.

frontiers | Frontiers in Oncology

ORIGINAL RESEARCH
published: 07 June 2022
doi: 10.3389/fonc.2022.846840

A Dual-Energy CT Radiomics of the Regional Largest Short-Axis Lymph Node Can Improve the Prediction of Lymph Node Metastasis in Patients With Rectal Cancer

Dongqing Wang[1,2†], Zijian Zhuang[1,2†], Shuting Wu[2], Jixiang Chen[3], Xin Fan[3], Mengsi Liu[2], Haitao Zhu[1,2], Ming Wang[1], Jinmei Zou[1], Qun Zhou[1], Peng Zhou[2], Jing Xue[2], Xiangpan Meng[4,5], Shenghong Ju[4,5] and Lirong Zhang[1,4]*

[1] Department of Medical Imaging, The Affiliated Hospital of Jiangsu University, Zhenjiang, China, [2] School of Medicine, Jiangsu University, Zhenjiang, China, [3] Department of General Surgery, The Affiliated Hospital of Jiangsu University, Zhenjiang, China, [4] School of Medicine, Southeast University, Nanjing, China, [5] Department of Radiology, Zhongda Hospital, Southeast University, Nanjing, China

OPEN ACCESS

Edited by:
Pierfrancesco Franco,
University of Eastern Piedmont, Italy

Reviewed by:
Tian-Wu Chen,
Affiliated Hospital of North Sichuan Medical College, China
Satish E. Viswanath,
Case Western Reserve University, United States
Di Dong,
Institute of Automation (CAS), China
Bin Song,
Sichuan University, China

***Correspondence:**
Lirong Zhang
tianchen861@ujs.edu.cn

[†]These authors have contributed equally to this work

Specialty section:
This article was submitted to Cancer Imaging and Image-directed Interventions, a section of the journal Frontiers in Oncology

Received: 31 December 2021
Accepted: 19 May 2022
Published: 07 June 2022

Citation:
Wang D, Zhuang Z, Wu S, Chen J, Fan X, Liu M, Zhu H, Wang M, Zou J, Zhou Q, Zhou P, Xue J, Meng X, Ju S and Zhang L (2022) A Dual-Energy CT Radiomics of the Regional Largest Short-Axis Lymph Node Can Improve the Prediction of Lymph Node Metastasis in Patients With Rectal Cancer. Front. Oncol. 12:846840. doi: 10.3389/fonc.2022.846840

Objective: To explore the value of dual-energy computed tomography (DECT) radiomics of the regional largest short-axis lymph nodes for evaluating lymph node metastasis in patients with rectal cancer.

Materials and Methods: One hundred forty-one patients with rectal cancer (58 in LNM+ group, 83 in LNM- group) who underwent preoperative total abdominal DECT were divided into a training group and testing group (7:3 ratio). After post-processing DECT venous phase images, 120kVp-like images and iodine (water) images were obtained. The highest-risk lymph nodes were identified, and their long-axis and short-axis diameter and DECT quantitative parameters were measured manually by two experienced radiologists who were blind to the postoperative pathological results. Four DECT parameters were analyzed: arterial phase (AP) normalized iodine concentration, AP normalized effective atomic number, the venous phase (VP) normalized iodine concentration, and the venous phase normalized effective atomic number. The carcinoembryonic antigen (CEA) levels were recorded one week before surgery. Radiomics features of the largest lymph nodes were extracted, standardized, and reduced before modeling. Radomics signatures of 120kVp-like images (Rad-signature$_{120kVp}$) and iodine map (Rad-signature$_{Imap}$) were built based on Logistic Regression *via* Least Absolute Shrinkage and Selection Operator (LASSO).

Results: Eight hundred thirty-three features were extracted from 120kVp-like and iodine images, respectively. In testing group, the radiomics features based on 120kVp-like images showed the best diagnostic performance (AUC=0.922) compared to other predictors [CT morphological indicators (short-axis diameter (AUC=0.779, IDI=0.262) and long-axis diameter alone (AUC=0.714, IDI=0.329)), CEA alone (AUC=0.540, IDI=0.414), and normalized DECT parameters alone (AUC=0.504-0.718, IDI=0.290-0.476)](*P*<0.05 in Delong test). Contrary, DECT iodine map-based radiomic signatures

showed similar performance in predicting lymph node metastasis (AUC=0.866). The decision curve showed that the 120kVp-like-based radiomics signature has the highest net income.

Conclusion: Predictive model based on DECT and the largest short-axis diameter lymph nodes has the highest diagnostic value in predicting lymph node metastasis in patients with rectal cancer.

Keywords: rectal cancer (RC), lymph node metastasis, radiomics, dual-energy scanned projection, machine learning, clinical prediction rule

INTRODUCTION

Colorectal cancer is the most common gastrointestinal tumor and the third most diagnosed cancer in men and women. It has the second-highest mortality rate after lung cancer (1). Rectal cancer accounts for more than one-third of colon cancer cases (2). The occurrence of lymph node (LN) metastasis in patients with rectal cancer is highly correlated with poor clinical prognosis and tumor recurrence (2). Yet, different lymph node staging obtained by preoperative imaging evaluation may lead to different clinical decisions and, consequently, different treatment options (3). For example, surgery is usually recommended for patients with N0 (no regional LN metastasis), while preoperative neoadjuvant therapy is often used for those with N1 (1–3 regional LNs metastasis) or N2 (4 or more LNs metastasis).

So far, various traditional imaging modalities, including ultrasound, computed tomography (DECT), magnetic resonance (MR) imaging, and positron emission tomography (PET), have been applied to analyze the lymph node metastasis in patients with rectal cancer; yet, none of them have satisfactory diagnostic performance. Moreover, the diagnosis of LN status relies on their size and the reader's subjective judgment (4, 5). Recently, Gao et al. assessed the methodological and reporting quality of systematic reviews that evaluated the diagnostic value of four different imaging modalities (CT, endorectal ultrasonography (ERUS), endoscopic ultrasound (EUS), and MRI) for LN involvement in patients with rectal cancer. He concluded that no modality was particularly accurate (6). For example, preoperative high-resolution MR shows high soft-tissue resolution and can improve the accuracy of preoperative staging of rectal cancer; yet, its accuracy in detecting N staging is lower than 60% (7, 8). Moreover, no standard criteria for LN evaluation have been proposed so far. For example, some studies emphasized the importance of LN morphological predictors (8), while others disagreed with this data (9).

DECT is an emerging imaging technology (10) used to obtain mixed-energy images, single-energy images, or separate base material images through instantaneous switching of the tube or dual-tube. This feature enables selective quantification of different image materials with different electron density characteristics and atomic numbers, creating material-specific image datasets. The iodine map of DECT, which represents the iodine content in tumor tissues, has been considered a powerful tool for tumor diagnosis and characterization (11). Iodine maps and spectral CT have been useful in assessing rectal cancer by displaying more lesions with higher sensitivity (12) and distinguishing lesions from intestinal contents (13). In terms of LN, previous studies have suggested that quantitative parameters such as normalized iodine concentration (NIC) and effective atomic number (Z_{eff}) can be used to evaluate the LN status of rectal cancer (14). However, these studies only measured the average value of the whole lymph node on DECT while ignoring a large amount of heterogeneous texture and morphological information.

Radiomics is a relatively new quantitative approach to medical imaging. It uses characterization algorithms to extract quantitative features from medical images, such as shape features, intensity-based statistical features, texture features and so on (15, 16). Some studies have suggested that radiomic analysis of rectal tumor images might improve the prognostic evaluation of the tumor and the patients' characterization. For example, Huang et al.(17) found that radiomic score (rad-score) of primary lesions combined with clinical feature nomogram based on readers' subjective evaluation of nodules can improve the accuracy of detecting LN metastasis in patients with colorectal cancer. Yet, the final performance of the model was poor (AUC=0.778). In addition, the study did not examine the regional lymph nodes.

Based on the data reported above, we summarized three main deficiencies in the imaging evaluation of lymph nodes in rectal cancer: (1) the diagnostic criteria and methods for assessing LN, which have not yet reached a consensus. There is no clear threshold for lymph node size and other indicators for reference. (2) The repeatability of some ambiguous subjective signs has not been yet verified, which reduces the accuracy of the diagnosis. (3) Lack of quantitative and heterogeneous analysis of lymph nodes, especially on images with high spatial resolution and thin slices, such as DECT. Thus, in this study, we further explored the value of DECT radiomics of the regional lymph nodes for evaluating lymph node metastasis in patients with rectal cancer.

MATERIALS AND METHODS

Patients

Patients diagnosed with rectal cancer by colonoscopy who underwent a spectral CT (a kind of DECT) scan for preoperative evaluation between June 2017 to May 2021 were

included in this study. The inclusion criteria were: 1. no history of another type of cancer; 2. patients without prior radiotherapy and/or chemotherapy; 3. rectal cancer pathologically confirmed after surgery; 4. total mesorectal resection; suspicious lymph nodes were dissected; 5. lymph node metastasis was determined based on the final pathology report of the surgical specimen. Exclusion criteria were: 1. poor CT image quality; 2. patients with no regional lymph nodes available for analysis; 3. incomplete pathological or baseline-related information (**Figure 1**).

Finally, 141 patients (101 males, 40 females; median age 67, IQR: 58-73; range: 32-87 years old) were included in the study. The T tumor stage was recorded according to the guideline of NCCN (18). The carcinoembryonic antigen (CEA) index level was recorded one week before surgery. LNM+ patients were defined as those having one or more lymph node metastasis (identified by the pathologists); otherwise, patients were classified as LNM-. According to the examination time of DECT, the patients were assigned to the training and testing groups using a ratio of 7:3. Splitting patients by examination time is called temporal validation, which is recommended by many experts (19, 20).

The institutional review board approved this prospective study, and all patients signed an informed consent form.

CT Reconstruction and Post-Processing

All patients underwent head-first scanning in the supine position. Before the exam, patients fasted for 6 hours without undergoing bowel cleansing preparation. Patients were asked to hold their breath during the scanning. DECT (Revolution CT, GE Healthcare, USA) with Gemstone Spectral Imaging (GSI) mode was used to perform a plain scan and enhanced scan (from the diaphragm to the lower edge of the pubic symphysis). The non-ionic contrast agent ioversol (350 mg/ml, Jiangsu Hengrui Pharmaceutical Co., Ltd., China; 1.5ml/Kg, injection rate: 3.0 or 3.5ml/s) was applied for enhancement by the nursing staff. Then, 30ml of normal saline was injected intravenously at the same rate. The spectral scanning parameters were: the tube voltage was instantaneously switched between 140kVp and 80kVp, the tube current was set to the automatic tube current, and the maximum reference tube current was 600mA; the tube rotation speed was 0.5 sec/r; the pitch was set to 1.984:1. The 120kVp-like image in the

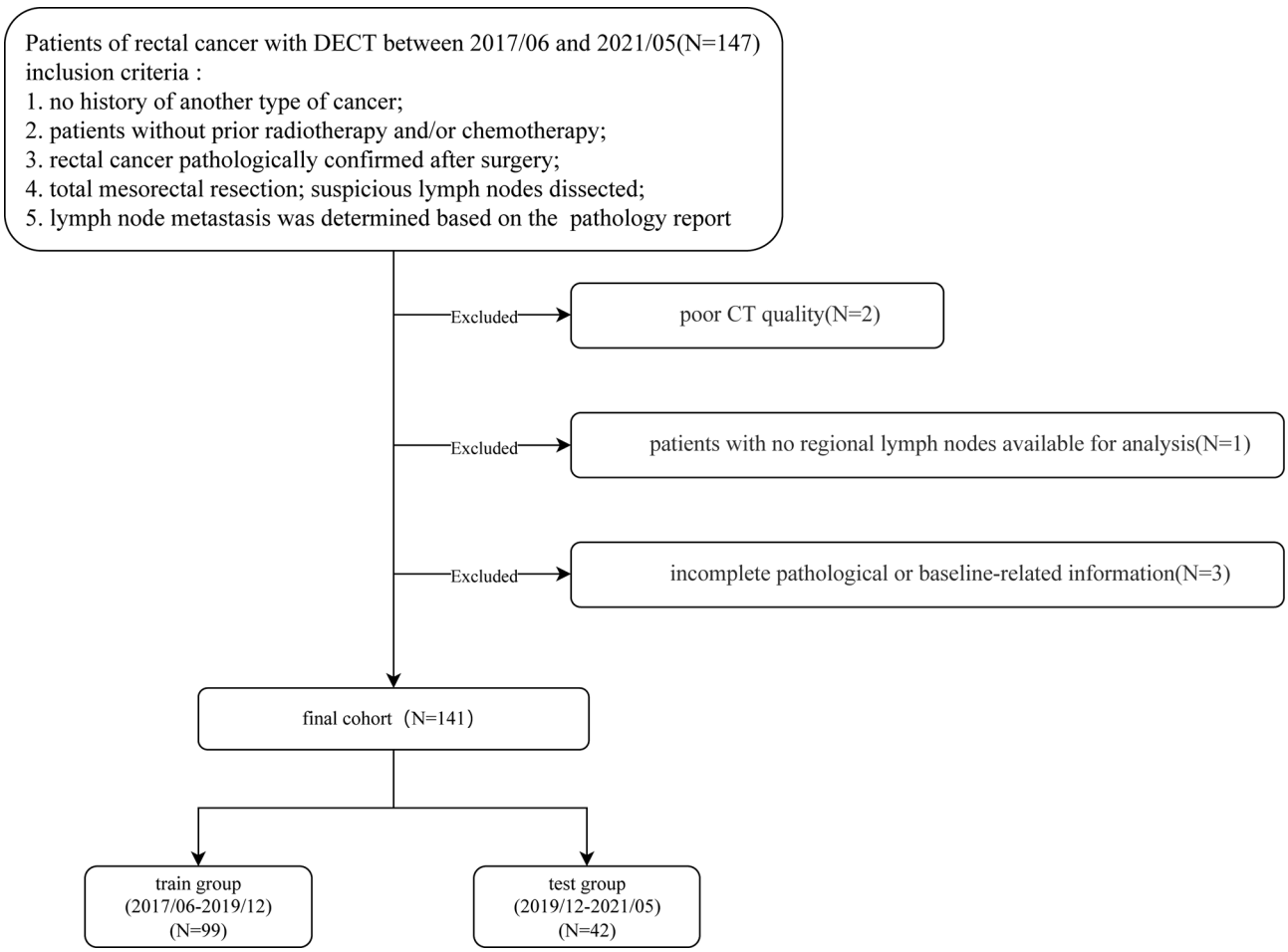

FIGURE 1 | Patient selection flowchart.

venous phase was automatically reconstructed according to the kVp-like kernel function after scanning, and the thickness was 1.25mm. The CT data were reconstructed using 50% adaptive statistical iterative reconstruction (ASIR, GE Healthcare) and then transferred to an advanced workstation (AW4.7, GE Healthcare) for analysis and post-processing.

Raw data were loaded to the GSI Viewer software application, after which an iodine (water) map was obtained. Iodine concentration was 100mg/cm^3. Since the 120kvp-like and iodine maps were reconstructed from the same raw data, the layer thickness, spacing, and spatial position information were the same (no registration was required).

Selection of the Largest Regional Lymph Node

On the 120kVp-like venous phase image, lymph nodes inside and outside the mesorectum along the superior rectal artery were examined. The areas included the mesorectum and the anterior sacrum. The largest lymph node was defined as the lymph node with the longest short-axis diameter for the superior rectal artery and the lateral mesangial inner iliac lymph nodes. If there were multiple large lymph nodes with similar diameters (the difference is ≤1mm), the following classification criteria were applied: 1. lymph nodes that are heterogeneously enhanced, including necrosis or mucinous texture; 2. lymph nodes that are round rather than oval; 3. lymph nodes that are closer to the lesion; 4. lymph nodes that are located above but not below the lesion.

The above annotation process was not repeated for arterial phase images or iodine maps, but the lymph node determined by the venous phase was searched and matched to the corresponding position.

All lymph nodes were analyzed by two experienced radiologists (Zhou Q. and Zou J.M. with more than 10 years of experience in abdominal imaging diagnosis) who were blind to the postoperative pathological results. A third radiologist (Zhang L.R., with more than 20 years of experience in abdominal imaging diagnosis) was invited if there were any disagreements. The two readers manually measured the long and short-axis diameter of the selected lymph node using the workstation on the 120 kVp-like axial images, and the average of the measured values of the two was recorded.

Quantitative Parameters of DECT for Evaluating Largest Regional Lymph Nodes

This method was performed as previously described (21). The whole measurement process was carried out in the GSI VIEWER of the workstation. Two readers (Zhou Q. and Zou J.M.) manually drew ROI on the cross-sectional image to cover the entire lymph node as much as possible, excluding the surrounding mesangial tissue. ROI was also placed on the descending aorta at the bifurcation of the right renal artery. The iodine concentration (IC) and effective atomic number (Z_{eff}) of the largest lymph nodes and aorta in the arterial and portal phases were obtained. The normalized iodine concentration (NIC) value is the iodine uptake value of the lymph nodes divided by the iodine uptake value of the aorta.

$$NIC_{LN} = IC_{LN}/IC_{aorta}$$

The normalized Z_{eff} is the effective atomic number of the lymph node divided by the effective atomic number of the aorta.

$$NZ_{eff_{LN}} = Z_{eff_{LN}}/Z_{eff_{aorta}}$$

Four DECT quantitative parameters included: AP NIC, AP normalized Z_{eff}, VP NIC, and VP normalized Z_{eff}. The above parameters were analyzed by averaging the measured values of the two readers.

Radiomics Feature Extraction

All segmentation was performed on 3D Slicer v. 4.8.1. A reader (Zou J.M.) outlined all the slices of the largest lymph node on the venous iodine map. Thirty cases were randomly selected, and two radiologists (Zou J.M. and Zhou Q.) redrew their ROIs one month later for the repeatability test of features. The obtained mask was also suitable for 120kVp-like images in the venous phase. (**Figure 2**) Using pyradiomics for feature extraction based on 3D ROIs, 833 features were extracted from 120kVp-like and iodine images. The specific features are shown in **Table 1**. Intraclass correlation coefficient (ICC) was used for analyzing the consistency at intraobserver and interobserver; the features of *r* value greater than 0.7 were analyzed in the follow-up.

Selection of Radiomics Features and Establishment of the Models

This part was completed on the software FAE v3.7.0 (20). All models were built based on the same training group, and all features were standardized to a standard normal distribution using Z-score to reduce the difference in the range of feature values. Pearson correlation coefficients (PCC) were used to reduce the dimensionality of features. When the coefficient was >0.86, one of them was randomly removed for dimensionality reduction. Then recursive feature elimination (REF) was used to filter features; Logistic Regression *via* Lasso was used as a classifier for modeling. To avoid overfitting, each feature requires at least 10-15 patients to participate in the radiomic signature (22, 23). The maximum number of features was limited to 10 because the number of patients in the training group was 99. Then 10-fold cross-validation was used to select the best model based on the means of AUCs. Finally, a radiomic model of the regional largest lymph node (Rad-signature$_{120kVp}$) based on venous phase images of 120kVp-like and a radiomics model of regional largest lymph node based on venous phase iodine maps (Rad-signature$_{Imap}$), were established. The flow chart of the whole research scheme is shown in **Figure 3**.

Statistical Analysis

For continuous variables, the Kolmogorov-Smirnov was used to compare the cumulative distributions of the data sets. The mean ± standard deviation was used to express normal distribution, and the T-test was used to compare the differences between groups with normal distribution; the

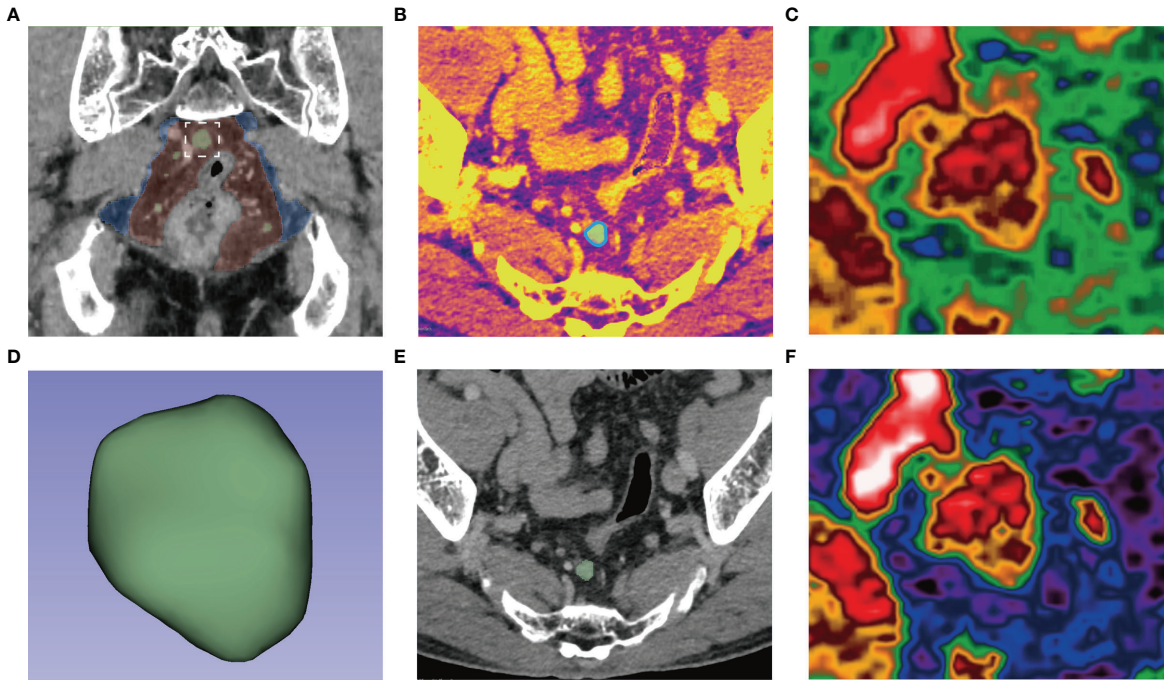

FIGURE 2 | **(A)** After searching for lymph nodes in the mesorectum (red) and extramesenteric (blue) areas, the largest lymph nodes (white box) were delineated along its edge (blue line) in the axial iodine map **(B)** to form a 3D-ROI **(D)**. The ROI could be used for 120kVp-like images without registration **(E)**. The pseudocolor map of the largest lymph nodes in the iodine map **(C)** and 120kVp-like image **(F)** show apparent internal heterogeneity.

median and quartile were used for the values that did not meet the normal distribution, and the Mann-Whitney U test was used to compare the differences between these groups.

The Chi-square test or Fisher's exact test was used for categorical variables. The receiver operator characteristic (ROC) curves were drawn for each model or indicator, and the area under the Curve (AUC) was used to measure diagnostic performance. The Delong test was used to compare the differences in ROC curves. The point with the largest Youden index in each ROC curve was selected as the optimal threshold of the model. The Youden index, sensitivity, specificity, and accuracy were calculated. The integrated discrimination improvement (IDI) value of two radiomics signature to other predictors were computed. Finally, a decision curve was used for different models or predictors in the testing group to analyze their clinical applicability.

The radiomic signatures and the long-axis and short-axis diameter of the lymph node were used, and the Spearman correlation analysis to evaluate the correlation between the established radiomic signatures and the lymph node size index. Statistical analyses were performed using SPSS software 26.0, MedCalc 20.0, and R software 3.6.1. A P-value<0.05 was considered to be statistically significant.

TABLE 1 | The list of the radiomics features.

Feature category	Feature number
original	
shape	14
first order	18
GLCM	22
GLRLM	16
GLSZM	16
NGTDM	5
GLDM	14
wavelet	
LLH	91
LHL	91
LHH	91
HHL	91
HLL	91
HLH	91
HHH	91
LLL	91
TOTAL	**833**

GLCM, gray-level co-occurrence matrix; GLRLM, gray-level run-length matrix; GLSZM, gray-level size zone matrix; NGTDM, neighbourhood gray-tone difference matrix; GLDM, gray level dependence matrix; L, lowpass filters; H, highpass filters.
In bold: "TOTAL" is just the sum of feature numbers.

RESULTS

Patient Characteristics

A total of 141 patients with rectal cancer were included in this study. The characteristics of the patients in the training cohort and testing cohort are shown in **Table 2**. There were 99 patients in the training group and 42 in the testing group. There were 58 patients (41.13%) in the LNM+ group and 83 (58.87%) in the

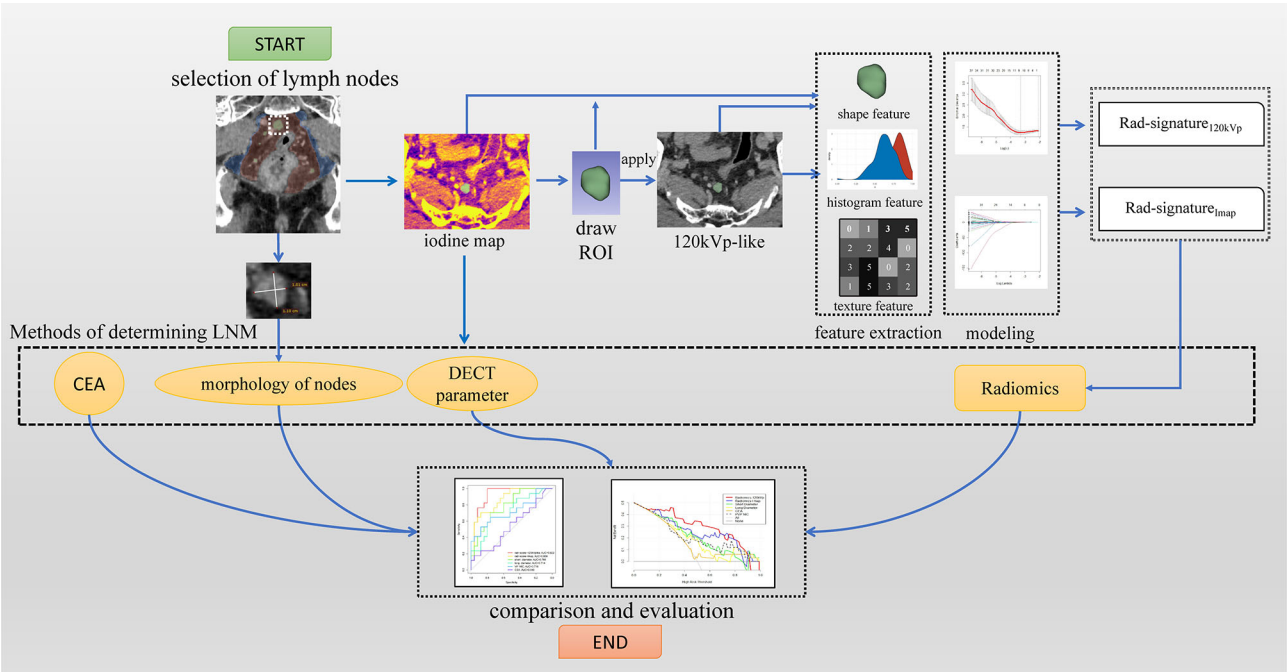

FIGURE 3 | A study workflow. Imaging processing began by selecting the largest lymph nodes; finally, four categories of methods were evaluated.

TABLE 2 | Study sample demographics and clinical characteristics.

Characteristics	Training group (n=99)	Testing group (n=42)	*P*
Sex, No. (%)			0.208
male	74 (74.7%)	27 (64.3%)	
female	25 (25.3%)	15 (35.7%)	
Age (IQR)	67 (57–73)	67.5 (58-72.25)	0.787
Long diameter, mm (IQR)	7.85 (6.06-9.88)	7.03 (5.69-9.45)	0.668
Short diameter, mm (IQR)	5.68 (4.64-8.02)	5.56 (4.39-7.19)	0.573
T stage			0.971
1	10 (10.1%)	5 (11.9%)	
2	27 (27.3%)	10 (23.8%)	
3	53 (53.5%)	23 (54.8%)	
4	9 (9.1%)	4 (9.5%)	
CEA, ng/ml (IQR)	3.91 (2.18-7.17)	3.47 (1.92-7.85)	0.690
LNM, No. (%)			0.918
positive	41 (41.4%)	17 (40.5%)	
nagetive	58 (58.6%)	25 (59.5%)	

IQR, interquartile range.

LNM- group. Clinical characteristics (gender, age, long-axis diameter, and short-axis diameter of the largest regional lymph node, pathological T stage, CEA, and lymph node metastasis) were not statistically different between the training group and the testing group (all $P>0.05$); while the long-axis diameter, short-axis diameter, and T stage of the lymph node were statistically different between the LNM+ group and the LNM- group (all $P<0.05$), in both training and the testing groups. Moreover, CEA was statistically different between patients with different N stages in the training group (**Table 3**).

The Efficiency of Long-Axis and Short-Axis Diameter and CEA in Predicting LN Metastasis

The median value of the long-axis diameter of the largest lymph nodes was 7.57 (IQR: 5.88-9.73), while the median value for short-axis diameter was 5.62 (IQR: 4.63-7.66). For LNM- patients, the median value of a long-axis diameter was 7.00 (IQR: 5.52-8.89) and 4.99 (IQR: 4.02-6.28) for the short-axis diameter; for patients with LNM+, the median value of the long-axis diameter was 8.79 (IQR: 6.81-11.60), and the median value of the short-axis diameter was 7.05 (IQR: 5.27-10.10)(**Table 4**,

TABLE 3 | Study sample demographics and clinical characteristics of patients with LNM+ and LNM- rectal cancer.

Characteristics	Training group		*P*	Testing group		*P*
	LNM+	LNM-		LNM+	LNM-	
Sex, No. (%)			0.525			
male	32 (78%)	42 (72.4%)		13 (76.5%)	11 (44%)	0.174
female	9 (22%)	16 (27.6%)		4 (23.5%)	14 (56%)	
Age (IQR)	66 (59.5-73)	68 (55.75-73.25)	0.991	68.53 ± 9.04	64.52 ± 9.55	0.176
Long-axis diameter, mm(IQR)	8.84 (6.73-11.7)	7.15 (5.53-8.98)	0.002	8.74 (6.87-13.1)	6.88 (5.44-8.02)	0.02
Short-axis diameter, mm(IQR)	7.29 (5.25-10.28)	5.06 (4.21-6.29)	<0.001	6.8 (5.28-9.88)	4.97 (3.89-6.08)	0.002
T stage, No. (%)			0.005			<0.001
1	0 (0%)	10 (17.2%)		0 (0%)	5 (20%)	
2	8 (19.5%)	19 (32.8%)		0 (0%)	10 (40%)	
3	27 (65.9%)	26 (44.8%)		13 (76.5%)	10 (40%)	
4	6 (14.6%)	3 (5.2%)		4 (23.5%)	0 (0%)	
CEA, ng/ml(IQR)	4.53 (3.42-11.08)	3.31 (1.93-5.51)	0.003	3.69 (1.94-9.51)	3.2 (1.88-7.86)	0.663

IQR, interquartile range.

Figures 4A, B); the difference in the long-axis diameter and short-axis diameter between patients with LNM- and LNM+ was statistically significant ($P<0.001$).

In the overall cohort, the short-axis diameter of the largest lymph node has a higher AUC in predicting lymph node metastasis than the long-axis diameter (0.755 [95%CI:0.676-0.824] vs. 0.691 [95%CI:0.608-0.766]; $P=0.004$). When the short-axis diameter threshold was 6.45mm, the sum of sensitivity and specificity was the highest (62.1%and 80.7%, respectively), and the corresponding accuracy was 73.0%. Furthermore, when the long-axis diameter threshold was 8.19 mm, the sum of sensitivity and specificity was the highest (60.3% and 71.1%, respectively), and the corresponding accuracy rate was 66.7% (**Table 4**).

The median value of CEA was 3.73 (IQR: 2.17-7.58); the median value of CEA in group LNM- was 3.26 (IQR: 1.94-6.04), and the median value of CEA in group LNM+ was 4.42 (IQR: 3.08-10.83) (**Table 4**, **Figure 4C**), and the difference was significant ($P=0.006$). The AUC of CEA in predicting lymph node metastasis was 0.631 [95%CI:0.538-0.723] in all patients. When the threshold was 3.0, the accuracy was the highest (the sensitivity was 77.6% and the specificity was 45.8%), and the corresponding accuracy was 58.9%; when the threshold was 5 (abnormal clinical value), the sensitivity was 46.6%, the specificity was 68.7%, and the corresponding accuracy was 57.5%.

Diagnostic Efficacy of DECT Quantitative Parameters for Regional Lymph Nodes in Predicting

The distributions, AUCs, cut-offs, sensitivities, and specificities of 4 DECT quantitative parameters in the overall population are shown in **Table 4**. The ROC curves of the four DECT quantitative parameters are shown in **Figure 4**. The AUC of VP NIC was significantly higher than AP normalized Z_{eff} ($P=0.0286$) and VP normalized Z_{eff} ($P=0.0059$). There was no statistical difference between VP NIC and AP NIC ($P=0.2506$).

Radiomics Models and Their Diagnostic Power in Predicting Lymph Node Metastasis

After the intra-observer and inter-observer ICC tests, 424 and 542 features of the largest lymph nodes in the 120kVp-like image and the iodine map, respectively, were extracted. The results of cross-validation with different feature numbers are shown in **Supplementary Figure 1**. Rad-signature$_{120kVp}$ is composed of 10 features (violin plots of 10 features are shown in **Supplementary Figure 2;** coefficients of features are shown in **Supplementary Table 1**). The AUC of signatures in the training group and the testing group were 0.916 [95%CI: 0.861-0.963] and 0.922 [95% CI: 0.825-0.990], respectively (**Figure 5**).

Rad-signature$_{Imap}$ is composed of 8 features (**Supplementary Figure 2** and **Supplementary Table 2**). The AUC of signature in the training group was 0.949 [95%CI: 0.901-0.980], and the AUC in the testing group was 0.866 [95%CI: 0.742-0.961]. The feature contribution and ROC curve of the iodine map radiomics signature are shown in **Figure 6**. The cut-offs with the highest Youden index, sensitivities, specificities and IDI values of two radiomics signatures in the testing group are listed in **Table 5**. The *r* values of the Spearman correlation analysis between Rad-signature$_{120kvp}$ and the short-axis diameter and long-axis diameter are 0.534 and 0.487, respectively, suggesting a moderate correlation (23) between Rad-signature$_{120kvp}$ and the morphological indicators of node size.

Comparison of Different Models and Indicators in Predicting Lymph Node Metastasis

The area under the curve of the six models in the testing group was compared, and Delong test results are shown in **Table 6**.

TABLE 4 | Comparison of morphology predictors, CEA and DECT quantitative parameters on distributions, AUCs, cut-offs, sensitivities and specificities.

Predictor	Overall	LNM-	LNM+	*P*	AUC	CUT-OFF	Sensitivity	Specificity
long-axis diameter, mm	7.57 (5.88-9.73)	7.00 (5.52-8.89)	8.79 (6.81-11.60)	<0.001	0.691 (0.608-0.766)	6.45	62.1	80.7
short-axis diameter, mm	4.99 (4.02-6.28)	4.99 (4.02-6.28)	7.05 (5.27-10.10)	<0.001	0.755 (0.676-0.824)	8.19	60.3	71.1
APNIC	0.1786 (0.1425-0.2323)	0.1889 (0.1530-0.2448)	0.1710 (0.1374-0.2128)	0.053	0.596 (0.510-0.678)	0.1760	60.4	60.3
VPNIC	0.6622 (0.5535-0.7604)	0.6937 (0.6036-0.7800)	0.6288 (0.4715-0.7303)	0.002	0.655 (0.536-0.702)	0.5545	84.3	41.4
$APNZ_{eff}$	0.7512 (0.7247-0.7843)	0.7563 (0.7233-0.7858)	0.7494 (0.7280-0.7777)	0.56	0.596 (0.443-0.613)	0.7537	53	58.6
$VPNZ_{eff}$	0.9458 (0.9195-0.9656)	0.9530 (0.9311-0.9676)	0.9421 (0.9057-0.9595)	0.014	0.622 (0.536-0.702)	0.9551	48.2	70.7
CEA, ng/ml	3.90 (2.17-7.58)	3.35 (1.94-6.04)	4.42 (2.94-10.83)	0.008	0.631 (0.538-0.723)	3.36	70.7	50.6

Data are reported as medians with interquartile ranges. P values comes from Mann-Whitney U test. AUCs are reported with 95% confidence interval. The selection of cut-off was based on the maximum Youden index. APNIC: arterial phase normalized iodine concentration; VPNIC: venous phase normalized iodine concentration; $APNZ_{eff}$: arterial phase normalized effective atomic number; $VPNZ_{eff}$: venous phase normalized effective atomic number.

$Rad\text{-}signature_{120kVp}$ achieved the highest AUC (AUC=0.922) in prediction lymph node metastasis compared with other predictors [short-axis diameter (AUC=0.779, IDI=0.262) and long-axis diameter alone (AUC=0.714, IDI=0.329); CEA (AUC=0.540, IDI=0.414), and normalized DECT parameters (AUC=0.504~0.718, IDI=0.290-0.476)](*P*<0.05 in Delong tests). The ROC curve of 6 models is shown in **Figure 7**.

In order to evaluate the clinical practicability, a decision curve of six indicators or signatures has also been drawn (**Figure 8**). When the threshold probability was between 0 and 0.9, $Rad\text{-}signature_{120kvp}$ had a higher net profit than other indicators and was only slightly lower than the $Rad\text{-}signature_{Imap}$ when the threshold probability was 0.7.

DISCUSSION

This study explored the value of dual-energy computed tomography (DECT) radiomics of the regional largest lymph node for evaluating lymph node metastasis in patients with rectal cancer. We discovered that DECT radiomics of the regional largest short-axis lymph node could improve the prediction of lymph node metastasis in patients with rectal cancer.

The method used to determine patients' lymph node metastasis status was based on the regional largest short-axis diameter lymph nodes. Adopting this method was based on the following: 1. In clinical practice, size is still the primary criterion for judging the status of LN (4, 8, 24). Other measures include the

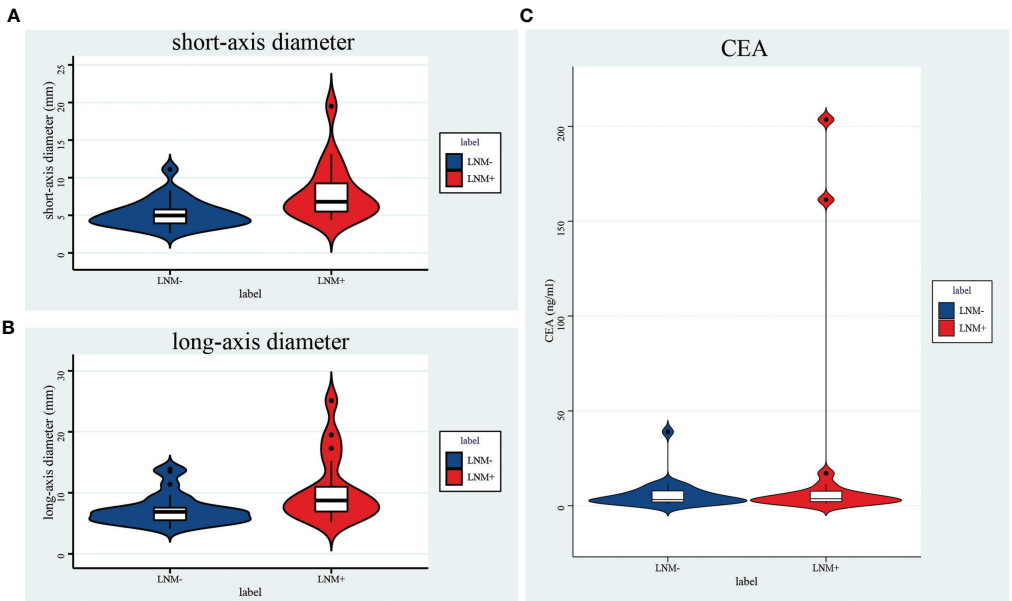

FIGURE 4 | Violin plot of a short-axis diameter **(A)**, a long-axis diameter **(B)**, and CEA **(C)**. All of them were significantly different between LNM+ and LNM- groups.

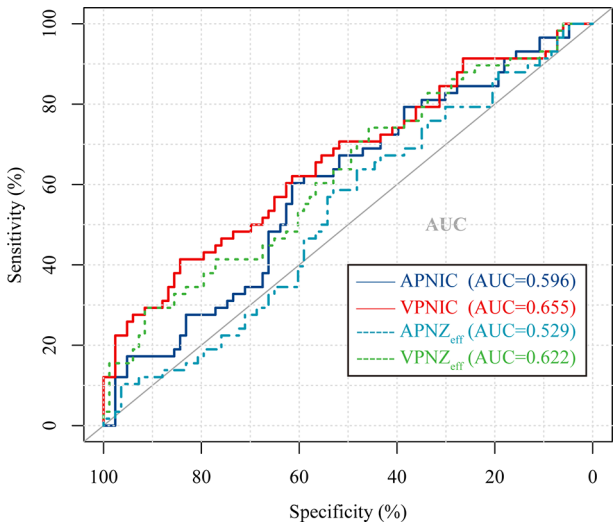

FIGURE 5 | Receiver operating characteristic (ROC) curve of 4 different normalized DECT parameters used to discriminate LNM (+) from LNM (-) in the overall cohort. APNIC, arterial phase normalized iodine concentration; VPNIC, venous phase normalized iodine concentration; $APNZ_{eff}$, arterial phase normalized effective atomic number; $VPNZ_{eff}$, venous phase normalized effective atomic number.

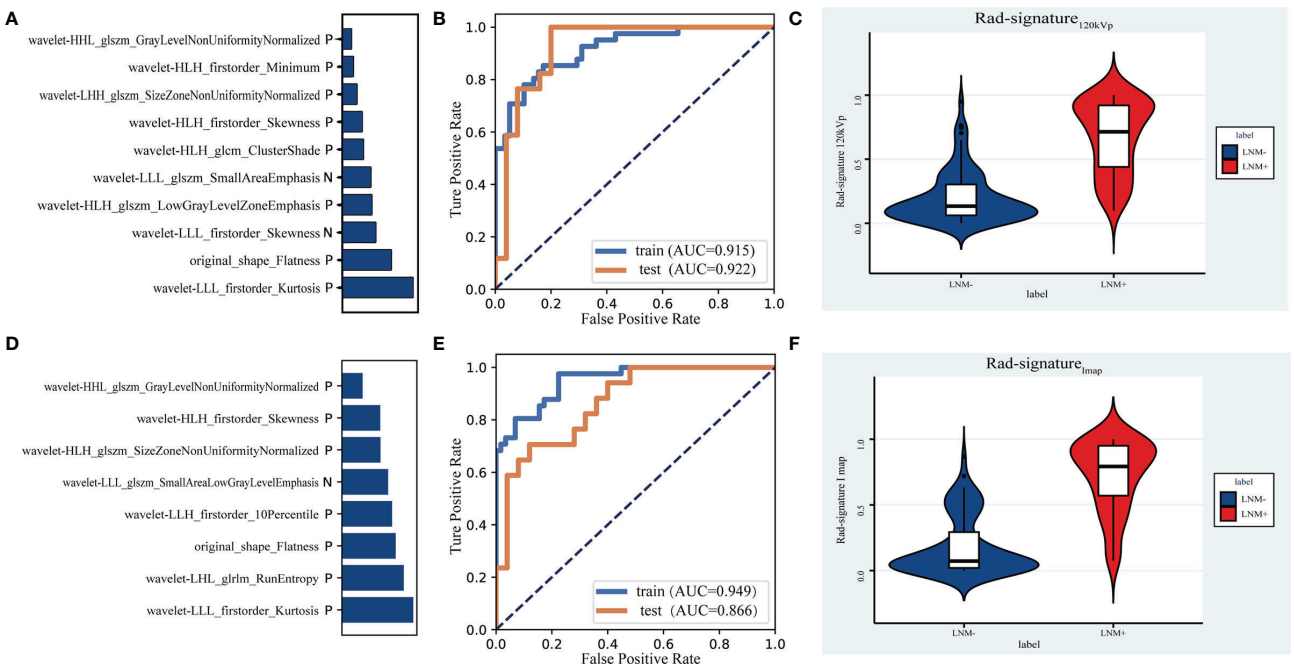

FIGURE 6 | The contribution of 10 features in the signature of 120kVp-like images **(A)** and the signature of iodine map **(D)**. Receiver operating characteristic (ROC) curves to discriminate LNM (+) from LNM **(-)** for the 120kvp-like radiomics model **(B)** and iodine map **(E)** radiomics model in the training and testing cohort. Violin plots of $Rad\text{-}signature_{120kvp}$ **(C)** and $Rad\text{-}signature_{Imap}$ **(F)** to discriminate LNM (+) from LNM (-).

shape (circle) (4) and heterogeneity (8). Combined with the above criteria, the "largest short-axis diameter lymph node" was defined as the highest risk lymph node in the region. 2. Rectal cancer's lymph node metastasis area is relatively fixed. Langman et al. (25) showed that most rectal cancer metastatic lymph nodes are located in the mesorectum close to the tumor and along the superior rectal artery. Therefore, the area defined in this study was sufficient to include metastatic lymph nodes. 3. Another

TABLE 5 | The cut-offs, sensitivities, specificities and IDI index of two radiomics signatures in the testing group.

	Rad-signature120kvp	Rad-signatureImap
cut-off	0.1851	0.5122
Sensitivity (%)	100.0 [95CI%:80.5-100.0]	70.59 [95CI%:44.0-89.7]
Specificity (%)	80.0 [95CI%:59.3-93.2]	88.00 [95CI%:68.8-97.5]
IDI to SD	0.262	0.133
IDI to LD	0.329	0.199
IDI to VPNIC	0.29	0.161
IDI to CEA	0.414	0.285

The selection of cut-off was based on the maximum Youden index. Only the IDI index to DECT quantitative parameter with the highest AUC (VPNIC) was calculated. SD, short-axis diameter; LD, long-axis diameter; VPNIC, venous phase normalized iodine concentration.

TABLE 6 | *P*-values of DeLong test for AUC of 6 different signatures or indicators.

	Rad signature120kvp	Rad signaturel map	Short diameter	Long diameter	VP NIC	CEA
Rad-signature120kvp (AUC=0.922)	–	0.2299	0.0473*	0.013*	0.0359*	0.0001*
Rad-signatureImap (AUC=0.866)	0.2299	–	0.2063	0.0333*	0.1167	0.0018*
Short-axis diameter (AUC=0.779)	0.0473*	0.2063	–	0.1682	0.1719	0.0098*
Long-axis diameter (AUC=0.714)	0.013*	0.0333*	0.1682	–	0.9731	0.1049
VP NIC (AUC=0.718)	0.0359*	0.1167	0.5739	0.9731	–	0.1719
CEA (AUC=0.540)	0.0001*	0.0018*	0.0098*	0.1049	0.5739	–

**P-value<0.05; VP NIC, venous phase normalized iodine concentration.*

reason was based on previous study data, which suggested that mapping LNs on CT may be challenging (21, 26). More lymph nodes can be seen in the specimen than on CT (26, 27). In addition, the inclusion of all lymph nodes for research has increased the number of target nodes but the uncertainty of image-specimen-pathology correspondence. We also noted that many studies adopted a method similar to ours (21, 28–30), which confirmed its feasibility. The excellent final performance of the established model also ensures the effectiveness of this method.

In this study, the predictive model based on a 120kVp-like image showed the highest diagnostic value in predicting lymph node metastasis in patients with rectal cancer. We also found that using an iodine map does not increase the extra performance compared to the 120kVp-like image reproduced by DECT. CT images combined with radiomics of the primary lesion to predict the status of lymph nodes in colorectal cancer have been reported before, showing an AUC of 0.778 (17, 30). Yet, these studies used radiomics features of primary tumors combined with clinical features (CEA levels), and CT reported the LN status. Therefore, we believe that the objective quantitative radiomics information of the lymph node itself should not be ignored.

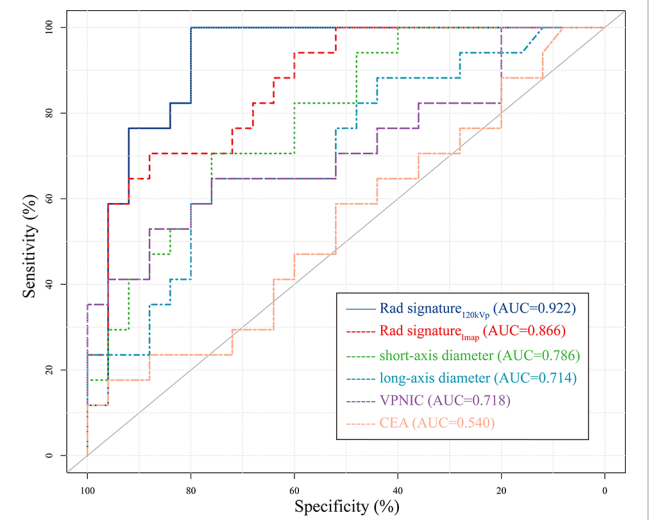

FIGURE 7 | Receiver operating characteristic (ROC) curve of 6 different signatures or indicators in the testing cohort. The 120kVp-like radiomics signature had the highest area under Curve (AUC). Only the curve of the DECT quantitative parameter with the highest AUC (VPNIC) was drawn to improve readability. VPNIC: venous phase normalized iodine concentration.

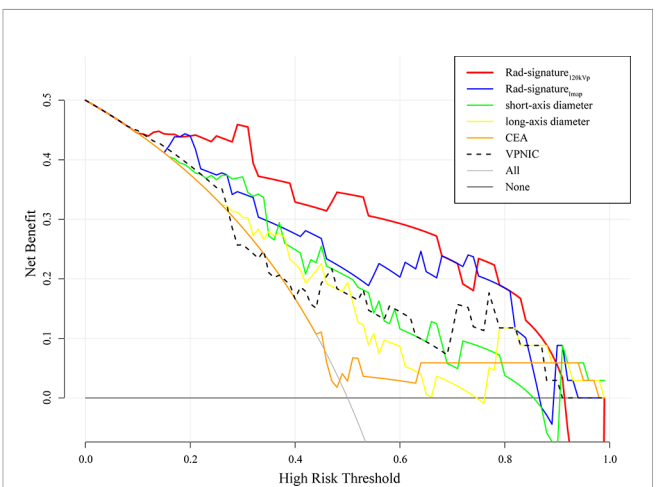

FIGURE 8 | Decision curve of 6 different signatures or indicators in the testing cohort. The 120kVp-like radiomics signature had the highest area under Curve (AUC) in the majority range of risk thresholds. Only the curve of DECT quantitative parameter with the highest AUC was drawn to improve readability. VPNIC: venous phase normalized iodine concentration.

After the preprocessing and selection, 10 and 8 features of the largest lymph nodes in the common portal phase image and the iodine map, respectively, were reserved. Flatness was the only morphological feature contained in the two imaging radiomics signatures. It represents the ratio of the long-axis length to the shortest-axis length (31); the closer it is to the spherical shape, the closer it is to 1. In other words, "round" lymph nodes tend to be malignant, which is consistent with previous studies (32) and guidelines (4).

Intensity-based statistical features shared by the iodine map and the 120kVp-like signatures included Skewness and Kurtosis. Moreover, each of the two signatures has a different histogram feature. Minimum was found in the 120kVp-like signature and 10Percentile (P10) in the iodine map signature. In fact, the meaning of the two is similar. P10 is more robust to grey level outliers than the minimum grey level (31). Skewness and Kurtosis may represent low-enhancement areas in the lymph nodes. Necrosis is the most common type of metastatic lymph node, and the low-enhancement areas in the lymph nodes indicate necrotic components in the lymph nodes. The feature Minimum and 10Percentile may indicate that the infiltration of surrounding fat may increase the density of low-density fat in the ROI. It is worth mentioning that some of the DECT quantitative parameters, such as NIC, are essentially Intensity-based statistical feature Mean based on the iodine map.

Texture features were also found to be relevant. Observing the meaning of these texture features and related conditions, the heterogeneity of metastatic lymph nodes was higher, which is also in line with our conventional cognition. Rectal benign lymph nodes include follicle, sinusoidal and mixed types, while metastatic lymph nodes include two major types of partial and complete tumor invasion and four subtypes of cellular proliferation, fibrosis, necrosis, and cyst formation (33). Thus, the heterogeneity analysis of lymph nodes is crucial. Establishing a correlation between conventional imaging findings and metastatic infiltration is challenging (25, 34), which is why size is always the main assessment parameter. The radiomics features quantify these heterogeneous manifestations to a certain extent; these features are usually not recognized and distinguished by the naked eye (16). The study found that texture features, shape, and histogram features overlap between the signature of the iodine map and the 120kVp-like image. Some features are slightly different but similar in meaning. It is generally believed that radiomics features lack repeatability, especially from different CT modalities. Nevertheless, these features remain stable in different reconstructed images. Therefore, these features should be further explored and validated. On the other hand, no feature directly reflects the size of the lymph node. Correlation analysis indicated that the *r*-value of the radiomic score and size parameter is around 0.5, which means that the radiomic signature still has a moderate correlation with the size of the lymph node.

The sensitivity and specificity of the maximum short-axis diameter of regional lymph nodes in this study were similar to those of CT reported by META analysis (34) and comparative analysis (6) but also higher than those of long-axis diameter and CEA. This shows that in the absence of radiomics or other analysis methods, short-axis diameter is still one of the most effective criteria for judging lymph node involvement of rectal cancer in clinical practice. It should be noted that, in this study, we measured the long-axis diameter of the highest-risk lymph node, which does not represent the longest diameter of all regional lymph nodes. Therefore, the diagnostic efficiency of the actual maximum longest diameter of lymph nodes in the region may be lower. In addition, because some benign lymph nodes tend to show slender type, not included by our criteria, it significantly reduces the specificity of diagnosis.

The value of DECT quantitative parameters assessing rectal cancer's benign and malignant lymph nodes has attracted attention in recent years. However, the results from previous studies are not consistent (8, 21, 35). Nevertheless, no consensus on the diagnostic efficacy of DECT quantitative parameters in lymph node diagnosis has been proposed. Our results suggested an AUC of 0.7 when using DECT quantitative parameters alone, which is similar to data reported by Al-Najami et al. (36) but lower than others' reports (21, 24). Based on the above results, we think that some studies may overestimate the diagnostic performance of DECT parameters. The result also confirms that the efficiency of the iodine map signature is not better than that of the 120kVp-like venous phase signature. The essence of these quantitative parameters reflects the enhanced regional iodine concentration. Metastatic lymph nodes of rectal cancer show relatively low iodine concentration due to necrosis and tumor infiltration. These concentrations can also be quantified by ordinary portal phase CT images. Yet, the factors that lead to the iodine uptake of lymph nodes may vary, such as circulatory status and lymph node blood supply. Therefore, simply measuring a lymph node's average iodine concentration or atomic number without considering the morphological characteristics or heterogeneity of nodes does not provide sufficient diagnostic value.

Serum CEA (carcinoembryonic antigen) is one of the most important and commonly used tumor markers for rectal cancer (35). CEA is overexpressed in more than 70% of rectal cancer and can guide tumor detection and treatment (37). In this study, the accuracy of CEA to predict the N stage was only 57% when the abnormal value standard was 5ng/ml (Clinical threshold); however, the specificity of the diagnosis of lymph node metastasis was higher than the sensitivity, which was similar to data reported by Moertel et al. (38). This data indicates that lymph node metastasis can be suspected when CEA is greater than 5ng/ml, and regional lymph nodes should be more carefully evaluated. Yet, our data suggest that CEA alone may not be the best indicator of lymph node metastasis and could be jointly used with other indicators, as reported by some previous studies (17, 37).

This study still has some limitations: 1. this is a single-center study with relatively small sample size. 2. Subjects of this study are patients who have undergone surgery without neoadjuvant therapy: yet, assessing the nature of lymph nodes after neoadjuvant therapy has always been a challenging process. 3. This study did not consider some semantic features used in clinical practice such as "texture", "border", and "shape" for comparison. 4. This study did not discuss the combined value of some indicators and radiomics signatures. 5. The patient's overall lymph node metastasis status is judged based on the highest-risk lymph nodes. There is no one-to-one correspondence between

the pathology and the lymph nodes on the image. The model cannot distinguish the N1 or N2 stage from LNM. Previous reports showed that metastatic lymph nodes could be found in images (39), but if these small lymph nodes are the only metastatic lymph nodes of the patient, it is impossible to make a correct diagnosis using pure imaging methods. 6. Finally, the reproducibility of radiomics features has always been questioned. Further research is needed to establish a more robust model.

To sum up, a predictive radiomics model based on a 120kVp-like image and the largest short-axis diameter lymph node showed the highest diagnostic value in predicting lymph node metastasis in patients with rectal cancer and may become an effective biomarker for assessing the patient's lymph node status in these patients. Contrary, DECT quantitative parameters and iodine maps do not provide enough information to determine the nature of lymph nodes in rectal cancer. In the absence of radiomics methods, the diagnosis should be based on an assessment of the short-axis diameter of the lymph node and subjective assessment (e.g., whether LN is round and heterogeneous).

DATA AVAILABILITY STATEMENT

The original contributions presented in the study are included in the article/**Supplementary Material**. Further inquiries can be directed to the corresponding author.

ETHICS STATEMENT

The studies involving human participants were reviewed and approved by Ethics Committee of Affiliated Hospital of Jiangsu University. The patients/participants provided their written informed consent to participate in this study.

AUTHOR CONTRIBUTIONS

DW and ZZ contribute equally to this work. DW, ZZ, LZ, and SJ contributed to the conception of the study. ZZ, LZ, JZ, and QZ performed the data measurement. DW, ZZ, and SW performed the model development. ZZ, DW, and ML contributed significantly to analysis and manuscript preparation. ZZ, XM, PZ, and JX performed the data analysis and wrote the manuscript. HZ, MW, JC, XF, and XM helped perform the analysis with constructive discussions. All authors contributed to the article and approved the submitted version.

FUNDING

This study was supported by the Key project of Jiangsu Provincial Health Commission (Project No.: K2019024), Natural Science Foundation of Jiangsu Province (Project No.: BK20191223), Special Funds for Roentgen Imaging Research of Jiangsu Medical Association (Project No.: SYH-3201150-0023), PhD research startup foundation of Jiangsu University Affiliated Hospital (Project No.: jdfyRC2017010), Young medical talents in Jiangsu Province (Project No.: QNRC2016831), Scientific research project of Jinshan Talent Training Program for high-level leading Talents, Postdoctoral Research Program of Jiangsu Province (Project No.: 2018K299C), and China Postdoctoral Science Foundation (Project No.: 2018M640446).

SUPPLEMENTARY MATERIAL

The Supplementary Material for this article can be found online at: https://www.frontiersin.org/articles/10.3389/fonc.2022.846840/full#supplementary-material

REFERENCES

1. Bray F, Ferlay J, Soerjomataram I, Siegel RL, Torre LA, Jemal A. Global Cancer Statistics 2018: GLOBOCAN Estimates of Incidence and Mortality Worldwide for 36 Cancers in 185 Countries. *CA Cancer J Clin* (2018) 68:394–424. doi: 10.3322/caac.21492
2. Brenner H, Kloor M, Pox CP. Colorectal Cancer. *Lancet* (2014) 383:1490–502. doi: 10.1016/S0140-6736(13)61649-9
3. Horvat N, Carlos Tavares Rocha C, Clemente Oliveira B, Petkovska I, Gollub MJ. MRI of Rectal Cancer: Tumor Staging, Imaging Techniques, and Management. *RadioGraphics* (2019) 39:367–87. doi: 10.1148/rg.2019180114
4. Beets-Tan RGH, Lambregts DMJ, Maas M, Bipat S, Barbaro B, Curvo-Semedo L, et al. Magnetic Resonance Imaging for Clinical Management of Rectal Cancer: Updated Recommendations From the 2016 European Society of Gastrointestinal and Abdominal Radiology (ESGAR) Consensus Meeting. *Eur Radiol* (2018) 28:1465–75. doi: 10.1007/s00330-017-5026-2
5. Elsholtz FHJ, Asbach P, Haas M, Becker M, Beets-Tan RGH, Thoeny HC, et al. Introducing the Node Reporting and Data System 1.0 (Node-RADS): A Concept for Standardized Assessment of Lymph Nodes in Cancer. *Eur Radiol* (2021) 31:6116–24. doi: 10.1007/s00330-020-07572-4
6. Gao Y, Li J, Ma X, Wang J, Wang B, Tian J, et al. The Value of Four Imaging Modalities in Diagnosing Lymph Node Involvement in Rectal Cancer: An Overview and Adjusted Indirect Comparison. *Clin Exp Med* (2019) 19:225–34. doi: 10.1007/s10238-019-00552-z
7. Al-Sukhni E, Milot L, Fruitman M, Beyene J, Victor JC, Schmocker S, et al. Diagnostic Accuracy of MRI for Assessment of T Category, Lymph Node Metastases, and Circumferential Resection Margin Involvement in Patients With Rectal Cancer: A Systematic Review and Meta-Analysis. *Ann Surg Oncol* (2012) 19:2212–23. doi: 10.1245/s10434-011-2210-5
8. Brown G, Richards CJ, Bourne MW, Newcombe RG, Radcliffe AG, Dallimore NS, et al. Morphologic Predictors of Lymph Node Status in Rectal Cancer With Use of High-Spatial-Resolution MR Imaging With Histopathologic Comparison. *Radiology* (2003) 227:371–7. doi: 10.1148/radiol.2272011747
9. Gröne J, Loch FN, Taupitz M, Schmidt C, Kreis ME. Accuracy of Various Lymph Node Staging Criteria in Rectal Cancer With Magnetic Resonance Imaging. *J Gastrointest Surg* (2018) 22:146–53. doi: 10.1007/s11605-017-3568-x
10. Goo HW, Goo JM. Dual-Energy CT: New Horizon in Medical Imaging. *Kor J Radiol* (2017) 18:555–69. doi: 10.3348/kjr.2017.18.4.555
11. Agrawal MD, Pinho DF, Kulkarni NM, Hahn PF, Guimaraes AR, Sahani DV. Oncologic Applications of Dual-Energy CT in the Abdomen. *Radiographics* (2014) 34:589–612. doi: 10.1148/rg.343135041
12. Boellaard TN, Henneman ODF, Streekstra GJ, Venema HW, Nio CY, van Dorth-Rombouts MC, et al. The Feasibility of Colorectal Cancer Detection Using Dual-Energy Computed Tomography With Iodine Mapping. *Clin Radiol* (2013) 68:799–806. doi: 10.1016/j.crad.2013.03.005
13. Özdeniz İ, İdilman İS, Köklü S, Hamaloğlu E, Özmen M, Akata D, et al. Dual-Energy CT Characteristics of Colon and Rectal Cancer Allows Differentiation

From Stool by Dual-Source CT. *Diagn Interv Radiol* (2017) 23:251–6. doi: 10.5152/dir.2017.16225
14. Chuang-Bo Y, Tai-Ping H, Hai-Feng D, Yong-Jun J, Xi-Rong Z, Guang-Ming M, et al. Quantitative Assessment of the Degree of Differentiation in Colon Cancer With Dual-Energy Spectral CT. *Abdom Radiol (NY)* (2017) 42:2591–6. doi: 10.1007/s00261-017-1176-6
15. Lambin P, Leijenaar RTH, Deist TM, Peerlings J, de Jong EEC, van Timmeren J, et al. Radiomics: The Bridge Between Medical Imaging and Personalized Medicine. *Nat Rev Clin Oncol* (2017) 14:749–62. doi: 10.1038/nrclinonc.2017.141
16. Gillies RJ, Kinahan PE, Hricak H. Radiomics: Images Are More Than Pictures, They Are Data. *Radiology* (2016) 278:563–77. doi: 10.1148/radiol.2015151169
17. Huang Y, Liang C, He L, Tian J, Liang C, Chen X, et al. Development and Validation of a Radiomics Nomogram for Preoperative Prediction of Lymph Node Metastasis in Colorectal Cancer. *JCO* (2016) 34:2157–64. doi: 10.1200/JCO.2015.65.9128
18. Benson AB, Venook AP, Al-Hawary MM, Arain MA, Chen Y-J, Ciombor KK, et al. NCCN Guidelines Insights: Rectal Cancer, Version 6.2020. *J Natl Compr Canc Netw* (2020) 18:806–15. doi: 10.6004/jnccn.2020.0032
19. Papanikolaou N, Matos C, Koh DM. How to Develop a Meaningful Radiomic Signature for Clinical Use in Oncologic Patients. *Cancer Imaging* (2020) 20:33. doi: 10.1186/s40644-020-00311-4
20. Halligan S, Menu Y, Mallett S. Why did European Radiology Reject My Radiomic Biomarker Paper? How to Correctly Evaluate Imaging Biomarkers in a Clinical Setting. *Eur Radiol* (2021) 31:9361–8. doi: 10.1007/s00330-021-07971-1
21. Yang Z, Zhang X, Fang M, Li G, Duan X, Mao J, et al. Preoperative Diagnosis of Regional Lymph Node Metastasis of Colorectal Cancer With Quantitative Parameters From Dual-Energy CT. *Am J Roentgenol* (2019) 213:W17–25. doi: 10.2214/AJR.18.20843
22. Peduzzi P, Concato J, Kemper E, Holford TR, Feinstein AR. A Simulation Study of the Number of Events Per Variable in Logistic Regression Analysis. *J Clin Epidemiol* (1996) 49:1373–9. doi: 10.1016/s0895-4356(96)00236-3
23. Schober P, Boer C, Schwarte LA. Correlation Coefficients: Appropriate Use and Interpretation. *Anesth Analg* (2018) 126:1763–8. doi: 10.1213/ANE.0000000000002864
24. Liu H, Yan F, Pan Z, Lin X, Luo X, Shi C, et al. Evaluation of Dual Energy Spectral CT in Differentiating Metastatic From non-Metastatic Lymph Nodes in Rectal Cancer: Initial Experience. *Eur J Radiol* (2015) 84:228–34. doi: 10.1016/j.ejrad.2014.11.016
25. Langman G, Patel A, Bowley DM. Size and Distribution of Lymph Nodes in Rectal Cancer Resection Specimens. *Dis Colon Rectum* (2015) 58:406–14. doi: 10.1097/DCR.0000000000000321
26. Al-Najami I, Beets-Tan RGH, Madsen G, Baatrup G. Dual-Energy CT of Rectal Cancer Specimens: A CT-Based Method for Mesorectal Lymph Node Characterization. *Dis Colon Rectum* (2016) 59:640–7. doi: 10.1097/DCR.0000000000000601
27. Cui C, Cai H, Liu L, Li L, Tian H, Li L. Quantitative Analysis and Prediction of Regional Lymph Node Status in Rectal Cancer Based on Computed Tomography Imaging. *Eur Radiol* (2011) 21:2318–25. doi: 10.1007/s00330-011-2182-7
28. Choi J, Oh SN, Yeo D-M, Kang WK, Jung C-K, Kim SW, et al. Computed Tomography and Magnetic Resonance Imaging Evaluation of Lymph Node Metastasis in Early Colorectal Cancer. *World J Gastroenterol* (2015) 21:556–62. doi: 10.3748/wjg.v21.i2.556
29. Brunette LL, Bonyadlou S, Ji L, Groshen S, Shuster D, Mehta A, et al. Predictive Value of FDG PET/CT to Detect Lymph Node Metastases in Cervical Cancer. *Clin Nucl Med* (2018) 43:793–801. doi: 10.1097/RLU.0000000000002252
30. Chen L-D, Liang J-Y, Wu H, Wang Z, Li S-R, Li W, et al. Multiparametric Radiomics Improve Prediction of Lymph Node Metastasis of Rectal Cancer Compared With Conventional Radiomics. *Life Sci* (2018) 208:55–63. doi: 10.1016/j.lfs.2018.07.007
31. Zwanenburg A, Vallières M, Abdalah MA, Aerts HJWL, Andrearczyk V, Apte A, et al. The Image Biomarker Standardization Initiative: Standardized Quantitative Radiomics for High-Throughput Image-Based Phenotyping. *Radiology* (2020) 295:328–38. doi: 10.1148/radiol.2020191145
32. Hulsmans FH, Bosma A, Mulder PJ, Reeders JW, Tytgat GN. Perirectal Lymph Nodes in Rectal Cancer: *In Vitro* Correlation of Sonographic Parameters and Histopathologic Findings. *Radiology* (1992) 184:553–60. doi: 10.1148/radiology.184.2.1620864
33. Detry RJ, Kartheuser AH, Lagneaux G, Rahier J. Preoperative Lymph Node Staging in Rectal Cancer: A Difficult Challenge. *Int J Colorectal Dis* (1996) 11:217–21. doi: 10.1007/s003840050050
34. Bipat S, Glas AS, Slors FJM, Zwinderman AH, Bossuyt PMM, Stoker J. Rectal Cancer: Local Staging and Assessment of Lymph Node Involvement With Endoluminal US, CT, and MR Imaging–a Meta-Analysis. *Radiology* (2004) 232:773–83. doi: 10.1148/radiol.2323031368
35. Stiksma J, Grootendorst DC, van der Linden PWG. CA 19-9 as a Marker in Addition to CEA to Monitor Colorectal Cancer. *Clin Colorectal Cancer* (2014) 13:239–44. doi: 10.1016/j.clcc.2014.09.004
36. Al-Najami I, Lahaye MJ, Beets-Tan RGH, Baatrup G. Dual-Energy CT can Detect Malignant Lymph Nodes in Rectal Cancer. *Eur J Radiol* (2017) 90:81–8. doi: 10.1016/j.ejrad.2017.02.005
37. Spindler BA, Bergquist JR, Thiels CA, Habermann EB, Kelley SR, Larson DW, et al. Incorporation of CEA Improves Risk Stratification in Stage II Colon Cancer. *J Gastrointest Surg* (2017) 21:770–7. doi: 10.1007/s11605-017-3391-4
38. Moertel CG, O'Fallon JR, Go VL, O'Connell MJ, Thynne GS. The Preoperative Carcinoembryonic Antigen Test in the Diagnosis, Staging, and Prognosis of Colorectal Cancer. *Cancer* (1986) 58:603–10. doi: 10.1002/1097-0142(19860801)58:3<603::aid-cncr2820580302>3.0.co;2-k
39. Horvat N, Petkovska I, Gollub MJ. MR Imaging of Rectal Cancer. *Radiol Clinics North America* (2018) 56:751–74. doi: 10.1016/j.rcl.2018.04.004

Conflict of Interest: The authors declare that the research was conducted in the absence of any commercial or financial relationships that could be construed as a potential conflict of interest.

Frontiers in Oncology

Advances knowledge of carcinogenesis and tumor progression for better treatment and management

The third most-cited oncology journal, which highlights research in carcinogenesis and tumor progression, bridging the gap between basic research and applications to imrpove diagnosis, therapeutics and management strategies.

Discover the latest Research Topics

See more →

Frontiers

Avenue du Tribunal-Fédéral 34
1005 Lausanne, Switzerland
frontiersin.org

Contact us

+41 (0)21 510 17 00
frontiersin.org/about/contact